Imperial College London

Carborane-Induced Deformation of Polycyclic Aromatic Hydrocarbons, and Their Intriguing Emissive Properties

Adam Patrick Vincent Marsh

Submitted in partial fulfilment of the requirements for the degree of

Doctor of Philosophy

Department of Chemistry

Imperial College London

July 2019

‘“I knew exactly what to do…

But in a much more real sense,

I had no idea what to do.”

– Michael Scott’

– Adam Marsh

Declaration of Originality

I declare that the work presented herein is the result of my own work, except where specific references to the contributions of others is given in the text. This thesis has not previously submitted for the award of a degree at this, or any other, institution. This work was carried out within the Department of Chemistry at Imperial College London between October 2014 and July 2019, under the supervision of Professor Martin Heeney.

Adam V. Marsh

July 2019

Copyright Declaration

The copyright of this thesis rests with the author. Unless otherwise indicated, its contents are licensed under a Creative Commons Attribution-Non Commercial 4.0 International Licence (CC BY-NC). Under this licence, you may copy and redistribute the material in any medium or format. You may also create and distribute modified versions of the work. This is on the condition that: you credit the author and do not use it, or any derivative works, for a commercial purpose. When reusing or sharing this work, ensure you make the licence terms clear to others by naming the licence and linking to the licence text. Where a work has been adapted, you should indicate that the work has been changed and describe those changes. Please seek permission from the copyright holder for uses of this work that are not included in this licence or permitted under UK Copyright Law.

Contributions

The work in this thesis would not have been possible without the support of others. I would like to highlight the contributions made by the following people:

Photoluminescence measurements in all chapters were carried out in collaboration with Dr Nathan Cheetham at Imperial College London (ICL). Data collection and analysis carried out by Dr Cheetham on my behalf is highlighted in the text. Low-temperature measurements and analysis in Chapters 3 and 5 were undertaken by Dr Matthew Dyson at ICL and Eindhoven University of Technology, respectively. The synthesis in Chapters 4 and 5 was a collaborative process with constant input from Dr Mark Little at ICL. Temperature-dependent nuclear magnetic resonance measurements in Chapter 2 were performed at ICL by Peter Haycock. Mass spectrometry data in Chapters 2, 4, and 5 were obtained by Dr Lisa Haigh at ICL, with contributions from the EPSRC UK National Mass Spectrometry Facility at Swansea University. Single-crystal X-Ray diffraction measurements in Chapters 2, 4, and 5 were carried out at Imperial College London by Dr Andrew White. Scanning and transmission-electron microscopy measurements in Chapter 3 were undertaken by David Poussin at ICL. Calculations in Chapter 5 were made possible with the help of functional tuning scripts provided by Dr Karl Thorley at ICL.

Lastly, the illustrations in this thesis are a combination of the superb talents of Marissa Lewis and Marina Parras.

Thank you all.

Acknowledgements

I am still not sure how I got towards the end of a PhD, never mind that I started one. I am sure, however, that without the following people I would not have got nearly this far.

First, I would like to thank Prof. Martin Heeney for his supervision and guidance over the past four-and-a-bit years. He has given me huge amounts of freedom to explore ideas that I find interesting, and simply for their own sake. I have come to learn how rare that freedom is, and how rare a supervisor like Martin is. Looking back, the only time I can ever question his judgement is when he decided to give a very average Chemistry graduate (i.e. me) a chance to study for a PhD. Since I started here, I've worked to try and repay this immense favour. Thank you, Martin! Thanks also go to Peter, Colin, Tony, and Nick from AWE for the financial support that made this research possible, and all the thought-provoking conversations over the past few years.

In my time at Imperial I have been welcomed into the larger, Harwood Lab family. I would like to thank Pierre, Josh, Abby, Rolf, Yang, Brett, Simeng, Haojie, Shengyu, Notina, Charlotte, Petr, Munazza, Florian, Qiao, Martina and every member of the Heeney group. Special thanks go to Iain and Tom, my fumehood neighbours for most of the PhD, for all our conversations about, well, everything. To Creamer for chats about comedy and our shared love of Karl Pilkington. And of course, thanks go to Fei, a source of chemistry knowledge, humour, and football on the weekends.

The lab would not be the same if not for the McCulloch group, who are all brilliant too. Special thanks go to Mark, who was always available for discussions about chemistry, which formed the foundation of most of this work. Truly, without meeting him, the pages of this thesis would look very different, and would probably be a lot less interesting. I already miss those discussions, but I will mostly miss that beautiful beard. I am also very grateful to Alex and Cameron for their encouragement and ideas, which helped me get through tough times. Thanks too to Karl, the computational wizard who was always more than willing to share with me everything he knew. And to Matt B, for the quick after-work beers, and chats in the lab.

In the course of this work, I have met a lot of utterly superb people around the university. First, I would like to thank Nathan, for all the time spent on the FluoroMax, all the discussions about the data, and everything that came from it. I would also like to thank Matt D for all the help with temperature-dependent PL studies and all the insightful Skype conversations. I have learned so much from both of

you (I would expect no less from Durham graduates) - and I had great fun throughout! Thanks also go to David P for all the time and effort on the microscopy work. You'll never get back those many hours lining up the beams of the TEM, but I appreciate every minute you took to help me out.

The support staff and students in the CPE have all been amazing. Thanks go to Lisa and Steph for all the work in making the CPE such a great place to be. An additional thanks to Prof. Paul Stavrinou who interviewed me, and later generously gave a significant amount of his time to help in the publication of our carborane paper. I have loved meeting and getting to know all the Cohorts, but especially everyone in Cohort 6: Ali, Stefan, Ada, Seb, Tingmang, Bob, Wenmin, Kevin, Oli, Becky, and Adam.

I have met some brilliant people whilst subwardening at Imperial. Thanks go to Amy, Paul, Melis, Eirik from Wilson House, and Becky and Chloe from Selkirk. An extra special thanks goes to Marissa, someone who I am so proud to call a friend. All our coffee chats over the years have been so important to me and just brilliant. Thanks go to David, the Warden of Selkirk, for being such an incredibly supportive influence since literally the first time we met. Many times over the past couple of years you have taken time out of your exceedingly busy schedule to talk over chemistry, work, and life, and I have valued every minute of those conversations. Thanks also go to the Wardens in Southside, Phil, and Martyn, for creating such a pleasant environment in which to work. And a second thanks to Martyn for the projects abroad, which were such a good laugh.

To my great friends, Alex, Phil, Ryan, Tim, and Tom. Your understanding when I had no money and helping me correct things when my work/life balance was so wrong, is massively appreciated. I look forward to many great times in the years to come. I'd also like to thank my friends from school, Jose, Nathan, and Danny; you guys have played a big part in me getting to this point.

Lastly, I want to thank my family. To my siblings, Peter and Penny, I am incredibly grateful for the indescribably large amount of support over the years. I am so proud of how well you both are doing and cannot wait to see what you do in the future. Thanks also to Francesca for being an all-round brilliant sister-in-law. To Auntie Bett, for helping raise us and being such a huge part of our lives. To Freddie, one of the few cats in the world well-versed on carboranes. To my grandparents, and especially Vincent and Betty, who saw the start of this project, but not the end. And mum and dad, simply, thank you for everything.

To mum and dad,

Abstract

Carboranes, $C_2B_{10}H_{12}$, are bulky, icosahedral cluster compounds, with unique molecular bonding and electronic properties. Since their discovery in the middle of the 19th century, they have been studied and used in a wide range of chemical fields, with the aims of exploiting their excellent thermal and chemical stability, electron-withdrawing capability, and, more recently, their ability to act as modifiers and promotors of photoluminescence (PL). The effects of carboranes on PL have now been widely reported in the literature, but questions remain about the underlying processes dictating these behaviours. This work is an attempt to answer some of those questions.

In this thesis, the three structural isomers of carborane (*ortho*, *meta* and *para*) have been incorporated into a range of linear and non-linear aromatic systems, forming highly sterically strained structures. This phenomenon correlates with reduced carborane rotation, as determined by DFT and NMR investigations. All carboranes studied are fluorescent, showing local emission (LE) from the aromatic moiety, however the *ortho*-carborane compounds also demonstrate multi-emissive behaviour, as the carborane introduces a delocalised emissive species, associated with intramolecular charge-transfer (ICT) and twisted-ICT (TICT) states, the latter of which occurs when the carboranyl C-C bond is perpendicular to the aromatic plane. By introducing phenyl groups to *ortho*-carborane, it was shown that the ground state could be tuned to favour TICT formation, through favourable π-π interactions between the aromatic substituents 'locking' the C-C bond in the perpendicular arrangement.

Chrysene and phenanthrene-based *ortho*-carborane compounds were found to exhibit a peculiar, concentration-dependent, low-energy emissive peak. Through detailed temperature-dependent optical studies, these emissive excited states were assigned to excimers, the first time such species, involving a carborane in a charge-transfer state, has been observed.

In aggregated states, formed in bad solvents, the PL intensity for the *meta* and *para*-carboranes is reduced, but for the *ortho*-carborane compounds the intensity increases enormously, as a result of aggregation-induced emission (AIE). AIE is determined to be as a result of TICT emissive species, where the excited state is localised inside *ortho*-carborane, reducing non-radiative decay routes and boosting PL quantum yield. The aggregates were directly imaged with a combination of scanning and transmission electron microscopy (SEM and TEM respectively) and were found to form spherical nanoparticles, with evidence of crystallinity.

Publications

Published:

A. V. Marsh, R. Simpson, P. D. Marsh, Cocaine on banknotes - Late Night Science - YouTube, https://www.youtube.com/watch?v=dyT8nuMR238&t=77s, (accessed 21 March 2019).

A. V. Marsh, N. J. Cheetham, M. Little, M. Dyson, A. J. P. White, P. Beavis, C. N. Warriner, A. C. Swain, P. N. Stavrinou and M. Heeney. Carborane-Induced Excimer Emission of Severely Twisted Bis-o-Carboranyl Chrysene. *Angewandte Chemie International Edition*, 2018, **57**, 10640–10645.

Precursory studies to the work presented in Chapter 5.

In Preparation:

A. V. Marsh, M. Dyson, D. Poussin, N. J. Cheetham, M. Bidwell, A. J. P. White, P. Boufflet, P. Beavis, C. N. Warriner, A. C. Swain and M. Heeney. The structural and photophysical properties of *ortho*, *meta*, and *para*-carboranyl anthracene dyads.

Based on the work presented in Chapter 2 and 3.

A. V. Marsh, N. J. Cheetham, M. Little, M. Dyson, A. J. P. White, P. Beavis, C. N. Warriner, A. C. Swain and M. Heeney. Unprecedented aromatic deformation of phenyl-*ortho*-carboranyl non-linear acenes.

Based on the work presented in Chapter 4.

Published Collaborations:

A. Creamer, A. Casey, **A. V. Marsh**, M. Shahid, M. Gao and M. Heeney. Systematic Tuning of 2,1,3-Benzothiadiazole Acceptor Strength by Monofunctionalization with Alkylamine, Thioalkyl, or Alkoxy Groups in Carbazole Donor–Acceptor Polymers. *Macromolecules*, 2017, **50**, 2736–2746.

A. Creamer, C. S. Wood, P. D. Howes, A. Casey, S. Cong, **A. V. Marsh**, R. Godin, J. Panidi, T. D. Anthopoulos, C. H. Burgess, T. Wu, Z. Fei, I. Hamilton, M. A. McLachlan, M. M. Stevens and M. Heeney.

Post-polymerisation functionalisation of conjugated polymer backbones and its application in multi-functional emissive nanoparticles. *Nature Communications*, 2018, **9**, 3237.

M. Rimmele, K. Ableidinger, **A. V. Marsh**, N. J. Cheetham, M. J. Taublaender, A. Buchner, J. Prinz, J. Fröhlich, M. M. Unterlass, M. Heeney and F. Glöcklhofer. Thioalkyl- and sulfone-substituted poly(p-phenylene vinylene)s. *Polym. Chem.*, 2019, **10**, 738–750.

S. Pont, S. Osella, A. Smith**, A. V. Marsh**, Z. Li, D. Belionne, J. Cabral and J. Durrant. Evidence for strong and weak PCBM photo-dimer populations in organic solar cells. *Chemistry of Materials*, (Under Review) (2019).

Q. He, S. Munazza, J. Panidi, **A. V. Marsh**, W. Huang, M. Daboczi, J-S. Kim, F. Zhuping, T. Anthopoulos and M. Heeney. A versatile star-shaped organic semiconductor based on benzodithiophene and diketopyrrolopyrrole. *Journal of Materials Chemistry C*, (Under Review) (2019).

Abbreviations

ACQ – Aggregation Caused Quenching
AIBN – Azobisisobutyronitrile
AIE – Aggregation-Induced Emission
ATRC – Atom Transfer Radical Cyclisation
BDT – Benzo[2,1-b:3,4-b']dithiophene
BHQ – Bull-Hutching-Quayle (reaction)
Bmim(Cl) – 1-Butyl-3-methylimidazolium chloride
BZTT – Benzocarborano[2,1-b:3,4-b']dithiophene
CV – Cyclic Voltammetry
DCB – 1,2-Dichlorobenzene
DCM – Dichloromethane
DDQ – 2,3-Dichloro-5,6-dicyano-1,4-benzoquinone
DLS – Dynamic Light Scattering
DMF – Dimethylformamide
DP – Degree of Polymerisation
DSC – Differential Scanning Calorimetry
DSD – Diamond-Square-Diamond
E_0 – Emissive Energy Maximum
ESIPT – Excited State Intramolecular Proton Transfer
ESR – Electron Spin Resonance (spectroscopy)
f.p. – Freezing Point
FWHM – Full Width Half Maximum
HEF – High Energy Fuel
HOMO – Highest Occupied Molecular Orbital
HPLC – High-Performance Liquid Chromatography
HR – Huang-Rhys Parameter
ICT – Intramolecular Charge Transfer
IRF – Instrument Response Function
LE – Localised Emission
LUMO – Lowest Occupied Molecular Orbital
MED – Minimal Erythemal Dose
MM – Molecular Mechanics
m.p. – Melting Point
NBS – *N*-Bromosuccinimide
NMR – Nuclear Magnetic Resonance (spectroscopy)
NOESY – Nuclear Overhauser Effect Spectroscopy
NTP – Naphtho[2,3-b]thiophene
OFET – Organic Field Effect Transistor
OLED – Organic Light-Emitting Diode
ONIOM – Own N-Layer Integrated Molecular Orbital + Molecular Mechanics (method)
ORTEP – Oak Ridge Thermal Ellipsoid Plot
OPV – Organic photovoltaics
P3HT – Poly(3-hexylthiophene)
PAH – Polycyclic Aromatic Hydrocarbon
PCM – Polarisation Continuum Model
PES – Potential Energy Surface
Pet. Ether – Petroleum ether, b.p. 40-60 °C.
PL – Photoluminescence Emission (spectroscopy)
PLE – Photoluminescence Excitation (spectroscopy)
PLED – Polymer Light-Emitting Diode
R.T. – Room Temperature
SCRF – Self-Consistent Reaction Field
SEM – Scanning Electron Microscopy
SOMO – Singly Occupied Molecular Orbital
SOP – Standard Operating Procedure
TBAF – Tetrabutylammonium Fluoride
TD-DFT – Time-Dependent Density Functional Theory
TEM – Transmission Electron Microscopy
TFR – Triangular Face Rotation
T_g – Glass Transition Temperature
TGA – Thermogravimetric Analysis
THF – Tetrahydrofuran
TICT – Twisted Intramolecular Charge Transfer
TIPS – Triisopropylsilane
TMEDA – Tetramethylethylenediamine
TMS – Trimethylsilyl
TNT – Trinitrotoluene
UV – Ultraviolet Light
UV-Vis – Ultraviolet-Visible (spectroscopy)
XRD – X-ray Diffraction
2c2e – 2-Centre 2-Electron (bond)
δ – Chemical Shift
λ – Wavelength
λ_{em} – Maximum Emissive Wavelength
λ_{max} – Maximum Wavelength
σ – Peak Line-Width
Φ – Photoluminescence Quantum Yield.

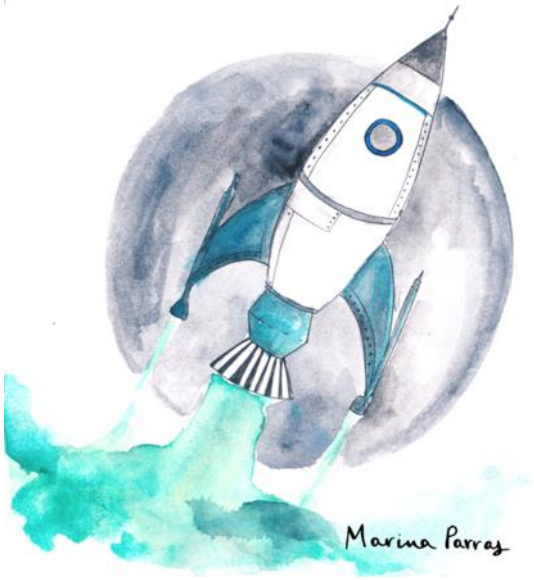
Contents

Declaration of Originality ... **iii**
Copyright Declaration ... **iv**
Contributions ... **v**
Acknowledgements ... **vi**
Abstract ... **ix**
Publications ... **x**
Abbreviations ... **xii**
Contents ... **xiii**

Preface ... **1**
Chapter 1 - Introduction ... **4**
1.1 – Early History ... 4
1.2 – Bonding, Structure and Properties of Carboranes ... 6
1.3 – Synthesis of Carboranes ... 8
1.4 – Carbon Substitution ... 13
1.5 – Boron Substitution ... 17
1.6 – Applications of Carboranes ... 19
1.7 – Carboranes in Conjugated Systems ... 22
1.8 – Carboranes in Conjugated Polymers ... 27
1.9 –Carboranes in Luminescent Materials ... 33
1.10 – In This Thesis ... 40
1.11 – References ... 42
Chapter 2 – The Synthesis, Structure, and Properties of Tricyclic-Substituted Carboranes ... **47**
2.1 – Introduction ... 47
2.2 – Synthesis of Anthracenyl Carboranes ... 50
2.3 – Thermogravimetric Analysis ... 53
2.4 – X-ray Crystallography ... 54
2.5 – Calculations ... 55
2.6 – NMR ... 60
2.7 – Tricyclic Heterocyclic Carboranes ... 63

2.8 – Synthesis of Tricyclic Heterocyclic Carboranes 64
2.9 – X-ray Crystallography 69
2.10 – Calculations 71
2.11 – NMR 80
2.12 – Conclusions 81
2.13 – Experimental 82
2.14 – References 97
Chapter 3 – The Photoluminescence of Tricyclic-Substituted Carboranes; Understanding AIE 99
3.1 – Introduction 99
3.2 – Optical Studies of the Anthracenyl Carboranes 102
3.3 – Aggregation-Induced Emission 119
3.4 – Solution, Aggregated and Solid-State Emission 123
3.5 – Tricyclic Heteroaromatic *ortho*-Carboranes 125
3.6 – The Nature of the Aggregation 130
3.7 – Crystallinity of the Nanoparticles 137
3.8 – Conclusions 140
3.9 – Experimental 142
3.10 – References 144
Chapter 4 – The Synthesis, Structure and Properties of *ortho*-Carboranyl Non-Linear Acenes 146
4.1 – Introduction 146
4.2 – Synthesis 148
4.3 – X-ray Crystallography 154
4.4 – Calculations 158
4.5 – Optical Studies of the Carboranyl Non-Linear Acenes 159
4.6 – Conclusions 170
4.7 – Experimental 172
4.8 – References 185
Chapter 5 – Carborane-Induced Excimer Emission of Twisted Bis-*ortho*-Carboranyl Chrysene 186
5.1 – Introduction 186
5.2 – Synthesis 188
5.3 – X-ray Crystallography 190
5.4 – Calculations 193
5.5 – Optical Studies of Ph*o*Cb_2Chry 199
5.6 – Conclusions 214
5.7 – Experimental 216

5.8 – References 222
Conclusions and Further Work **223**
Appendix I – Page of Numbered Structures **227**
Appendix II – Crystal Data and Structure Refinements **228**
Appendix III – Aromatic Deformation Parameters **235**
Appendix IV – Cyclic Voltammetry **236**
Appendix V – Optical Data from Chapter 3 ..... **238**
Appendix VI – Lippert-Mataga Equation **245**
Appendix VII – Optical Data from Chapter 4 ..... **246**
Appendix VIII – Optical Data from Chapter 5 ..... **250**
Appendix IX – Biodegradable UV Filters **251**



Preface

Carboranes have a particularly curious history. Like many areas of science, their existence can be ascribed to an intense period of research triggered by war. The classified beginnings of carborane research predate their appearance in the literature, and accordingly, this short preface is an attempt to document their 'prehistory'.

The arrival of the German V-2 rocket in the autumn of 1944 was a shock to the US Army. It was a long-range guided ballistic missile, capable of leaving Earth's atmosphere and, importantly, the US had no such capability.[1] As a response, in the winter of the same year, the Hermes Project was undertaken to assess the missile needs of the US military, with a particular focus on understanding the science and engineering behind the advanced V-2.[2]

Not long after the war in Europe was over, and after racing to capture the rocket manufacturing plants, parts and plans to build around one hundred V-2 rockets were transported to the US for further research, along with many of the senior German aerospace engineers.[3] This expedited advanced rocketry in the US, with people and money poured into all areas of aerospace research.

One such area was propellants. Any way to make rockets or jet engines more powerful and efficient was of interest to the US military, and the Hermes Project investigated many potential fuels. Of these, boranes seemed to be particularly promising; they have a heat of combustion about 50% higher than

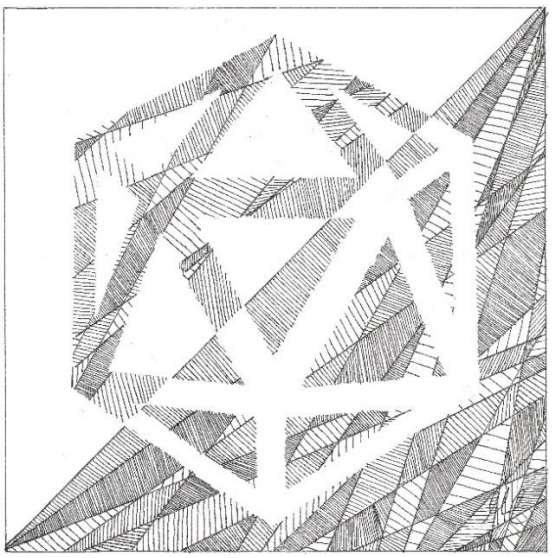
kerosene,[4,5] their mass and density is low, and boron is an easily obtainable element. Such was the promise, the US Navy started Project Zip in 1952 with the specific purpose of investigating borane-based fuels and promptly invested around $1 billion dollars into the project.[6]

Initial tests were carried out on a hypergolic combination of liquid oxygen oxidiser and either diborane or pentaborane fuel, which burned to leave a distinctive bright-green exhaust flame. The performance was very poor, and a glassy residue of B_2O_3 was left in the reaction chamber which would easily shred any finely tuned jet engine.[4] Fluorine was then tested as an oxidiser, forming gaseous BF_3 as the product of combustion and solving the B_2O_3 problem, but the temperature in the nozzle was exceedingly high, and the engine would melt without engineering a complex (and heavy) cooling system.[7] Toxicity and safety was also a major consideration, and so the focus changed to a decaborane fuel source, which was significantly more stable and less toxic. Alkyl groups were attached to liquify the decaborane at room temperature and reduce the hydrolysis rate, thereby allowing for long term storage.[8] High energy fuels (HEF) containing decaborane were produced on plant scale, and such was the optimism of their potential that many new strategic nuclear bombers were designed specifically to use HEF.[9] Ultimately, however, the B_2O_3 problem was never solved and HEF fuel was never used outside the testing laboratories. Further, the contemporary rocket engine designs made use of the much simpler kerosene/liquid oxygen propellant mix and could achieve their aims without the extra thrust boranes could provide. Notably, however, a triethylaluminium/triethylborane mix is used as a pyrophoric ignitor of the Merlin engines on the SpaceX Falcon 9.[10]

The propellant fuel project proved unsuccessful, but there was still hope for borane monopropellants, that is, fuels that require no separate oxidiser. One such monopropellant was $B_{10}H_{12}.2NH_3$ dissolved in hydrazine, which would detonate to produce BN and H_2 stoichiometrically.[7] It was synthesised by the Hawthorne group at Rohm and Haas in 1958, after they reacted the acetonitrile adduct of decaborane with hydrazine, aiming, unsuccessfully, to incorporate an N-N group into the basket structure. Ultimately the mixture was unsuitable for use as a monopropellant, being almost as unstable as TNT. At some point the same year, the Cohen group at Reaction Motors found that a C-C bond *could* be incorporated into decaborane,[7] forming an exceedingly stable compound with formula $C_2B_{10}H_{12}$, later to be named ‘carborane’.

Carborane monopropellant research were ultimately proved unsuccessful, but the unique properties of the carborane were of great interest to many at the time, including Cohen and Hawthorne who were to be pioneers in carborane research, aided by the stockpiles of boranes made available following the conclusion of Project Zip in 1959. Incidentally, the Soviet Union was also active in this

area,[11] publishing their first papers on carboranes in 1963, with both sides benefitting from the declassification of their borane research during this decade. From this point on, carborane research was published openly, and so began the 60 years of literature on these remarkable compounds.



Chapter 1 – Introduction

1.1 – Early History

The appearance of carboranes in the literature came soon after the isolation of the icosahedral borate, $[B_{12}H_{12}]^{2-}$, which years earlier was predicted to be stable based on a molecular orbital analysis.[1,2] Following this, it was theorised that the molecule $C_2B_{10}H_{12}$ could also be stable as 'CH' is isolable to 'BH^-', thus this molecule would be electronically equivalent to $[B_{12}H_{12}]^{2-}$.[3] Within a year, in a series of papers in the December of 1963, two American and one Russian group simultaneously published the isolation of this new compound (named 'carborane' by the former and 'barene' by the latter – eventually 'carborane' became the accepted nomenclature), and made the first observations of its properties.[*3–11] It was immediately clear that this molecule was quite unique, especially with regard to its stability, a thought exemplified by Zakharkin et al. in their initial paper:

> *"Barene ($C_2B_{10}H_{12}$) and its derivatives have great thermal stability, are stable in air, do not undergo change when heated with strong mineral acids, and also are rather stable toward the action of bases and oxidizing agents…."*[11]

[*] The two American groups were sponsored by Olin Mathieson Chemical and Thiokol respectively, both of whom were heavily involved in Project Zip, demonstrating how declassification allowed for the immediate dissemination of their borane research.

In all cases, carborane had been isolated via a reaction between decaborane and acetylene in the presence of a Lewis base; a synthetic route which, as will be discussed in detail later, is still very much in use today.

Whilst carborane had been isolated, its structure was still to be determined. Similar reactions of lower order boranes had produced nest-like structures which preserved the C-C bond of the acetylene starting material.[12] The same was true of carborane; initial X-ray investigations suggested that the structure involved two adjacent carbon atoms atop a decaborane-like cage,[13] akin to a wicker basket. This was mostly accurate, but the correct structure was later confirmed to be a near-perfect icosahedron,[14] and it was named '*ortho*-carborane' (**1**), recognising that the carbon atoms were nearest neighbours in the 1 and 2 positions of the cage. The carborane atom numbering system is presented in **Appendix I**.

The question was then whether the two other possible carborane structural isomers could be isolated – and they quickly were. It was discovered that heating *ortho*-carborane at around 500 °C for 12 hours yielded *meta*-carborane (**2**) (originally named neocarborane),[15] and if one heated *that* at 600 °C for 12 hours, *para*-carborane (**3**) was formed, **Figure 1-1**.[16] Details of the thermal isomerisation will be discussed later.

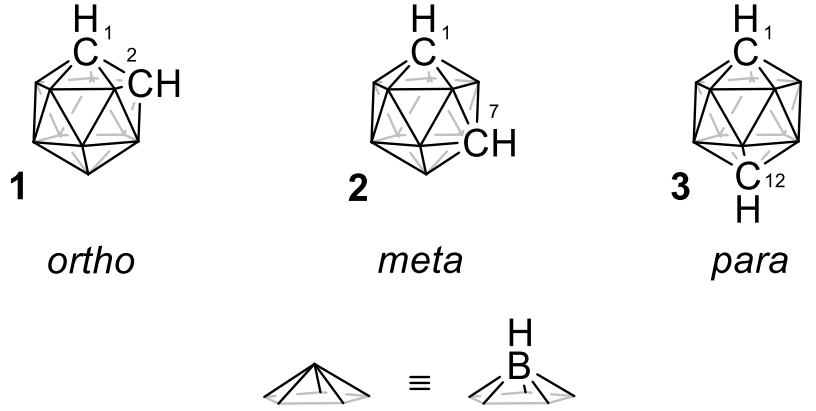


Figure 1-1 – The structure of *ortho*, *meta,* and *para*-carborane, with carbon atom numbers labelled. For clarity and in accordance with convention, the BH groups are displayed as blank vertices on the icosahedron.

By the end of 1964 the three parent carboranes had been discovered, the flood of post-declassification publications had been quelled, and attention turned to exploring and exploiting the fascinating properties of the carborane.

1.2 – Bonding, Structure and the Properties of Carboranes

Upon introduction to the structure of carboranes, any trained chemist will look twice; they appear to be quite strange. More specifically, each carbon atom in carboranes have 6 nearest neighbours (to a first approximation) which is precisely two more than what is ordinarily considered the maximum for carbon.

This is a clear structural indication that the bonding in carboranes is non-classical, and indeed, a classical approach to the bonding of carboranes predicts properties that do not bear out experimentally. When one considers the atomic orbitals involved in bonding, 2s and $2p_{x,y,z}$ for each boron and carbon, and 1s for each hydrogen, the number totals 60. Electron occupation of these orbitals dictates that carbon contributes four, boron three, and hydrogen one electron to the total cage electron count, totalling 50. This description, based on a classical 2-centre-2-electron (2c2e) model, suggests that the carborane has too few electrons to be stable, or is 'electron-deficient'.[17] This description sits in stark contrast to their extreme thermal and chemical stability and it is therefore clear that the 2c2e description is not sufficient to explain bonding in carboranes.

1.2.1 – Wade-Mingos Rules

A more informative model is provided by Wade-Mingos rules; a system in which borane clusters can be considered to be formed from smaller, covalently bonded subunits.[18,19] Importantly, each of these uses three orbitals in cage bonding: two p-orbitals tangential to the cluster, forming $\sigma_{x,y}$ molecular orbitals on the surface; and one sp-orbital directed inwards, constructively overlapping to form a single, unique molecular orbital at the centre of the cluster.[17] For an *n* vertex cluster the model predicts *n* + 1 bonding molecular orbitals, which for carboranes is 13. One must then consider the electron contributions from each subunit involved in the bonding cluster framework, i.e. not including the two valence electrons involved with each 'external' B-H and C-H bond. The ten BH subunits have 2, and the two CH subunits have 3 valence electrons, totalling 26 and completely filling the 13 bonding molecular orbitals of the carborane, **Figure 1-2**.

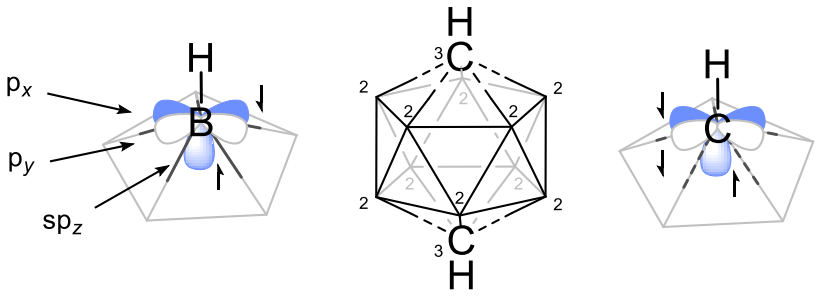


Figure 1-2 – A depiction of the atomic orbitals and electrons contributed by boron and carbon vertices to the skeletal bonding of *para*-carborane.

Wade-Mingos rules go further than rationalising the stability of carboranes. They can be used to predict the geometry of a huge variety of compounds, from transition metal clusters to fullerenes and fused polyhedra.[17,20] They also predict the structure of open-cage (non-*closo*) carboranes species, such as those that form following electrochemical reduction; the anion $[C_2B_{10}H_{12}]^{2-}$ is an open-cage, *nido* species owing to the $2n + 4$ skeletal electron count, and the monoanion radical $[C_2B_{10}H_{12}]^{-\cdot}$ with a $2n + 3$ electron count is somewhere between *closo* and *nido*. Monoanion radicals of *ortho*-carborane are particularly interesting as ESR spectra reveal that the unpaired electron is likely delocalised across the cage framework.[21] This is a demonstration of another unique property of carboranes, the three-dimensional 'cluster aromaticity'.

1.2.2 – Cluster Aromaticity

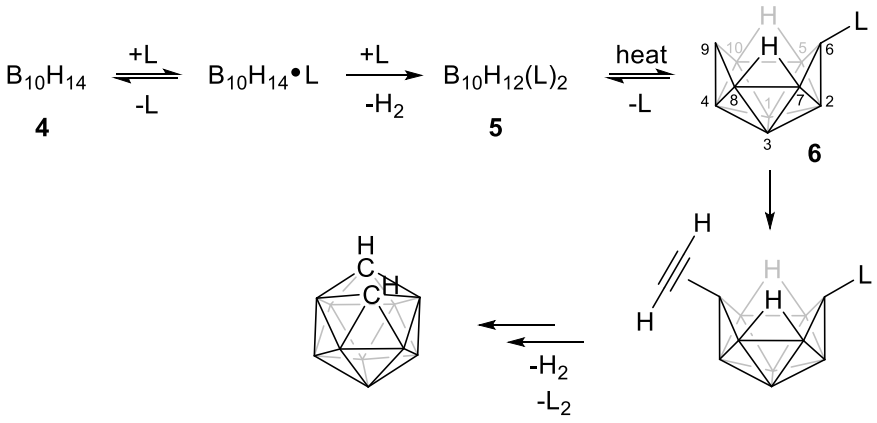
Conventional aromatic systems are composed of delocalised π-electrons, but carboranes contain no such π-system; the skeletal framework is constructed solely from σ-orbitals. However, there are 26 electrons involved in bonding, which is $2\frac{1}{6}$ per vertex, so clearly there must be some sharing of electrons around the cage. This has led many people to describe boranes as having cluster aromaticity, and in the case of the *closo*-boranes and carboranes: superaromaticity.[17] This comparison to arenes is generally quite apt; both show enhanced thermal and chemical stability compared to otherwise similar non-aromatics, both react with electrophiles in aromatic substitution reactions, and even the substitution patterns are similar.[17] More direct evidence for cluster aromaticity has been provided by NMR studies which have shown the nuclear independent chemical shift, which is the negative of the magnetic shielding at the centre of a ring or cluster, is large and negative for a series of carboranes.[22,23] Negative values are associated with diamagnetism due to cyclic conjugation. A second aromaticity criterion, the topological resonance energy, which is the stabilisation energy introduced by cyclic conjugation, correlates strongly with those measurement.[24,25]

It is therefore accepted that carboranes are somewhat aromatic; however, the delocalisation does not necessarily extend into π-systems to which the carborane is attached. Indeed, incorporating the desirable electronic properties of the carborane into larger π-systems is a real challenge in many fields. Encouragingly, the synthetic versatility of carboranes means that there are many possible ways of achieving this goal.

1.3 – Synthesis of Carboranes

1.3.1 – *Ortho*-carborane

Ortho-carborane was first synthesised via the coupling of acetylene and decaborane in the presence of a Lewis base in a two-step procedure.[3,7,11] First, decaborane is dissolved in a small excess of the Lewis base ('L'), e.g. acetonitrile or diethyl sulfide, and heated to reflux for about one hour, evolving H_2 and forming the decaborane complex 6,9-$L_2B_{10}H_{12}$.[26] This species is stable and can be isolated and stored in bulk for use in future reactions. The acetylene (or acetylenic derivative) is then added and the mixture is refluxed in a non-polar solvent, often toluene, until the reaction is completed, usually about 24 hours. A recent adaptation has been to include catalytic amounts of a Lewis acid, specifically $AgNO_3$ and other silver(I) salts, as they reportedly reduce hydroboration side reactions and increase yields.[27,28] The reaction can also be performed in one-step, with significantly reduced reaction times and at reduced temperature, in a procedure using an ionic liquid as a catalyst.[29–31] Whilst the ionic liquids are cheap and non-toxic, they do tend to be highly hygroscopic and so more rigorous water-exclusion measures are required.[32] The original procedure is therefore still predominant in the literature, and the proposed mechanism is presented in **Scheme 1-1**. It should be noted that the mechanism is still not precisely understood, especially regarding the icosahedron forming step, thus the description shown is based on the best available evidence from the literature.



Scheme 1-1 – The proposed mechanism for the formation of *ortho*-carborane from decaborane and acetylene, in the presence of a Lewis base, 'L'.

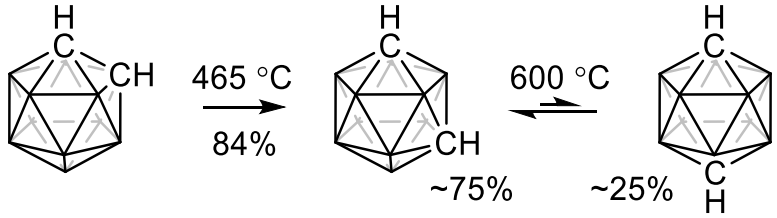
The decaborane complex $L_2B_{10}H_{12}$ (**5**) is formed following a rapid, reversible first-step in which decaborane (**4**) reacts with a Lewis base ligand.[33–36] Only when the second ligand reacts and H_2 produced is the stable complex created. Dissociation still occurs however, and the loss of a ligand from the complex creates a highly reactive intermediate (**6**), the exact structure of which is not clear,[35] although many have been proposed.[37,38] The acetylene reacts with this complex, then proton abstraction from the 7-8 boron position B-H-B bridge generates an electron pair which is shared with an empty orbital on the boron in the 6 position.[36] This displaces the ligand on that side, and triggers a 'twist-collapse' process that initiates the formation of the icosahedron.[35,39]

The mechanism for reactions with decaborane and acetylenes catalysed by ionic liquids has also been proposed and is perhaps better understood than the Lewis base procedure. Decaborane is first deprotonated to form the $B_{10}H_{13}^-$[ionic liquid cation]$^+$ salt, followed by proton rearrangement to an electrophilic structure with a highly localised LUMO on the boron in the 6 position.[31] The acetylene binds to the $B_{10}H_{13}^-$ anion to form an *arachno*-adduct, with then reacts with a proton source (e.g. an acidic group of the ionic liquid cation) to form the carborane product with evolution of H_2.[31]

There are an increasingly wide range of reported substituted acetylenes which can react with decaborane in this way, where the R groups include aryl, alkyl, alkenyl, alkynyl (although disubstitution problems are likely to occur), amino, carbamate, carbonyl, ester, halo, hydroxy, and nitriles.[27,28,31] However, there are still many functional groups which cannot be tolerated, such as carboxylic acids and nitro groups, both of which react with decaborane. And there are other cases where steric hindrance prohibits the acetylenic approach, e.g. silyl groups or large aromatic systems, and in all cases where an internal acetylene is used.[17] It is therefore often desirable to use different carbon-substitution methods, to be covered later.

1.3.2 – *Meta* and *para*-carborane

Clearly, reactions of decaborane and acetylene cannot produce *meta* and *para*-carborane as the carbon-carbon bond is always preserved. Experimentally it was demonstrated very early on that the reactivity of the series decreases on the order *ortho* > *meta* > *para* for all kinds of chemistry;[40] the more uniform distribution of electron density as the carbon atoms are separated increases the stability of the compounds. It followed that thermodynamic stability would increase in the same fashion,[41] and indeed this is the case. One can synthesise *meta* and *para*-carborane by heating *ortho*-carborane at high temperature, under a flow of nitrogen, for about 24 h,[†] **Scheme 1-2**.[15,16,40]



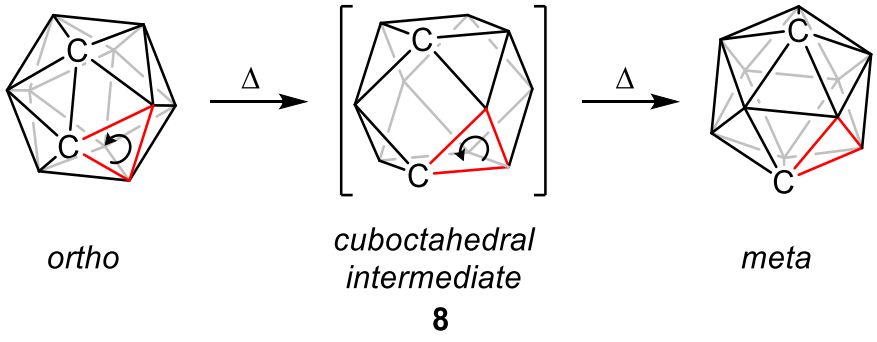
Scheme 1-2 – The synthesis of *meta* and *para*-carborane through thermal isomerisation of *ortho*-carborane. The *meta* and *para* isomers are in equilibrium and can be separated by chromatography, yielding *para*-carborane in ca. 22% yield under optimum conditions.[43]

The mechanism of isomerisation is quite difficult to probe experimentally. The very high temperatures required for reaction means it is practically not possible to isolate any reaction intermediates, even if they were stable enough to isolate in the first place. Vertex labelling offers a convenient solution; label one or more vertices of the starting material isotopically or chemically by substituting the protons, then isomerise and deduce the mechanism by analysing the products. Again however, there are challenges. ^{10}B Isotopic enrichment of carboranes is possible, but upon thermal treatment the rearrangement of the boron atoms occurs much faster than the isomerisation of *ortho* to *meta*-carborane, scrambling the labelling.[44] This is still an interesting result in its own right, but not useful for probing how the isomerisation occurs. Labelling by substitution of the protons is also problematic, as it has been demonstrated some groups can drastically lower the temperature required for *ortho* to *meta* isomerisation,[45,46] raising questions as to whether these groups are also changing the mechanism they were introduced to understand.

[†] It is important to note that carboranes are expensive, with the price increasing drastically from *ortho* to *para*. The high-temperature processes described above, coupled with the low yield and chromatographic separation required, makes carboranes very difficult to make on industrial scales. Currently there is only one manufacturer – worldwide – for all carboranes,[42] and accordingly, the prices are very high.

Halogen labelling has provided the best experimental evidence for understanding the rearrangement pathways, and the development of computational methods over the past few decades has contributed significantly to the discussion. There is now little debate in the literature that thermal isomerisation of *ortho* to *meta*-carborane (only) occurs via a diamond-square-diamond (DSD) mechanism through a cuboctahedral intermediate (**7**).

The cuboctahedral intermediate was thought to play a role in the transformation very early on, in fact this was even hypothesised before *ortho*-carborane had been isolated.[47,48] It was realised that the square faces of the cuboctahedron could collapse to form diamonds in which two, previously adjacent, atoms would move into non-adjacent positions; the essence of the DSD mechanism.[49] Later, experimental evidence gained from isomerisation of halogenated carboranes demonstrated that the model would have to be adjusted to allow for triangular face rotation (TFR) in order for the theoretical distribution of products to match the experimental distribution.[46] Forty years later, density functional theory (DFT) calculations have all but confirmed the role of DSD and TFR in the isomerisation of *ortho* to *meta*-carborane,[50] and a simplified version is shown in **Scheme 1-3**.

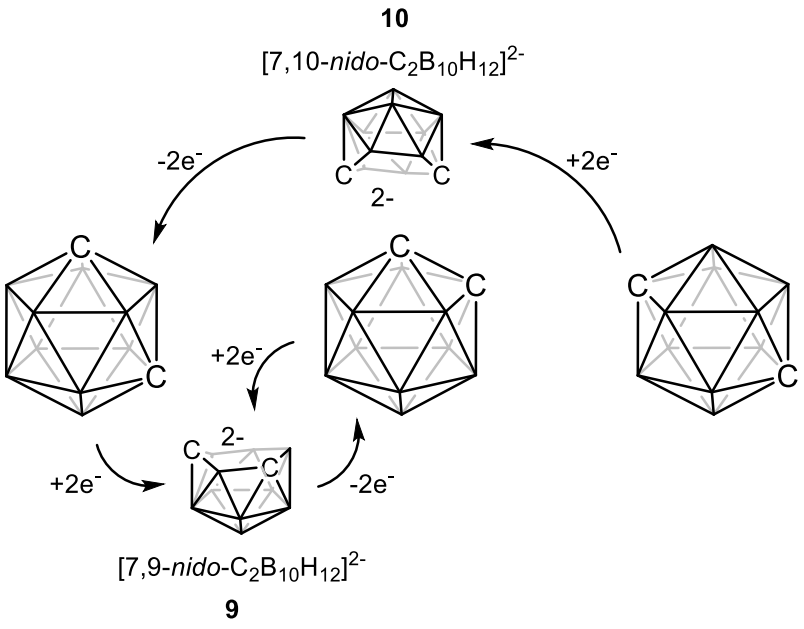


Scheme 1-3 – The thermal isomerisation of *ortho* to *meta*-carborane according to the DSD mechanism. The arrows represent the TFR.

Isomerisation to *para*-carborane is not as simple. If one assumes ideal transformations, then during DSD the centre of symmetry is retained which, due to the structure of an icosahedron, means that two initially adjacent atoms cannot reach opposite positions on the cage.[49] DFT studies have also contributed here, suggesting that the *meta* to *para* isomerisation takes place through DSD operations on a series of pseudo-*nido* geometries;[50,51] the exact structures, of which there are many, are beyond the scope of this review. In fact, the mechanism described is very similar to that of *ortho* to *meta* isomerisation, just that in the reality the symmetry transformations are *not* quite ideal, thus the formation of *para*-carborane can rationalised from essentially the same arguments.

1.3.3 – Reverse Isomerisation

Reverse isomerisation, i.e. *para* to *meta* to *ortho*-carborane, is also possible. When *meta*-carborane is reduced to the dianion a stable *nido*-structure is created, but when oxidised back to the neutral *closo*-carborane the *ortho* isomer is formed, as the rearrangement barrier from the *nido*-species back to *meta*-carborane is higher than that of *ortho*.[52,53] *Ortho*-carborane can also undergo redox reactions, reversibly forming the starting material back from the intermediate *nido*-species. Chemically, this is achieved by reducing carborane with sodium metal in liquid ammonia at low temperature, forming the monoanion radical, and then the dianion in succession, with the latter occurring much more slowly than the former.[52] In the case of *meta*-carborane, the dianion isomerises to form [7,9-*nido*-$C_2B_{10}H_{12}]^{2-}$ (**9**), which is the same intermediate that *ortho*-carborane forms when subjected to the same conditions.[54] In both cases, oxidation of this intermediate using $KMnO_4$ reliably forms *ortho*-carborane in essentially quantitative yield. Identical treatment of *para*-carborane forms *meta*-carborane through the similar intermediate [7,10-*nido*-$C_2B_{10}H_{12}]^{2-}$ (**10**) which, if heated under reflux, can be isomerised into [7,9-*nido*-$C_2B_{10}H_{12}]^{2-}$ and oxidised to *ortho*-carborane.[54,55] These processes are summarised in **Scheme 1-4**.



Scheme 1-4 – The reverse, redox isomerisation of *ortho*, *meta*, and *para*-carborane.

One may ask why this would be useful; as noted previously, carboranes increase drastically in expense from *ortho* to *para*, so it may seem odd to pursue any synthetic pathway in which *meta* or *para*-carborane is used to then isomerise to cheaper carborane. This chemistry is not purely academic however, there are some reactions, e.g. the disubstitution of the carbon atoms in carboranes using a

copper-mediated cross-coupling procedure, which are possible for *meta* and *para*-carborane but not for *ortho*.[17] If the *ortho* product is desired one can form the *meta* product and reverse isomerise. In practise there are few occasions where this strategy is needed, but it is a method that has proved useful to synthesise carboranes which could not be formed directly.[56]

1.4 – Carbon Substitution

Carbon substitution of carboranes via decaborane-acetylene couplings has already been explored but, as noted, there are many functional groups whose presence make this strategy not feasible. In addition, like other boranes, decaborane is highly toxic.[57] One can somewhat circumvent this by using the more stable bis(ligand) complex, ideally made in a big batch and stored,[58] or even make the bis(ligand) complex without using a decaborane starting material at all.[59] In other cases, it is easier and safer not to use decaborane, and substitute the protons on the parent carboranes. Carboranes have an 'organomimetic' reactivity,[60] and as such they can be substituted using similar types of chemistry.

1.4.1 – S_N2 Reactions

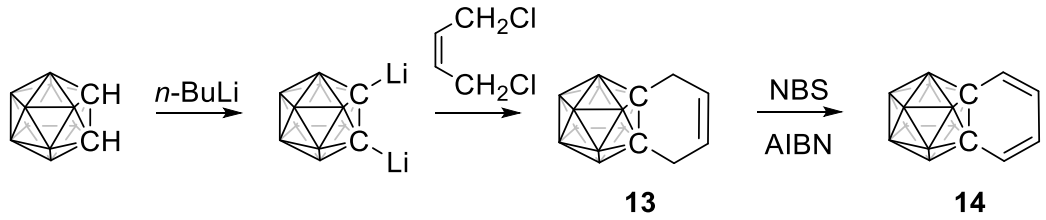
Deprotonation at the C-H vertices of all carborane isomers can be achieved using metal amides, Grignard reagents and other strong bases, most often *n*-butyllithium (*n*-BuLi).[15,40,61] One can achieve mono or dilithiation using stoichiometric amounts of the base, however, the reactive nature of *n*-BuLi means it is often used in slight excess. For *ortho*-carborane monolithiation can be aided by using a coordinating solvent such as diethyl ether.[62] The ether coordinates to the monolithiated carborane (**11**) and sterically blocks the second cage carbon from reacting to the dilithiated carborane (**12**). Clearly this is not possible for *meta* and *para*-carborane where the carbon atoms are not adjacent in the cage. Monosubstitution of these isomers is challenging, and even in ideal cases there is still an inherent problem in that an equilibrium of species forms, due to the disproportionation of the monolithiated product, **Equation 1-1**.[63]

$$1,12\text{-}LiC_2B_{10}H_{11}\ (\mathbf{11}) \leftrightharpoons 1,12\text{-}Li_2C_2B_{10}H_{10}\ (\mathbf{12}) + 1,12\text{-}C_2B_{10}H_{12} \qquad \text{[Equation 1-1]}$$

In general however, these difficulties are overcome by carefully monitoring the lithiation by NMR and separation of the product mixtures following the reaction.[64]

Lithiated carboranes can react directly with a huge number of compounds, including alkyl,[62] allyl,[65] silyl,[66] stannyl,[67] and mercury halides in S_N2 reactions,[67] aluminium hydrides, chalcogens,[66,68] iron

complexes,[69] palladium complexes,[70] platinum complexes,[70] halides;[71,72] the list goes on. One of the most structurally intriguing carboranes, 'benzocarborane' (**14**),[73] is synthesised from dihydrobenzocarborane (**13**) via a dilithiated starting material, **Scheme 1-5**. Benzocarborane is the fusion of two different types of delocalised bonding systems, and as such one would expect suitably unique and fascinating properties. This will be explored later.

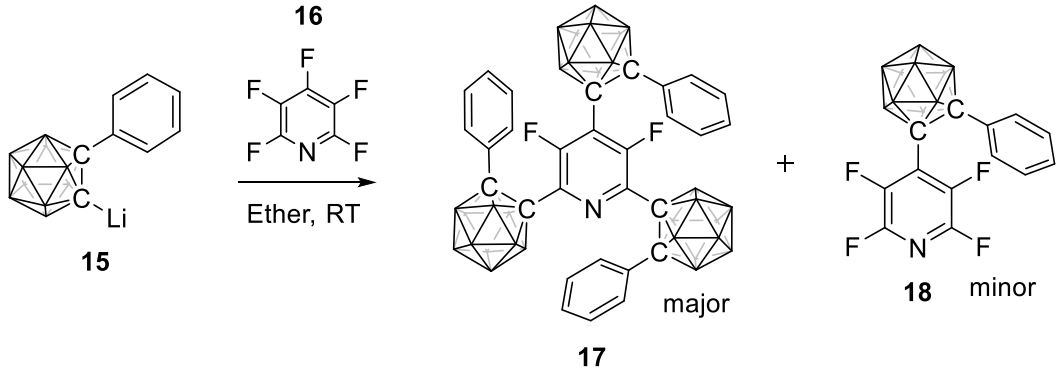


Scheme 1-5 – The synthesis of benzocarborane.

Clearly lithiated carboranes are extremely versatile and useful reactive species, but they are unable to react directly with aromatic compounds except in some specific cases, such as S_NAr reactions with perfluorinated aryl groups.

1.4.2 – S_NAr Reactions

Lithiated carboranes of all isomers are sufficiently nucleophilic to attack aromatic C-F bonds; a S_NAr reaction that was reported quite early on in the carborane literature.[74–76] Interestingly, when *ortho* and *meta*-carborane react with hexafluorobenzene, the 1,4-disubstituted aromatic product is formed, even when the aromatic is used in excess.[74] Similarly, when lithiated phenyl-*ortho*-carborane (**15**) reacts with pentafluoropyridine (**16**), the major and minor products are 2,4,6-trisubstituted (**17**) and 4-monosubstituted (**18**) respectively, **Scheme 1-6**.[77]



Scheme 1-6 – An S_NAr reaction of lithiated phenyl-*ortho*-carborane and pentafluoropyridine. Carborane-induced C-F activation causes the formation of the trisubstituted major product, with small amounts of the monosubstituted also present. The lack of any disubstituted product suggests the activation effect of the carboranes is additive.

Following the insertion of one carborane into hexafluorobenzene and pentafluoropyridine, the fluorine atoms around the molecule are activated towards substitution, at the *para* position (to the carborane) in the former case, and the *meta* positions in the latter case. For *para*-carborane the activating effect is not as strong, so the monoarylated product is formed in about double the yield of the diarylated.[78] These observations demonstrate a property of the carborane not yet mentioned, that they are (usually)[‡] strongly electron-withdrawing. This is an inductive effect of the electrophilic cage carbon atoms decreasing on the order *ortho* > *meta* > *para* and is a feature of carboranes which has made them highly desirable functional groups in several fields, to be discussed in detail later.

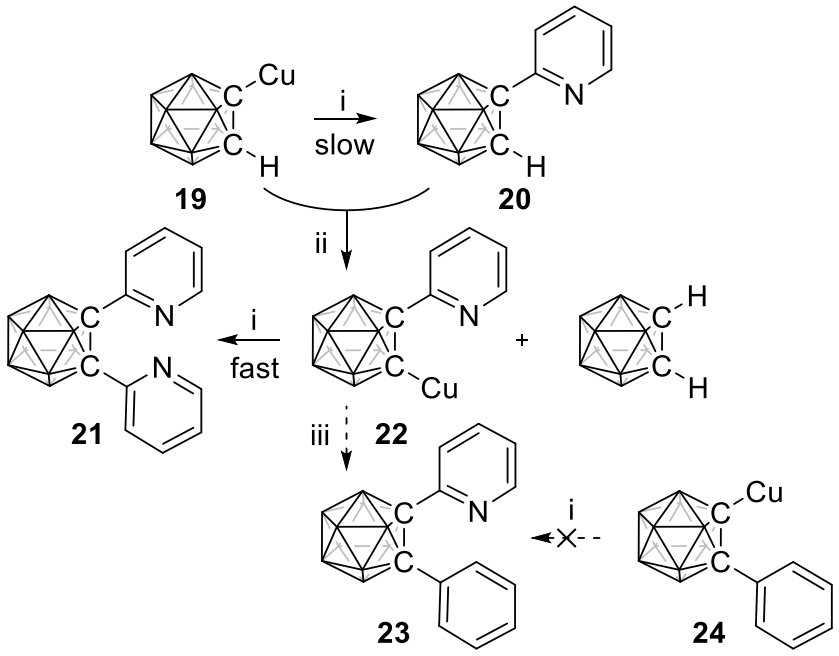
In order to explore the curious 'superaromatic' properties of carboranes in a wider, non-fluorinated, range of aromatic systems, a new and more general approach to arylation was required. Copper(I)-mediated (Ullmann-like) cross-coupling allows for exactly this.

1.4.3 – Copper(I)-Mediated Cross-Couplings

The first attempts at copper cross-coupling involved reacting aromatic iodides with lithiated carboranes mediated by CuCl in DMF, or $CuCl_2$ in THF.[79] Both produced the desired aromatic carboranes via cupra-*ortho*-carborane (**19**), but in low yields. Later, the methodology was significantly improved through the addition of pyridine after the formation of the lithiocarborane,[80] and heating to reflux for approximately 24 hours; the long reaction times a result of the poor solubility of the copper(I) carborane derivatives.[80] Using this procedure copper-mediated cross-couplings have been used to substitute the cage carbons with alkenes,[79] acetylenes,[79,81,82] and even other carboranes. In fact, the bis-carboranes of all three isomers have been synthesised.[83–85]

For *meta* and *para*-carborane one can synthesise the mono or diarylated compound in high yield through appropriate stoichiometry, however for *ortho*-carborane generally only the monoarylated product is formed.[80] One peculiar exception to this is the reaction of *ortho*-carborane with 2-bromopyridine where, even when equimolar amounts of all reactants are used, the monoarylated (**20**) product is not isolated; the diarylated derivative is the major product (**21**).[80] Further, if 1-cupra-2-pyridyl-*ortho*-carborane (**22**) is used as a starting material and reacted with iodobenzene, the disubstituted product forms (**23**), but if the aryl groups are switched in an otherwise identical method with 1-cupra-2-phenyl-*ortho*-carborane (**24**) as the starting material, no reaction occurs, **Scheme 1-7**.

[‡] Carboranes are electron-withdrawing when substituted at the carbon atoms but can be electron-donating when substituted at the boron atoms. Indeed, a phosphinocarborane is the most electron-donating carbon-based ligand ever reported.[60]



Scheme 1-7 – A schematic for the unusual formation of disubstituted *ortho*-carboranes via reactions of cupra-*ortho*-carborane derivatives. The labelled processes are (i) coupling with 2-bromopyridine in the presence of pyridine, (ii) disproportionation of the cupra-carborane with 2'-pyridyl-*ortho*-carborane and (iii) coupling with iodobenzene in the presence of pyridine. Note for (iii) the monosubstituted carborane starting material is formed by decaborane acetylene coupling.[80]

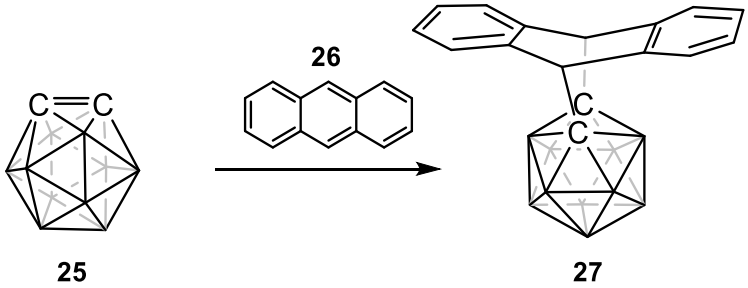
This suggests that it is not a steric problem which stops disubstitution, but by either deactivation of the reactivity at the C(2) carbon following monosubstitution, or a more general solubility issue with 1-cupra-2-aryl-*ortho*-carborane intermediates, which happens not to be a problem in the example described.[80] In any case, disubstitution of *ortho*-carborane via copper coupling is generally not possible except in a few isolated examples.

1.4.4 – Carboryne Reactions

Akin to the benzene derivative, benzyne, it is possible to deprotonate the two carbon vertices for *ortho*-carborane to create 1,2-$C_2B_{10}H_{10}$ or 'carboryne' (**25**). There are two ways to synthesis carboryne (always *in-situ*); the first method is to form the α-bromo carboranyl anion at low temperature, then warming to eliminate a bromide and form the product.[86] The second method is to form the silylated precursor phenyl[*ortho*-(trimethylsilyl)carboranyl]iodonium acetate which is stable and can be stored, only to form carboryne when a desilylating agent such as CsF is added.[87]

Like benzyne, carboryne is highly unstable as a result of the high energy π-bond and can undergo Diels-Alder cycloadditions. For reactions with carboryne the diene is present in solution when the nascent carboryne forms, ready to immediately react with or 'trap' it. Carboryne can generally react in [4+2]

and [2+2] cycloadditions with all suitable dienes,[88] which has produced a wide range of compounds including anthracene (**26**) to form the aesthetically pleasing symmetrical carborane derivative (**27**) shown in **Scheme 1-8**.[86]



Scheme 1-8 – The reaction of carboryne with anthracene in a [4+2] cycloaddition.

Other types of cyclisation have been reported, including a nickel-mediated [2+2+2] cycloaddition with alkenes and alkynes,[89] and [5+2] (via a series of [3+2]) cycloadditions of nitrones.[90] In addition, benzocarborane and similar exocyclic-substituted derivatives can be formed through the reaction of carboryne with thiophene.[91]

The, seemingly few, synthetic strategies described in this section encompass the vast majority of the carbon-substituted carborane derivatives presented in the literature. This is testament to the ease and versatility of carbon-substitution for carboranes which, unfortunately, cannot be said for the chemistry of the boron vertices.

1.5 – Boron Substitution

Substitution at the boron vertices is more difficult than at those of carbon. The electronegativity of boron and hydrogen are very similar, making B-H bonds much less polar than C-H bonds, and in turn less acidic and reactive towards nucleophilic strong bases. This is highly fortuitous in many ways; had this not been the case, the chemistry at the carbon vertices of carboranes would be significantly more difficult. The situation is further complicated by the fact that both *ortho* and *meta*-carborane have four electronically distinct boron environments each with different reactivities, **Figure 1-3**.

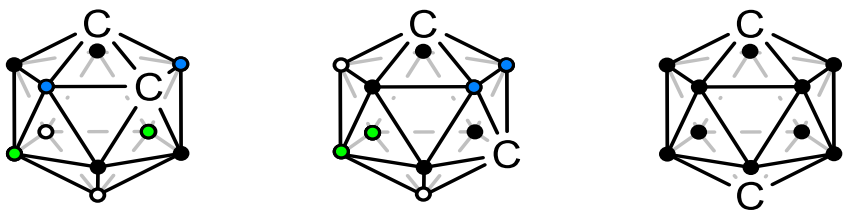


Figure 1-3 – A depiction of the electronically distinct boron environments within each of the carborane isomers. For *ortho* and *meta*-carborane there are four environments with occupancy [4,2,2,2], but for *para*-carborane the symmetry dictates that there is only one.

A full discussion of boron chemistry in carboranes is beyond the scope of this review, however there are two main reactions which together allow for substitution at all the boron atoms around the cage. These are electrophilic attack and boron insertion into *nido* dianions.

1.5.1 – Electrophilic Substitution

The carboranyl boron atoms, and importantly not the carbon atoms, are susceptible to attack by electrophiles.[92] Electrophilic alkylation is possible through treatment of alkyl halides in the presence of $AlCl_3$ under Friedel-Crafts conditions, leading to carboranes with (up to) ten alkyl groups.[93] In the case of methyl substitution of *ortho*-carborane the octakis product is formed in two days, but after ten days the octakis, nonakis and decakis products are present in the reaction mixture in a 1:1:1 ratio. For *meta*-carborane the octakis compound is produced, but for *para*-carborane only the decakis is formed. This demonstrates a general rule for boron substitution, which is that electrophilic attack occurs first at the most electron rich boron atoms (those furthest away from the carbon atoms) and continue towards the most electron deficient boron atoms in a step-wise manner. For *ortho*-carborane those closest to the two carbon atoms, B(3) and B(6), are significantly less reactive towards electrophiles;[§] this makes substitution at those positions quite challenging. In addition, methyl groups are inductively electron-*withdrawing* when attached to the boron atoms due to the larger electronegativity of carbon.[94] This means that successive methylations make the cage more electron-deficient, and so less able to undergo electrophilic alkylation.

Electrophilic halogenation proceeds in much the same manner; reactions of the elemental halogens and carboranes occur in the presence of $AlCl_3$ or similar catalyst, but substitution occurs only at the four most electron rich boron atoms, with disubstituted products dominating.[17] These compounds are

[§] For *meta*-carborane the B(2) and B(3) atoms are more electron deficient than the B(3) and B(6) for the *ortho* isomer, as they have two carbon atom nearest neighbours. For this reason, electrophilic alkylation is extremely difficult at those positions. For *para*-carborane all the boron atoms have one carbon nearest neighbour, making electrophilic reactions difficult but achievable at all the vertices.

interesting in themselves medicinally as X-ray contrast agents, due to iodine atoms being opaque to X-rays, but they can also act as starting materials for B-C bond formation using a Pd-catalysed cross-coupling.[95] In different conditions, such as iodination using ICl in the presence of triflic acid, *ortho*-carborane can react to form the octakis-iodinated product,[96] or even the decakis product if the 3,6-I_2-$C_2B_{10}H_{10}$ starting material is used; formed first through a boron insertion reaction.[97]

1.5.2 – Nucleophilic Substitution

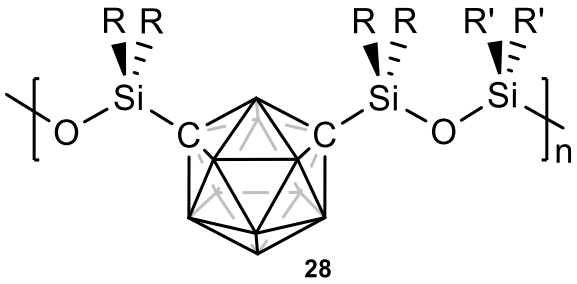
The two most electron deficient boron atoms in *ortho*-carborane, B(3) and B(6), can be attacked by a variety of nucleophiles leading to deboronation and the formation of an open-cage *nido* salt.[98] Treatment with *n*-BuLi affords the dianion, and the carborane can be reformed following insertion of a suitable RBX_2 or BX_3, where R includes halogens, amines, alkyl, aryl and alkoxy groups, and X can be any (stable) halogen.[98,99] It is also possible to substitute *meta*-carborane in this way,[100] but for *para*-carborane there are no difficult-to-substitute boron vertices, so other electrophilic or nucleophilic methods are more convenient.

With the above two methods one can produce a huge range of boron-substituted carboranes and, importantly, create the starting materials for further reactions, such as nucleophilic displacement of those substituents, at all the boron vertices.

1.6 – Applications of Carboranes

1.6.1 – Polysiloxanes

As noted previously, carboranes found application even before they appeared in the literature, and the volumes of research into them since have meant they can now be found in papers from a wide variety of fields. The first commercial applications for carboranes were siloxy-*meta*-carborane polymers, which are used as stationary phases for high-temperature gas chromatography. Dexsil 300 (**28**), **Figure 1-4**, is reported to have outstanding chemical and thermal stability, maintaining rubberlike properties even up to 500 °C.[101,102] There is still no equivalent to these exceptional materials for this purpose, and similar derivatives of these early siloxanes, known as ‘HT5’, are still available to buy today.[103]



28

Figure 1-4 – The structure of Dexsil 300. R and R' represent alkyl chains of 1-6 carbons atoms or aryl groups of not more than 8 carbon atoms.

1.6.2 – Strong Acids

Apart from siloxy-carboranes and the parent carboranes (and simple derivatives) used for academic research, there is currently no other commercial carborane material on the market. It is somewhat true that carboranes have yet to 'break-out' in some field and provide an innovative solution to a difficult problem, but that does a disservice to the achievements of carborane chemists. For example, the carborane $H(CHB_{11}Cl_{11})$ 'carborane acid' was for a long time the strongest Brønsted acid known, able to protonate even benzene.[104,105] This was only recently overtaken in acidity by another carborane, $H(CHB_{11}H_{11})$, which will react with butane and hexane to form isolable carbocation salts.[106] These acids are also 'strong yet gentle',[104] meaning that they are non-corrosive owing to the extraordinary stability of the carborane anion.[105] These carboranes are of huge interest academically but have no obvious commercial application (yet), so are unlikely to be present in large-scale commercial products. However, there are also fields in which carboranes still hold promise for commercial applicability. Firstly, medicine.

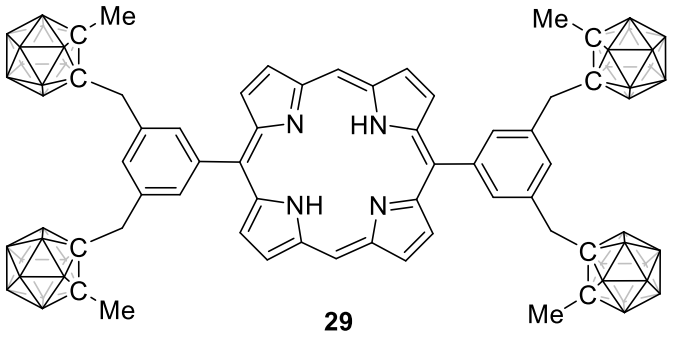
1.6.3 – Medicine

One area of medicine where carboranes are particularly of interest is boron neutron capture therapy (BNCT). It is an effective treatment for recurrent head and neck cancers which are often resistant to less invasive radio and chemical therapies, and would otherwise necessitate surgery.[107] Surgery in this area can severely disfigure and impair the functions of the oro-facial region, and so BNCT offers a non-invasive therapy alternative in which boron containing compounds are concentrated in tumour cells, and are then subjected to bombardment with a neutron beam.[108] ^{10}B isotopes have a large cross-section for capturing slow thermal neutrons (n_{th}) and, after absorption, an excited $^{11}B^*$ nucleus is formed which breaks up into an alpha particle (α) and a lithium nucleus, with the release of high energy gamma radiation (γ) as in **Equation 1-2**:

$$^{10}B + n_{th} \rightarrow [^{11}B]^* \rightarrow \alpha + {}^{7}Li + \gamma \quad \text{[Equation 1-2]}$$

This radiation does irreversible damage to the machinery and DNA of the tumour cell and decays over <10 μm; significantly smaller than the diameter of the tumour cell, so nearby healthy tissue is left unaffected.[108]

Carboranes have a very high boron density and the natural isotopic abundance means that on average exactly two boron atoms in each carborane are ^{10}B. This can be increased dramatically through enrichment, and >99.5% ^{10}B enriched parent carboranes can be purchased commercially.[42] Carboranes are also lipophilic, but can be made water-soluble as salts of the *nido*-C_2B_9 anions;[109] a combination of these two properties is a requirement for passing the blood-brain barrier. They are also highly stable and accordingly non-toxic.[109] In short, carboranes are highly attractive as potential boron delivery agents and there have been many approaches to the formation of compounds for precisely that purpose. These include carbohydrates, phenanthridines (DNA intercalators), polyamines, nucleosides, liposomes, nanoparticles, and porphyrins (**29**), **Figure 1-5**.[17,109,110]



29

Figure 1-5 – A carboranylporphyrin 'H_2DCP' delivery agent for BNCT.

Whilst no carborane-containing delivery agents have yet reached clinical trials, $[B_{12}H_{12}]^{2-}$ derivatives have, and $Na_2B_{12}H_{11}SH$ (known as BSH) is one of only two drugs being used clinically, treating high grade gliomas.[110] There is still a need for a new, better, generation of boron delivery agents for BNCT, and it is hoped that some of the carborane derivatives mentioned above may eventually reach clinical stages.

1.6.4 – Organic Semiconductors

A second field in which carboranes may offer some degree of commercial applicability is organic semiconductors. When incorporated into larger conjugated systems, carboranes can confer increased stability, modulate the band-gap, and even introduce new desirable properties such as increasing the

quantum yield of fluorophores in the aggregated state. As will be discussed later, luminescent carboranes have been the subject of a huge number of academic papers in the past few years, but first, the effects of introducing carboranes into conjugated systems will be reviewed.

1.7 – Carboranes in Conjugated Systems

1.7.1 – Benzocarborane

One of the most direct attempts at trying to exploit the unique electronic properties of carboranes in larger, supraicosahedral systems was the direct fusion of carborane and benzene, forming benzocarborane,[73] **Scheme 1-5**. The p-orbitals of the two carboranyl carbons atoms can be considered in such a way that they are oriented to complete the π-system of the benzoid ring, however, the multicentre bonding of the icosahedron puts the highest electron density inside the cage.[111] One can, therefore, expect little interaction between these p-orbitals and those of the ring, a prediction supported by earlier studies of other aryl carboranes:

"[The data provides] no evidence for ground-state extension of electron delocalisation by interaction of the aryl group with the highly delocalised [ortho-carborane] group"[112]

There are many properties of benzocarborane that seem to contradict this however, suggesting that the *exo*-ring is not like any ordinary diene. Benzocarborane is unaffected by concentrated sulfuric acid at 100 °C; it reacts extremely slowly with bromine in carbon tetrachloride or potassium permanganate (atypical olefin behaviour);[73] the benzoid protons have a chemical shift centred at 6.35 ppm, somewhere between conventional aromatics and olefins; and the UV-Vis spectrum has a fine structure very reminiscent of benzene.[111] Upon closer inspection however, these properties of the *exo*-ring can be explained away without the need for aromaticity: the relative stability to strong acids and oxidising agents is also seen for vinyl and allylcarboranes (including dihydrobenzocarborane), and is probably a result of the strong electron-withdrawing nature, large steric bulk, and extreme rigidity of the carborane;[111] the NMR spectrum of benzocarborane is very similar to cyclopentenocarborane which has no π-system; and the UV-Vis spectrum of cyclohexadiene, another sterically rigid diene, shows a similarly resolved fine structure.[111] In addition, single-crystal X-ray diffraction (XRD) studies have demonstrated that the C-C bond lengths in the *exo*-ring alternate between single and double bonds, comparable to other cyclic dienes, **Figure 1-6**.[113]

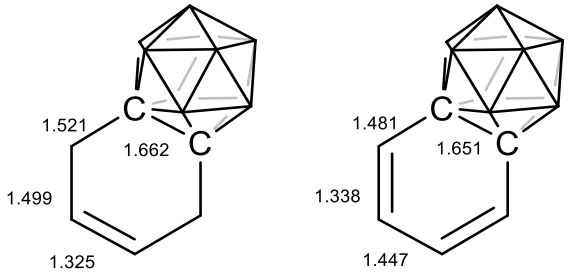


Figure 1-6 – The structures and bond distances (Å) for dihydrobenzocarborane (left), and benzocarborane (right).

There are also minimal differences between the cage structures of dihydrobenzocarborane and benzocarborane, except that the C_{cage}-B(3) and B(6) distances are longer for the latter. It has since been suggested that this is evidence of an 'enhanced structural carborane effect', meaning that the cage carbon atoms are bonded less strongly to B(3) and B(6) due to their p-orbitals being, to some extent, involved in the *exo*-ring bonding, yielding a small degree of aromaticity.[114]

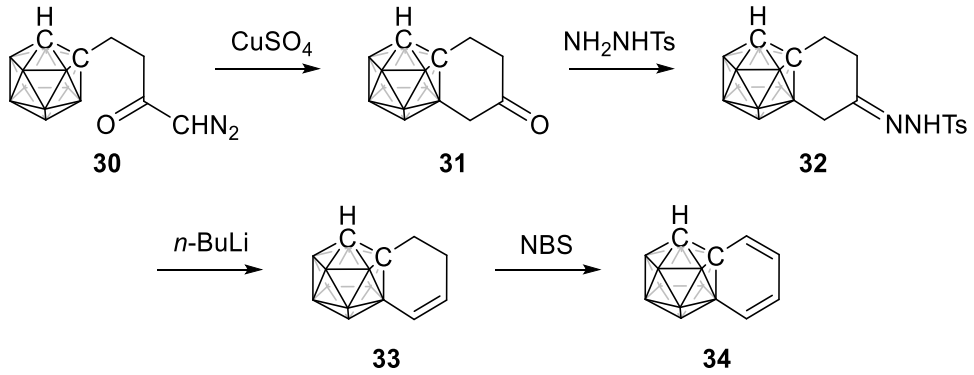
The *exo*-rings of napthocarborane have also been shown to exhibit an extremely low degree of aromaticity, in fact, its properties are explained just as well if one assumes no ring-cage π-bonding at all.[115] Other thiophene-fused,[116–119] biphenyl and *p*-terphenyl benzocarborane derivatives have similarly found no aromaticity;[120] the carborane acts more like a strongly electron-withdrawing group due to induction, as opposed to an aromatic electron-sink.[116] However, carborane-fused heterocycles including furan, thiophene, and pyrrole, have very recently been suggested to exhibit significant aromatic character in the *exo* five-membered ring:

"*…the fused five-membered rings in the [carborane-fused heterocycles] have considerable aromatic character, and the conjugation between a 3-D cluster and a fused 2-D π system has been realised by the π donation of the exo heteroatom/carbanion.*"[121]

Corroboration of these claims in the years to come may lead to a new, exciting, area of hybrid σ/π-bonding chemistry.

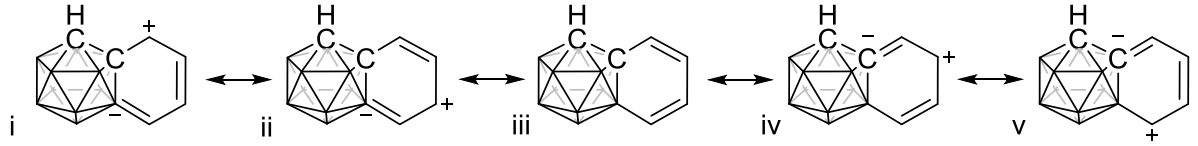
1.7.2 – Carbon-to-Boron Bridged Benzocarborane

There are also benzocarborane-type compounds formed through carbon-to-boron bridges, from C(1) to B(4) of *ortho*-carborane.[122,123] These are formed in several steps starting with the carbon-substituted carboranyl diazo ketone (**30**), itself not simply made in a three-step synthesis from *ortho*-carborane, then proceeding to B-H insertion via carbene intermediate in a Wolff rearrangement occurring preferentially at the B(4) position (**31**).[124] Functional group interconversion (**32**), reduction (**33**), then subsequent oxidation leads to the product (**34**),[122] **Scheme 1-9**.



Scheme 1-9 – The synthesis of carbon-to-boron bridged benzocarborane.

One can again consider whether there is measurable delocalised bonding between the cage and cycle for these compounds. It is believed that, unlike for benzocarborane, there is a significant amount of cage-ring conjugation, as when the p-orbitals of the ring bond with p-type surface orbitals of the cage, a series of resonance structures can be drawn, **Scheme 1-10**.



Scheme 1-10 – The resonance structures of carbon-to-boron bridged benzocarborane.

The partially positively charged cage carbons are better electron-acceptors of both of σ and π electrons than the cage borons, so the structures (iv) and (v) with the negative charge on the cage carbon are likely to be the larger contributing resonance structures. For (v), the positively charged carbon atom in the ring can also be somewhat stabilised by the partially negatively charged boron atom situated adjacent in the cage.[122] For these reasons some degree of ring-cage conjugation seems likely, however this is not the case for aromaticity; NMR studies have demonstrated that, as for the conventional carbon-to-carbon bridged benzocarborane, there is no observable ring-current for these compounds.[122]

1.7.3 – π-Donor Substituted Carboranes

Carborane-substituent delocalised bonding has also been investigated for more conventionally substituted (i.e. non-*exo*-cyclic fused) carboranes. Upon the introduction of π-donor substituents such as F, OH, O^-, NH_2 or NH^- at the available cage carbon atom of phenyl-*ortho*-carborane, the structures of the resulting compounds show remarkable variation, particularly with regard to the carboranyl C-C bond length.[125] As one increases the π-donor capability of the substituent, the C-C bond distance also

increases, opening the carborane cage from a *closo* towards a *nido* species. This is consistent with increased electron density in the cage (c.f. Wade-Mingos rules), and as such, suggests that the carborane can interact with the substituent through *exo* π-bonding.[125] Further, the preferred orientation of the substituent, as determined by single-crystal XRD, suggests that this bonding uses a tangential atomic orbital on the cage carbon. The p-orbital of the substituent donates into this orbital and reduces its availability for cage C-C σ-bonding, causing the cage to open.

1.7.4 – Aryl-Carboranes

Similar, but less pronounced, C-C bond variations have been observed for carboranes bearing solely electron-donating aryl substituents.[126] A marginal increase in the C-C bond length occurs for phenyl-*ortho*-carborane compared to the parent carborane, owing to a weak π-bonding interaction, but only when the plane of the aromatic is perpendicular to the C-C bond. This effect approximately doubles when two aryl groups are present and perpendicular. The explanation for this observation is akin to the non-aryl π-donors, where p-orbitals of the carboranyl carbon and proximal carbon of the aryl substituent must be in the same plane for π-bonding to occur, **Figure 1-7**.[125]

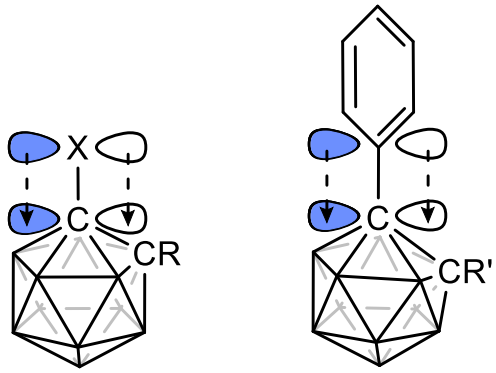
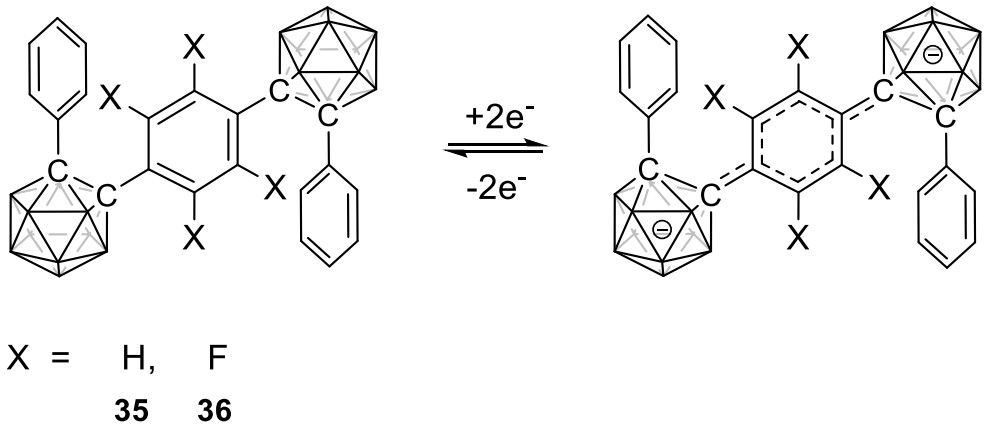


Figure 1-7 – Exo π-bonding between electron-donating substituents and *ortho*-carborane, leading to elongation of the carboranyl C-C bond. X = F, OH, O^-, NH_2, N^-; R = Ph; R' = H, Ph.

Once again, in these cases the π-conjugation is restricted to essentially the cage carbon and the bond to the substituent; it does not involve the whole cage. The effect is much weaker for carboranes substituted with electron-donors at the boron atoms, and there is no orientational preference for attached phenyl groups.[127,128] The same is true for *meta*-carborane,[129] but for *para*-carborane it has been demonstrated there can be communication from a group at the *para*-position of a carbon-bonded carborane substituent to the *other* carbon atom across the whole carborane.[130] It is believed that these electronic couplings are akin to those observed for 'staffane'.[130] Further exploration of this property will be discussed later.

1.7.5 – Carborane-to-Carborane Electronic Communication

Electronic communication between carboranes in the reduced, monoanion radical (2n + 3 skeletal electron count) state and their aromatic cage carbon-bonded substituents has also been studied. As mentioned earlier, for the monoanion radical of diphenyl-*ortho*-carborane the extra electron is delocalised around the carborane, however no significant π-bonding interactions between the cage and the phenyl substituents are observed.[21] However, similar carboranes bearing highly electron-withdrawing perfluorinated aromatic groups have shown significant electrochemical stabilisation of the monoanion radical state,[77,131] and DFT studies of these molecules have shown delocalisation of the LUMO over both the ring substituents and the cage carbons.[131] When two carboranes are attached at the *para*-position of a perfluorinated aromatic this effect can be extended remarkably, as exemplified by the bridged compound $[1,4\text{-}(PhC_2B_{10}H_{10})_2C_6H_4]^{2-}$ (**35**) and its fluorinated analogue (**36**), **Scheme 1-11**.[132]



Scheme 1-11 – The structures of the neutral and dianion species, with both carboranes in the monoanion radical state, of $1,4\text{-}(PhC_2B_{10}H_{10})_2C_6X_4$ following chemical reduction with sodium metal.

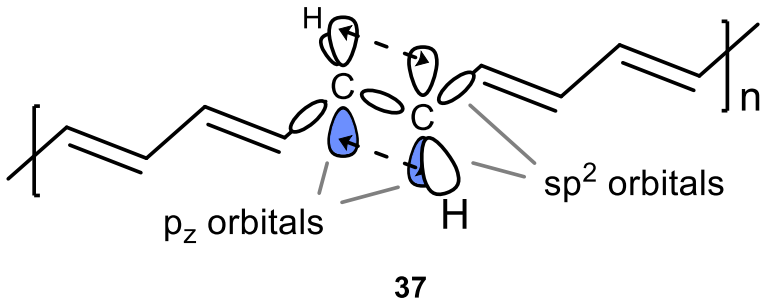
Cyclic voltammetry (CV) of both **35** and **36** shows two, two-electron, reversible reduction waves. These waves occur at lower (less negative) potentials, and are spaced wider for the fluorinated analogue, suggesting an extra degree of stabilisation introduced by fluorination of the phenylene bridge. Interestingly, the presence of only two waves compared to four for the structural isomer $1,3\text{-}(PhC_2B_{10}H_{10})_2C_6H_4$ where, due to a *meta* substitution pattern, the phenylene acts as an electronic insulator, suggests that the carboranes may be communicating.[132] This hypothesis was confirmed by the crystal structures of the salts of **35** and **36** which show, remarkably, that the bond lengths of all C-C bonds between the two carboranes are essentially identical; the phenylene bridge is quinoidal.[132] This demonstrates that the carboranes are both participating in, and are stabilised by, a π-conjugated system across a phenylene spacer. Moreover, this effect is exacerbated when strongly electron-

withdrawing groups are introduced into the spacer region. This is perhaps the best example of the ability of carboranes to contribute to wider conjugated systems, albeit in highly specific electronic and geometric conditions.

1.8 – Carboranes in Conjugated Polymers

The ability of carboranes to participate in conjugated systems in the excited state, along with their strongly electron-withdrawing capability, makes them attractive for use as acceptors in organic electronics. More specifically, they have been incorporated into donor-acceptor conjugated polymers for use in organic field-effect transistors (OFETs), light-emitting diodes (OLEDs), and photovoltaics (OPVs).

The simplest conjugated polymer is polyacetylene (**37**) which, not incidentally, was also the first reported conducting polymer.[133] It consists of a chain of sp^2 hybridised carbon atoms, with all three of these orbitals in the plane of the backbone, and one p-orbital perpendicular, **Figure 1-8**.



37

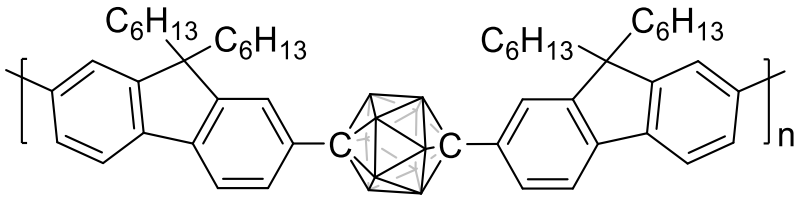
Figure 1-8 – The bonding of the simplest conjugated polymer, polyacetylene.

The favourable overlap of these orbitals forms π-bonds that can extend over multiple atoms, allowing for electron conductivity along the polymer chain and between chains. Such substances offer the possibility of replacing silicon in various semiconductor devices, where their low-cost, solution processability, mechanical flexibility, and electronic (band-gap) tunability make them highly attractive materials.[134]

1.8.1 – Backbone-Incorporated Carborane Polymers

There have been many approaches to carborane-based donor-acceptor copolymers. One such strategy is to incorporate the carborane directly into the backbone, achieved via decaborane coupling with an acetylenic monomer which is later polymerised, as in the case of alternating *ortho*-carborane and *para*-phenylene-ethynylene.[135]

The v-shaped nature of the polymer, imposed by the geometry of *ortho*-carborane, makes conjugation more difficult than for a linear polymer, but optical studies suggest that the conjugation length of each phenylene-ethynylene segment is mildly increased following introduction of the carborane. Such a small increase suggests that through-conjugation, i.e. electron delocalisation from one donor unit to the other through the carborane, is unlikely to be occurring.[135] A similar observation had been made for otherwise identical polymers containing *meta*-carborane.[136] For *para*-carborane in the backbone of conjugated polymers the situation is somewhat different; the polymer is linear and, as described previously, communication between aromatic groups attached at antipodal positions of *para*-carborane is possible. However, in the case of polyfluorene with *para*-carborane in the backbone (**38**), **Figure 1-9**, the effect on conjugation is identical to the *ortho* and *meta* derivatives.[137]



38

Figure 1-9 – The structure of polyfluorene with *para*-carborane incorporated directly in the backbone.

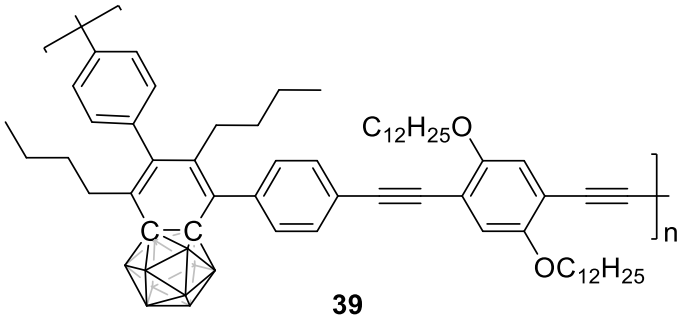
It seems that this type of architecture does not allow for extended delocalised π-systems and indeed the carboranes are essentially insulators in this respect. These materials do however have interesting luminescent properties, as will be discussed later.

Similarly structured poly[di(2-thiophenyl)carborane]s of all three isomers have also been investigated. These materials can be easily synthesised from the di(2-thiophenyl)carboranes via electrochemical polymerisation, and it was envisioned that, like in the case of poly(carborane-siloxane)s, the carboranes would confer significant chemical and thermal stability onto the polythiophene derivatives.[138] Addition of the carboranes has a detrimental effect on the conductivity, which is on the order of 3-5 times lower than the parent polythiophene. This is not unsurprising when one compares the bulky carborane to the compact, planar thiophene unit; charge-carriers also mobilise between chains, not just along them.[134] The *ortho*-carborane polymer has the best conductivity, possibly due to a more planar conformation of the backbone as a result of an intramolecular β-β' cyclisation forming fused dithiophenyl-carborane subunits.[138,139] A similar polycyclic dithiophenyl-carborane moiety will be presented shortly. Thermogravimetric analysis (TGA) and CV of the materials shows significantly enhanced thermal and electrochemical stabilities respectively, compared to the parent polymer. For example, for polythiophene TGA under N_2 reveals a continuous loss of mass up to ~80%

at 600 °C, however for the *ortho*-carborane polythiophene derivative only a 10% mass loss up to 800 °C is observed.[138] Whilst these properties are impressive, the loss of conductivity is significant and remains a challenge to overcome for these electropolymerized materials.[139]

1.8.2 – Benzocarborane Polymers

A second approach is to incorporate carboranes indirectly in the backbone, via the use of (carbon-to-carbon bridged) benzocarborane. The first reported benzocarborane conjugated polymer was another *para*-phenylene-ethynylene derivative (**39**), and like the similar *ortho* and *meta*-carborane polymers described previously, it is also non-linear.[140] The carborane monomer is synthesised via a nickel-mediated regioselective [2+2+2] cycloaddition of carboryne, which yields a 1,3-substituted benzocarborane. The resulting polymer therefore suffers a 60° bend, **Figure 1-10**.

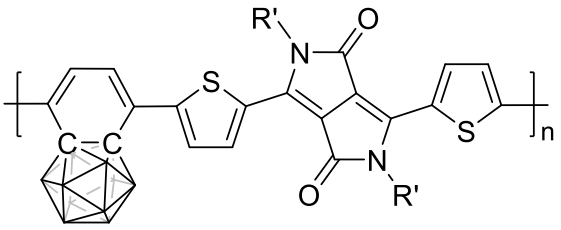


39

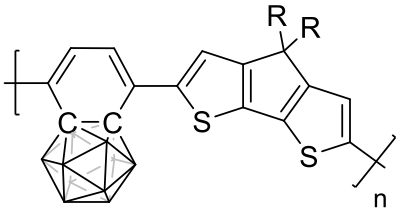
Figure 1-10 – The structure of the polymer formed from the reaction of benzocarborane and *para*-phenylene ethynylene. Each repeat unit is bent 60° off the backbone axis due to the 1,3-substitution of benzocarborane.

The degree of polymerisation is relatively unaffected by the non-linearity of the newly forming chain, in fact, the open structure of the monomer is suggested to aid polymerisation.[140] This is evidenced by a degree of polymerisation (DP) between 8-24, depending on the substituted phenylene derivative, which is significantly larger than those of the v-shaped *ortho*-carborane polymers produced by the same researchers.[135,140] Optical studies of this polymer demonstrate a red-shifted absorbance relative to a *para*-phenylene ethynylene model compound, suggesting an extension of the π-delocalisation onto the butadiene portion of the benzocarborane moiety. However, the photoluminescence emission spectrum is virtually identical to the model compound. In addition, DFT calculations show no orbital density on the carborane in either the highest occupied molecular orbital (HOMO) or lowest occupied molecular orbital (LUMO). Based on this data it was concluded that the carborane cage acts only as a simple electron-withdrawing group, and does not otherwise affect the π-conjugated system.[140]

A logical progression from this work was to form conjugated polymers in which the benzocarborane unit is linked in the backbone via a 1,4-substitution, so that the polymer remains linear and the π-conjugated system is proximal to the cage at both carbon sites in the molecule. This has been achieved using bis-1,4-stannylated-benzocarborane formed by the treatment of benzocarborane with *n*-BuLi and TMEDA, which results in exclusive deprotonation at the 1,4-positions, followed by tributyltin chloride to trap the resulting anion.[141] Stille copolymerisations of the tin monomer with brominated comonomers yield the desired linear polymers, **Figure 1-11**.



pBZ-DPP **40**



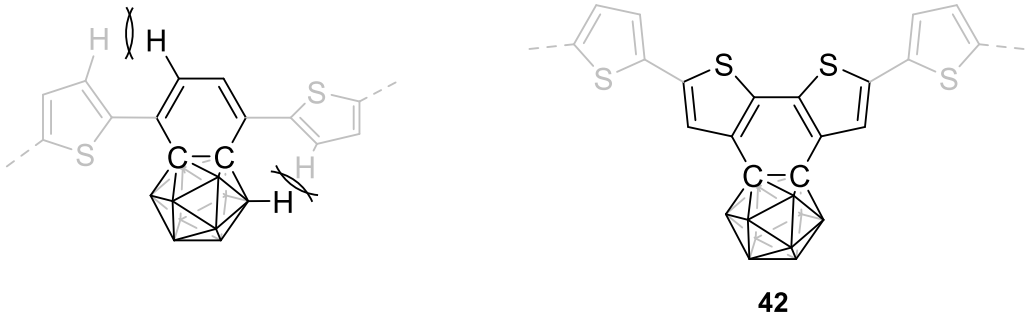
pBZ-CDT **41**

Figure 1-11 – The structures of 1,4-substituted-benzocarborane copolymerised with diketopyrrolopyrrole (DPP) and cyclopentadithiophene (CDT). R = dodecyl and R' = 2-octyldecyl solubilising side-chains.

Differential scanning calorimetry (DSC) of the DPP polymer (**40**) was initially quite exciting, as endotherms and exotherms can be observed on heating and cooling respectively, likely corresponding to melting and crystallisation of the backbone.[141] Similarly, X-ray diffraction of a drop-cast film show a clear diffraction peak which increased upon annealing at 160 °C. These measurements suggest that the polymer films have a degree of crystallinity, demonstrating that the bulky benzocarborane does not appear to impede the aggregation characteristics of DPP;[141] such properties are generally considered favourable for the conduction of charge carriers in organic electronics. However, the performance of the DPP polymer in an OFET is poor, to the point where it could not be reliably calculated. For the CDT polymer (**41**), for which there was no evidence of crystallinity, the mobility is calculated to be a rather low 1.7 x 10^{-5} cm^2 V^{-2}. These results were rationalised with the help of DFT calculations which suggested that the CDT polymer was planar, but the DPP polymer suffered a severe twist in the backbone, which is likely suppressing charge carrier mobility for the latter. Frontier

molecular orbital visualisation for both polymers show that there is no electronic communication between the carborane and the polymer backbone, and once again that benzocarborane acts only as an electron-withdrawing diene.[141]

A further iteration on this theme was to use the benzocarborane derivative benzocarborano[2,1-b:3,4-b']dithiophene (BZTT) (**42**),[116] where two thiophenes flank the benzoidal ring, as the electron-acceptor in conjugated copolymers.[142] BZTT has several advantages over benzocarborane. First, large fused aromatic systems are well known to aid charge carrier mobility in both polymers and small molecules. Adding the thiophene units creates a larger, planar, π-system which should help to increase mobility. More specifically, the benzocarborane polymers previously considered suffered from steric interactions between the *α*-protons of neighbouring moieties and the proximal protons of both the benzoidal ring *and* the carborane, which is thought to increase out-of-plane twisting for pBZ-DPP.[141] The structure of BZTT eliminates all but eliminates this problem, **Figure 1-12**.



42

Figure 1-12 – Structures of benzocarborane (left) and BZTT (right) polymers, flanked by thiophenes with steric interactions shown.

BZTT was functionalised and polymerised in the same fashion as benzocarborane to form pBZTT-CDT and pBZTT-DPP.[142] The properties of the polymers were found to be broadly similar to the benzocarborane analogues; pBZTT-CDT shows no observable solid-state ordering via XRD, but pBZTT-DPP exhibits some degree of crystallinity which increases following high-temperature annealing. DFT calculations demonstrate complete delocalisation of the frontier orbitals along the whole polymer backbone, however there is no orbital density on the carborane cage. From the optical absorption data, it was concluded that the BZTT acts as a mild, inductively electron-withdrawing moiety in both polymers.[142] Charge carrier mobilities of both pBZTT-CDT and pBZTT-DPP are relatively poor, however, the latter exhibits ambipolar transistor characteristics; the first time such properties have been observed in a carborane-containing polymer, and which may be useful in the development of electronic sensors.[142]

1.8.3 – Carboranes as Pendant Groups

It is fair to say that the introduction of carboranes has generally had a detrimental effect on the electronic properties of the polymers described above. However, the increased thermal and chemical stability is advantageous for organic electronic materials which are generally rather unstable towards light and oxidation. In addition, long solubilising chains are often required for these materials to overcome the very strong intermolecular interactions which would otherwise make them insoluble in even the best solvents. Being bulky, carboranes offer the possibility of aiding solubility, whilst also introducing the favourable stability properties just described.

One such example is that of polycarboranylpyrroles, where methyl-*ortho*-carborane is attached at the 3-position via an ethyl spacer.[143,144] The polycarboranylpyrroles were found to be significantly more electrochemically stable, oxidising at much higher potentials than the non-carborane-containing analogue. The difference was ascribed to the highly hydrophobic and electron-withdrawing nature of the carborane, protecting the polymer backbone from OH^- nucleophiles present in solution.[143,144] Carboranes have been similarly incorporated as pendant groups attached to polythiophene via an ethylene spacer, **Figure 1-13**.[145]

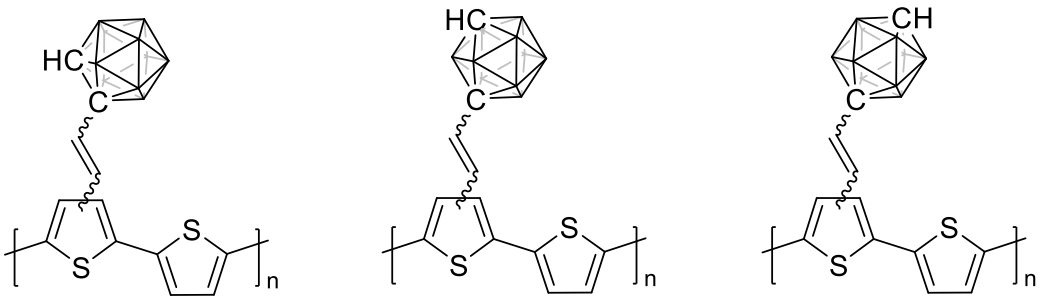
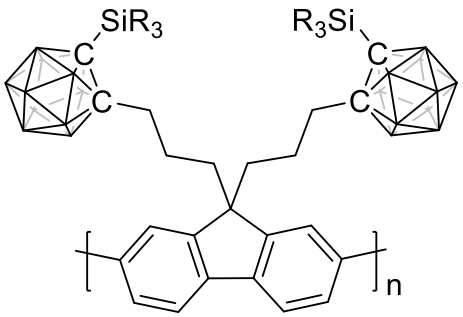


Figure 1-13 – Regiorandom polythiophenes containing *ortho*, *meta* or *para*-carborane (left to right) pendant groups linked in a *cis* or *trans* configuration to the polymer backbone via an ethylene spacer.

The resulting polymers (**43**-**48**) are generally suitably soluble without the need for additional side chains; often polythiophenes are solubilised with hexyl groups in the 3-position, forming poly(3-hexylthiophene) (P3HT). OFET performance is generally low however, similar to regiorandom P3HT, which is not that surprising as the carborane polymers were also regiorandom in terms of head and tail linkages.[145] OPV performance is similarly poor, and this was ascribed to the relatively low degree of structural order, brought about by the inclusion of the carboranes. There were differences between the isomers in terms of performance, with the *para*/*cis* isomer, to this day, having the highest power

conversion efficiency (PCE) of any carborane-containing polymer,[145] however the low performance and non-idealised devices make it unwise to draw conclusions on any structure/property relationship.

Highly bulky *tert*-butyldimethylsilyl carboranes doubly substituted, via a propyl linker, to the apex carbon of the cyclopentadiene of polyfluorene (**49**), **Figure 1-14**, have been found to have increased glass transition temperature (T_g) of polyfluorene and increase the photochemical stability and purity of the photoluminescence emission (PL) colour; in this case blue.[146]



49

Figure 1-14 – The structure of polyfluorene with bulky silyl carborane pendant groups.

The explanation of these phenomena is that the carborane pendant groups hinder chain packing, which reduces excimer and keto defects often observed for polyfluorene upon annealing, where they have a tendency to aggregate.[146] The PL properties of this material make them suitable for polymer-light-emitting diodes (PLEDs), where stable blue emitters are difficult to synthesise due to the high-energy excited states required to achieve high energy emission. Such materials are also of interest for neutron scintillators,[147] where the ^{10}B dense carborane pockets can accept neutrons and later undergo fission, releasing *γ*-radiation which could be detected, or to changes in the PL spectrum of the material which would indicate the presence of neutrons. In the latter case, however, one may expect such a device formed from this material not to have high sensitivity, as the carborane has no direct, electronic effect on the emissive properties of the polymer.[146] There are many materials where carboranes *are* directly involved in this way, and these are described below.

1.9 – Carboranes in Luminescent Materials

The parent carboranes are very weakly absorbing and weakly photoluminescent in solution.[148] They each have an emissive wavelength maximum (λ_{max}) of ca. 325 nm with photoluminescence quantum

yields (Φ) below 5% in cyclohexane, and have no measurable PL in the solid state.[149**] Similar properties are observed for other simple carboranes such as alkyl, silylalkyl, thiol and thioalkyl derivatives.[149] Conversely, there are a huge number of carboranes which are known to be highly luminescent, such as rhenium,[150] and nickel *closo*-metallocarboranes;[151] carborane-containing gold,[152] iridium,[153] iron,[69] mercury,[69] and platinum metal complexes.[154] Discussion of these materials is beyond the scope of this review, but of greater interest are the luminescent carboranes derivatised with aromatic rings.

There are a huge number of photoluminescent carboranes of this nature, and their emissive properties are generally as a result of a few, repeating processes, namely: localised emission (LE), intramolecular charge transfer (ICT) emission, twisted intramolecular charge transfer (TICT) emission, and aggregation-induced emission (AIE).

1.9.1 – Localised Emission

LE refers to photoluminescent emission associated with the radiative relaxation of an excited electronic species, whose wavefunction is confined to a space that does not include the whole molecule. In this context, LE means emission from an excited species localised on an aromatic group attached to a carborane, where the carborane is not electronically involved. Due to the Franck-Condon Principle, the LE generally has a 'vibronic' characteristic, which is to say that the emissive band-shape represents the relative intensity of allowed vibronic transitions for the system, **Figure 1-15**.

** There is a report that *ortho*-carborane displays a relatively intense phosphorescence at 77 K either in an ethanol glass or in the solid state.[148] However, the possibility that the luminescence was a result of an impurity could not be completely discounted.

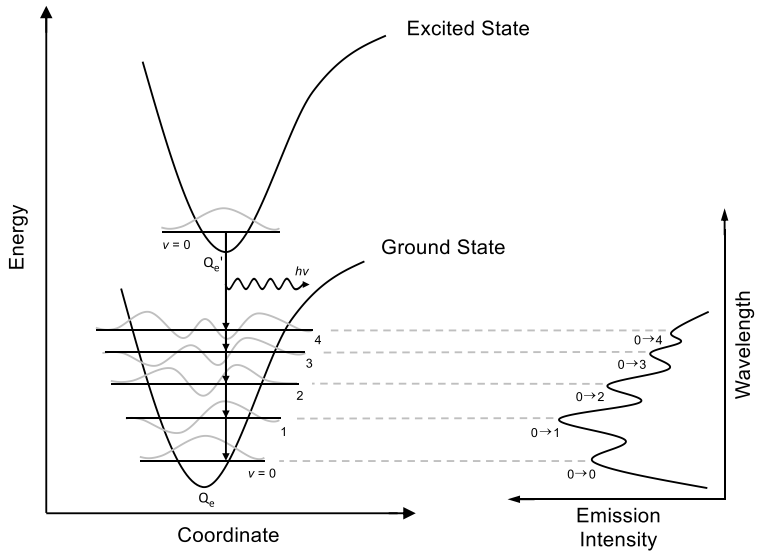


Figure 1-15 – A schematic of the Franck-Condon Principle and the resulting vibronic emissive band-shape. Q_e and Q_e' are the equilibrium nuclear positions in the ground and excited states respectively, where ΔQ_e is the equilibrium position offset.

The UV-Vis absorbance of carboranes is significantly lower than that of aromatic groups; the extinction coefficient of all three isomers is approximately two orders of magnitude lower than that of benzene,[149,155] which itself is considered a relatively poor chromophore. The absorption spectra of aryl carboranes are therefore dominated by the aromatic system, which has the physical effect of the excitation being initially localised in this area. In some cases, the excited state can then extend onto the carborane through charge transfer, which will be described later, but often no such delocalisation occurs (or is simply not possible). The excited state remains localised, and some degree of non-radiative relaxation takes place before finally radiative relaxation in the form of fluorescence, with an emissive band-shape that is a mirror of the vibronic absorbance, and virtually identical to the parent aromatic compound.

Aryl *Meta* and *para*-carboranes generally behave in this way. Mono and disubstituted phenyl and naphthyl *meta* and *para*-carboranes have an emission λ_{max} of ca. 290 and 340 nm respectively in cyclohexane, compared to a λ_{max} of 285 and 322 nm of benzene and naphthalene respectively in the same solvent.[56] This is due to charge transfer not being easily achievable for these carborane isomers, causing the aromatic rings to be essentially isolated from the cage. The same is true for polymers with this architecture; polyfluorene with *para*-carborane in the backbone, encountered earlier, has a LE that is relatively unchanged relative to the parent polyfluorene.[137] The former is more stable however, and shows promise for PLED applications.

Aryl *ortho*-carboranes can also show LE, such as 1-(2'-pyridyl)-*ortho*-carborane,[149] 1,2-dinaphthyl-*ortho*-carborane,[56] and 1,2-bis(4-(*N*-carbazolyl)phenyl)-*ortho*-carborane,[156] to name only a few of many examples, but in these cases, as in most, the LE is accompanied by other types of emission.

1.9.2 – ICT and TICT Emission

ICT and TICT are two highly-related concepts which have often been confused in the carborane literature. An ICT state, or more specifically a photoinduced ICT state, is formed when a large fraction of an electronic charge is transferred from one region of a molecule, the donor, to another region, the acceptor, following photoexcitation. In this context, the carborane is the acceptor, and the aryl group is the donor. For a TICT state:

> *"this [intramolecular charge] transfer is subsequently followed by intramolecular twisting of the donor and acceptor about a single bond and produces a relaxed perpendicular structure and emits from a lower energy band due to [the] TICT state."*[157]

ICT is readily achievable for aryl *ortho*-carboranes, particularly when the plane of the aromatic is approximately parallel to the C-C bond of the cluster.[158] Once formed, such ICT states can lead to emission with a band-shape that is broad, featureless, and red-shifted relative to the LE. However, if the C-C bond of the carborane becomes perpendicular to the aromatic plane, a larger amount of charge can transfer, accompanied by a dramatic lengthening of this bond, and an overall reduction in the energy of the excited state.[158] These are generally referred to as TICT states in the carborane literature, and also have a broad, featureless emissive band-shape, but are always red-shifted relative to ICT emission. This red-shift is due to the highly elastic C-C bond, which in TICT states elongates and vibrates to non-radiatively dissipate energy, and can even quench emission completely, as in the case of mono and diphenyl-*ortho*-carborane.[56]

Rotation around the bond connecting the carborane and the aromatic is generally possible, even for very bulky groups such as anthracene.[159] Thus, for aryl *ortho*-carboranes, ICT states will often become TICT states as the carborane is able to rotate into a geometry enabling TICT formation, which leads to a more energetically favourable excited state. The processes involved in LE, ICT and TICT emission are summarised in **Figure 1-16**.

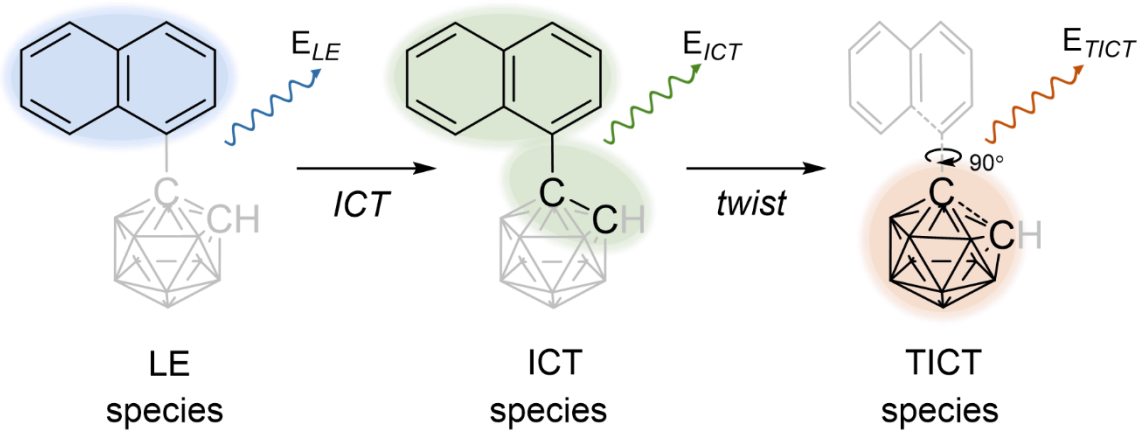


Figure 1-16 – A simplified schematic of the emission processes from the photoexcited states of a generalised aryl *ortho*-carborane. Black bonds represent approximately where the excited state electron density is localised, and grey bonds represent where the density is low (or zero). In the TICT state there is a 90° angle along the dashed dihedral between the aromatic and the carborane. The energy of emission, E, decreases on the order $E_{LE} > E_{ICT} > E_{TICT}$.

The TICT definition was not first applied to carboranes and is not well suited to them. Carboranes are spheroids, so the perpendicular nature of the TICT state does not apply; there are never two planes which can be perpendicular! This issue is somewhat overcome by defining the carborane plane as that which contains both the cage carbons, but this is only satisfactory if the carboranes have their centre of mass in the plane of the aromatic substituent. For some compounds like 9-anthracenyl-*ortho*-carborane (**50**), this is not the case, the carborane is bent significantly out of the aromatic plane.[159] Incidentally, the presence of the carborane also significantly distorts the ring system, curving the, famously planar, aromatics.[159,160] For these molecules TICT states can only be formed when the cage C-C bond is both perpendicular and on the same side of the plane in which the carborane is situated, **Figure 1-17**. The usual TICT definition is therefore not adequate for these materials.

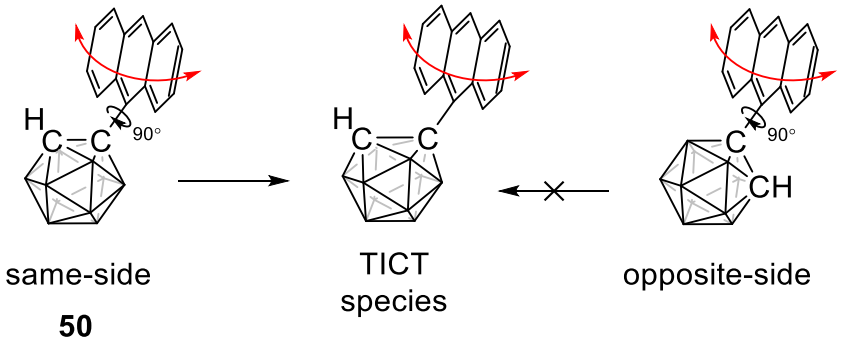


Figure 1-17 – A depiction of the geometry dependence of TICT species formation in anthracenyl-*ortho*-carborane, where the carborane is bent significantly out of the plane of the anthracene ring system. The curvature of anthracene is indicated.

Another shortcoming of the TICT definition is that, for carboranes whose ground state geometry, as obtained through single-crystal XRD, already has the C-C bond perpendicular to the aromatic plane,

no twisting need occur following excitation for the LE state to relax into the TICT state. The formation of the TICT state for these molecules is therefore simply a further relaxation of the ICT state in a process which is unique to *ortho*-carborane, due to the flexible C-C bond. Further, as even highly sterically hindered carboranes can rotate freely at room temperature in solution and in the solid state,[159] the same situation is true for aryl-carboranes that have their C-C bond parallel to the aromatic in their ground state. The traditional *ortho*-carborane TICT species can therefore be simultaneously described as both a ICT or TICT for almost all carborane, a fact that has certainly led to confusion in the literature. A new definition could be applied to dispel this confusion, providing a term to describe an ICT for *ortho*-carborane with an elongated C-C bond, without the need to describe how the species was formed.

1.9.3 – Aggregation Induced Emission

For most fluorophores, luminescence is quenched at high concentrations or in the solid state. This is due to the formation of aggregates, which introduces new, non-radiative decay pathways for the excited states, such as intermolecular π-π stacking.[161] This reduces luminescence in a process known as aggregation-caused quenching (ACQ). However, for some fluorophores precisely the opposite happens; materials which are either weakly or non-luminescent in dilute solutions become highly luminescent when aggregated. This is known as AIE and is a property that has gained significant attention for its potential use in solid-state light-emitting applications.[161]

Aryl-*ortho*-carborane compounds were first reported to exhibit AIE in 2009,[162] and are now well known to be moieties which aid it.[160,163–171] For these materials AIE is often achieved either in the solid state as polycrystalline samples or thin films, or through the introduction of bad solvents into good solutions, such as the addition of water into tetrahydrofuran (THF) to form 99/1 (v/v) H_2O/THF solutions.

The enhanced emission from these carboranes is thought to be due to the TICT state. Whilst TICT states are often emissive, the vibration of the flexible C-C bond can lead to non-radiative relaxation, but aggregation helps to ‘freeze’ this vibration.[162] In addition, localisation of the excited state inside the carborane prohibits the efficient non-radiative decay routes involving the aromatic ring systems (e.g. π-π stacking or excimer formation). A combination of these two factors causes the enormous increase in emissive intensity. This can also be achieved at low temperatures in aggregated states or glasses formed from dilute solutions of the carboranes in good solvents (e.g. 2-methyl-THF). The latter suggest that whilst aggregation can bring about this reduction in vibration and therefore enhanced

emission, the same can sometimes be achieved for isolated molecules when thermal vibration has been significantly reduced.[162]

1.10 – In This Thesis

Carboranes have now been incorporated in a wide range of π-conjugated systems for various material purposes and, of these, the luminescent small molecules are perhaps the most promising. In the last ten years, many fluorescent carboranes have been synthesised and great strides have been made in understanding the structure-property relationships. However, one can still find confusion in the literature in this regard, especially with regard to ICT and TICT states, and how this relates to AIE. In addition, much of this research has focused on aryl *ortho*-carboranes whilst the luminescence properties of the analogous *meta* and *para*-carboranes remain relatively unexplored, most likely because of the price of the parent carboranes.

The ability of carboranes to act as AIE inducing element blocks makes them of great interest for solid-state light applications, and this, coupled with their high boron density, makes them excellent candidate materials for neutron scintillator detectors. Whilst additives of the parent carboranes have been used successfully for this purpose in polysiloxane based scintillators, there has been no report of carborane derivatives being used for both ^{10}B carrier and luminescence material (in the same molecule).

With these observations in mind, this thesis aims to better understand the underlying principles of the various types of luminescence exhibited by aryl substituted carboranes, through the design and synthesis of new materials, which may find applications as intrinsic scintillators in neutron scintillator devices:

- Chapter 2 focuses on the three isomers of carborane, forming structurally isomeric aryl carboranes, and looks at the effect of carborane incorporation on the geometry and rigidity of these molecules. These ideas are extended to other heterocyclic tricyclic systems, with the aim of understanding the effect of steric hinderance on the rotation of *ortho*-carborane.

- Chapter 3 explores the various emissive behaviours of the molecules synthesised in Chapter 2. Using these molecules, the fundamentals of AIE is investigated, particularly concerning the precise nature of the aggregation, and how this relates to the excited state structure of each isolated molecule.

- Chapter 4 looks at using *ortho*-carborane as a means of causing severe deformation of the aromatic backbone of a range of polycyclic aromatic hydrocarbons (PAHs). The PL and PLE studies of these molecules enable a detailed examination of ICT and TICT states.

- Chapter 5 probes *ortho*-carborane involvement in other types of luminescence, namely excimers, via symmetrical bis-carborane substitution on the four ring-fused PAH, chrysene. Low temperature PL studies aid this examination and help to rationalise the novel emissive behaviours of this compound.

1.11 – References

1 A. R. Pitochelli and F. M. Hawthorne, *J. Am. Chem. Soc.*, 1960, **82**, 3228–3229.
2 H. C. Longuet-Higgins and M. D. V. Roberts, *Proc. R. Soc. Lond. A*, 1955, **230**, 110–119.
3 T. L. Heying, J. W. Ager, S. L. Clark, D. J. Mangold, H. L. Goldstein, M. Hillman, R. J. Polak and J. W. Szymanski, *Inorg. Chem.*, 1963, **2**, 1089–1092.
4 H. Schroeder, T. L. Heying and J. R. Reiner, *Inorg. Chem.*, 1963, **2**, 1092–1096.
5 T. L. Heying, J. W. Ager, S. L. Clark, R. P. Alexander, S. Papetti, J. A. Reid and S. I. Trotz, *Inorg. Chem.*, 1963, **2**, 1097–1105.
6 S. Papetti and T. L. Heying, *Inorg. Chem.*, 1963, **2**, 1105–1107.
7 M. M. Fein, J. Bobinski, N. Mayes, N. Schwartz and M. S. Cohen, *Inorg. Chem.*, 1963, **2**, 1111–1115.
8 M. M. Fein, D. Grafstein, J. E. Paustian, J. Bobinski, B. M. Lichstein, N. Mayes, N. N. Schwartz and M. S. Cohen, *Inorg. Chem.*, 1963, **2**, 1115–1119.
9 D. Grafstein, J. Bobinski, J. Dvorak, H. Smith, N. Schwartz, M. S. Cohen and M. M. Fein, *Inorg. Chem.*, 1963, **2**, 1120–1125.
10 D. Grafstein, J. Bobinski, J. Dvorak, J. E. Paustian, H. F. Smith, S. Karlan, C. Vogel and M. M. Fein, *Inorg. Chem.*, 1963, **2**, 1125–1128.
11 L. I. Zakharkin, V. I. Stanko, V. A. Brattsev, Y. A. Chapowskii and O. Y. Okhlobystin, 1.
12 T. P. Onak, R. E. Williams and H. G. Weiss, *J. Am. Chem. Soc.*, 1962, **84**, 2830–2831.
13 L. I. Zakharkin, V. I. Stanko, V. A. Brattstev, Yu. A. Chapovskii and Yu. T. Struchkov, *Bulletin of the Academy of Sciences, USSR Division of Chemical Science*, 1963, **12**, 1911–1911.
14 J. A. Potenza and W. N. Lipscomb, *Inorg. Chem.*, 1964, **3**, 1673–1679.
15 D. Grafstein and J. Dvorak, *Inorg. Chem.*, 1963, **2**, 1128–1133.
16 Stelvio. Papetti and T. L. Heying, *J. Am. Chem. Soc.*, 1964, **86**, 2295–2295.
17 R. N. Grimes, *Carboranes*, Academic Press, Amsterdam; Boston, Third edition., 2016.
18 K. Wade, *J. Chem. Soc. D*, 1971, **0**, 792–793.
19 D. M. P. Mingos, *Nature Physical Science*, 1972, **236**, 99–102.
20 E. D. Jemmis and M. M. Balakrishnarajan, *J. Am. Chem. Soc.*, 2001, **123**, 4324–4330.
21 M. A. Fox, C. Nervi, A. Crivello and P. J. Low, *Chem. Commun.*, 2007, **0**, 2372–2374.
22 P. von R. Schleyer and K. Najafian, *Inorg. Chem.*, 1998, **37**, 3454–3470.
23 P. von R. Schleyer, K. Najafian and A. M. Mebel, *Inorg. Chem.*, 1998, **37**, 6765–6772.
24 J. Aihara, *J. Am. Chem. Soc.*, 1978, **100**, 3339–3342.
25 J. Aihara, *Inorg. Chem.*, 2001, **40**, 5042–5044.
26 V. V. Murakhtanov, T. M. Polyanskaya and V. V. Volkov, *J Struct Chem*, 1996, **37**, 562–571.
27 A. Toppino, A. R. Genady, M. E. El-Zaria, J. Reeve, F. Mostofian, J. Kent and J. F. Valliant, *Inorg. Chem.*, 2013, **52**, 8743–8749.
28 M. E. El-Zaria, K. Keskar, A. R. Genady, J. A. Ioppolo, J. McNulty and J. F. Valliant, *Angew. Chem. Int. Ed.*, 2014, **53**, 5156–5160.
29 U. Kusari, Y. Li, M. G. Bradley and L. G. Sneddon, *J. Am. Chem. Soc.*, 2004, **126**, 8662–8663.
30 U. Kusari, P. J. Carroll and L. G. Sneddon, *Inorg. Chem.*, 2008, **47**, 9203–9215.
31 Y. Li, P. J. Carroll and L. G. Sneddon, *Inorg. Chem.*, 2008, **47**, 9193–9202.
32 K. R. Seddon, A. Stark and M.-J. Torres, *Pure and Applied Chemistry*, 2000, **72**, 2275–2287.
33 H. C. Beachell and B. F. Dietrich, *J. Am. Chem. Soc.*, 1961, **83**, 1347–1351.
34 M. Frederick. Hawthorne, R. L. Pilling and R. N. Grimes, *J. Am. Chem. Soc.*, 1964, **86**, 5338–5339.
35 M. Frederick. Hawthorne, R. L. Pilling and R. N. Grimes, *J. Am. Chem. Soc.*, 1967, **89**, 1067–1074.
36 M. Frederick. Hawthorne, R. L. Pilling and R. C. Vasavada, *J. Am. Chem. Soc.*, 1967, **89**, 1075–1078.
37 M. Thornton-Pett, M. A. Beckett and J. D. Kennedy, *J. Chem. Soc., Dalton Trans.*, 1986, **0**, 303–308.

38 M. Hofmann and P. von R. Schleyer, *Inorg. Chem.*, 1998, **37**, 5557–5565.
39 A. R. Pitochelli, Raymond. Ettinger, J. A. Dupont and M. Frederick. Hawthorne, *J. Am. Chem. Soc.*, 1962, **84**, 1057–1058.
40 L. I. Zakharkin, V. N. Kalinin and L. S. Podvisotskaya, *Russ Chem Bull*, 1970, **19**, 1227–1231.
41 W. N. Lipscomb, *PNAS*, 1961, **47**, 1791–1795.
42 Katchem, http://www.katchem.cz/en/, (accessed 4 December 2018).
43 S. Papetti, C. Obenland and T. L. Heying, *I&EC Product Research and Development*, 1966, **5**, 334–337.
44 G. M. Edvenson and D. F. Gaines, *Inorg. Chem.*, 1990, **29**, 1210–1216.
45 R. M. Salinger and C. L. Frye, *Inorg. Chem.*, 1965, **4**, 1815–1816.
46 H. D. Kaesz, Robert. Bau, H. A. Beall and W. N. Lipscomb, *J. Am. Chem. Soc.*, 1967, **89**, 4218–4220.
47 A. Kaczmarczyk, R. D. Dobrott and W. N. Lipscomb, *PNAS*, 1962, **48**, 729–733.
48 R. Hoffmann and W. N. Lipscomb, *Inorg. Chem.*, 1963, **2**, 231–232.
49 W. N. Lipscomb, *Science*, 1966, **153**, 373–378.
50 C. A. Brown and M. L. McKee, *J Mol Model*, 2006, **12**, 653–664.
51 I. J. Sugden, D. F. Plant and R. G. Bell, *Chem. Commun.*, 2013, **49**, 975–977.
52 L. I. Zakharkin, V. N. Kalinin and L. S. Podvisotskaya, *Russ Chem Bull*, 1967, **16**, 2212–2217.
53 G. B. Dunks, R. J. Wiersema and M. Frederick. Hawthorne, *J. Am. Chem. Soc.*, 1973, **95**, 3174–3179.
54 S. Zlatogorsky, D. Ellis, G. M. Rosair and A. J. Welch, *Chem. Commun.*, 2007, **0**, 2178–2180.
55 L. I. Zakharkin and V. N. Kalinin, *Russ Chem Bull*, 1969, **18**, 192–192.
56 R. A. Harder, PhD Thesis, Durham University, 2012.
57 L. L. Naeger and K. C. Leibman, *Toxicology and Applied Pharmacology*, 1972, **22**, 517–527.
58 M. A. Fox, PhD Thesis, Durham University, 1991.
59 J. M. Makhlouf, W. V. Hough and G. T. Hefferan, *Inorg. Chem.*, 1967, **6**, 1196–1198.
60 A. M. Spokoyny, *Pure Appl. Chem.*, 2013, **85**, 903–919.
61 L. I. Zakharkin, V. I. Stanko, A. I. Klimova and Yu. A. Chapovskii, *Russ Chem Bull*, 1963, **12**, 2072–2072.
62 C. Vinas, R. Benakki, F. Teixidor and J. Casabo, *Inorg. Chem.*, 1995, **34**, 3844–3845.
63 C. Malan and C. Morin, *Tetrahedron Letters*, 1997, **38**, 6599–6602.
64 J. Marshall, PhD Thesis, 2014.
65 A.-R. Popescu, A. D. Musteti, A. Ferrer-Ugalde, C. Viñas, R. Núñez and F. Teixidor, *Chemistry – A European Journal*, 2012, **18**, 3174–3184.
66 B. Wrackmeyer, E. V. Klimkina and W. Milius, *Zeitschrift für anorganische und allgemeine Chemie*, 2011, **637**, 1895–1902.
67 A. I. Kovredov, V. A. Ol'shevskaya and L. I. Zakharkin, *Russ Chem Bull*, 1977, **26**, 146–148.
68 B. Wrackmeyer, E. V. Klimkina and W. Milius, *European Journal of Inorganic Chemistry*, 2013, **2013**, 398–408.
69 T. W. Bitner, T. J. Wedge, M. F. Hawthorne and J. I. Zink, *Inorg. Chem.*, 2001, **40**, 5428–5433.
70 S. Bresadola, A. Frigo, B. Longato and G. Rigatti, *Inorg. Chem.*, 1973, **12**, 2788–2793.
71 W. Clegg, D. A. Brown, S. J. Bryan and K. Wade, *Journal of Organometallic Chemistry*, 1987, **325**, 39–46.
72 S. Wang, X. Yan, Z. Cheng, H. Zhang, Y. Liu and Y. Wang, *Angew. Chem. Int. Ed.*, 2015, **54**, 13068–13072.
73 N. K. Hota and D. S. Matteson, *J. Am. Chem. Soc.*, 1968, **90**, 3570–3572.
74 L. I. Zakharkin and V. N. Lebedev, *Russ Chem Bull*, 1970, **19**, 914–914.
75 L. I. Zakharkin and V. N. Lebedev, *Russ Chem Bull*, 1972, **21**, 2273–2275.
76 R. L. Thomas and A. J. Welch, *Acta Cryst C*, 1996, **52**, 1689–1691.
77 A. V. Marsh, Masters Thesis, Durham University, 2014.

78 A. S. Batsanov, M. A. Fox, J. A. K. Howard and K. Wade, *Journal of Organometallic Chemistry*, 2000, **597**, 157–163.
79 L. I. Zakharkin and A. I. Kovredov, *Russ Chem Bull*, 1974, **23**, 710–710.
80 R. Coult, M. A. Fox, W. R. Gill, P. L. Herbertson, J. A. H. MacBride and K. Wade, *Journal of Organometallic Chemistry*, 1993, **462**, 19–29.
81 L. I. Zakharkin, A. I. Kovderov and V. A. Ol'shevskaya, *Russ Chem Bull*, 1986, **35**, 1260–1266.
82 N. Y. Bian Deqian, *Chinese J. Org. Chem.*, 2013, **33**, 1774–1781.
83 X. Yang, W. Jiang, C. B. Knobler and M. F. Hawthorne, *J. Am. Chem. Soc.*, 1992, **114**, 9719–9721.
84 S. Ren and Z. Xie, *Organometallics*, 2008, **27**, 5167–5168.
85 S. Stadlbauer, P. Lönnecke, P. Welzel and E. Hey-Hawkins, *European Journal of Organic Chemistry*, 2010, **2010**, 3129–3139.
86 H. L. Gingrich, T. Ghosh, Q. Huang and M. Jones, *J. Am. Chem. Soc.*, 1990, **112**, 4082–4083.
87 J. Jeon, T. Kitamura, B.-W. Yoo, S. O. Kang and J. Ko, *Chem. Commun.*, 2001, **0**, 2110–2111.
88 Y. Zhu, X. Siwei, J. A. Maguire and N. S. Hosmane, *Molecules*, 2010, **15**, 9437–9449.
89 Z. Qiu and Z. Xie, *J. Am. Chem. Soc.*, 2009, **131**, 2084–2085.
90 D. Zhao, J. Zhang and Z. Xie, *J. Am. Chem. Soc.*, 2015, **137**, 13938–13942.
91 L. Barnett-Thamattoor, G. Zheng, D. M. Ho, M. Jones and J. E. Jackson, *Inorg. Chem.*, 1996, **35**, 7311–7315.
92 D. Olid, R. Núñez, C. Viñas and F. Teixidor, *Chem. Soc. Rev.*, 2013, **42**, 3318–3336.
93 A. Herzog, A. Maderna, G. N. Harakas, C. B. Knobler and M. F. Hawthorne, *Chemistry – A European Journal*, 1999, **5**, 1212–1217.
94 F. Teixidor, G. Barberà, A. Vaca, R. Kivekäs, R. Sillanpää, J. Oliva and C. Viñas, *J. Am. Chem. Soc.*, 2005, **127**, 10158–10159.
95 Z. Zheng, W. Jiang, A. A. Zinn, C. B. Knobler and M. F. Hawthorne, *Inorg. Chem.*, 1995, **34**, 2095–2100.
96 R. R. Srivastava, D. K. Hamlin and D. S. Wilbur, *J. Org. Chem.*, 1996, **61**, 9041–9044.
97 F. Teixidor, G. Barberà, C. Viñas, R. Sillanpää and R. Kivekäs, *Inorg. Chem.*, 2006, **45**, 3496–3498.
98 M. F. Hawthorne, D. C. Young, P. M. Garrett, D. A. Owen, S. G. Schwerin, F. N. Tebbe and P. A. Wegner, *J. Am. Chem. Soc.*, 1968, **90**, 862–868.
99 H. Yamazaki, K. Ohta and Y. Endo, *Tetrahedron Letters*, 2005, **46**, 3119–3122.
100 L. I. Zakharkin, A. I. Kovredov, V. A. Ol'shevskaya and Zh. S. Shaugumbekova, *Journal of Organometallic Chemistry*, 1982, **226**, 217–222.
101 United States, US3388092A, 1968.
102 J. Plesek, *Chem. Rev.*, 1992, **92**, 269–278.
103 HT5, http://www.sge.com/products/columns/gc-columns/ht5, (accessed 15 December 2018).
104 M. Juhasz, S. Hoffmann, E. Stoyanov, K.-C. Kim and C. A. Reed, *Angew. Chem. Int. Ed.*, 2004, **43**, 5352–5355.
105 C. A. Reed, *Acc. Chem. Res.*, 2013, **46**, 2567–2575.
106 M. Nava, I. V. Stoyanova, S. Cummings, E. S. Stoyanov and C. A. Reed, *Angew Chem Int Ed Engl*, 2014, **53**, 1131–1134.
107 I. Kato, K. Ono, Y. Sakurai, M. Ohmae, A. Maruhashi, Y. Imahori, M. Kirihata, M. Nakazawa and Y. Yura, *Applied Radiation and Isotopes*, 2004, **61**, 1069–1073.
108 K. Nedunchezhian, N. Aswath, M. Thiruppathy and S. Thirugnanamurthy, *J Clin Diagn Res*, 2016, **10**, ZE01–ZE04.
109 J. F. Valliant, K. J. Guenther, A. S. King, P. Morel, P. Schaffer, O. O. Sogbein and K. A. Stephenson, *Coordination Chemistry Reviews*, 2002, **232**, 173–230.
110 R. F. Barth, P. Mi and W. Yang, *Cancer Communications*, 2018, **38**, 35.
111 D. S. Matteson and N. K. Hota, *J. Am. Chem. Soc.*, 1971, **93**, 2893–2897.
112 M. F. Hawthorne, T. E. Berry and P. A. Wegner, *J. Am. Chem. Soc.*, 1965, **87**, 4746–4750.

113 R. C. B. Copley, M. A. Fox, W. R. Gill, J. A. K. Howard, J. A. Hugh MacBride, R. J. Peace, G. P. Rivers and K. Wade, *Chemical Communications*, 1996, **0**, 2033–2034.
114 S. L. Powley, W. Y. Man, G. M. Rosair and A. J. Welch, *Journal of Organometallic Chemistry*, 2015, **792**, 51–54.
115 D. S. Matteson and R. A. Davis, *Inorg. Chem.*, 1974, **13**, 859–862.
116 Y. Morisaki, M. Tominaga and Y. Chujo, *Chem. Eur. J.*, 2012, **18**, 11251–11257.
117 Y. Li, H.-Q. Wu, H.-L. Xu, S.-L. Sun and Z.-M. Su, *J Mol Model*, 2013, **19**, 3741–3747.
118 M. Tominaga, K. Nishino, Y. Morisaki and Y. Chujo, *Journal of Organometallic Chemistry*, 2015, **798**, 165–170.
119 K. Nishino, K. Hashimoto, K. Tanaka, Y. Morisaki and Y. Chujo, *Tetrahedron Letters*, 2016, **57**, 2025–2028.
120 Y. Morisaki, M. Tominaga, T. Ochiai and Y. Chujo, *Chemistry – An Asian Journal*, 2014, **9**, 1247–1251.
121 T. Long Chan and Z. Xie, *Chemical Science*, 2018, **9**, 2284–2289.
122 S. Wu and M. Jones, *Inorg. Chem.*, 1988, **27**, 2005–2008.
123 Y. Quan and Z. Xie, *J. Am. Chem. Soc.*, 2015, **137**, 3502–3505.
124 S. H. Wu and M. Jones, *Inorg. Chem.*, 1986, **25**, 4802–4803.
125 L. A. Boyd, W. Clegg, R. C. B. Copley, M. G. Davidson, M. A. Fox, T. G. Hibbert, J. A. K. Howard, A. Mackinnon, R. J. Peace and K. Wade, *Dalton Trans.*, 2004, **0**, 2786–2799.
126 E. S. Alekseyeva, M. A. Fox, J. A. K. Howard, J. A. H. MacBride and K. Wade, *Applied Organometallic Chemistry*, 2003, **17**, 499–508.
127 C. Viñas, G. Barberà, J. M. Oliva, F. Teixidor, A. J. Welch and G. M. Rosair, *Inorg. Chem.*, 2001, **40**, 6555–6562.
128 T. Vondrák, J. Plešek, S. Heřmánek and B. Štíbr, *Polyhedron*, 1989, **8**, 805–811.
129 I. V. Glukhov, K. A. Lyssenko, A. A. Korlyukov and M. Y. Antipin, *Faraday Discuss.*, 2006, **135**, 203–215.
130 M. A. Fox, J. A. H. MacBride, R. J. Peace and K. Wade, *J. Chem. Soc., Dalton Trans.*, 1998, **0**, 401–412.
131 H. Tricas, M. Colon, D. Ellis, S. A. Macgregor, D. McKay, G. M. Rosair, A. J. Welch, I. V. Glukhov, F. Rossi, F. Laschi and P. Zanello, *Dalton Trans.*, 2011, **40**, 4200–4211.
132 J. Kahlert, H.-G. Stammler, B. Neumann, R. A. Harder, L. Weber and M. A. Fox, *Angew. Chem. Int. Ed.*, 2014, **53**, 3702–3705.
133 C. K. Chiang, C. R. Fincher, Y. W. Park, A. J. Heeger, H. Shirakawa, E. J. Louis, S. C. Gau and A. G. MacDiarmid, *Phys. Rev. Lett.*, 1977, **39**, 1098–1101.
134 C. Wang, H. Dong, W. Hu, Y. Liu and D. Zhu, *Chem. Rev.*, 2012, **112**, 2208–2267.
135 K. Kokado and Y. Chujo, *Macromolecules*, 2009, **42**, 1418–1420.
136 K. Kokado, Y. Tokoro and Y. Chujo, *Macromolecules*, 2009, **42**, 2925–2930.
137 J. J. Peterson, Y. C. Simon, E. Bryan Coughlin and K. R. Carter, *Chemical Communications*, 2009, **0**, 4950–4952.
138 E. Hao, B. Fabre, F. R. Fronczek and M. G. H. Vicente, *Chem. Commun.*, 2007, **0**, 4387–4389.
139 N. Zhao, B. Fabre, P. Bobadova-Parvanova, F. R. Fronczek and M. G. H. Vicente, *Journal of Organometallic Chemistry*, 2017, **828**, 157–165.
140 K. Kokado, M. Tominaga and Y. Chujo, *Macromol. Rapid Commun.*, 2010, **31**, 1389–1394.
141 J. Marshall, Z. Fei, C. P. Yau, N. Yaacobi-Gross, S. Rossbauer, T. D. Anthopoulos, S. E. Watkins, P. Beavis and M. Heeney, *J. Mater. Chem. C*, 2013, **2**, 232–239.
142 J. Marshall, B. C. Schroeder, H. Bronstein, I. Meager, S. Rossbauer, N. Yaacobi-Gross, E. Buchaca-Domingo, T. D. Anthopoulos, N. Stingelin, P. Beavis and M. Heeney, *Macromolecules*, 2014, **47**, 89–96.
143 B. Fabre, S. Chayer and M. G. H. Vicente, *Electrochemistry Communications*, 2003, **5**, 431–434.
144 B. Fabre, J. C. Clark and M. G. H. Vicente, *Macromolecules*, 2006, **39**, 112–119.

145 J. Marshall, J. Hooton, Y. Han, A. Creamer, R. Shahid Ashraf, Y. Porte, T. D. Anthopoulos, P. N. Stavrinou, M. A. McLachlan, H. Bronstein, P. Beavis and M. Heeney, *Polymer Chemistry*, 2014, **5**, 6190–6199.

146 Y. C. Simon, J. J. Peterson, C. Mangold, K. R. Carter and E. B. Coughlin, *Macromolecules*, 2009, **42**, 512–516.

147 S. Carturan, A. Quaranta, T. Marchi, F. Gramegna, M. Degerlier, M. Cinausero, V. L. Kravchuk and M. Poggi, *Radiat Prot Dosimetry*, 2011, **143**, 471–476.

148 H. Kunkely and A. Vogler, *Inorganica Chimica Acta*, 2004, **357**, 4607–4609.

149 L. Böhling, A. Brockhinke, J. Kahlert, L. Weber, R. A. Harder, D. S. Yufit, J. A. K. Howard, J. A. H. MacBride and M. A. Fox, *European Journal of Inorganic Chemistry*, 2016, **2016**, 403–412.

150 M. J. Fischer, P. A. Jelliss, J. H. Orlando, L. M. Phifer and N. P. Rath, *Journal of Luminescence*, 2005, **114**, 60–64.

151 A. V. Safronov, N. I. Shlyakhtina, T. A. Everett, M. R. VanGordon, Y. V. Sevryugina, S. S. Jalisatgi and M. F. Hawthorne, *Inorg. Chem.*, 2014, **53**, 10045–10053.

152 O. Crespo, M. Concepción Gimeno, A. Laguna, I. Ospino, G. Aullón and J. M. Oliva, *Dalton Transactions*, 2009, **0**, 3807–3813.

153 H. Jin Bae, H. Kim, K. Mun Lee, T. Kim, M. Eo, Y. Sup Lee, Y. Do and M. Hyung Lee, *Dalton Transactions*, 2013, **42**, 8549–8552.

154 A. M. Prokhorov, P. A. Slepukhin, V. L. Rusinov, V. N. Kalinin and D. N. Kozhevnikov, *Chem. Commun.*, 2011, **47**, 7713–7715.

155 M. Taniguchi and J. S. Lindsey, *Photochemistry and Photobiology*, 2018, **94**, 290–327.

156 K.-R. Wee, W.-S. Han, D. W. Cho, S. Kwon, C. Pac and S. O. Kang, *Angew. Chem. Int. Ed.*, 2012, **51**, 2677–2680.

157 G. P. C. Drummen, *Molecules*, 2012, **17**, 14067–14090.

158 L. Weber, J. Kahlert, R. Brockhinke, L. Böhling, A. Brockhinke, H.-G. Stammler, B. Neumann, R. A. Harder and M. A. Fox, *Chem. Eur. J.*, 2012, **18**, 8347–8357.

159 H. Naito, K. Nishino, Y. Morisaki, K. Tanaka and Y. Chujo, *Angew. Chem. Int. Ed.*, 2017, **56**, 254–259.

160 H. Naito, K. Nishino, Y. Morisaki, K. Tanaka and Y. Chujo, *J. Mater. Chem. C*, 2017, **5**, 10047–10054.

161 Y. Hong, J. W. Y. Lam and B. Z. Tang, *Chem. Soc. Rev.*, 2011, **40**, 5361–5388.

162 K. Kokado and Y. Chujo, *Macromolecules*, 2009, **42**, 1418–1420.

163 X. Li, Y. Yin, H. Yan and C. Lu, *Chem. Asian J.*, 2017, **12**, 2207–2210.

164 Y. Chen, J. Guo, X. Wu, D. Jia and F. Tong, *Dyes and Pigments*, 2018, **148**, 180–188.

165 K. Nishino, K. Uemura, K. Tanaka, Y. Morisaki and Y. Chujo, *European Journal of Organic Chemistry*, 2018, **2018**, 1507–1512.

166 K. Nishino, H. Yamamoto, K. Tanaka and Y. Chujo, *Org. Lett.*, 2016, **18**, 4064–4067.

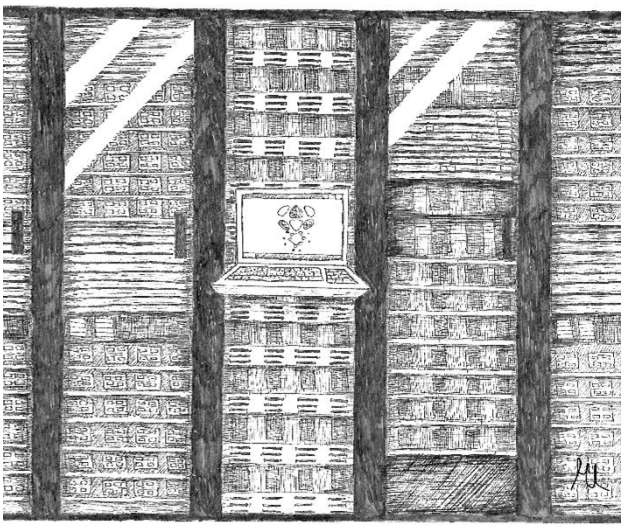
167 H. Naito, K. Nishino, Y. Morisaki, K. Tanaka and Y. Chujo, *Chem. Asian J.*, 2017, **12**, 2134–2138.

168 H. Naito, Y. Morisaki and Y. Chujo, *Angew. Chem. Int. Ed.*, 2015, **54**, 5084–5087.

169 K. Nishino, K. Uemura, M. Gon, K. Tanaka and Y. Chujo, *Molecules*, 2017, **22**, 2009.

170 J. Li, C. Yang, X. Peng, Y. Chen, Q. Qi, X. Luo, W.-Y. Lai and W. Huang, *Journal of Materials Chemistry C*, 2018, **6**, 19–28.

171 K. Nishino, Y. Morisaki, K. Tanaka and Y. Chujo, *Chemistry – An Asian Journal*, 2019, **14**, 789–795.



Chapter 2 – The Synthesis, Structure, and Properties of Tricyclic-Substituted Carboranes

2.1 – Introduction

Carboranes are highly dense molecules; they contain many atoms in a relatively small, rigid, icosahedron. As a result, substitution of the protons at any of the vertices brings the substituent atoms in close proximity to the Van der Waals radius of the rest of the cage. This is particularly a problem for carbon-substitution of *ortho*-carborane. The carboranyl C-C bond is smaller than B-C or B-B bonds (1.62, 1.69 and 1.77 Å respectively),[1] and the bond length between a cage carbon atom and the substituent is also smaller than in the boron case (0.92 and 1.07 Å for cage C-H and B-H bonds respectively).[1] As a result of these structural impositions, substituted carboranes can be very sterically hindered structures. A well-known consequence of this is the increase in the C-C bond length of *ortho*-carborane with the increase in the steric bulkiness of the substituents, exacerbated when both carbon vertices are substituted, as evidenced in **Table 2-1**.[2]

Compound	Bond Length (Å)		
	C(1)-C(2)	C(1)-C(1')	C(2)-C(1')
ortho-$C_2B_{10}H_{12}$	1.620	-	-
1-Ph-*ortho*-$C_2B_{10}H_{11}$	1.649	1.511	-
1-(1'-naphthyl)-*ortho*-$C_2B_{10}H_{11}$	1.677	1.516	-
1,2-Ph_2-*ortho*-$C_2B_{10}H_{10}$	1.726	1.507	1.505
1,2-(1'-dinaphthyl)$_2$-*ortho*-$C_2B_{10}H_{10}$	1.791	1.517	1.516

Table 2-1 – Selected bond lengths for the parent, phenyl and naphthyl *ortho*-carboranes.

The rotation barrier for substituents also increases with steric size ('rotation' here is describing movement about the dihedral angle between the carborane and the substituent). The rotational barrier between energy minima geometries for phenyl *ortho*-carborane is 1 kcal / mol, rising to 3 kcal / mol for the analogous naphthyl compound.[2] Rotation barriers are even higher for disubstituted carboranes.

A restriction in the rotation may be a useful property for photoluminescent materials. *Ortho*-carborane compounds have been demonstrated to exhibit AIE; a property in which photoluminescence intensity increases dramatically in aggregated materials where intramolecular motion is restricted. This inhibits non-radiative decay routes, thus excited states relax preferentially through radiative means, and the photoluminescence quantum yield increases. Therefore, increasing molecular rigidity, by raising the barrier to rotation, may aid photoluminescence in aggregated or even non-aggregated states. It should also be noted that AIE for *meta* and *para*-carboranes is yet to be explored extensively in the literature.

One such way to increase the rotation barrier of aryl carboranes is to extend the size of the aromatic substituent. Mono and disubstituted phenyl and naphthyl carboranes are all known,[3] however this is not true for anthracene. Monosubstituted 9'-anthracenyl-*para*-carborane was reportedly synthesised in very small yields, but it could not be isolated,[2] and purification efforts were halted when it was determined this molecule was likely to be unstable. DFT calculations of the ground state of this compound suggested that the carborane and end rings of the anthracene moiety have a large sterical clash, due to the 'pocket' of space between the protons attached to the 1 and 8 position carbons of anthracene being too small to fit the bulky carborane substituent (numbering nomenclature for all acenes in this thesis are presented in **Appendix I**). To resolve this energetically unfavourable geometry, the backbone of the anthracene curves away from the carborane. Simultaneously, the carborane is bent out of the plane of the ring system. It was thought that such a molecule would be

too unstable to exist, although a cage-boron substituted carboranyl anthracene has been reported with no mention of instability.[4]

A similar DFT-based observation of carborane-induced aromatic deformation was reported for bis-*para*-carborane substituted benzo[2,1-b:3,4-b']dithiophene (BDT), however, a bis-*ortho*-carboranyl derivative of this molecule, 4,8-bis-(1'-*ortho*-$C_2B_{10}H_{11})_2$-BDT (***o*Cb$_2$BDT**) (**51**), was later synthesised and found to be stable.[5] The single-crystal XRD structure of this compound, drawn as an Oak Ridge thermal ellipsoid plot (ORTEP) with atomic ellipsoid types determined in **Appendix II**, is presented in **Figure 2-1**.

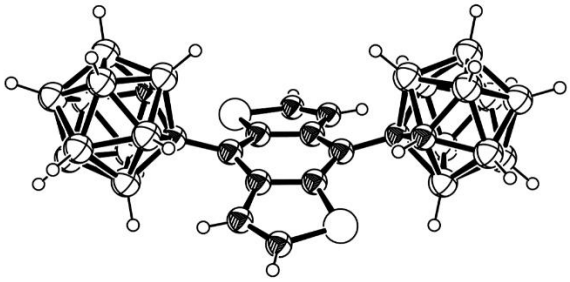


Figure 2-1 – An ORTEP of the molecular structure of ***o*Cb$_2$BDT**.

This leads to at least the possibility that anthracenyl-substituted carboranes may indeed be stable, like their BDT counterparts.* Moreover, if stable, the molecules are likely to be highly rigid, as a result of the large rotation barriers imposed by the bulky substituent.

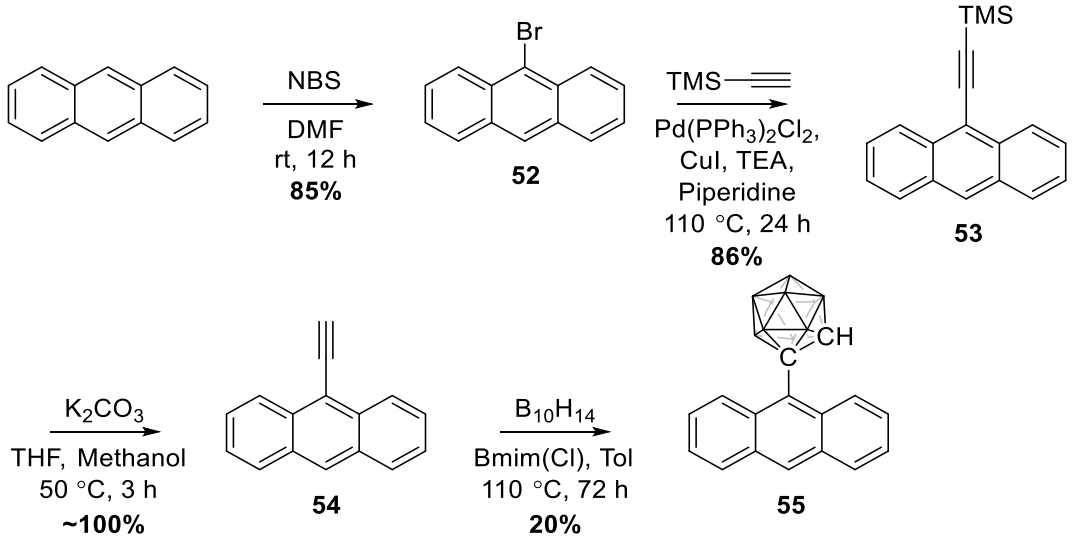
Hence, in this chapter, an investigation into the synthesis, structure, and properties of the anthracenyl *ortho*, *meta* and *para*-carborane are presented. Through single-crystal XRD, the aromatic deformations of these compounds are analysed, and the differences between the carboranes are rationalised with structural arguments. This series of highly sterically congested compounds is then expanded by varying the architecture around the carborane, using structural similar tricyclic heterocycles. In this manner, a systematic tuning of the rotational barrier is explored, with a view to creating a range of new, structurally rigid carboranes for photoluminescence purposes.

* Since this work was completed the cage-carbon substituted anthracenyl *ortho*-carborane isomer has been reported, as detailed in the introduction.

2.2 – Synthesis of Anthracenyl Carboranes

2.2.1 – *Ortho*-carborane isomer

Of the three isomers, in theory, the *ortho* isomer is the easiest to synthesise; one can follow either of two synthetic strategies, decaborane-acetylene coupling or copper-mediated cross-coupling. Due to the previously reported success of the decaborane coupling with a sterically crowded BDT-acetylene,[5] and the formation of two naphthyl *ortho*-carborane structural isomers using this method, it seemed sensible to start with this approach. The synthesis of 1-(9'-anthracenyl)-*ortho*-$C_2B_{10}H_{11}$ (***o*CbAnth** (**55)**) is summarised in **Scheme 2-1**.



Scheme 2-1 – The synthesis of ***o*CbAnth** via ionic liquid catalysed decaborane-acetylene coupling.

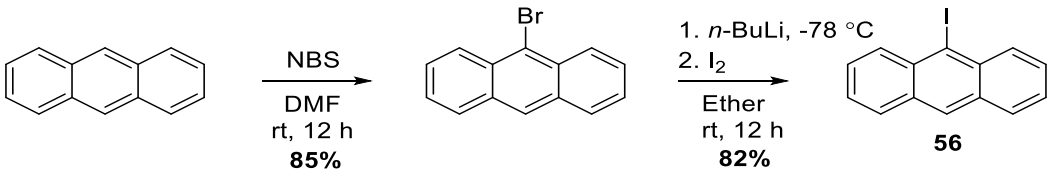
First, anthracene was monobrominated with NBS in DMF solvent in a clean, mild and high yielding reaction.[6] Bromination occurred at the most electron-rich 9-position, and a simple precipitation and recrystallisation yielded 9-bromoanthracene (**52**) in excellent purity. The acetylene was then installed via the reaction of 9-bromoanthracene with trimethylsilyl (TMS) acetylene under classical Sonogashira conditions,[7] with high temperature (110 °C) according to a literature procedure.[8] The boiling point of TMS-acetylene (53 °C) is much lower than the reaction temperature, and so it is somewhat surprising this reaction proceeds at all; one may expect all the acetylene to boil off quickly before a reaction can occur. It may be that the formation of the copper acetylide in the Cu-cycle occurs quickly at a lower temperature, and this compound has a much higher boiling point than its precursor. In any case, the product (**53**) is formed in high yield. Desilylation was achieved efficiently using K_2CO_3 in a THF /

methanol solvent mixture, the latter of which reacts with K_2CO_3 to form non-trivial amounts of methoxide according to **Equation 2-1**.

$$K_2CO_3 + CH_3OH \leftrightharpoons CH_3O^-K^+ + KHCO_3 \qquad \text{[Equation 2-1]}$$

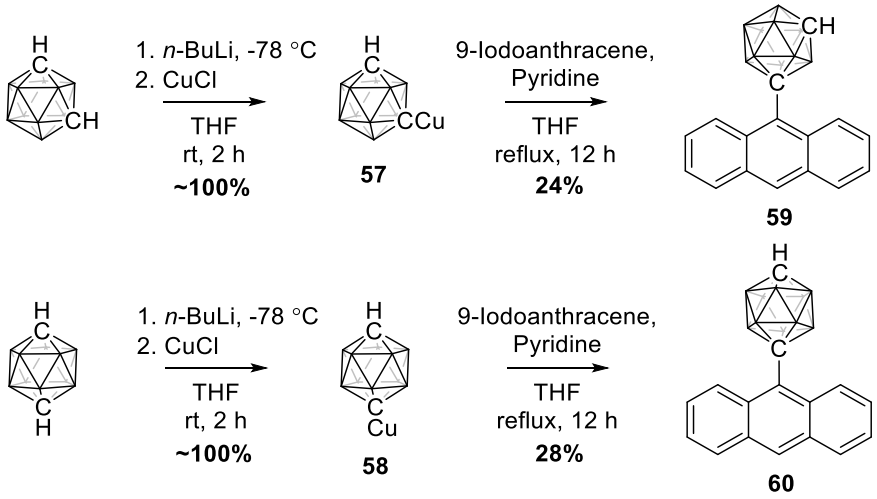
Methoxide is an excellent nucleophile and likely the desilylating agent in this reaction. The resulting terminal acetylene (**54**) is highly electron rich and was unstable towards light and oxidation, thus it was used immediately in the next reaction. The coupling of decaborane and 9-ethynylnthracene was achieved using the ionic liquid procedure described in the introduction, with 1-butyl-3-methylimidazolium chloride bmim(Cl) as the catalyst. As with all reactions with (water-sensitive) decaborane, rigorous exclusion of moisture was required, as it can react rapidly with water and transform into intermediate products that are eventually degraded to boric acid.[9] This was particularly problematic for the method in question, as bmim(Cl) is highly hygroscopic and often kept in a glove box, which was not available. Therefore, after weighing out the bmim(Cl) it must be dried; it was added to dry toluene and the mixture was vigorously stirred and refluxed under a stream of argon in a Dean-Stark apparatus. Once the formation of water droplets ceased to be observed in the burette, the Dean-Stark head was removed and replaced with a condenser, and the reaction proceeded as described in the schematic. The product was purified by column chromatography and recrystallised from dichloromethane (DCM) to afford ***o*CbAnth** (**55**) as yellow crystals which, importantly, proved to be chemically stable.

As will be clear from the introduction, it is not possible to make the *meta* and *para* isomers directly from the above synthetic strategy. Thermal isomerisation of ***o*CbAnth** is also not possible (nor at all practical) as the anthracene moiety will not be stable at the high temperatures required. Copper-mediated cross-coupling of 9-bromoanthracene and *para*-carborane has been reported, however, the yield of the reaction was very low and the product could not be isolated.[2] For these types of couplings often iodinated aromatics are used due to the more reactive C-I bond, but it was stated that there were problems with the formation of 9-iodoathracene (**56**), as in **Scheme 2-2**.[10]



Scheme 2-2 – The synthesis of 9-iodoanthracene from 9-bromoanthracene.

We found no such problem with the formation of the iodinated compound from 9-bromoanthracene, with an excellent yield on reasonably large scales. The product was, however, much more sensitive to light and air than its precursor, turning noticeably darker in colour over a period of two days. This decomposition was delayed when the compound is kept in a light-sensitive vial and in the refrigerator, keeping for months without discolouration. Following this success, the copper-mediated cross-coupling reaction via the *meta* and *para*-carborane cuprates (**57** and **58** respectively) was attempted. The synthesis of 1-(9'-anthracenyl)-*meta*-$C_2B_{10}H_{11}$ (***m*CbAnth**) (**59**) and 1-(9'-anthracenyl)-*para*-$C_2B_{10}H_{11}$ (***p*CbAnth**) (**60**) is presented in **Scheme 2-3**.



Scheme 2-3 – The synthesis of ***m*CbAnth** via CuCl mediated cross-coupling of *meta*-carborane and iodoanthracene. The analogous reaction starting with *para*-carborane yields ***p*CbAnth**.

Synthesis proceeded efficiently for both isomers; NMR studies suggested that the products had been formed, but isolation of the products was not easy. 9-Iodoanthracene has very similar physical properties to the anthracenyl carboranes, and separation via recrystallisation was not possible. Functional group interconversion at the C-I bond is possible however, and chemical reduction using Zn metal and aq. ammonium chloride in THF enabled the transformation of iodoanthracene to anthracene, without affecting the carborane product. The resulting compounds had suitably dissimilar properties such that successive (>3) recrystallisation by slow evaporation from DCM yielded small amounts of the pure anthracenyl carboranes, which were used for characterisation. Purification on larger scales required a different strategy, and we found preparative gel permeation chromatography (GPC) on the crude reaction products (i.e. no reduction of the iodoanthracene), followed by recrystallisation afforded both ***m*CbAnth** and ***p*CbAnth** species as bright green crystals.

2.3 – Thermogravimetric Analysis

As discussed earlier, previous reports of ***p*CbAnth**, and DFT studies of the *ortho* and *meta* isomer, suggested that these molecules were unlikely to be stable.[2] Observational evidence in the laboratory suggested that the compounds were indeed stable in air and light, with no discolouration occurring days after isolation in solid form and in transparent vials; for comparison, 9-ethynylanthracene is a yellow solid which oxidises and begins to brown noticeably over that period of time. Before moving on to explore the properties of these new materials, it seemed prudent to test their stability with more objective methods. TGA allows for the study of thermal stability of compounds in an inert atmosphere, **Figure 2-2**.

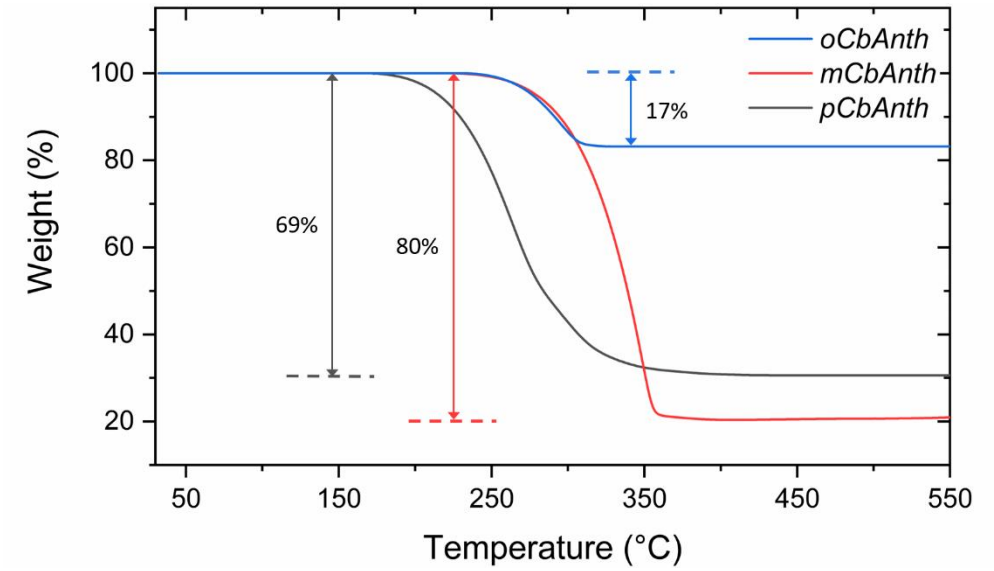


Figure 2-2 – TGA under an N_2 flow of the three isomers of anthracenyl carboranes. ***o*CbAnth** shows only 17% weight loss up to 550 °C, smaller than the 80% and 69% respectively for ***m*CbAnth** and ***p*CbAnth** isomers. The onset of decomposition occurs on the order *para* > *meta* ≈ *ortho*.

The onset of decomposition suggests that ***p*CbAnth** is the least thermally stable of the three isomers. This is somewhat counterintuitive because, of the parent isomers, *para*-carborane is the most stable. However, it can be rationalised in terms of the electron-withdrawing effect of the carboranes, which increases the stability of the electron-rich anthracene on the order *para* < *meta* < *ortho*. The onset of decomposition for pure anthracene in similar conditions is almost identical to that of ***p*CbAnth**, at about 180 °C.[11] Anthracene thermally decomposes completely, reaching this point at about 270 °C, but the carborane compounds do not; the decomposition of ***m*CbAnth** and ***p*CbAnth** plateaus at around 70-80% weight loss, and ***o*CbAnth** at only 17% weight loss. Clearly, these compounds are, contrary to previous reports, not only thermally stable, but more stable than the parent anthracene, and ***o*CbAnth** shows a significant stability enhancement.

2.4 – X-ray Crystallography

Recrystallisation by slow evaporation of pure samples of the three isomers in DCM afforded single-crystals, which were submitted for XRD analysis. Crystal structures were obtained and are shown in **Figure 2-3**.

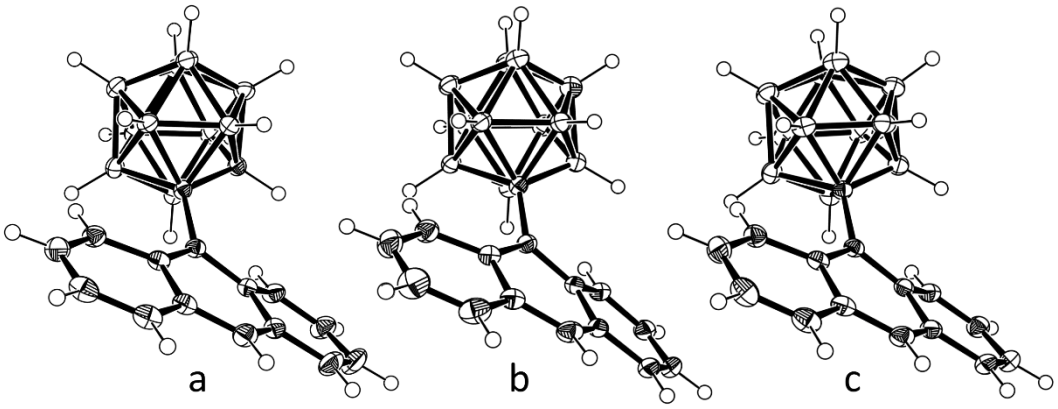


Figure 2-3 – ORTEPs of the molecular structures of (a) ***o*CbAnth**, (b) ***m*CbAnth**, and (c) ***p*CbAnth**, as obtained from single-crystal XRD.

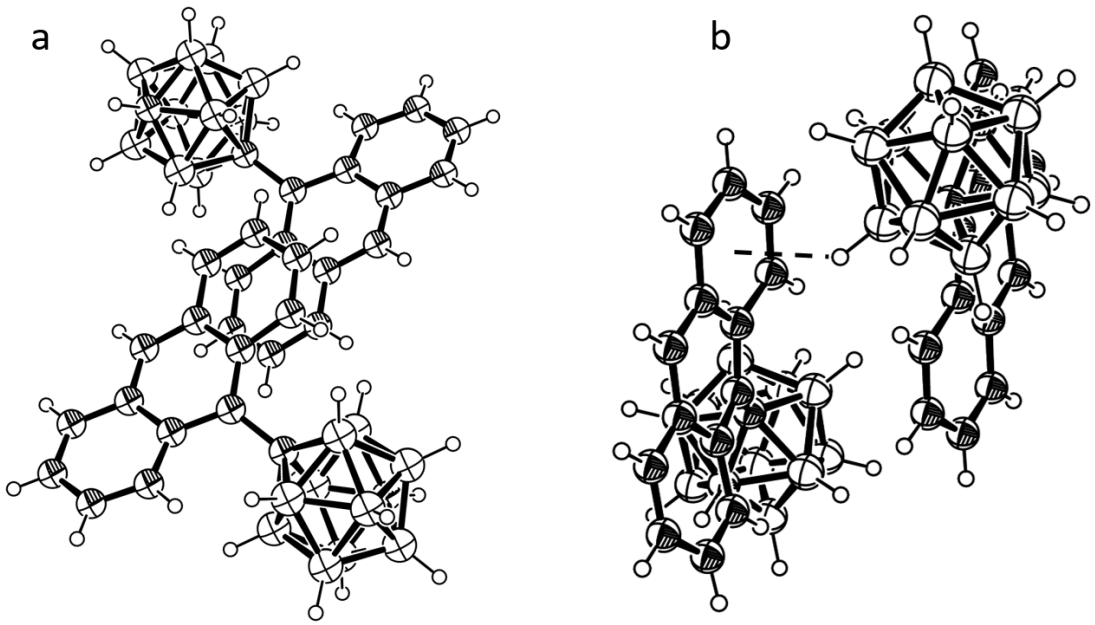


Figure 2-4 – ORTEPs of (a) anthracene π-overlapping dimers, and (b) carborane B-H / π-system hydrogen bond observed for ***o*CbAnth**.

***o*CbAnth** crystallises into the orthorhombic, Pbca space group, whilst ***m*CbAnth** and ***p*CbAnth** isomers crystallise into the monoclinic, $P2_1/n$ and $P2_1/c$ space groups respectively. There are similarities that extend over all three isomers however, such as the intermolecular interactions, with each displaying a degree of overlap between the π-systems of two neighbouring anthracene end ring dimers. An

example of this is demonstrated in **Figure 2-4a**. The ***o*CbAnth** and ***m*CbAnth** isomers also show a curious intermolecular interaction between the anthracene π-system and a B-H proton, **Figure 2-4b**. This is not the first time such an interaction has been reported,[12] where it was described as a new type of nonclassical hydrogen bond. This description has been disputed and instead characterised as a nonspecific dispersion-driven contact,[13] but the original work has since been vehemently defended.[14] On the basis of the latest paper we are persuaded that a hydrogen bond is indeed the correct term.

The individual molecules have strikingly similar structures; each shows a highly distorted anthracene ring system with the carboranes bent significantly out of the aromatic plane. There are differences between the structures however, and these are highlighted in **Table 2-2**, with reference to the physical quantities presented in **Appendix III**.

Compound	α (°)	β (°)	α + β (°)	θ (°)
*o*CbAnth	13.39	7.28	20.67	7.87
*m*CbAnth	14.89	5.65	20.54	4.32
*p*CbAnth	13.33	5.62	18.95	3.10

Table 2-2 – The angles of deformation for the three anthracenyl carborane isomers.

The sum of the α and β angles are similar for the ***o*CbAnth** and ***m*CbAnth** isomers, which are both larger than ***p*CbAnth**. In addition, the θ angle, which is the deviation from the ideal carborane axis of rotation angle of 180°, is significantly larger for ***o*CbAnth**.

The factors affecting the difference in these values between the carboranes are, if considering all the underlying bonding principles, incredibly complex, however, there are qualitative explanations of these phenomena. For example, of the five cage atoms surrounding the C(1) atom, i.e. the front 'face' of the carborane, only *ortho*-carborane has a carbon nearest neighbour. The C-C bond has a length which is ~5% shorter than the B-C bonds, which has the effect of narrowing the angle at which the C-H bond protrudes from the cage. This forces the C-H vertex closer to the anthracene substituent than all B-H vertices during rotation. Steric hindrance increases as a result and the carborane of ***o*CbAnth** is forced to bend further out of the aromatic plane than the other isomers to compensate. A similar argument can be made for the θ angle.

2.5 – Calculations

Based on the single-crystal XRD information, it could be presumed that steric hindrance, and therefore the barrier towards carborane rotation, will increase on the order *para* < *meta* < *ortho*. However, this

ignores the possibility that the aromatic substituent will also undergo geometric rearrangement during the rotation to reduce the overall energy of the molecule. It also does not consider the possible bonding implications of moving the second cage carbon atom around the cage relative to the ring system. To investigate this, a DFT study was undertaken to examine the change in total energy of the three isomers, as a function of rotation of the dihedral angle between the carborane and anthracene, **Figure 2-5**.

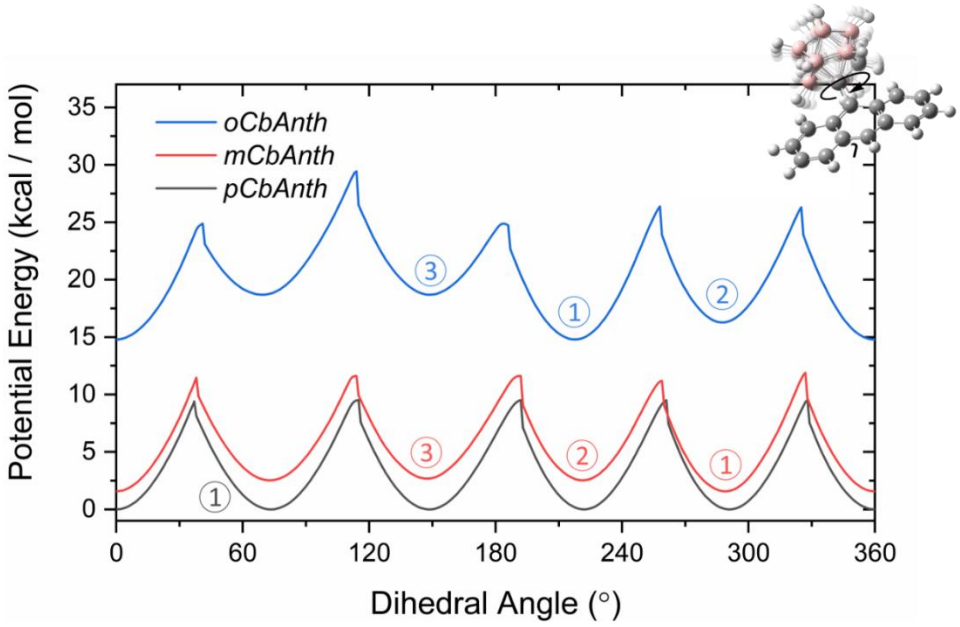


Figure 2-5 – DFT (B3LYP/6-31G(d,p); gas phase) calculated potential energy surface (PES) of *ortho*, *meta* and *para* isomers of anthracenyl carborane, as a function of dihedral angle at 1° intervals, relative to the ground state energy of ***p*CbAnth** (which has the lowest total energy of the three). The arbitrarily defined 0° state is the global ground state geometry, and unique ground state geometries are labelled in the order of increasing energy. Rotation occurs in the direction depicted, and the direction-dependent shape around the peak maxima are artefacts of the calculation.

There are clear differences in the ground state energies of the three isomers, which follows the order of stability of the parent carboranes. There are also five total energy minima for each compound, reflecting the rotating front pentagonal face of the carborane perpendicular to the plane of the aromatic system. For ***p*CbAnth**, all energy minima are virtually identical in energy, which is to be expected from the five-fold symmetry of *para*-carborane (i.e. there is one unique ground state geometry). For ***o*CbAnth** and ***m*CbAnth** isomers, there is no rotational symmetry, but there is dihedral symmetry due to the plane of symmetry perpendicular to the molecular axis of anthracene. Therefore, these isomers have three unique ground state geometries with occupancy 1:2:2.

It is still somewhat surprising however that there is an observable difference in energy for the three unique ground states of ***m*CbAnth**. The front face of this compound is functionally identical to the *para* isomer, so the energy differences cannot be explained using steric arguments; there must be an orbital

contribution from the carborane to the HOMO which varies depending on where the C(7) atom is situated relative to the ring system. More clearly, the C(7) atom must have a small orbital contribution to the HOMO, and this is demonstrated in **Figure 2-6**.

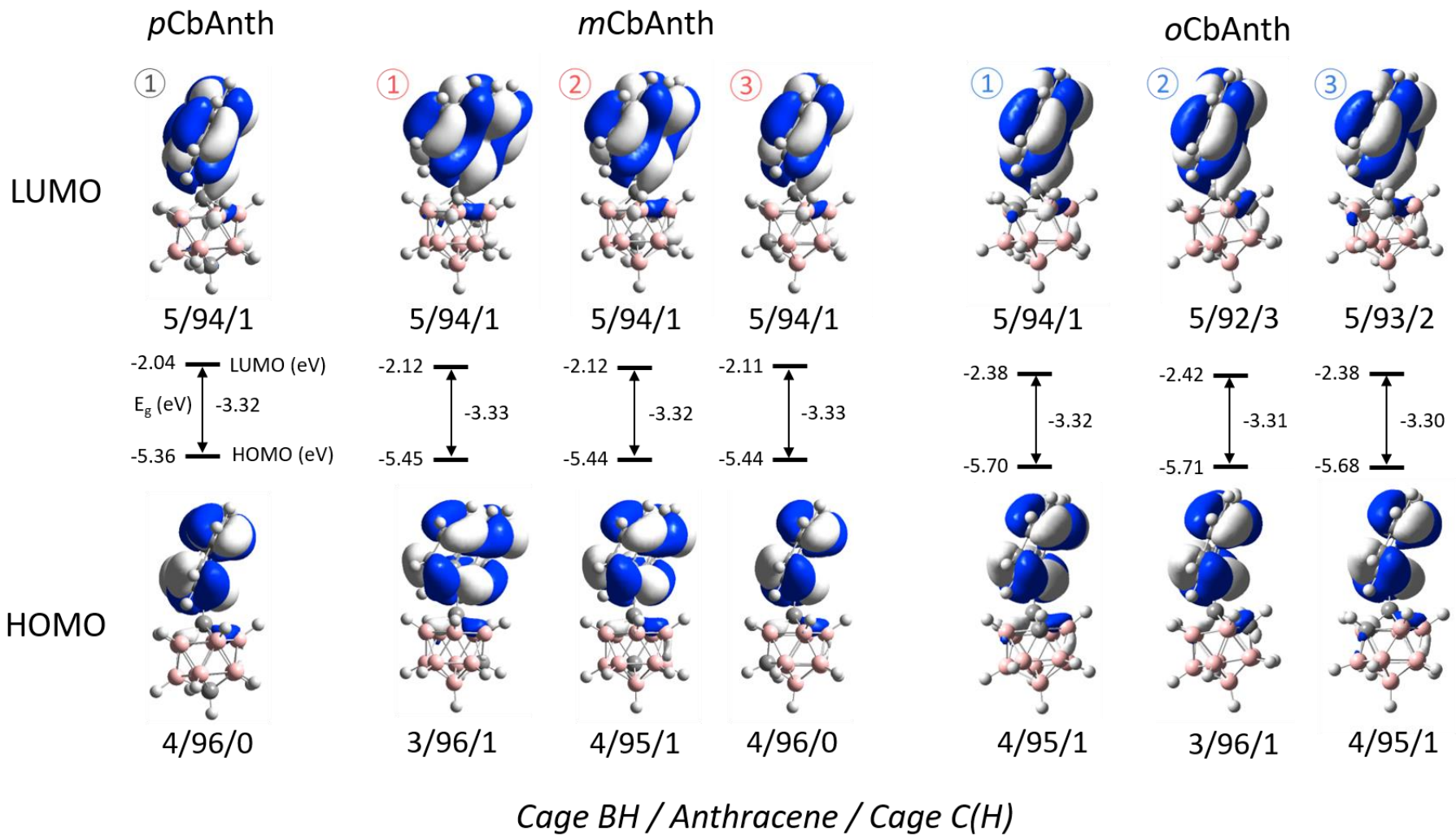


Figure 2-6 – DFT (B3LYP/6-31G(d,p); gas phase) calculated geometries, molecular orbitals, and energies of the HOMO and LUMO states of the ground state energy minima for *ortho*, *meta* and *para* anthracenyl carboranes. Relative orbital contributions of the cage B-H, anthracene and cage C (and C-H) moieties are presented.

The molecular orbital contributions demonstrate some common trends in carborane-aromatic dyads; bonding in the HOMO does not extend across the whole carborane and is mostly restricted to the aromatic group. The LUMO contains a larger contribution from the carborane as its inductive electron-withdrawing nature helps stabilise the higher energy species. This stabilisation is evident in the HOMO and LUMO energy levels as calculated in **Figure 2-6**, which are both lower for ***o*CbAnth** compared to ***m*CbAnth** or ***p*CbAnth**, **Figure 2-7**.

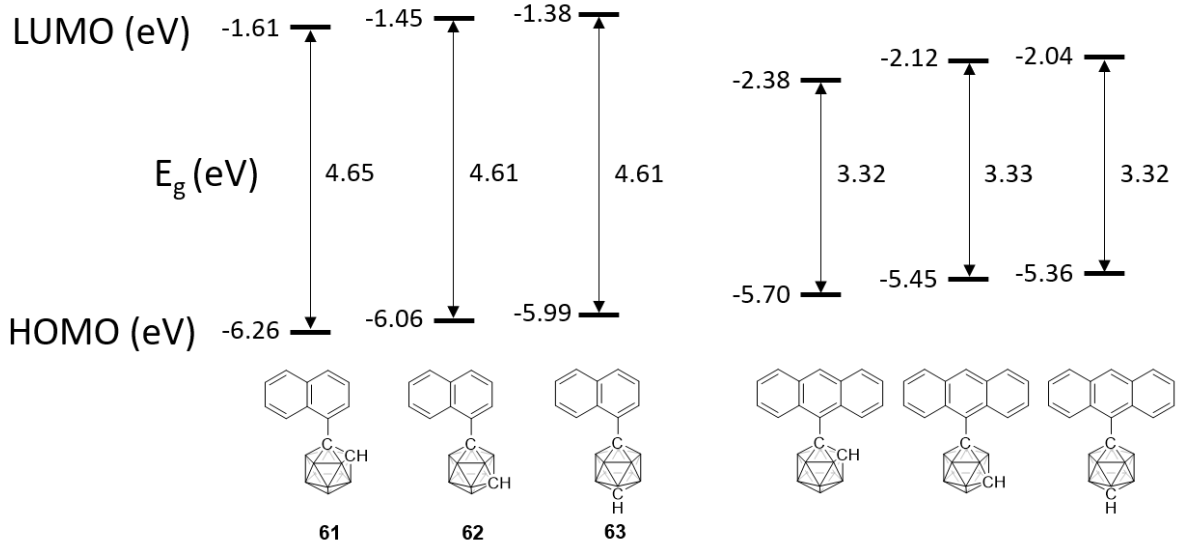


Figure 2-7 – DFT calculated (B3LYP/6-31G(d,p); gas phase) HOMO and LUMO energy levels and E_g of naphthyl,[2] and anthracenyl *ortho*, *meta* and *para* carboranes. Values were obtained from the global ground state geometries.

The stabilising effect has also been observed in calculations reported for naphthyl-*ortho*-carborane (**61**),[2] which has reduced HOMO and LUMO energies relative to the *meta* and *para* isomers (**62** and **63** respectively), however, the degree of stabilisation relative to the E_g is lower. This is somewhat surprising as the extent of carborane orbital involvement in the LUMO for naphthyl *ortho*-carborane is quite significantly larger than that of the analogous anthracenyl *ortho*-carborane in **Figure 2-6**,[2] where it is likely that the out-of-plane deformation of the carborane hinders its electronic involvement in the LUMO. This seeming anomaly so far escapes an explanation. The calculated LUMO value of ***o*CbAnth** compares relatively favourably with the experimental value, derived from CV, of -2.94 (CV data can be found in **Appendix IV**). Note that parent *meta* and *para*-carboranes are not stable to electrochemical reduction.

Interestingly, a weak π-bonding interaction from anthracene to *ortho*-carborane can be observed, as the C-C bond length increases when it is perpendicular to the aromatic ring (geometry (2) as presented in **Figures 2-5** and **2-6**) compared to the other energy minima states (geometries (1) and (3)) where it is smaller (1.727 Å, 1.667, and 1.664 Å respectively). The E_g for this the (2) geometry is lower than the

other ground states of ***o*CbAnth** and indeed of all the isomers, due to better LUMO stabilisation because of this π-bonding interaction. The maximum energy barrier to rotation, that is, the difference between the global energy maximum and minimum, are presented in **Table 2-3**.

Compound	Energy Barrier to Rotation (kcal / mol)
*o*CbAnth	14.6
*m*CbAnth	10.3
*p*CbAnth	9.5
1-Ph-*ortho*-$C_2B_{10}H_{11}$	<1
1,2-Ph_2-*ortho*-$C_2B_{10}H_{10}$	~4.0
1-(1'-naphthyl)-*ortho*-$C_2B_{10}H_{11}$	~4.0
1,2-(1'-dinaphthyl)$_2$-*ortho*-$C_2B_{10}H_{10}$	9.6

Table 2-3 – DFT calculated energy barriers to rotation for the three isomers of anthracenyl carboranes, with the data from selected similar compounds.[2]

The rotational barrier values for the anthracenyl carboranes are clearly large, in fact, ***o*CbAnth** and ***p*CbAnth** isomers have a barrier of rotation which is larger than even that of 1,2-(1'-$C_{10}H_7$)$_2$-*ortho*-$C_2B_{10}H_{11}$; a severely congested carborane bearing naphthyl groups at each of the two cage carbon atoms. It was hypothesised that such an energy barrier may cause restricted rotation of the carboranes in solution, and an NMR study was undertaken to investigate this.

2.6 – NMR

A comparison of the ^{1}H NMR spectra of three substituted anthracenes, including ***o*CbAnth**, is presented in **Figure 2-8**.

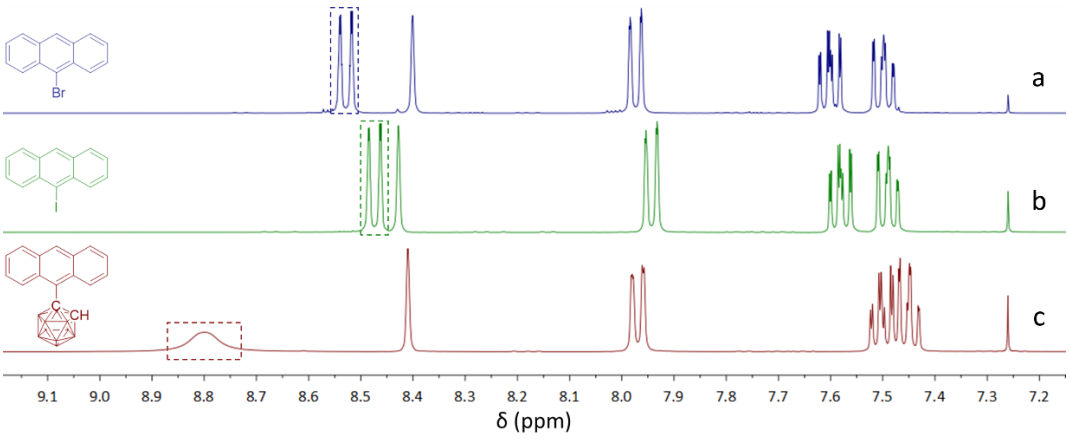


Figure 2-8 – The aromatic region of ^{1}H NMR ($CDCl_3$) spectra of (a) 9-bromoanthracene, (b) 9-iodoanthracene and (c) ***o*CbAnth**. Highlighted peaks each correspond to the protons at the 1 and 8 positions of anthracene.

The spectra of bromo and iodoanthracene are very similar, which is unsurprising given that the substituents have highly comparable properties. Curiously, however, the doublets at ca. δ = 8.5, relating to the 1 and 8 protons of anthracene, seem to 'disappear' for the carborane compound, and a new, broad peak appears further downfield. Integration of the aromatic peaks in all three spectra provides the occupancy 2:1:2:2:2, which suggests no protons are left unaccounted. The broad peak seen for ***o*CbAnth** is indeed the 1 and 8, anthracenyl protons.

The phenomenon is further elucidated with nuclear Overhauser effect spectroscopy (NOESY) of the carborane compound, which demonstrates that the protons at δ = 8.8 have a through-space correlation with the carboranyl C-H proton, and B-H protons of the cage. No such interactions exist for any of the other aromatic peaks, **Figure 2-9**.

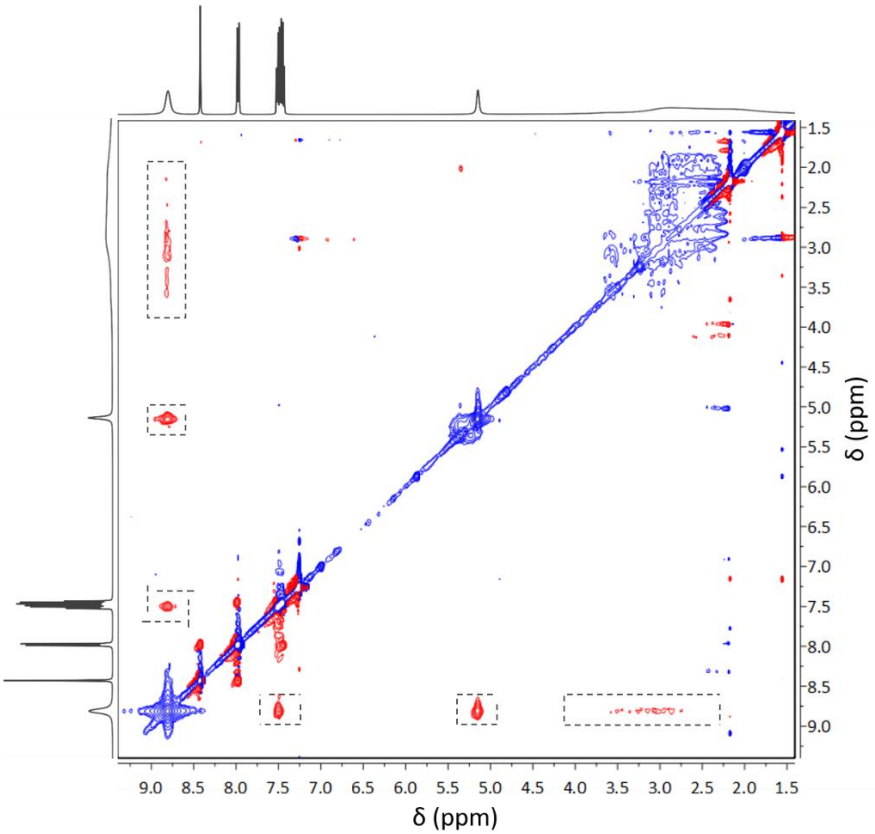


Figure 2-9 – ^{1}H-NOESY ($CDCl_3$) spectrum of ***o*CbAnth**. Chemical exchange correlations appear blue (negative) and conformational exchange correlations (positive) appear red.

The broadness of the peak is interesting, broad aromatic NMR peaks are only generally observed in highly concentrated (aggregated) samples or at low temperature, and even then, usually all peaks are broadened. Of the three isomers, it is also unique to ***o*CbAnth** at room temperature, as shown in **Figure 2-10**.

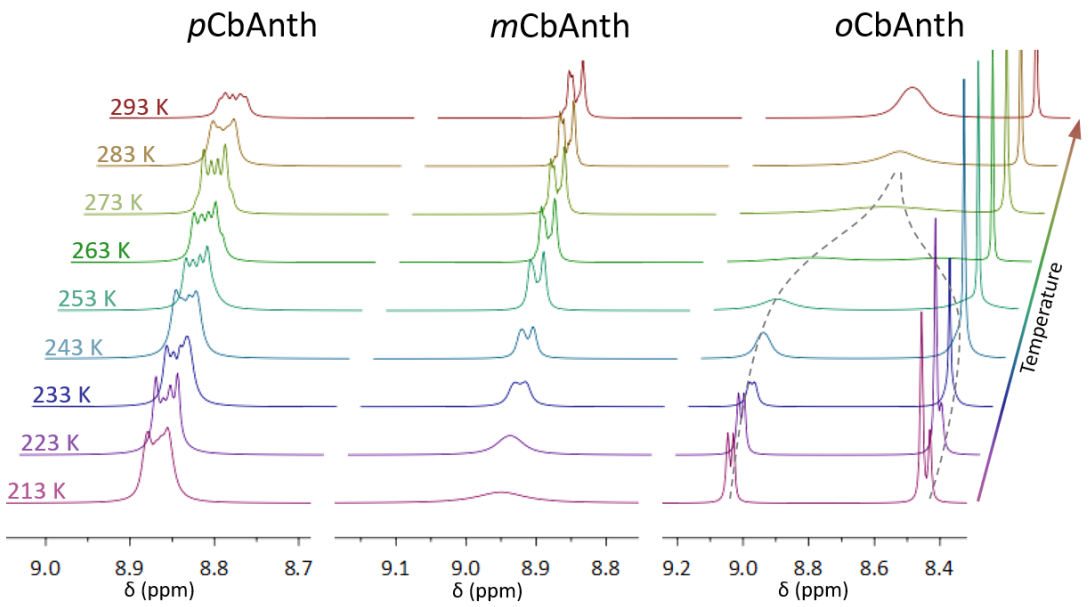


Figure 2-10 – Temperature-dependent ^{1}H NMR study of the anthracenyl carboranes in $CDCl_3$ (m.p. = 210 K), concentration = 3 x 10^{-3} M. The aromatic region incorporating the 1 and 8 protons of anthracene is presented, demonstrating the relative effect of temperature on rotation for the three isomers. The singlet at δ = 8.45 for ***o*CbAnth** is the proton in the 10 position of anthracene.

An explanation of this phenomena can be found by considering the varying barriers to rotation of the carboranes. In the temperature window studied, cooling of ***p*CbAnth** has no perceivable effect on the NMR spectrum, which is left unchanged. This is because on the timescale of the NMR experiment. the carborane rotates many times, so all the 1 and 8 anthracenyl protons in the solution experience the same, averaged out, electronic environment from the carborane, **Figure 2-11a**. For ***m*CbAnth** at room temperature the same is true, but upon cooling, rotation becomes slower such that some protons feel a different electronic environment than others, depending on the geometry of the carborane during the data acquisition period. A gaussian set of electron environments is produced, and the peak coalesces accordingly, **Figure 2-11b**.

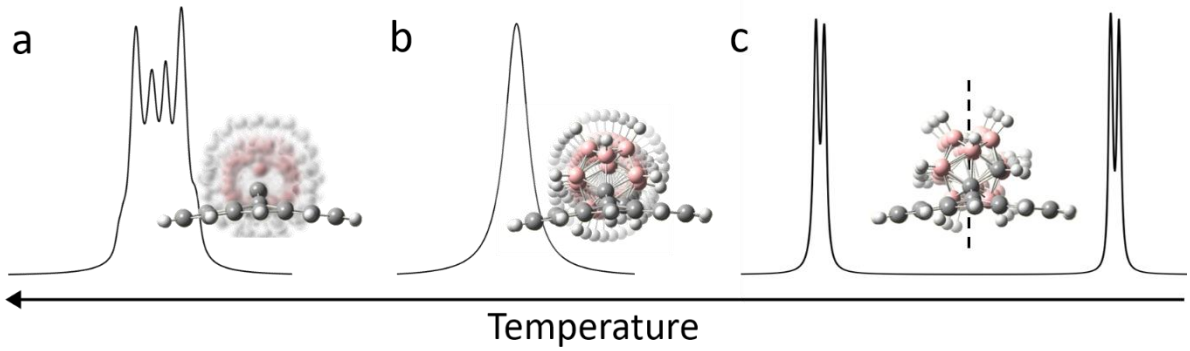


Figure 2-11 – A depiction of the effect of temperature on the 1 and 8 anthracenyl ^{1}H NMR peaks. Rotation is fast in (a) the high-temperature regime, slower in (b) the coalescence temperature regime and slow in (c) the low-temperature regime.

For ***o*CbAnth** the same is true at room temperature, but upon cooling the rotation further slows, to the point where the 1 and 8 protons on the anthracene become electronically inequivalent. This is possible due to the carborane is rotating less than 360° per acquisition period, so the 1 and 8 protons feel different electronic environments depending on which is nearer the carboranyl C-H vertex. At 213 K these peaks have sharpened to two doublets. This also occurs for the anthracenyl 4 and 5 protons, such that the initial multiplet also turns into two doublets at low temperature. It could be that at this temperature, rotation is significantly less than 360° per acquisition period, and the peaks sharpen as a result, demonstrated in **Figure 2-11c**. Very similar phenomena have been reported for other compounds, such as highly strained heterocycles.[15]

This temperature-dependent NMR study is a macroscopic reflection of the molecular-level properties explored via crystallography and DFT studies. The effect of restricted rotation increasing across the carboranes is of great interest with regards to PL and specifically AIE, where emission intensity increases when molecular motion is decreased. This will be explored in **Chapter 3**. First, given that of all isomers ***o*CbAnth** has the highest energy barrier to rotation, it seemed pertinent to explore how the barrier to rotation for *ortho*-carboranes can be affected by other aromatic systems.

2.7 – Tricyclic Heterocyclic Carboranes

Like anthracene, BDT is a tricyclic aromatic system, but with two thiophenes, as opposed to benzenes, flanking the middle ring. The pentagonal structures of thiophenes mean that, when fused with benzene, the proton in the 3 position is bonded not at 90° from the molecular axis, but 60°. This allows for more space between a substituent on the middle ring and that proton, thereby reducing steric interactions relative to anthracene. Moreover, naphtho[2,3-b]thiophene (NTP) allows for an in-between state, with one anthracene-like proton on one side of the substituent, and one BDT-like proton on the other, **Figure 2-12**.

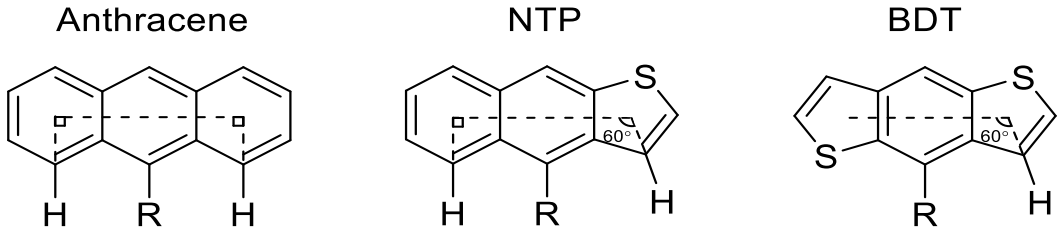


Figure 2-12 – The molecular structures of anthracene, NTP and BDT with the proximal protons to substituent -R shown, labelled with their relative angle from the molecular axis.

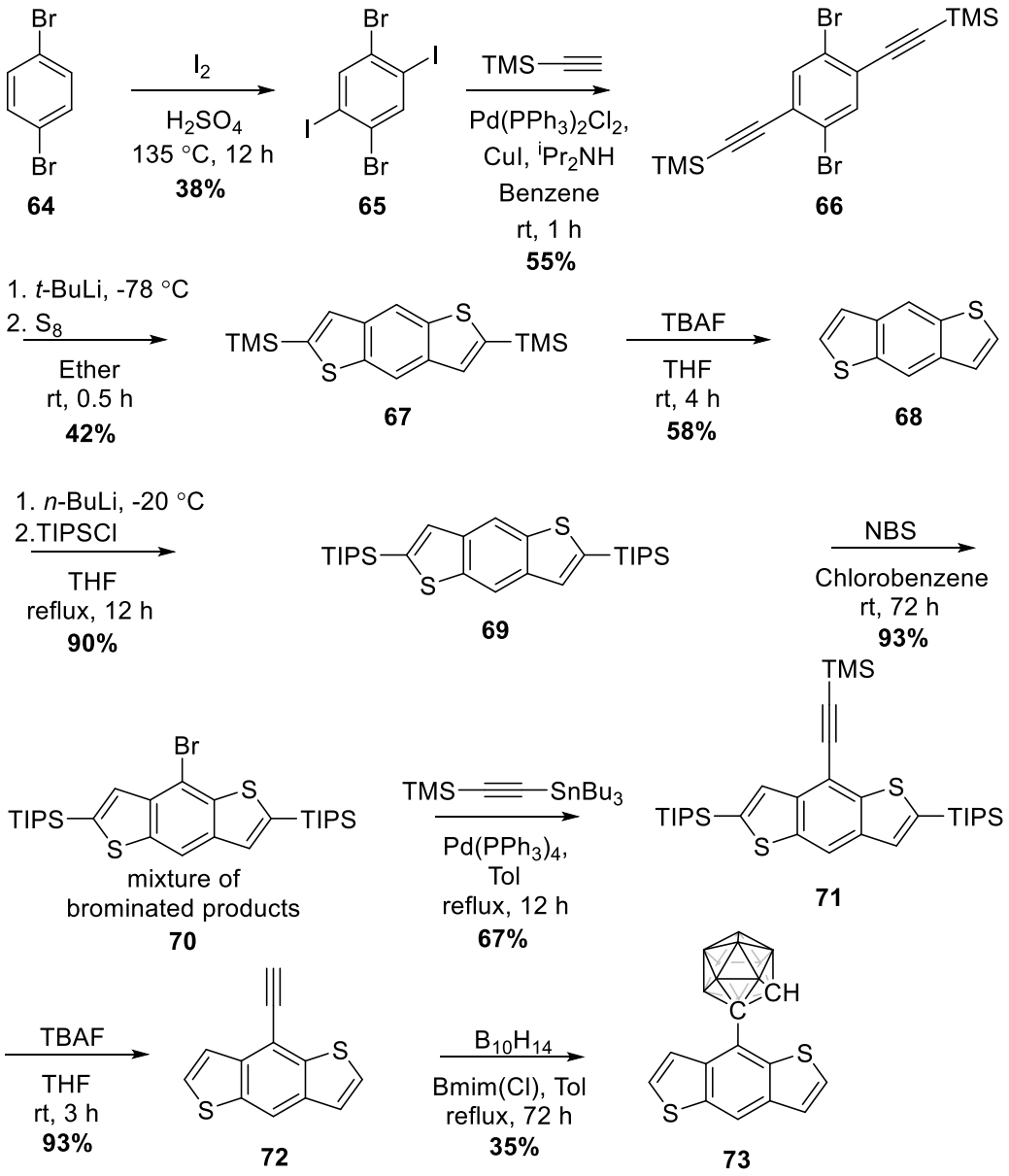
It was therefore theorised that it is possible to tune the degree of deformation of the molecule, and accordingly the rotation of the carborane, by varying the space between the carborane and proximal protons, using architecturally similar, monosubstituted tricyclic heterocyclics.

2.8 – Synthesis of Tricyclic Heterocyclic Carboranes

2.8.1 – *Ortho*-carboranyl BDT

Substitution of BDT at the middle ring positions is usually achieved via the reaction of an organometallic at both ketones of the BDT-dione, followed by reduction using $SnCl_2$ in acidified conditions. Alkylated and triisopropyl (TIPS) acetylene derivatives used in organic electronics are all usually made in this way,[16,17] as was the acetylenic precursor to the carborane compound ***o*Cb$_2$BDT**.[5] However, this route is not available as, whilst through careful stoichiometry it is possible to monosubstitute and form the monohydroxy species, it is not possible to reduce this intermediate to the aromatic BDT. It is similarly not possible to reduce BDT-dione to the parent BDT compound; we have observed that the dihydroxy intermediate, formed through $NaBH_4$ reduction, is highly unstable towards oxidation and will return to the dione once the aq. $SnCl_2$ is added.

A new synthetic approach, therefore, had to be identified to form a BDT species monosubstituted at the middle ring, where the substituent can easily be displaced by a lithiated carborane, or by an acetylene to later form the carborane through decaborane coupling. Such a strategy was achieved and 1-(4'-benzo[1,2-*b*;4,5-*b'*]dithiophenyl)-*ortho*-$C_2B_{10}H_{11}$ (***o*CbBDT**) was synthesised as outlined in **Scheme 2-4**.



Scheme 2-4 – The synthesis of ***o*CbBDT** via a novel monobrominated BDT intermediate. Yield of reaction forming **70** refers to the yield of the multiple brominated mixture of products.

First, 1,4-dibromobenzene (**64**) was iodinated with H_2SO_4 catalyst to form 1,4-dibromo-2,5-diiodobenzene (**65**). A Sonogashira procedure was then used to regioselectivity substitute the iodides to create the TMS-acetylated product (**66**). The heterocyclic core (**67**) was synthesised via the intramolecular cyclisation reaction between the acetylene substituents and the sulfur anion intermediate according to a literature procedure.[18] The resulting BDT compound was flanked by two TMS protecting groups, which were removed simply using TBAF to form BDT (**68**) in high yield, and replaced with TIPS protecting groups (**69**). The TIPS groups were required because the NBS in the next step brominates BDT at the alpha position of the thieno groups, and indeed, the reagent will also

displace TMS groups,[19] achieving the same result. Two steps could have been avoided if TIPS-acetylene was used instead of TMS-acetylene in the step proceeding cyclisation, but TIPS-acetylene is, per mole, about four times more expensive than TMS-acetylene, and the latter was already present in the laboratory. It therefore seemed sensible to use the latter and utilise the slightly extended synthetic pathway.

Selective bromination of the TIPS-protected BDT proved difficult; the 4 and 8 positions of BDT are more reactive towards electrophilic substitution than the 3 and 7 positions, however the difference is quite small. This means that bromination is only mildly selective, and so it is impossible to avoid the formation of unwanted side products found in mixture **70**, **Figure 2-13**.

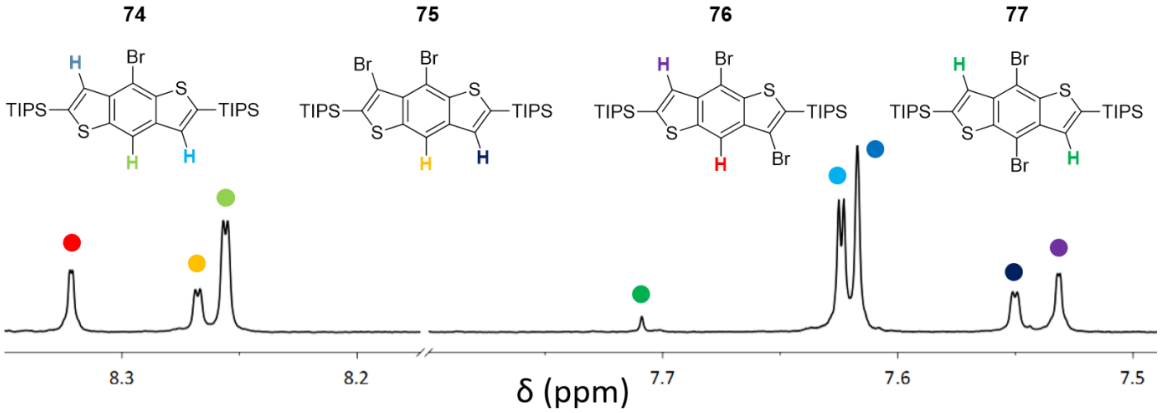


Figure 2-13 – The aromatic region of the ^{1}H NMR ($CDCl_3$) spectra of the isolated products of NBS bromination of TIPS-protected BDT, with peaks and protons colour labelled.

Whilst myriad products were formed from this reaction (**74**-**77**), monobrominated BDT (**70**) was the major product. We were unable to separate the isomers by chromatographic means, so the mixture was carried through into the next stage of the synthesis.

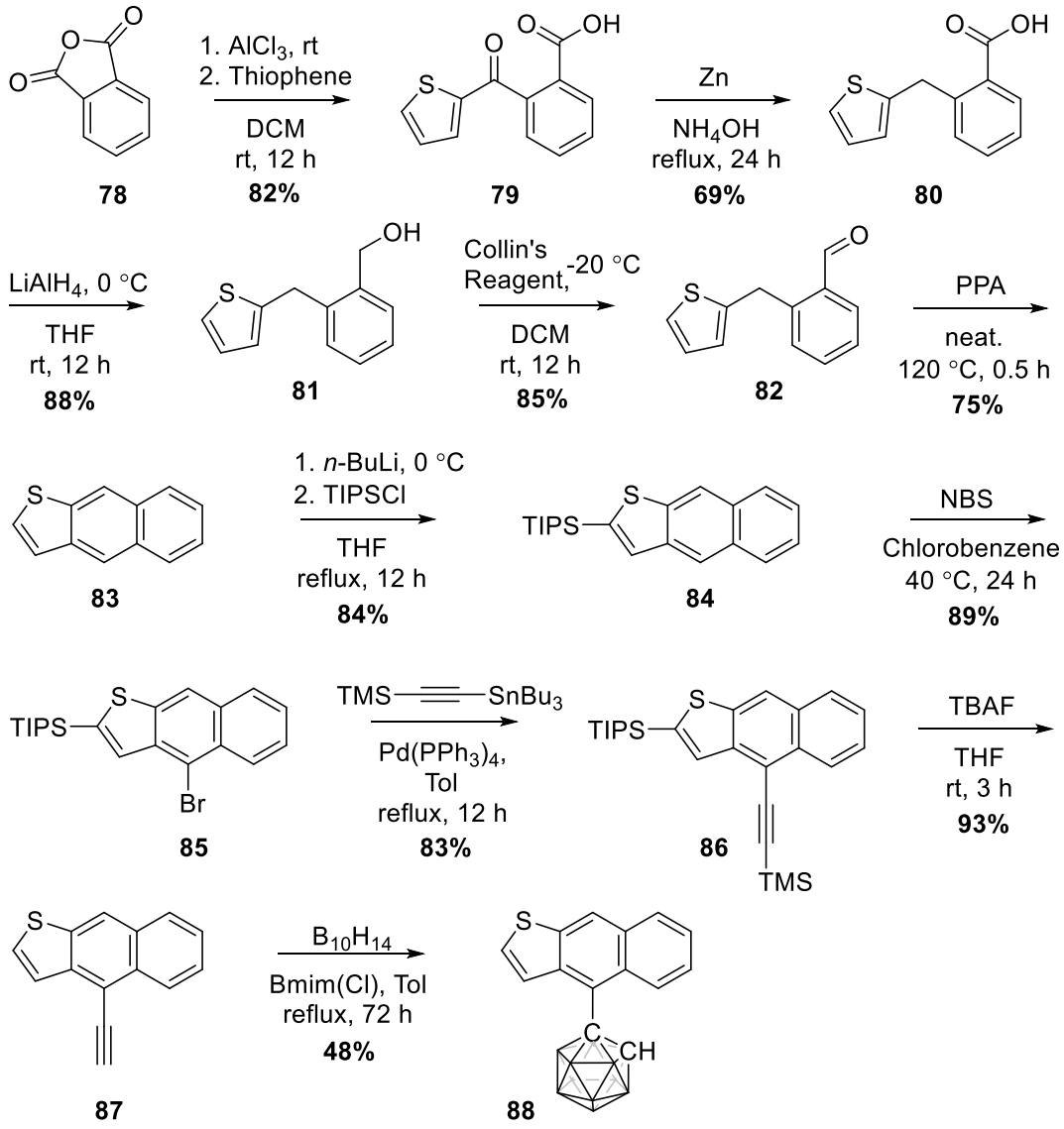
This is, to the best of our knowledge, the first example of a BDT compound monohalogenated at the middle ring. Such a species is a precursor to asymmetric donor-acceptor small molecules or monomers in polymer systems and may find use in the area of organic semiconductors. It therefore seemed fruitful to characterise the compound, which was first desilylated using TBAF. Separation of the resulting isomers was achieved using column chromatography (made significantly easier without the highly hydrophobic TIPS groups), followed by repeated crystallisation from DCM and hexane. This yielded the desired compound as white crystals, from which single-crystal XRD data was obtained.[20]

Installing the acetylene group was also somewhat problematic; Sonogashira coupling for this compound proved ineffective at displacing the bromide, yielding only starting material and a small amount of the non-brominated precursor. It was theorised that the BDT core was too electron rich for

the catalytic combination; a problem for many electron-rich aryl bromides.[21] Stille cross-couplings are used extensively in electron-rich systems, many of those being polymers for use in OPVs or OFETs. A Stille reaction was therefore attempted and yielded the desired product (**71**) in good yield. TBAF deprotection followed by decaborane coupling with the terminal acetylene (**72**) formed ***o*CbBDT** (**73**), which was isolated as colourless crystals.[20]

2.8.2 – *Ortho*-carboranyl NTP

Whilst NTP and BDT have a similar chemical structure, the non-symmetrical nature of NTP requires a very different synthetic pathway, but 1-(4'-naphtho[2,3-*b*]thiophenyl)-*ortho*-$C_2B_{10}H_{11}$ (***o*CbNTP)** was synthesised as in **Scheme 2-5**.



Scheme 2-5 – The synthesis of ***o*CbNTP**.

Synthesis of the NTP core was achieved following a five-step literature procedure.[22] First, thiophene was subjected to an $AlCl_3$-catalysed Friedel-Crafts reaction with phthalic anhydride (**78**), forming a thienyl benzoic acid (**79**). The ketone group was then reduced efficiently using Zn dust and ammonium hydroxide and following this the carboxylic acid is also carefully reduced with $LiAlH_4$, forming the benzyl alcohol (**80**).

In the literature, oxidation of the alcohol to the aldehyde (**82**) was achieved with the use of Sarett Reagent; a chromium trioxide complex with formula $CrO_3 \cdot 2$ pyridine. The reaction of chromium trioxide and pyridine is highly exothermic, and the resulting complex is also both hygroscopic and pyrophoric,[23] which makes the preparation of the complex tedious and dangerous.[24] A significant improvement in the safety of the reagent can be achieved using the Collins protocol, in which stoichiometric amounts of pyridine are added to a cold, stirring solution of DCM.[23†] Using this procedure the alcohol was oxidised safely in high yield and on large scale.

Cyclisation to NTP (**83**) was achieved with polyphosphoric acid (PPA), the exact mechanism of which is unknown. There is a dearth of mechanisms involving PPA in the literature, which is a result of the extreme difficulty in investigating them; PPA contains a range of molecules, any of which can be the catalytic compound in a reaction, and its highly viscous nature prevents the isolation of reactive intermediates by crystallisation.[26] In any case, the reaction proceeded in good yield.

A TIPS protection group was then installed at the (most) electron-rich thienyl 2 position (**85**), ensuring that the both the 2 and 3 position are sterically blocked from bromination by NBS in the next reaction. It was initially not clear where bromination should occur and this reaction was not previously investigated in the literature to the best of my knowledge. Upon first appearance, one may expect bromination to occur at the 9 position, proximal to the sulfur atom as is the case for BDT. However, for benzothiophene (**89**), assuming the thioenyl protons are similarly protected, electrophilic attack occurs preferentially at the 4 position (incidentally the equivalent site in NTP is also the 4 position).[27] DFT calculated electrostatic potential charges are most negative at this position.[28] Accordingly, the NMR spectra confirmed that bromination had indeed occurred at the 4 position of NTP (**85**). Moreover, *only* this species was observed as a product of the reaction, even when NBS was used in large excess. Stille cross-coupling installed the protected acetylene (**86**) and TBAF desilylation

† The Collins protocol in fact calls for the Sarett reagent to be synthesised and dried for storage.[25] It can then be later dissolved in DCM for oxidation of alcohols without the need for excess oxidant and in almost neutral conditions. The initial synthesis is essentially unchanged, however. Only later was it realised that preparation *in situ* in DCM solution was a much safer procedure.

proceeded as in the analogous BDT reactions, and decaborane coupling with the terminal acetylene (**87**) yielded ***o*CbNTP** (**88**) as bright yellow crystals.

2.9 – X-ray Crystallography

For both compounds, recrystallisation by slow evaporation of a biphasic mixture of DCM and hexane afforded single crystals. These were submitted for XRD and crystal structures were obtained. Molecular structures are presented in **Figure 2-14** and unit cell packing in **Figure 2-15**.

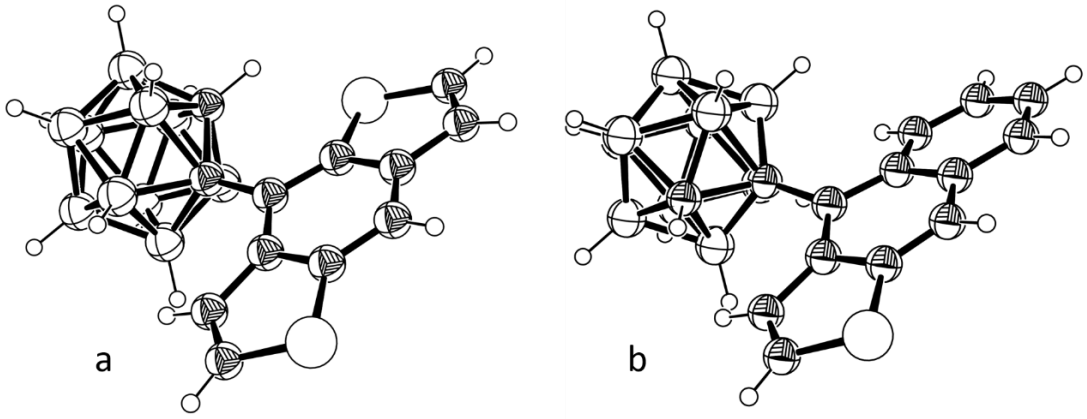


Figure 1-14 – ORTEPs of the molecular structures of (a) ***o*CbBDT** and (b) ***o*CbNTP**, as obtained from single-crystal XRD.

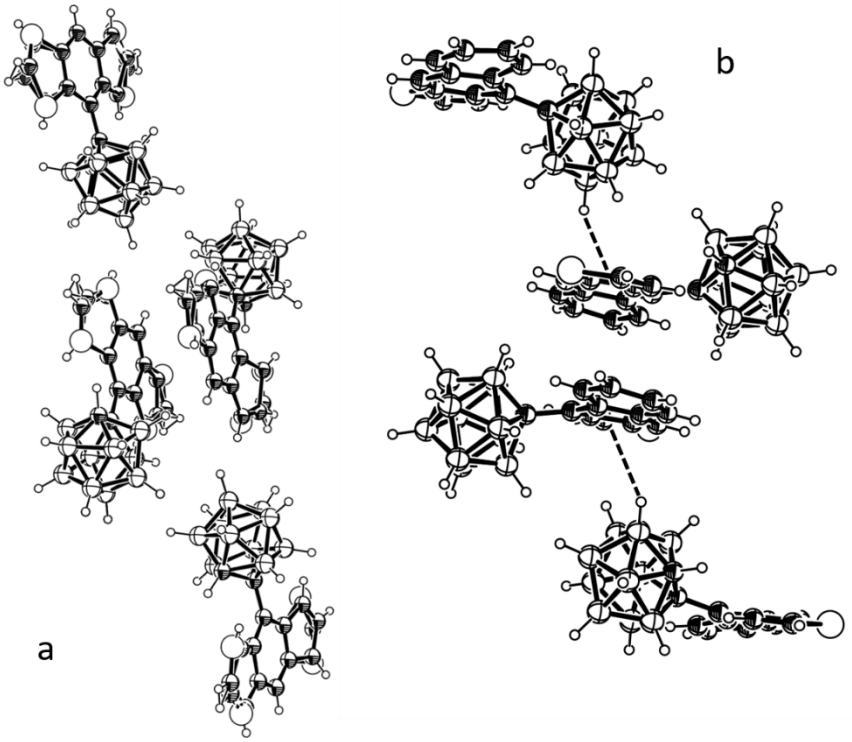


Figure 2-15 – ORTEPs of the molecular packing of (a) ***o*CbBDT** with disorder shown and (b) ***o*CbNTP**. Both compounds exhibit dimerisation of the aromatic cores, and the NTP also shows B-H / π-system hydrogen bonding.

The ***o*CbBDT** and ***o*CbNTP** compounds crystallise into the monoclininc, $P2_1/c$ and $P2_1/n$ respectively. Both exhibit dimerisation of the aromatic cores, and ***o*CbNTP** also shows hydrogen bonding between the carboranes and the ring system. ***o*CbBDT** is disordered at the sulfur positions; the core can be rotated 180° about the carborane-BDT dihedral bond, which has the effect of exchanging the sulfur for a carbon atom at these positions, as shown in **Figure 2-15a**. The occupancy of these two spatial arrangements is approximately identical, and as such, one might also expect the disorder at the C(2) position of the carborane cage, such that the C-H vertex is always 'close' to the sulfur. There is however no crystallographic evidence to support this. A similar observation has been made for ***o*Cb$_2$BDT**,[5] and for comparative purposes, the structure and packing are presented in **Figure 2-16**.

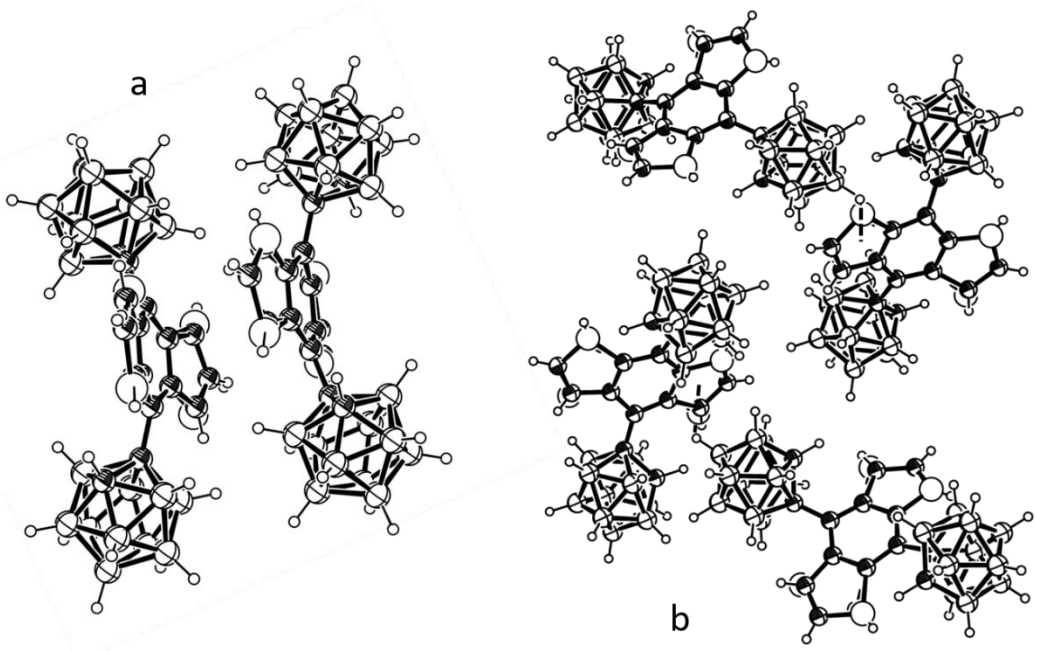


Figure 2-16 – ORTEPs of (a) BDT core dimerisation and (b) molecular packing of ***o*Cb$_2$BDT** with disorder shown. B-H / π-system hydrogen bonding is indicated.

The same type of disorder is present in this compound, however the occupancy of the two spatial arrangements is not equal in this case. The spatial arrangement in which the carborane C-H vertex is close to the sulfur accounts for about 90% occupancy, whilst the opposite arrangement accounts for the other 10%. It is possible to describe the disorder in these terms as the position of the carborane C-H vertex itself shows no disorder.

The deformation of the aromatic cores is much subtler than for the anthracenyl compounds, indeed, for ***o*CbBDT** a cursory glance at the structure may not be enough to see there is any deformation at all. However, there are distinct trends in this regard, as demonstrated by the physical quantities presented in **Table 2-4**.

Compound	α (°)	β (°)	α + β (°)	θ (°)	C(1)-C(2) Bond length (Å)
*o*CbBDT	6.79	1.14	7.93	4.55	1.665
*o*CbNTP	11.07	4.27	15.34	7.42	1.663
oCb_2BDT[5]	14.31	3.40	17.71	6.62	1.659
*o*CbAnth	13.39	7.28	20.67	7.87	1.664

Table 2-3 – The angles of deformation and cage C-C bond length for ***o*CbBDT** and ***o*CbNTP** carboranes, with ***o*Cb_2BDT** and ***o*CbAnth** for comparison. For ***o*Cb_2BDT**, which contains two carboranes, the mean of the measurements is used.

The α and β angles increase significantly from ***o*CbBDT** to ***o*CbNTP**, indeed the sum of those angles is twice as large for the latter. The out-of-plane deformation angle also increases such that ***o*CbNTP** is the significantly more deformed aromatic system of the two. The order of deformation increases on the order of *ortho*-carboranyl BDT < NTP < Anth, which is exactly as expected based on the geometric arguments described earlier. Interestingly however, the disubstituted compound ***o*Cb_2BDT**, is approximately as deformed as the monosubstituted anthracene compound ***o*CbAnth**, and therefore much more deformed than ***o*CbBDT**. This can be rationalised as follows; introduction of the second carborane further reduces aromaticity of the ring system. In turn, the flexibility of the tricyclic core increases, allowing for more severe deformation to reduce the energetically unfavourable steric interactions between it and the carborane. These processes happen simultaneously, there is no real cause and effect; it is simply the fact that upon introduction of a second carborane the stable state is one that is more deformed and less aromatic.

Lastly, it is noteworthy that there is essentially no difference in carboranyl C-C bond lengths between these compounds. Some disubstituted carboranes bearing bulky aromatic moieties show a relative increase in C-C bond length,[29] as will be demonstrated in **Chapter 4** and **5**, however this effect is clearly not replicated in sterically crowded monosubstituted systems.

2.10 – Calculations

Given that the degree of deformation increases as on the order of *ortho*-carboranyl BDT < NTP < Anth compounds, it was theorised that the barrier to rotation will similarly increase. To investigate this, a DFT study was undertaken to calculate the potential energy as a function of carborane rotation, **Figure 2-17**.

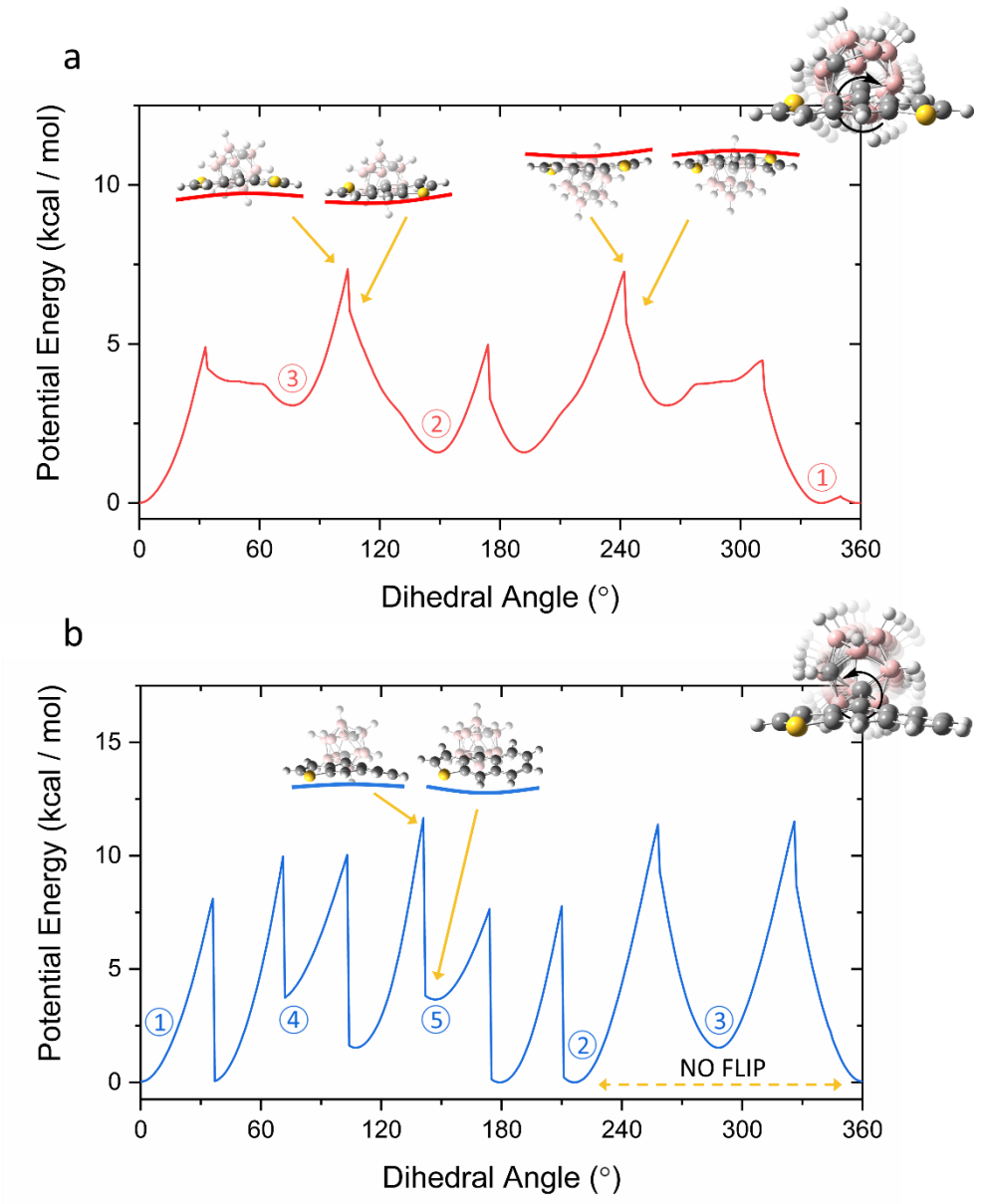


Figure 2-17 – DFT (B3LYP/6-31G(d,p); gas phase) calculated potential energy surface (PES) of (a) ***o*CbBDT**, and (b) ***o*CbNTP**, as a function of dihedral angle at 1° intervals, relative to the ground state energy. The arbitrarily defined 0° state is the global ground state geometry, and unique ground state geometries are labelled in the order of increasing energy. Rotation occurs in the direction depicted.

The PES of both compounds are noticeably different from the anthracenyl carboranes, where the five-fold rotational symmetry of the carborane is reflected in five energy minima situated ca. 72° apart. For ***o*CbBDT** there are six energy minima spaced unevenly, and for ***o*CbNTP** there are eight; six situated 36° apart, and two 72° apart. These phenomena can be understood by considering the geometries around the energy maxima; as the carborane rotates, potential energy increases as the carboranyl protons become closer to the protons of the substituent. The aromatic bends further away from planarity to reduce energy, until eventually it is more favourable for the aromatic to bend away from

the carborane in the opposite direction. At this point, the ring system flips from concave to convex, relative to the carborane, and a reduction in potential energy is observed. Ring flips such as these are important as they could provide a means of non-radiative energy loss of excited states; an issue investigated in **Chapter 3**. Such a process would be detrimental to the performance of luminescent materials.

For ***o*CbBDT** the ring system is still concave (bends away) relative to the carborane for all the energy minima, but the C-H vertex is always above the plane (c.f. ground state structure (3) for ***o*CbAnth** in **Figure 2-6**). Therefore, there are no longer five unique positions for the C-H vertex during rotation, but three, **Figure 2-18a**. For ***o*CbNTP** the situation is much more complex; there are still the five energy minima geometries as seen for ***o*CbAnth**, but between those there also three energy minima geometries in which the ring is system is flipped. These three are not unique however, they are duplicates of the three lowest energy minima in the original set of five, due to the plane of symmetry across the aromatic ring as it flips, **Figure 2-18b**.

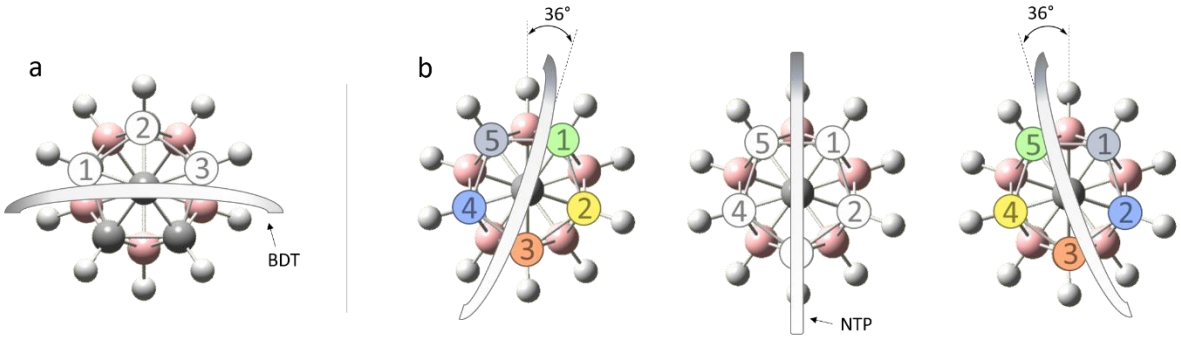


Figure 2-18 – A demonstration of the number of unique ground states for (a) ***o*CbBDT**, and (b) ***o*CbNTP**, as a result of the ring flip phenomena. The possible ground state positions for the C-H proton are numbered, and for (b) those which are identical are similarly coloured.

One can see in **Figure 2-18b** that at the instant of ring flipping, when the aromatic system is approximately planar, the ring can flip either way following a 36° rotation. The ring system then deforms such that three of the possible C-H positions are above the plane, and two below. Importantly, regardless of which way the ring flips, the same five possible positions for the C-H vertex positions are available. The last quirk of ***o*CbNTP** is that there is no ring flip about the geometry in which the C-C bond is perpendicular to the carborane, such that the two highest energy minima geometries appear only once per rotation. Therefore, whilst there are eight energy minima for the PES of ***o*CbNTP**, there are still only 5, unique, energy minima ground state geometries.

The calculated molecular orbitals for the HOMO and LUMO of ***o*CbBDT** and ***o*CbNTP** ground states are presented in **Figure 2-19**. For both compounds, the global ground state geometry in which the

carboranyl C-C bond is almost parallel to the aromatic plane has the largest contribution from the carborane to the HOMO. Due to neither BDT nor NTP having a plane of symmetry perpendicular to the molecular axis, there is a second geometry, in which the C-C bond is almost parallel to the aromatic plane but pointing in the other direction. The energies of these states are almost identical to the global ground state and accordingly, the orbital contribution from the carborane is also identical.

As in the case of the anthracenyl carboranes, the molecular orbital contribution from the carboranes increases in the LUMO state. Interestingly, the LUMO states for all ***o*CbBDT** ground state geometries have a larger orbital contribution from the carborane than the ***o*CbNTP** ground states. This could be an indication that, as in the case of naphthyl versus anthracenyl *ortho*-carborane, increased deformation of the carborane out of the plane reduces its ability to contribute to the molecular orbitals. For both compounds, the geometry in which the carboranyl C-C bond is perpendicular to the aromatic plane provides the largest orbital contribution from the carborane. Clearly, as observed previously, the carborane is most stabilising to the LUMO when in this state.

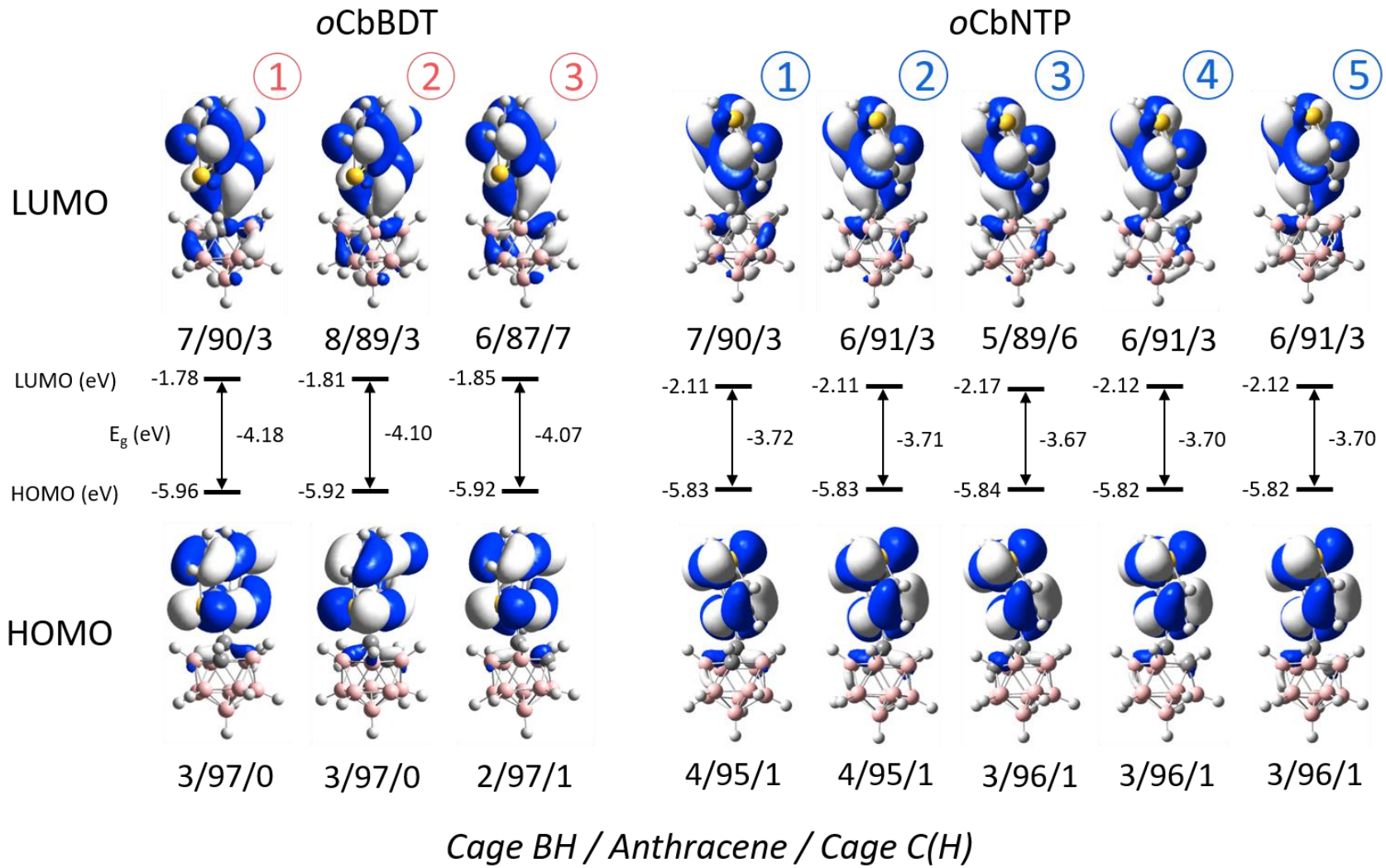


Figure 2-19 – DFT (B3LYP/6-31G(d,p); gas phase) calculated geometries, molecular orbitals, and energies of the HOMO and LUMO states of the ground state energy minima for ***o*CbBDT** and ***o*CbNTP**. Relative orbital contributions of the cage B-H, anthracene and cage C (and C-H) moieties are presented.

The calculated barriers to rotation for heterocyclic carboranes are presented in **Table 2-5**.

Compound	Energy Barrier to Rotation (kcal / mol)
*o*CbBDT	7.4
*o*CbNTP	11.7
*o*CbAnth	14.6

Table 2-4 – DFT calculated energy barrier to rotation for ***o*CbBDT** and ***o*CbNTP**, with ***o*CbAnth** for comparison.

The rotation barriers are exactly what one may expect for this series; the least sterically hindered ***o*CbBDT** has the smallest rotational barrier, ***o*CbAnth** the largest, and ***o*CbNTP** somewhere in-between. In fact, the latter has a rotational barrier very similar to ***m*CbAnth**, so one may expect to see the also observe the effect of this barrier in the ^{1}H NMR spectrum. This will be explored later.

To investigate the effect of *two* carboranes on the stability of these systems, a second, time-dependent (TD) DFT study was undertaken using the known compound ***o*Cb$_2$BDT** as a model system. Each carborane can rotate into five different geometries to achieve an energy minimum, so with two carboranes there are 10 unique ground state energy minima. Each of these was optimised to gain an insight into the HOMO and LUMO levels as a function of carborane rotation, creating a pseudo-PES in which each data point is an energy minimum, i.e. the energy barriers to rotation are ignored and not included in the PES.[‡] The data is presented in **Figure 2-20**.

[‡] A true PES in this study would be prohibitively long to calculate; on the computational cluster and level of theory used, a three-dimensional equivalent of the PES in **Figure 2-20** would take approximately one year in real-time, assuming five calculations were run in parallel throughout.

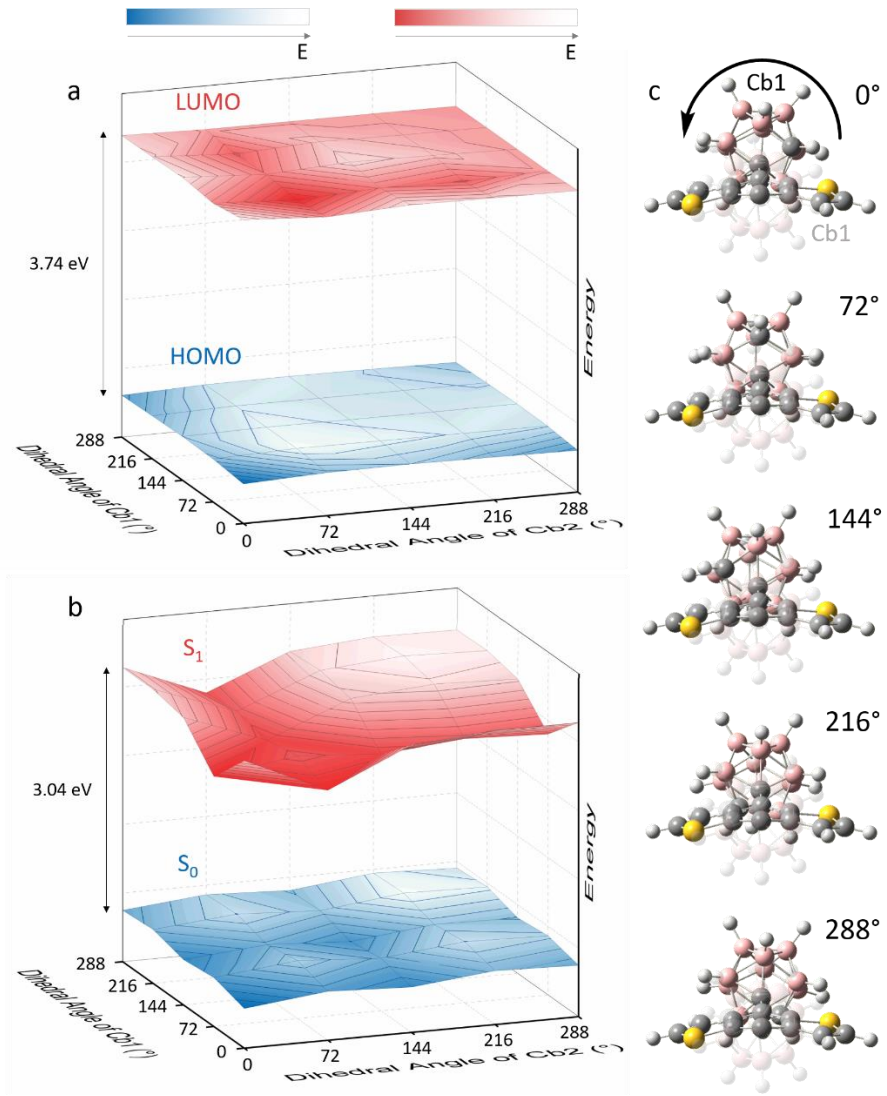


Figure 2-20 – DFT and TD-DFT calculated (B3LYP/6-31G(d,p) // B3LYP/6-31G-(d,p); gas phase) (a) HOMO and LUMO, and (b) S_0 ground and S_1 excited state, pseudo-PES of ***o*Cb$_2$BDT** as a function of the dihedral angle between the BDT core and the two carboranes Cb1 and Cb2. The global ground state geometry is defined in (c) and given the arbitrary angle of 0°,0° with rotation occurring as demonstrated with Cb2 transparent for clarity.

One can see from **Figure 2-20a** that whilst the lowest energy HOMO state is the 0°,0° geometry, the lowest energy LUMO state is the 72°,72° geometry, in which the C-C bonds of both carboranes are perpendicular to the aromatic plane. This stabilisation is also present, but to a lesser degree, when only one of the carboranes is in this state, suggesting the effect is additive. Clearly, the electron-withdrawing carborane stabilises the BDT core most efficiently when in this geometry. Conversely, this geometry increases the HOMO energy; the effect is very small however, but the molecular orbitals are subtly less delocalised onto the carborane than the other geometries.

A similar study in **Figure 2-20b** examines the effect of carborane geometry on the total energy (sum of all occupied molecular orbitals) of the S_0 ground, and S_1 excited states. The key difference in this

study is that the excited states can relax geometrically after the excitation. The S_0 ground state follows generally the same trend as the HOMO in **Figure 2-20a**, where the 0°,0° ground state structure has the lowest energy, and the S_1 excited does the same for the LUMO, but in the latter case, the magnitude of effect of geometry is much greater. When the C-C bond of one carborane is perpendicular to the aromatic plane (e.g. 0°,72°) the excited state energy is significantly reduced. This is coupled, geometrically, with a large increase in the C-C bond length, from ca. 1.712 to 2.387 Å, and is a mark of charge transfer from the BDT donor to the carborane acceptor, creating a TICT state. As noted in the introduction this is now a well-known property of *ortho*-carborane. Interestingly, however, when both carboranes have their C-C bond perpendicular to the aromatic plane (72°,72°) the stabilisation effect is *not* additive. Moreover, the C-C bond lengths of the carboranes are in fact both increased, measuring 2.226 Å, suggesting that charge transfer does indeed occur from the BDT core to both carboranes forming a 'bis-TICT' state. However, the slightly smaller C-C bond lengths for these carboranes relative to geometries where only one carborane is in the perpendicular state suggests the degree of charge transfer to each of these carboranes is lower than in the singular case. This may explain why this excited state is lower in energy than all states without a carborane with a perpendicular C-C bond, but still higher than all others.

This has implications for the emissive behaviour of such species, suggesting that whilst bis-TICT states are possible, relaxation from these states produces emissive energies that are essentially indistinguishable from a conventional, one-carborane TICT state. Indeed, the PL of a similar bis-*ortho*-carboranyl-BDT compound reported since this work was carried out shows no evidence of such a bis-TICT state.[30]

Structural and molecular orbital diagrams of the 0°,0°, 0°,72° and 72°,72° states are presented in **Figure 2-21**.

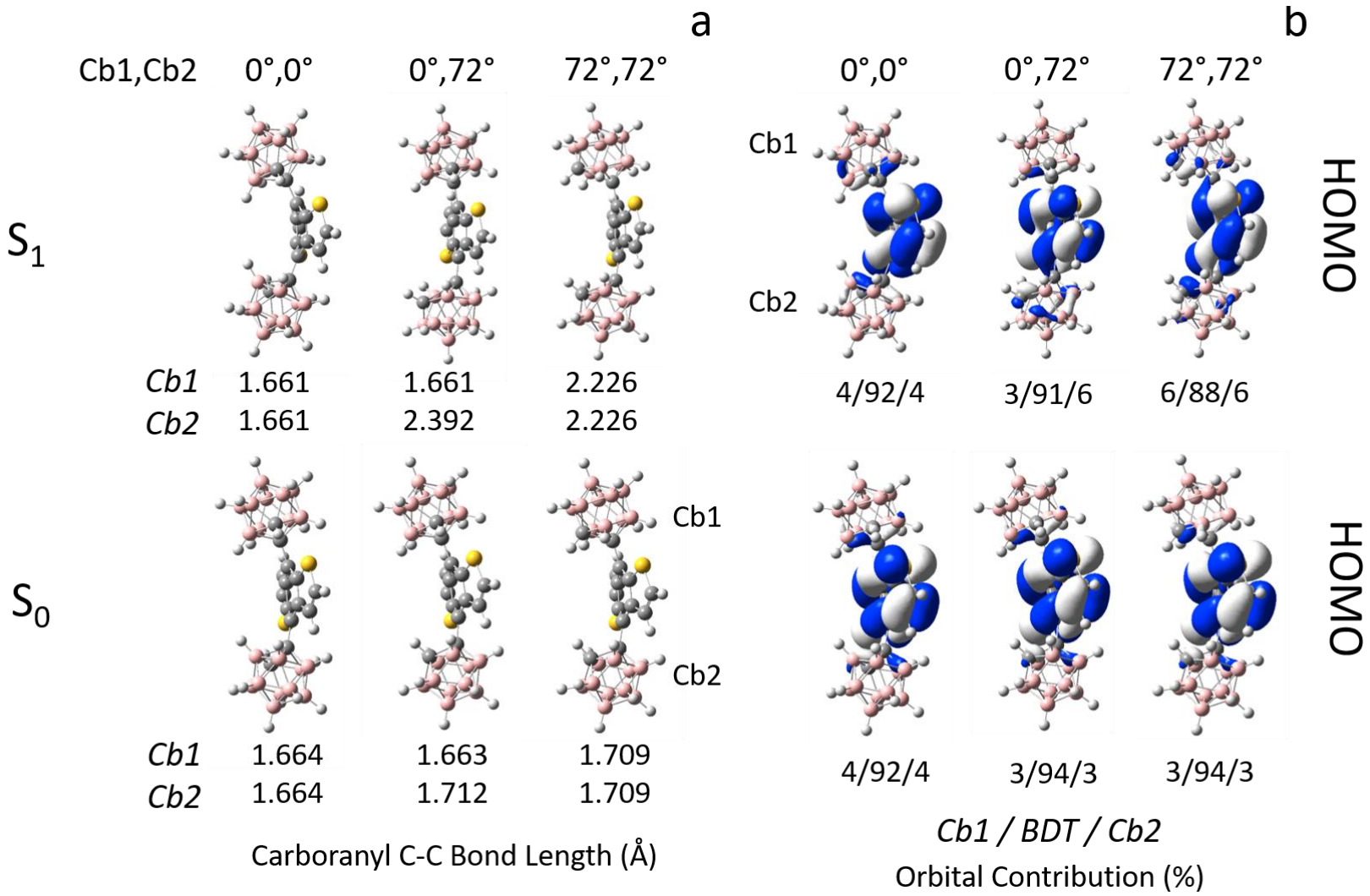


Figure 2-21 – DFT calculated (B3LYP/6-31G(d,p); gas phase) (a) structures with carboranyl C-C bond lengths, and (b) molecular orbital diagrams with percentage orbital contribution from carborane 1 (Cb1) / BDT / carborane 2 (Cb2), for the three selected geometries of *o*Cb_2BDT; 0°,0°, 0°,72°, 72°,72°.

2.11 – NMR

The DFT calculated rotation barrier of ***o*CbNTP** is relatively high, on the order of that of ***m*CbAnth**. It was therefore theorised that the effects of this would be seen in the ^{1}H NMR, as was the case for that compound, and as such the room temperature spectra of ***o*CbBDT** and ***o*CbNTP** are presented in **Figure 2-22**.

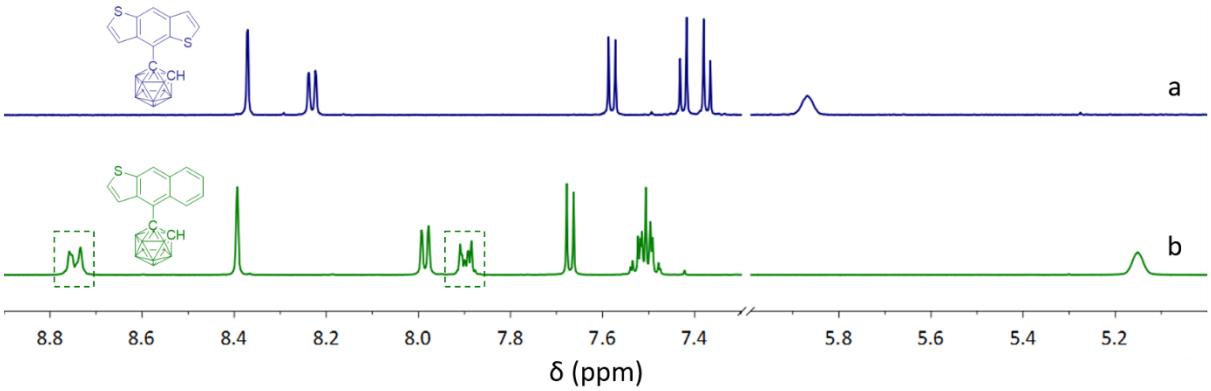


Figure 2-22 – ^{1}H NMR ($CDCl_3$) spectra of (a) ***o*CbBDT** and (b) ***o*CbNTP**. The highlighted peaks show a small degree of restricted rotation on the NMR timescale.

The ***o*CbBDT** compound shows no peak broadening relative to the parent heterocycle, but ***o*CbNTP** exhibits a definite lack of the splitting fine structure in the highlighted peaks, corresponding, left to right in the spectrum, to the 5 and 3 position protons of NTP respectively. These peaks have a structure somewhere between those of the broadened peaks of ***m*CbAnth** and ***o*CbAnth**, which is exactly what one would expect based on the rotation barrier of ***o*CbNTP**. Clearly then, the rotation of the carborane can be effectively tuned by varying the steric environment around it, imposed by the geometry of the aromatic system to which it is attached.

Interestingly, there is also a significant difference in the chemical shift of the carboranyl C-H proton, which is δ = 5.90 and 5.15 ppm for ***o*CbBDT** and ***o*CbNTP** carboranes respectively (for the parent carborane δ = 3.55 pm). The former is, to the best of our knowledge, the most deshielded carboranyl C-H proton peak recorded, with the closest example being ***o*Cb$_2$BDT**, where δ = 5.70. We tentatively assign this phenomenon to a degree of sulfur-proton hydrogen bonding, which deshields the C-H proton, pushing the peak downfield. The crystallographic evidence somewhat supports this theory, as the C-H proton preferentially is nearest the sulfur, and one would expect the interaction to be stabilising. Further studies, such as a DFT investigation, would be required to definitively explain this phenomenon.

2.12 – Conclusions

A series of sterically strained, monosubstituted tricyclic carboranes have been designed, synthesised and characterised successfully, with the *ortho*-carborane compounds formed through decaborane/acetylene couplings, and the *meta* and *para*-carborane compounds formed through copper(I) mediated cross-couplings. TGA of the series of anthracenyl carborane isomers, previously reported to be unstable, demonstrated that the compounds are at least as thermally stable as the parent anthracene, and that ***o*CbAnth** is significantly more stable to decomposition than the other isomers.

X-ray crystallography enabled the study of the ground state geometries of these compounds, and for the *ortho*-carborane compounds, the carboranyl C-C bond is, in all cases, almost parallel to the aromatic plane. The aromatic cores were found to be deformed due to significant steric interactions with the carboranes, and for the anthracenyl compounds, this deformation increased between the isomers on the order *para* < *meta* < *ortho*. Of the heterocyclic compounds, deformation increased from ***o*CbBDT** to ***o*CbNTP**, where the pocket of space around the carborane is more congested in the latter.

DFT calculations demonstrated that the barrier to carborane rotation increases as the degree of deformation increases and is, therefore, largest for the *ortho*-carborane compounds. NOESY and temperature dependent ^{1}H NMR studies corroborated this, proving that interactions between the carborane and proximal aromatic protons cause restricted rotation of the carborane, with a dramatic reduction in rotation at the lowest temperatures studied. The ***o*CbBDT** and ***o*CbNTP** compounds were found to ring-flip during carborane rotation, resulting in a decrease in potential energy. The complex PES was rationalised in terms of these phenomena, and it was observed that this may be an undesirable, non-radiative, decay route for the excited state of these compounds.

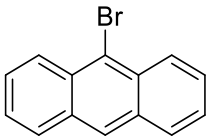
Calculations also highlighted the relative stability enhancement of *ortho*-carborane on the HOMO and LUMO of the tricyclic aromatics compared to the other isomers, and this stabilisation coincided with increased molecular orbital contributions from the carborane to these states. Similar TD-DFT studies, allowing for relaxation of the excited states, of ***o*Cb$_2$BDT** demonstrated the significant stabilisation effect of S_1 excited states when the carboranyl C-C bond is perpendicular to the aromatic plane, as a result of charge transfer coinciding with elongation of the C-C bond, forming a TICT state. No evidence of an additional stabilisation was found when two carboranes are in this geometry, however, a 'bis-TICT' state was formed in which the degree of charge transfer to each carborane is equal but lower than in the case of the singular carborane TICT species.

2.13 – Experimental

Dry solvents and reagents were purchased from Sigma Aldrich, VWR, Alfa Aesar, Acros organics or Apollo scientific and used without further purification, and all reactions were performed under BOC Pureshield Argon. Steady-state proton (^{1}H), boron (^{11}B), carbon (^{1}H-decoupled) (^{13}C{^{1}H}), and NOESY solution-state NMR spectra were obtained from a Bruker Avance-400 (400 MHz) spectrometer, and low-temperature proton NMR spectra were obtained from a Bruker Avance-500 (500 MHz) spectrometer. $CDCl_3$ was the deuterated solvent used in all cases. Chemical shift data was produced using residual solvent internal standards (^{1}H: $CHCl_3$ at 7.26 ppm; ^{13}C: $CDCl_3$ at 77.36 ppm); s = singlet, d = doublet, t = triplet, q = quartet, m = multiplet, br = broad. Mass spectrometry was carried out on an Agilent HP6890 GC (EI); Dionex Ultimate 3000 (APCI); and AB Sciex TOF/TOF 4800 (MALDI-ToF). TGA was achieved using a Mettler Toledo TGA. Infra-red spectroscopy measurements were obtained using a PerkinElmer FT-IR Spectrum 100 fitted with an ATR (Ge/Ge) accessory. X-ray crystallographic data was obtained at 173 K, using an Agilent Xcalibur PX Ultra A. Cyclic Voltammetry was carried out using a Metrohm Autolab PGSTAT101 potentiostat in dry DCM containing 0.1 M NBu_4PF_6 with a platinum working electrode, Pt counter electrode and an Ag/AgCl (Ag/Ag^{+}) reference electrode with ferrocene as internal reference. Prep. GPC was carried out on a JAI LaboAce LC-5060, fitted with a refractive index (RI) and UV detector and JAIGEL-HR series column.

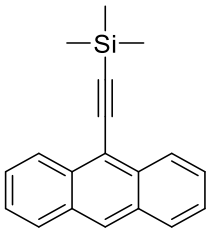
ORTEP visualisations were created using ORTEP 32 software and all diagrams are presented with 50% probability ellipsoids.[31] Computational studies were performed using Gaussian G09 rev. d01 and GaussView 5.0.9 visualization software.[32] DFT calculations were carried out using B3LYP[33,34] functional and 6-31G(d,p)[35,36] basis set, with no symmetry constraints, in the gas phase. Dihedral scans were obtained using OPT(Z-MAT), starting from the calculated global ground state geometry and commenced with 1° rotations around the bond connecting the carborane and the substituent. Direction of rotation is illustrated in the text. Where appropriate, energy minima were identified following geometry optimisation and frequency calculations returning zero imaginary frequencies. MO diagrams and orbital contributions were generated with the aid of the GaussView 5.0.9[37] and GaussSum[38] packages respectively.

9-Bromoanthracene[39] (52)



To a stirred solution of anthracene (5.00 g, 28.1 mmol) in dry DMF (200 mL) at 0 °C was added NBS (4.95 g, 27.8 mmol) in one portion. The mixture was allowed to slowly warm to room temperature overnight, and water (200 mL) was added in one portion. The precipitate was filtered and washed with water (100 mL) before being dissolved in hexane and dried with $MgSO_4$. The solution was concentrated *in vacuo* and left to recrystallize by slow evaporation, yielding the *title compound* as yellow crystals (6.08 g, 23.6 mmol, 85%). m.p. 100-101 °C. ^{1}H NMR (400 MHz, $CDCl_3$) δ 8.53 (2H, ddd, *J* = 8.9, 1.2, 0.8 Hz), 8.40 (1H, s), 7.97 (2H, ddt, *J* = 8.4, 1.2, 0.8 Hz), 7.60 (2H, ddd, *J* = 8.9, 6.5, 1.2 Hz), 7.50 (2H, ddd, *J* = 8.4, 6.5, 1.2 Hz) ppm. ^{13}C NMR (100 MHz, $CDCl_3$) δ 132.5, 130.9, 128.9, 127.9, 127.5, 127.4, 125.9, 122.7 ppm. HRMS (EI^+) $C_{14}H_9Br$ requires 255.9888, found 255.9882.

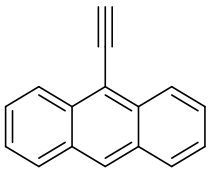
9-(Trimethylsilylethynyl)anthracene[40] (53)



To a solution of 9-bromoanthracene (0.40 g, 1.56 mmol) in triethylamine (10 mL) was added piperidine (2 mL), $Pd(PPh_3)_2Cl_2$ (0.11 g, 0.16 mmol) and CuI (0.03 g, 0.16 mmol). The solution was degassed with argon for 1 h, before trimethylsilylacetylene (0.64 mL, 4.50 mmol) was added in one portion, and the mixture was heated at 110 °C for 24 h with vigorous stirring and the rigorous exclusion of light. Upon cooling, water (10 mL) was added, and the solution was extracted with DCM (3 x 20 mL). The organic fractions were washed with water (3 x 20 mL), brine (1 x 20 mL) and dried over $MgSO_4$. The solvent was removed *in vacuo* and subjected to column chromatography with hexane eluent, yielding a yellow solution which was again evaporated *in vacuo*. The crude solid was recrystallized from hot acetonitrile to give the *title compound* as yellow crystals (370 mg, 1.35 mmol, 86%). m.p. 82-83 °C. ^{1}H NMR (400 MHz, $CDCl_3$) δ 8.62 (2H, dd, *J* = 8.6, 0.8 Hz), 8.41 (1H, s), 8.00 (2H, dd, *J* = 8.6, 0.8 Hz), 7.62 (2H, ddd, *J* = 8.8, 6.6, 1.2 Hz), 7.52 (2H, ddd, *J* = 8.8, 6.6, 1.2 Hz), 0.49 (9H, s) ppm. ^{13}C NMR (100 MHz, $CDCl_3$) δ

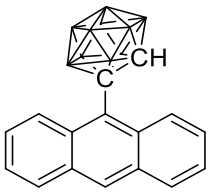
133.2, 131.4, 129.0, 128.2, 127.1, 127.0, 126.0 117.4, 106.5, 102.0, 0.65 ppm. HRMS (EI^+) $C_{19}H_{18}Si$ requires 274.1178, found 274.1183.

9-Ethynylanthracene[40] (**54**)



9-(Trimethylsilylethynyl)anthracene (0.37 g, 1.35 mmol) and K_2CO_3 (1.12 g 8.01 mmol) were stirred into a solution of THF (15 mL) and methanol (15 mL) under argon at 50 °C for 3 h. The mixture was poured into water (30 mL), extracted with ether (3 x 30 mL), washed with water (3 x 30 mL), brine (1 x 30 mL) and dried over $MgSO_4$. The solution was concentrated *in vacuo* and passed through a silica plug with hexane eluent. Removal of the solvent *in vacuo* yielded the *title compound* as a yellow oil which crystallised upon standing (205 mg, 75%). The unstable nature of this compound meant it was used immediately in a subsequent reaction.

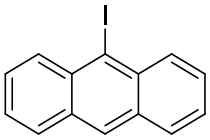
1-(9'-anthracenyl)-*ortho*-$C_2B_{10}H_{11}$ (**55**)



A stirred solution of bmim(Cl) (44 mg, 0.25 mmol) and dry toluene (10 mL) were dried by refluxing in a Dean-Stark apparatus for several hours, before 9-ethynylanthracene (148 mg, 0.73 mmol) and decaborane (100 mg, 0.82 mmol) were added and the mixture was heated to reflux for 72 h. The solvent was removed *in vacuo*, and the residue was subjected to column chromatography with Pet. ether eluent to yield an orange-red solution which was evaporated, and the solids recrystallised from DCM to yield the *title compound* as yellow crystals (45 mg, 0.14 mmol, 20%). Crystals suitable for X-ray diffraction analysis were grown by slow evaporation of a biphasic solution of DCM and hexane. m.p. 225-227 °C. ^{1}H NMR (400 MHz, $CDCl_3$) δ 8.80 (2H, br), 8.41 (1H, s), 7.97 (2H, d, J = 8.3 Hz), 7.53-7.42 (4H, m), 5.15 (1H, br), 4.4-1.4 (10H, br) ppm. ^{11}B NMR (128 MHz, $CDCl_3$) δ -0.61, -1.82, -2.57, -3.74, -7.94, -9.09, -10.31, -12.76, -13.98 ppm. ^{13}C NMR (100 MHz, $CDCl_3$) δ 132.2, 132.1, 129.6, 126.7, 125.3, 122.7, 78.2, 64.7 ppm. HRMS (EI^+) $C_{16}H_{20}B_{10}$ requires 320.2568, found 320.2569. ATR-IR (*v* cm^-

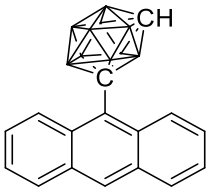
[1]) 3082, 2921, 2557 (B-H) br, 2358, 2195, 1965, 1739, 1623, 1444, 1174, 1157, 1066, 1012, 891, 843, 757, 736.

9-Iodoanthracene[41] (56)



To a stirred solution of 9-bromoanthracene (1.20 g, 4.67 mmol) in dry ether (50 mL) was added *n*-BuLi (2.30 mL, 2.5 M in hexanes, 5.84 mmol) dropwise over 1 minute at -78 °C. The mixture was allowed to warm to room temperature over 2 h and was stirred for a further 30 mins before being cooled again to -78 °C, and iodine (2.08 g, 8.18 mmol) was added in one portion. The dark black solution was shielded from light, allowed to warm to room temperature overnight, and was quenched with the addition of ether (50 mL). After washing with a 5% aq. solution of $Na_2S_2O_3$ (4 x 30 mL), water (3 x 30 mL) and brine (1 x 30 mL), the yellow solution was dried over $MgSO_4$, and then concentrated *in vacuo* before being eluted through a silica plug with ether. The filtrate was left to recrystallize by slow evaporation, yielding the *title compound* as bright yellow crystals (1.16 g, 3.81 mmol, 82%). m.p. 82-84 °C. ^{1}H NMR (400 MHz, $CDCl_3$) δ 8.47 (2H, dd, *J* = 8.4, 0.8 Hz), 8.43 (s, 1H), 7.94 (2H, ddt, *J* = 8.4, 0.8, 0.6 Hz), 7.58 (2H, ddd, *J* = 9.0, 6.5, 1.2 Hz), 7.49 (2H, ddd, *J* = 9.0, 6.5, 1.0 Hz) ppm. ^{13}C NMR (100 MHz, $CDCl_3$) δ 134.2, 133.5, 132.4, 129.2, 129.0, 128.0, 126.0, 105.1 ppm. HRMS (EI^+) $C_{14}H_9I$ requires 303.9749, found 303.9747.

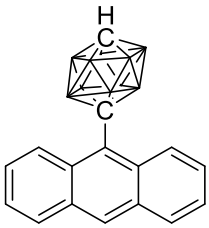
1-(9'-anthracenyl)-*meta*-$C_2B_{10}H_{11}$ (59)



To a solution of *meta*-carborane (235 mg, 1.63 mmol) in dry THF (10 mL) at 0 °C was added *n*-BuLi (0.72 mL, 2.5 M in hexanes, 1.79 mmol) dropwise over 5 mins, and the mixture was stirred at this temperature for 30 mins before being warmed to room temperature. Cuprous chloride (194 mg, 1.96 mmol) was added and the suspension was stirred for a further 2 h, before pyridine (0.36 mL, 4.48 mmol) and 9-iodoanthracene (547 mg, 1.8 mmol) were added, and the mixture was refluxed overnight. After cooling, inorganics were removed by filtration, washed with ether (20 mL), and the

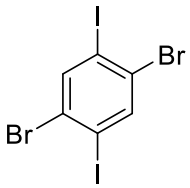
filtrate was washed with 1M HCl (10 mL), water (3 x 10 mL), brine (10 mL) and dried over $MgSO_4$. Solvent was removed *in vacuo* and the residue was purified by prep. GPC using THF eluent, followed by recrystallisation from DCM to afford the *title compound* as green crystals (124 mg, 0.39 mmol, 24%). Crystals suitable for X-ray diffraction analysis were grown by slow evaporation of a biphasic solution of DCM and hexane. m.p. 168-170 °C. ^{1}H NMR (400 MHz, $CDCl_3$) δ 9.03-8.96 (2H, m), 8.34 (1H, s), 7.94-7.87 (2H, m), 7.44-7.37 (4H, m), 4.2-1.3 (11H, br) ppm. ^{11}B NMR (128 MHz, $CDCl_3$) δ -2.53, -5.89, -8.57, -10.72, -12.71, -14.24 ppm. ^{13}C NMR (100 MHz, $CDCl_3$) δ 132.3, 131.2, 130.8, 128.8, 127.5, 124.7, 124.4, 78.8, 54.7 ppm. HRMS (EI^+) $C_{16}H_{20}B_{10}$ requires 320.2568, found 320.2603. ATR-IR (*v* cm^{-1}) 3052, 2598 (B-H) br, 2571 (B-H), 2031, 1621, 1443, 1316, 1273, 1147, 1104, 1008, 885, 840, 755, 737, 726.

1-(9'-anthracenyl)-*para*-$C_2B_{10}H_{11}$ (60)



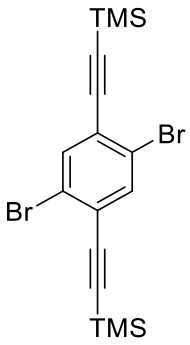
To a solution of *para*-carborane (268 mg, 1.86 mmol) in dry THF (10 mL) at 0 °C was added *n*-BuLi (0.82 mL, 2.5 M in hexanes, 2.05 mmol) dropwise over 5 mins, and the mixture was stirred at this temperature for 30 mins before being warmed to room temperature. Cuprous chloride (221 mg, 2.23 mmol) was added and the suspension was stirred for a further 2 h, before pyridine (0.41 mL, 5.13 mmol) and 9-iodoanthracene (608 mg, 2.0 mmol) were added, and the mixture was refluxed overnight. After cooling, inorganics were removed by filtration, washed with ether (20 mL), and the filtrate was washed with 1M HCl (10 mL), water (3 x 10 mL), brine (10 mL) and dried over $MgSO_4$. Solvent was removed *in vacuo* and the residue was purified by prep. GPC using THF eluent, followed by recrystallisation from DCM to afford the *title compound* as green crystals (167 mg, 0.52 mmol, 28%). Crystals suitable for X-ray diffraction analysis were grown by slow evaporation of a biphasic solution of DCM and hexane. m.p. 194-196 °C. ^{1}H NMR (400 MHz, $CDCl_3$) δ 8.92-8.83 (2H, m), 8.26 (1H, s), 7.88-7.80 (2H, m), 7.39-7.30 (4H, m), 3.9-0.8 (11H, br) ppm. ^{11}B NMR (128 MHz, $CDCl_3$) δ -10.3, -15.5 ppm. ^{13}C NMR (100 MHz, $CDCl_3$) δ 132.3, 130.8, 130.0, 128.5, 127.6, 125.9, 124.8, 124.2, 88.25, 65.54 ppm. HRMS (EI^+) $C_{16}H_{20}B_{10}$ requires 320.2568, found 320.2568. ATR-IR (*v* cm^{-1}) 3063, 2922, 2856, 2598 (B-H) br, 1990, 1677, 1514, 1443, 1310, 1279, 1157, 1138, 1107, 748, 838, 748, 725.

1,4-Dibromo-2,5-diiodobenzene[42] (65)



To a stirring solution of 1,4-dibromobenzene (19.80 g, 83.9 mmol) in concentrated sulfuric acid (300 mL) was added iodine (80.00 g, 315 mmol) and the mixture was heated to 135 °C overnight. After cooling, the mixture was poured into ice water (1 L), the remaining solids were broken up in a pestle and mortar, dissolved in DCM, and the two fractions were combined. The aq. solution was extracted with DCM (5 x 300 mL) and the organic layer was washed with sat. Na_2SO_3 solution (3 x 300 mL), neutralised with sat. $NaHCO_3$ solution, washed with water (5 x 300 mL), brine (1 x 300 mL) and dried over $MgSO_4$. The solution was concentrated *in vacuo* and methanol (200 mL) was added to precipitate the product. Filtration yielded the *title compound* was isolated as a white solid (15.50 g, 31.8 mmol, 38%). m.p. 165-166 °C. ^{1}H NMR (400 MHz, $CDCl_3$) δ 8.04 (2H, s) ppm. ^{13}C NMR (100 MHz, $CDCl_3$) δ 142.7, 129.6, 101.7 ppm. HRMS (EI^+) $C_6H_2Br_2I_2$ requires 485.6613, found 485.6603.

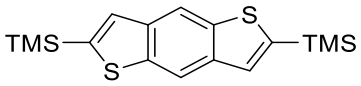
((2,5-Dibromo-1,4-phenylene)bis(ethyne-2,1-diyl))bis(trimethylsilane)[43] (66)



A mixture of 1,4-dibromo-2,5-diiodobenzene (15.00 g, 30.8 mmol), bis(triphenylphosphine)palladium(II) dichloride (2.5 mol%, 540 mg, 0.77 mmol), copper(I) iodide (5 mol%, 353 mg, 1.85 mmol) in dry benzene (150 mL) and diisopropylamine (90 mL) was purged with argon for 1 h. Ethynyltrimethylsilane (8.7 mL, 61.6 mmol) was added and the mixture was stirred at room temperature overnight before being quenched with water (100 mL). The resulting solution was extracted with ether, washed with water (4 x 100 mL), brine (1 x 100 mL) and dried over $MgSO_4$. Solvent was removed *in vacuo*, the residue was dissolved in a minimum amount of DCM and triturated 4 times with methanol, yielding the *title compound* as a tan solid (7.46 g, 17.4 mmol, 55%). m.p. 169-

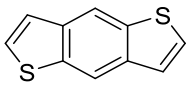
170 °C. ^{1}H NMR (400 MHz, $CDCl_3$) δ 7.67 (2H, s) ppm. ^{13}C NMR (100 MHz, $CDCl_3$) δ 136.8, 126.8, 124.1, 103.4, 101.7, 0.04 ppm. HRMS (EI^+) $C_{16}H_{20}Br_2Si_2$ requires 425.9470, found 425.9456.

2,6-Bis(trimethylsilyl)benzo[1,2-b:4,5-b']dithiophene[18] (67)



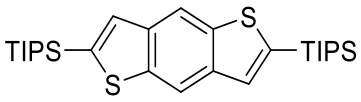
To a stirring solution of ((2,5-dibromo-1,4-phenylene)bis(ethyne-2,1-diyl))bis(trimethylsilane) (11.51 g, 26.9 mmol) in dry diethyl ether (300 mL) at -78 °C was added *t*-BuLi (63.00 mL, 1.7 M in pentane, 107 mmol) dropwise over 10 mins. The mixture was stirred for 15 mins before being allowed to warm to room temperature over 1 h. Sulfur (1.73 g, 54 mmol) was added in one portion, the mixture was stirred for a further 30 mins and ethanol (100 mL) was slowly added to quench the reaction. Water (300 mL) was added, extracted with chloroform and the washed with water (3 x 200 mL), brine (1 x 200 mL) and $MgSO_4$. Solvent was removed *in vacuo* and the solid was subjected to column chromatography with Pet. ether eluent. Product fractions were concentrated *in vacuo* and left to recrystalise by slow evaporation to afford the *title compound* as colourless crystals (3.80 g, 11.4 mmol, 42%). m.p. 182-184 °C. ^{1}H NMR (400 MHz, $CDCl_3$) δ 8.27 (2H, d, *J* = 0.5 Hz), 7.46 (2H, d, *J* = 0.5 Hz), 0.40 (9H, s) ppm. ^{13}C NMR (100 MHz, $CDCl_3$) δ 144.0, 141.0, 139.5, 130.2, 116.4, -0.02 ppm. HRMS (EI^+) $C_{16}H_{22}S_2Si_2$ requires 334.0702, found 334.0692.

Benzo[1,2-b:4,5-b']dithiophene[18] (68)



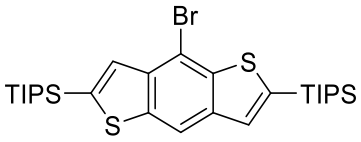
To a stirring solution of 2,6-bis(trimethylsilyl)benzo[1,2-b:4,5-b']dithiophene (3.8 g, 11.36 mmol) in THF (175 mL) was added TBAF (12.50 mL, 1.0 M in THF, 12.50 mmol) and the mixture was stirred at room temperature for 4 h. Water (200 mL) was added and the precipitate was washed with water (200 mL), ethanol (200 mL) and dried, yielding the *title compound* as a white solid (1.25 g, 6.57 mmol, 58%). m.p. 201-203 °C. ^{1}H NMR (400 MHz, $CDCl_3$) δ 8.32 (2H, s), 7.47 (2H, d, J = 5.5 Hz), 7.37 (2H, d, J = 5.5 Hz), ppm. ^{13}C NMR (100 MHz, $CDCl_3$) δ 137.8, 137.5, 127.4, 123.3, 117.2 ppm. HRMS (EI^+) $C_{10}H_6S_2$ requires 189.991, found 189.9903.

2,6-Bis(triisopropylsilyl)benzo[1,2-b:4,5-b']dithiophene[44] (69)



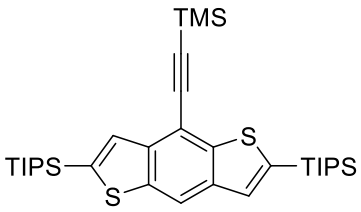
To a stirring solution of benzo[1,2-b:4,5-b']dithiophene (2.00 g, 10.5 mmol) in dry THF (125 mL) at -20 °C was added *n*-BuLi (12.6 mL, 2.5 M in hexanes, 31.5 mmol) dropwise over 10 mins. The mixture was stirred at this temperature for a further 10 mins, before being warmed to room temperature over 1 h. Triisopropylsilyl chloride (8.97 mL, 41.9 mmol) was added in one portion and the mixture was heated to reflux overnight. The solution was cooled to room temperature and poured into stirring 0.5 M HCl solution (400 mL). The precipitate was collected and washed with water (100 mL), methanol (100 mL) and -78 °C hexane (100 mL), affording the *title compound* as a white solid (4.76 g, 9.46 mmol 90%). m.p. 215-217 °C. ^{1}H NMR (400 MHz, $CDCl_3$) δ 8.30 (2H, s), 7.51 (2H, s), 1.49-1.37 (6H, m), 1.16 (36H, d, *J* = 7.4 Hz) ppm. ^{13}C NMR (100 MHz, $CDCl_3$) δ 140.9, 139.2, 138.6, 131.9, 115.9, 18.98, 12.18 ppm. HRMS (EI^+) $C_{28}H_{46}S_2Si_2$ requires 502.2571, found 502.2573.

(4-Bromobenzo[1,2-b:4,5-b']dithiophene-2,6-diyl)bis(triisopropylsilane) (70)



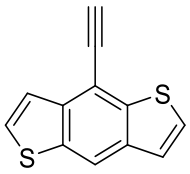
2,6-Bis(triisopropylsilyl)benzo[1,2-b:4,5-b']dithiophene (2.00 g, 3.98 mmol) was dissolved in dry chlorobenzene (200 mL) and NBS (708 mg, 3.98 mmol) was added. The mixture was stirred at room temperature and conversion was monitored by ^{1}H NMR every 24 h, with additional portions of NBS (3 x 0.5 eq.) added until full conversion was achieved. The solution was poured into water, extracted with chloroform, washed with water (4 x 100 mL), brine (1 x 100 mL) and dried over MgSO4. Solvent was removed *in vacuo*, the residue was dissolved in DCM triturated 3 times with methanol. The precipitate was collected, washed with methanol (100 mL) and ice-cold hexane (100 mL), affording the *title compound* as a tan solid (2.15 g, 3.70 mmol, 93%), with various mono and dibrominated regioisomers present as inseparable impurities. m.p. 215-216 °C. Major isomer: ^{1}H NMR (400 MHz, $CDCl_3$) δ 8.23 (1H, d, *J* = 0.7 Hz), 7.60 (2H, d, *J* = 0.7 Hz), 7.59 (2H, s), 1.50-1.36 (6H, m), 1.17 (36H, dd, *J* = 7.4, 1.5 Hz) ppm. ^{13}C NMR (100 MHz, $CDCl_3$) δ 142.6, 141.5, 140.2, 139.5, 139.5, 138.5, 132.6, 131.4, 115.1, 109.2 19.0, 12.2 ppm. HRMS (EI^+) $C_{28}H_{45}BrS_2Si_2$ requires 580.1685, found 580.1669.

(4-((Trimethylsilyl)ethynyl)benzo[1,2-b:4,5-b']dithiophene-2,6-diyl)bis(triisopropylsilane) (71)



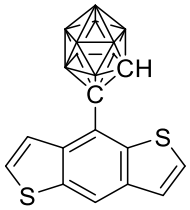
A stirring solution of (4-bromobenzo[1,2-b:4,5-b']dithiophene-2,6-diyl)bis(triisopropylsilane) (1.00 g, 1.72 mmol) and tetrakis(triphenylphosphine)palladium(0) (20 mol%, 398 mg, 0.344 mmol) in dry toluene (100 mL) was purged with argon for 1 h. Trimethyl((tributylstannyl)ethynyl)silane (1.32 g, 3.40 mmol) was added and the mixture was heated to reflux overnight. After cooling solvent was removed *in vacuo*, the oily residue was subjected to column chromatography on neutral alumina and eluted with Pet. ether, followed by 4:1 DCM:Pet. ether to elute the product. Solvent was removed *in vacuo*, yielding the *title compound* as a light yellow solid (0.69 g, 1.15 mmol, 67%). m.p. 129-130 °C. ^{1}H NMR (400 MHz, $CDCl_3$) δ 8.24 (1H, d, *J* = 0.7 Hz), 7.74 (1H, d, *J* = 0.7 Hz), 7.50 (1H, s), 1.50-1.37 (6H, m), 1.17 (36H, dd, *J* = 7.6, 4.0 Hz), 0.37 (9H, s) ppm. ^{13}C NMR (100 MHz, $CDCl_3$) δ 140.8, 140.7, 140.0, 139.2, 138.8, 138.6, 132.2, 131.6, 116.5, 110.5, 103.7, 101.9, 19.00, 12.19, 0.50 ppm. MS (MALDI-ToF) $C_{33}H_{54}S_2Si_3$ requires 599.17, found 598.7.

4-Ethynylbenzo[1,2-b:4,5-b']dithiophene (72)



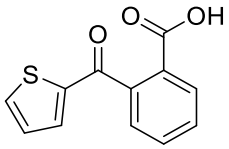
To a vigorously stirring solution of (4-((Trimethylsilyl)ethynyl)benzo[1,2-b:4,5-b']dithiophene-2,6-diyl)bis(triisopropylsilane) (650 mg, 1.10 mmol) in THF (50 mL) under argon at room temperature was added TBAF (6.0 mL, 1.0 M in THF, 6.00 mmol). After 3 h the mixture was diluted with ether (200 mL), washed with water (5 x 100 mL), brine (1 x 100 mL) and dried over $MgSO_4$. Solvent was removed *in vacuo* to yield the *title compound* as a brown oil (332 mg, 1.55 mmol, 93%). The unstable nature of this compound meant it was used immediately in a subsequent reaction without further purification.

1-(4'-benzo[1,2-*b*;4,5-*b'*]dithiophenyl)-*ortho*-$C_2B_{10}H_{11}$ (**73**)



A stirred solution of bmim(Cl) (61 mg, 0.35 mmol) and dry toluene (10 mL) were dried by refluxing in a Dean-Stark apparatus for several hours, before 4-ethynylbenzo[1,2-b:4,5-b']dithiophene (250 mg, 1.17 mmol) and decaborane (178 mg, 1.46 mmol) were added and the mixture was heated to reflux for 72 h. After cooling the solvent was removed *in vacuo* and the crude residue was subjected to column chromatography with Pet. ether, yielding the *title compound* as colourless crystals (136 mg, 0.41 mmol, 35%). Crystals suitable for X-ray diffraction analysis were grown by slow evaporation of a biphasic solution of DCM and hexane. m.p. 234-235 °C. ^{1}H NMR (400 MHz, $CDCl_3$) δ 8.40 (1H, s), 8.26 (1H, d, *J* = 6.0 Hz), 7.60 (1H, d, *J* = 6.0 Hz), 7.45 (1H, d, *J* = 5.7 Hz), 7.40 (1H, d, *J* = 5.7 Hz), 5.93-5.86 (1H, br), 3.89-1.48 (10H, br) ppm. ^{11}B NMR (128 MHz, $CDCl_3$) δ -1.42, -2.43, 3.51, 7.93, 9.09, 9.79, 11.66, 12.48, 13.75 ppm. ^{13}C NMR (100 MHz, $CDCl_3$) δ 140.5, 139.3, 136.7, 134.8, 128.2, 125.5, 125.3, 123.7, 123.1, 120.3, 78.41, 62.22 ppm. HRMS (EI^+) $C_{12}H_{16}B_{10}S_2$ requires 332.1697, found 332.1697. ATR-IR (*v* cm^{-1}) 3922, 3856, 3751, 3692, 3585, 3070, 2926, 2610 (B-H), 2576 (B-H) br, 2344, 2214, 2050, 1970, 1509, 1352, 1185, 1066, 861, 814, 766, 730.

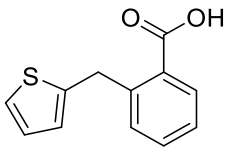
2-(Thiophene-2-carbonyl)benzoic acid[22] (**79**)



To a stirring suspension of phthalic anhydride (20.0 g, 135 mmol) in dry DCM (200 mL) was added $AlCl_3$ (37.8 g, 284 mmol) over a period of 20 mins. The mixture was stirred for a further 30 mins, then a solution of thiophene (11.91 mL, 149 mmol) in dry DCM (100 mL) was added dropwise over 45 mins, and the mixture was left to stir overnight. The reaction was poured into 0.2 M HCl solution (600 mL) and stirred for 1 h, after which the layers were separated, and the organic layer was extracted with 1.0 M NaOH solution (2 x 100 mL). The aqueous fractions were combined and acidified with 37% HCl solution (200 mL) and stirred to form a precipitate which was collected by vacuum filtration, washed with water (300 mL) and dried yielding the *title compound* as a light yellow solid (25.82 g, 111 mmol,

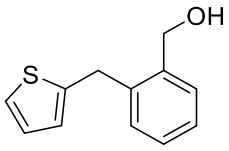
82%). m.p. 209-211 °C. ^{1}H NMR (400 MHz, $CDCl_3$) δ 9.16-7.83 (1H, br), 8.08 (1H, dd, *J* = 7.4, 0.8 Hz), 7.69 (1H, dd, *J* = 4.9, 1.0 Hz), 7.66 (1H, td, *J* = 7.4, 1.2 Hz), 7.57 (1H, td, *J* = 7.4, 1.2 Hz), 7.46 (1H, dd, *J* = 7.4, 0.8 Hz), 7.25 (1H, dd, *J* = 3.9, 1.0 Hz), 7.06 (1H, dd, *J* = 4.9, 3.9 Hz) ppm. ^{13}C NMR (100 MHz, $CDCl_3$) δ 189.4, 179.1, 144.7, 142.2, 134.9, 134.8, 133.4, 131.3, 130.2, 128.4, 128.3, 128.1 ppm. HRMS (APCI) $C_{12}H_8O_3S$ requires 233.0267, found 233.0268.

2-(Thiophen-2-ylmethyl)benzoic acid[22] (80)



2-(Thiophene-2-carbonyl)benzoic acid (25.82 g, 111 mmol) was dissolved into stirring ammonium hydroxide (450 mL) and zinc dust (65.00 g, 1.11 mol) was added slowly over 10 mins. The resulting mixture was heated to reflux for 24 h with an additional portion of ammonium hydroxide (150 mL) added after 12 h. After cooling, the mixture was filtered and precipitated with 37% HCl solution (200 mL). The precipitate was collected, washed with water (500 mL) and dried to yield the *title compound* as a white solid (16.72 g, 76.6 mmol, 69%). m.p. 160 °C. ^{1}H NMR (400 MHz, $CDCl_3$) δ 8.06 (1H, dd, *J* = 7.6, 1.3 Hz), 7.49 (1H, td, *J* = 7.6, 1.3 Hz), 7.36-7.28 (2H, m), 7.10 (1H, dd, *J* = 5.1, 0.8 Hz), 6.88 (1H, dd, *J* = 5.1, 3.6 Hz), 6.78 (1H, dd, *J* = 3.6, 0.8 Hz), 5.90-4.28 (1H, br) ppm. ^{13}C NMR (100 MHz, $CDCl_3$) δ 173.2, 144.4, 143.1, 133.3, 132.1, 131.6, 128.9, 127.0, 127.0, 125.7, 124.2, 34.5 ppm. HRMS (APCI) $C_{12}H_{10}O_2S$ requires 217.0323, found 217.0316.

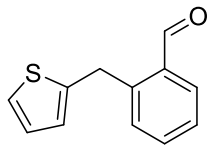
(2-(Thiophen-2-ylmethyl)phenyl)methanol[22] (81)



To a stirring solution of $LiAlH_4$ (261 mL, 1.0 M in THF, 261 mmol) in dry THF (450 mL) at 0 °C was added 2-(thiophen-2-ylmethyl)benzoic acid (15.00 g, 68.7 mmol) portionwise over 30 mins, after which cooling was removed and the mixture was allowed to reach room temperature overnight. The reaction was quenched by first cooling to 0 °C, then slowly adding water (100 mL) dropwise until effervescence could no longer be observed. The inorganic salts were dissolved by addition of 2 M HCl solution (600 mL), the aqueous layer was extracted with DCM and the combined organic fractions were washed with water (3 x 200 mL), sat. $NaHCO_3$ solution (2 x 200 mL), brine (1 x 200 mL) and dried over $MgSO_4$.

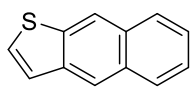
Solvent was removed *in vacuo* to yield the *title compound* as a brown oil (12.28 g, 60.1 mmol, 88%). ^{1}H NMR (400 MHz, $CDCl_3$) δ 7.44-7.39 (1H, m), 7.33-7.24 (3H, m), 7.15 (1H, d, *J* = 5.1 Hz), 6.92 (1H, dd, *J* = 5.1, 3.6 Hz), 6.75 (1H, d, *J* = 2.4 Hz), 4.70 (2H, s), 4.25 (2H, s), 3.40-2.62 (1H, br) ppm. ^{13}C NMR (100 MHz, $CDCl_3$) δ 144.1, 138.8, 138.5, 130.4, 128.8, 128.5, 127.5, 127.1, 125.4, 124.3, 63.4, 33.1 ppm. HRMS (EI^+) $C_{12}H_{12}OS$ requires 186.0503186.0494, found 186.0494.

2-(Thiophen-2-ylmethyl)benzaldehyde[22] (82)



Collin's reagent was prepared by slow addition of CrO_3 (1.45 g, 14.5 mmol) into a stirring solution of dry DCM (300 mL) and dry pyridine (2.94 mL, 36.5 mmol) at -20 °C over 20 mins, ensuring that the temperature of the reaction did not rise above 0 °C. Once addition was complete the mixture was allowed to warm to room temperature and stirred for an additional 30 mins, after which it was returned to -20 °C and (2-(thiophen-2-ylmethyl)phenyl)methanol (6.15 g, 30.4 mmol) in dry DCM (100 mL) was added dropwise over 10 mins. Cooling was removed and the reaction was left to warm to room temperature overnight. The inorganic solids were removed by filtration and washed with chloroform (200 mL), and the filtrate was washed with 2 M HCl solution (4 x 100 mL), sat. $NaHCO_3$ solution (4 x 100 mL), brine (1 x 100 mL) and dried over $MgSO_4$. Solvent was removed *in vacuo* to yield the *title compound* as a brown oil (5.23 g, 25.9 mmol, 85%) which was subsequently used without further purification. ^{1}H NMR (400 MHz, $CDCl_3$) δ 10.25 (1H, s), 7.86 (1H, dd, *J* = 7.6, 1.4 Hz), 7.55 (1H, td, *J* = 7.6, 1.4 Hz), 7.44 (1H, td, *J* = 7.6, 1.1 Hz), 7.35 (1H, d, *J* = 7.6 Hz), 7.14 (1H, dd, *J* = 5.1, 1.1 Hz), 6.91 (1H, dd, *J* = 5.1, 3.5 Hz), 6.76 (1H, dq, *J* = 3.5, 1.1 Hz), 4.62 (2H, s) ppm. ^{13}C NMR (100 MHz, $CDCl_3$) δ 192.7, 143.5, 142.7, 134.4, 134.0, 133.0, 131.5, 127.7, 127.2, 125.8, 124.5, 32.9 ppm. HRMS (EI^+) $C_{12}H_{10}OS$ requires 202.0460, found 202.0452.

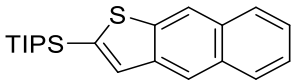
Naphtho[2,3-*b*]thiophene[22] (83)



Polyphosphoric acid (80.00 g, 816 mmol) was heated to 100 °C and poured into a 100 mL beaker containing 2-(thiophen-2-ylmethyl)benzaldehyde (4.00 g, 19.8 mmol) heated to 120 °C, and the mixture was mechanically stirred. After 30 mins the oily reaction mixture was poured into stirring ice-

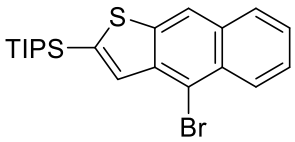
water (200 mL), the brown precipitate was collected by vacuum filtration, washed with water (100 mL), methanol (100 mL), and dried. Column chromatography using Pet. ether eluent yielded the *title compound* as a white crystalline solid (2.74 g, 1.49 mmol, 75%). m.p. 318-320 °C. ^{1}H NMR (400 MHz, $CDCl_3$) δ 8.37 (1H, s), 8.32 (1H, s), 8.00-7.94 (1H, m), 7.94-7.88 (1H, m), 7.51 (1H, d, *J* = 5.5 Hz), 7.49-7.45 (2H, m), 7.42 (1H, dd, *J* = 5.5, 0.5 Hz) ppm. ^{13}C NMR (100 MHz, $CDCl_3$) δ 139.2, 138.6, 131.3, 131.3, 128.6, 128.5, 127.6, 125.6, 125.3, 123.8, 122.2, 121.0 ppm. HRMS (EI^+) $C_{12}H_{10}OS$ requires 184.0338, found 184.0347.

Triisopropyl(naphtho[2,3-b]thiophen-2-yl)silane (84)



To a stirring solution of naphtho[2,3-b]thiophene (2.20 g, 11.9 mmol) in dry THF (100 mL) at 0 °C was added *n*-BuLi (8.80 mL, 1.6M in hexanes, 14.0 mmol) dropwise over 1 min. Cooling was removed and the reaction was allowed to warm to room temperature over 1 h. Triisopropylsilyl chloride (4.14 mL, 23.8 mmol) was added and the solution was heated to reflux overnight. After cooling, 0.5 M HCl solution (25 mL) was added, the organic layer was washed with water (3 x 50 mL), brine (1 x 50 mL) and concentrated *in vacuo*. Methanol (10 mL) was added and the precipitate was filtered under vacuum, washed with ice-cold methanol (20 mL), -78 °C hexane (10 mL) and dried, yielding the *title product* as a pale yellow solid (3.40 g, 9.99 mmol, 84%). m.p. 93 °C. ^{1}H NMR (400 MHz, $CDCl_3$) 8.34 (2H, d, *J* = 13.0 Hz), 8.00-7.87 (2H, m), 7.59 (1H, s), 7.49-7.42 (H, 2m), 1.51-1.39 (3H, m), 1.18 (18H, d, *J* = 7.4 Hz) ppm. ^{13}C NMR (100 MHz, $CDCl_3$) δ 141.9, 140.6, 140.0, 132.5, 131.2, 131.2, 128.7, 127.7, 125.6, 125.1, 121.7, 120.1, 19.0, 12.2 ppm. HRMS (EI^+) $C_{21}H_{28}SSi$ requires 340.1681, found 340.1683.

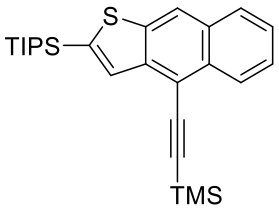
(4-Bromonaphtho[2,3-b]thiophen-2-yl)triisopropylsilane (85)



To a solution of triisopropyl(naphtho[2,3-b]thiophen-2-yl)silane (3.53 g, 8.37 mmol) in dry chlorobenzene (200 mL) was added NBS (1.60 g, 9.00 mmol) and the mixture was stirred at 40 °C for 24 h. After cooling, solvent was removed *in vacuo*, the residue was dissolved in a minimum amount of hot DCM (10 mL) and methanol (100 mL) was added. The precipitate was collected via vacuum filtration, washed with methanol and dried to yield the *title compound* as a light-yellow solid (3.14 g,

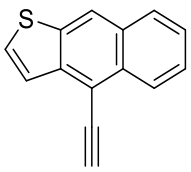
7.49 mmol, 89%). m.p. 132-133 °C. ^{1}H NMR (400 MHz, $CDCl_3$) δ 8.43-8.40 (1H, m), 8.32 (1H, s), 7.90 (1H, d, J = 8.2 Hz), 7.77 (1H, d, J = 0.8 Hz), 7.57 (1H, ddd, *J* = 8.7, 6.6, 1.2 Hz), 7.51 (1H, ddd, *J* = 8.7, 6.6, 1.2 Hz), 1.53-1.41 (3H, m), 1.19 (18H, d, *J* = 7.4 Hz) ppm. ^{13}C NMR (100 MHz, $CDCl_3$) δ 142.0, 141.4, 140.6, 133.1, 132.1, 129.4, 128.1, 127.5, 126.6, 126.1, 120.1, 116.5, 19.98, 12.20 ppm. HRMS (EI^+) $C_{21}H_{27}BrSSi$ requires 418.0790, found 418.0786.

Triisopropyl(4-((trimethylsilyl)ethynyl)naphtho[2,3-b]thiophen-2-yl)silane (86)



A stirring solution of (4-bromonaphtho[2,3-b]thiophen-2-yl)triisopropylsilane (2.00 g, 4.74 mmol) and tetrakis(triphenylphosphine)palladium(0) (10 mol%, 550 mg, 0.475 mmol) in dry toluene (200 mL) was purged with argon for 1 h. Trimethyl((tributylstannyl)ethynyl)silane (3.68 g, 9.49 mmol) was added and the mixture was heated to reflux overnight. After cooling solvent was removed *in vacuo*, the oily residue was loaded onto an alumina plug and eluted with 1:4 DCM:Pet. ether, until the filtrate ran clear. The filtrate was concentrated *in vacuo*, -78 °C methanol (100 mL) was added and the mixture was stirred whereupon the *title compound* precipitated as yellow microcrystals (1.72 g, 3.94 mmol, 83%). m.p. 102-104 °C. ^{1}H NMR (400 MHz, $CDCl_3$) δ 8.46 (1H, d, J = 8.3 Hz), 8.32 (1H, s), 7.89 (1H, d, J = 8.3 Hz), 7.86 (1H, d, J = 0.8 Hz), 7.55 (1H, ddd, J = 8.4, 6.6, 1.4 Hz), 7.49 (1H, ddd, *J* = 8.4, 6.6, 1.4 Hz), 1.51-1.38 (3H, m), 1.19 (18H, d, *J* = 7.4 Hz), 0.39 (9H, s) ppm. ^{13}C NMR (100 MHz, $CDCl_3$) δ 143.2, 141.8, 141.1, 132.7, 131.4, 130.8, 128.1, 126.9, 126.2, 126.0, 121.2, 104.5, 102.3, 19.0, 12.3, 0.54 ppm. HRMS (EI^+) $C_{26}H_{36}SSi_2$ requires 436.2076, found 436.2082.

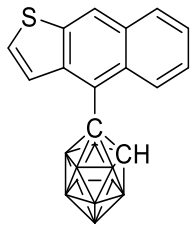
4-Ethynylnaphtho[2,3-b]thiophene (87)



To a vigorously stirring solution of triisopropyl(4-((trimethylsilyl)ethynyl)naphtho[2,3-b]thiophen-2-yl)silane (750 mg, 1.72 mmol) in THF (75 mL) at room temperature was added TBAF (2.4 mL, 1.0 M in THF, 2.40 mmol). After 3 h the mixture was diluted with ether (200 mL), washed with water (5 x 100

mL), brine (1 x 100 mL) and dried over $MgSO_4$. Solvent was removed *in vacuo* to yield the *title compound* as a yellow-orange oil (332 mg, 1.59 mmol, 93%). The unstable nature of this compound meant it was used immediately in a subsequent reaction without further purification.

1-(4'-naphtho[2,3-*b*]thiophenyl)-*ortho*-$C_2B_{10}H_{11}$ (**88**)



A stirred solution of bmim(Cl) (132 mg, 0.76 mmol) and dry toluene (10 mL) were dried by refluxing in a Dean-Stark apparatus for several hours, before 4-ethynylnaphtho[2,3-b]thiophene (332 mg, 1.59 mmol) and decaborane (329 mg, 2.69 mmol) were added, and the mixture was heated to reflux for 72 h. After cooling the solvent was removed *in vacuo* and the crude residue was subjected to column chromatography with Pet. ether, yielding the *title compound* as bright yellow crystals (249 mg, 0.75 mmol, 48%). Crystals suitable for X-ray diffraction analysis were grown by slow evaporation of a biphasic solution of DCM and hexane. m.p. 207-209 °C. ^{1}H NMR (400 MHz, $CDCl_3$) δ 8.77-8.71 (1H, m), 8.39 (1H, s), 7.99 (1H, d, J = 5.9 Hz), 7.92-7.87 (1H, m), 7.67 (1H, d, *J* = 5.9 Hz), 7.54-7.47 (2H, m), 5.18-5.12 (1H, br), 4.11-1.41 (10H, br) ppm. ^{11}B NMR (128 MHz, $CDCl_3$) δ -1.02, 2.28, 3.57, 8.04, 9.20, 10.66, 12.59, 13.92 ppm. ^{13}C NMR (100 MHz, $CDCl_3$) δ 139.9, 137.6, 132.1, 130.6, 128.8, 128.7, 125.9, 125.7, 125.4, 125.2, 124.2, 122.6, 78.2, 63.8 ppm. HRMS (EI^+) $C_{14}B_{10}H_{18}S$ requires 326.2132, found 326.2148. ATR-IR (*v* cm^{-1}) 3840, 3677, 3651, 3212, 3092, 2581 (B-H), 2544 (B-H) br, 2178, 2139, 2069, 2050, 1985, 1585, 1498, 1480, 1314, 1103, 1067, 1037, 1022, 875, 833, 766, 735, 704, 686.

2.14 – References

1 M. G. Davidson, T. G. Hibbert, J. A. K. Howard, A. Mackinnon and K. Wade, *Chem. Commun.*, 1996, **0**, 2285–2286.
2 R. A. Harder, PhD Thesis, Durham University, 2012.
3 R. N. Grimes, *Carboranes*, Academic Press, Amsterdam; Boston, Third edition., 2016.
4 C. Viñas, G. Barberà, J. M. Oliva, F. Teixidor, A. J. Welch and G. M. Rosair, *Inorg. Chem.*, 2001, **40**, 6555–6562.
5 A. V. Marsh, Masters Thesis, Imperial College London, 2015.
6 R. H. Mitchell, Y.-H. Lai and R. V. Williams, *J. Org. Chem.*, 1979, **44**, 4733–4735.
7 K. Sonogashira, Y. Tohda and N. Hagihara, *Tetrahedron Letters*, 1975, **16**, 4467–4470.
8 V. X. Truong, F. Li and J. S. Forsythe, *ACS Macro Lett.*, 2017, **6**, 657–662.
9 L. L. Naeger and K. C. Leibman, *Toxicology and Applied Pharmacology*, 1972, **22**, 517–527.
10 M. Shao, P. Dongare, L. N. Dawe, D. W. Thompson and Y. Zhao, *Org. Lett.*, 2010, **12**, 3050–3053.
11 F. Cataldo, D. A. García-Hernández and A. Manchado, Sonochemical Synthesis of Fullerene C60/Anthracene Diels-Alder Mono and Bis-adducts, https://www.ingentaconnect.com/content/tandf/fncn/2014/00000022/00000006/art00007, (accessed 23 January 2019).
12 X. Zhang, H. Dai, H. Yan, W. Zou and D. Cremer, *J. Am. Chem. Soc.*, 2016, **138**, 4334–4337.
13 J. Fanfrlík, A. Pecina, J. Řezáč, R. Sedlak, D. Hnyk, M. Lepšík and P. Hobza, *Physical Chemistry Chemical Physics*, 2017, **19**, 18194–18200.
14 W. Zou, X. Zhang, H. Dai, H. Yan, D. Cremer and E. Kraka, *Journal of Organometallic Chemistry*, 2018, **865**, 114–127.
15 J. M. V. Franco, T. Sasamori, G. Schnakenburg, A. E. Ferao and R. Streubel, *Chem. Commun.*, 2015, **51**, 3878–3881.
16 Y. Wang, S. R. Parkin and M. D. Watson, *Org. Lett.*, 2008, **10**, 4421–4424.
17 E. R. Biehl, *Progress in Heterocyclic Chemistry: Chapter 4.1. Five-Membered Ring Systems: Thiophenes and Se/Te Derivatives*, Elsevier Inc. Chapters, 2013.
18 K. Takimiya, Y. Konda, H. Ebata, N. Niihara and T. Otsubo, *J. Org. Chem.*, 2005, **70**, 10569–10571.
19 T. C. Parker and S. R. Marder, *Synthetic Methods in Organic Electronic and Photonic Materials: A Practical Guide*, Royal Society of Chemistry, 2015.
20 P. Ufimkin, Masters Thesis, Imperial College London, 2017.
21 R. Chinchilla and C. Nájera, *Chem. Soc. Rev.*, 2011, **40**, 5084–5121.
22 M. L. Tedjamulia, Y. Tominaga, R. N. Castle and M. L. Lee, *Journal of Heterocyclic Chemistry*, 1983, **20**, 1143–1148.
23 Ronald. Ratcliffe and Ronald. Rodehorst, *J. Org. Chem.*, 1970, **35**, 4000–4002.
24 G. Tojo and M. I. Fernandez, *Oxidation of Alcohols to Aldehydes and Ketones: A Guide to Current Common Practice*, Springer Science & Business Media, 2006.
25 J. C. Collins, W. W. Hess and F. J. Frank, *Tetrahedron Letters*, 1968, **9**, 3363–3366.
26 E. S. Krongauz, A. L. Rusanov and T. L. Renard, *Russ. Chem. Rev.*, 1970, **39**, 747.
27 N. Zhao, L. Qiu, X. Wang, Z. An and X. Wan, *Tetrahedron Letters*, 2014, **55**, 1040–1044.
28 Rupa Madyal, *Conference Proceedings. New Perspectives in Science Education*, Pixel, 2015.
29 K. Kokado, A. Nagai and Y. Chujo, *Tetrahedron Letters*, 2011, **52**, 293–296.
30 K. Nishino, K. Uemura, K. Tanaka, Y. Morisaki and Y. Chujo, *European Journal of Organic Chemistry*, 2018, **2018**, 1507–1512.
31 L. J. Farrugia, *J Appl Cryst*, 2012, **45**, 849–854.
32 Gaussian 09, Revision D.02, M. J. Frisch, G. W. Trucks, H. B. Schlegel, G. E. Scuseria, M. A. Robb, J. R. Cheeseman, G. Scalmani, V. Barone, G. A. Petersson, H. Nakatsuji, X. Li, M. Caricato, A. Marenich, J. Bloino, B. G. Janesko, R. Gomperts, B. Mennucci, H. P. Hratchian, J. V. Ortiz, A. F. Izmaylov, J. L. Sonnenberg, D. Williams-Young, F. Ding, F. Lipparini, F. Egidi, J. Goings, B. Peng,

A. Petrone, T. Henderson, D. Ranasinghe, V. G. Zakrzewski, J. Gao, N. Rega, G. Zheng, W. Liang, M. Hada, M. Ehara, K. Toyota, R. Fukuda, J. Hasegawa, M. Ishida, T. Nakajima, Y. Honda, O. Kitao, H. Nakai, T. Vreven, K. Throssell, J. A. Montgomery, Jr., J. E. Peralta, F. Ogliaro, M. Bearpark, J. J. Heyd, E. Brothers, K. N. Kudin, V. N. Staroverov, T. Keith, R. Kobayashi, J. Normand, K. Raghavachari, A. Rendell, J. C. Burant, S. S. Iyengar, J. Tomasi, M. Cossi, J. M. Millam, M. Klene, C. Adamo, R. Cammi, J. W. Ochterski, R. L. Martin, K. Morokuma, O. Farkas, J. B. Foresman, and D. J. Fox, Gaussian, Inc., Wallingford CT, 2016., *Gaussian 09, Revision D.01*, .

33 A. D. Becke, *J. Chem. Phys.*, 1993, **98**, 5648–5652.

34 C. Lee, W. Yang and R. G. Parr, *Phys. Rev. B*, 1988, **37**, 785–789.

35 G. A. Petersson and M. A. Al-Laham, *J. Chem. Phys.*, 1991, **94**, 6081–6090.

36 G. A. Petersson, A. Bennett, T. G. Tensfeldt, M. A. Al-Laham, W. A. Shirley and J. Mantzaris, *J. Chem. Phys.*, 1988, **89**, 2193–2218.

37 Roy Dennington, Todd A. Keith, and John M. Millam, *GaussView, Version 5.0.9*, Semichem Inc., Shawnee Mission, KS, 2016.

38 N. M. O'boyle, A. L. Tenderholt and K. M. Langner, *J. Comput. Chem.*, 2008, **29**, 839–845.

39 China, CN101139317A, 2008.

40 D. Liu, C. Li, S. Niu, Y. Li, M. Hu, Q. Li, W. Zhu, X. Zhang, H. Dong and W. Hu, *J. Mater. Chem. C*, 2019, **7**, 5925–5930.

41 Y. Zheng, X. Wang, Y. Bai, X. Wang, C. Ru, W. Chen, X. Lv, X. Pan and J. Wu, *Inorg. Chem.*, 2018, **57**, 13544–13551.

42 M. Modjewski, S. V. Lindeman and R. Rathore, *Org. Lett.*, 2009, **11**, 4656–4659.

43 K. Cho, J. Yoo, H.-W. Noh, S. M. Lee, H. J. Kim, Y.-J. Ko, H.-Y. Jang and S. U. Son, *J. Mater. Chem. A*, 2017, **5**, 8922–8926.

44 M. Nakano, S. Shinamura, R. Sugimoto, I. Osaka, E. Miyazaki and K. Takimiya, *Org. Lett.*, 2012, **14**, 5448–5451.



Chapter 3 – The Photoluminescence of Tricyclic-Substituted Carboranes; Understanding AIE

3.1 – Introduction

Carbon substituted mono, and dinaphthyl carboranes have been reported for all three isomers.[1] The *meta* and *para*-carborane isomers are fluorescent in good solvents, exhibiting a single, LE with a small Stokes shift consistent with the parent naphthalene.[2] The monosubstituted *ortho*-carborane derivative displays similar properties, but has an additional, lower energy emission with a much larger Stokes shift. DFT calculations suggest that the excited state responsible has the aromatic plane perpendicular to the cage C-C bond, with significant elongation of the latter, and accordingly a large electron density on the cage. This is a TICT state as conventionally described.[*] The disubstituted *ortho*-

[*] In the introduction the problems with the TICT terminology, as applied to carboranes, is described in detail. To avoid further confusion, in this thesis, excited states species where the cage C-C bond is significantly elongated due to charge transfer from the aromatic whose plane is perpendicular to this bond, will be described as TICT states, regardless of whether any rotation occurred in the excited state.

carborane compound (**89**) has a unique third emissive band which is as a result of excimer formation between the two naphthalene ring systems when they are structurally face-on,[3] **Figure 3-1**.

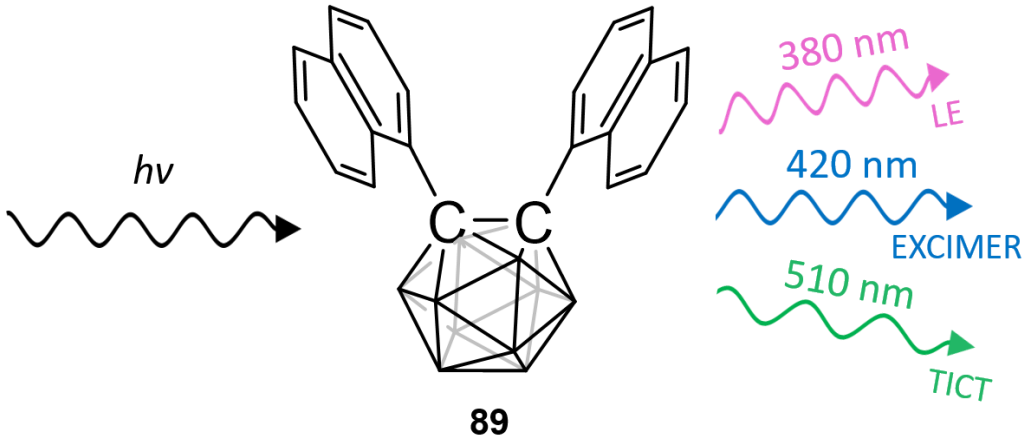


Figure 3-1 – Photoluminescence properties of dinaphthyl-*ortho*-carborane.

The emissive energy of the *meta* and *para* isomers was determined to be too high in energy (λ_{em} = ca. 350 nm), and the emissive quantum yield of the predominantly yellow fluorescing *ortho* isomer was too low, to be useful for light-emitting applications.[1,3] However, calculations suggest that anthracenyl carboranes would have a red-shifted emission energy that would be much more useful for these purposes. Having previously reported as being unstable, the anthracenyl *ortho*, *meta* and *para*-carboranes were synthesised and isolated in **Chapter 2**. A combination of single-crystal XRD, NMR and DFT calculations demonstrate that these are highly rigid molecules, and therefore may be very good candidates for exhibiting AIE.

Whilst AIE has been reported for a large range of *ortho*-carborane containing materials, there is a dearth of information about AIE for *meta* and *para*-carborane materials. These isomers cannot form TICT states due to the absence of a cage C-C bond, however AIE is a property far from restricted to *ortho*-carborane.[4] In fact, the introduction of bulky functional groups into structures of conventional luminogens (i.e. those that are luminescent in dilute solutions but undergo ACQ when concentrated) can be all that is required to trigger AIE. For example, 1,4-distyrylbenzene, a linear polyene, is strongly fluorescent in solution but exhibits ACQ when aggregated, however the situation is changed when the α-olefinic protons are exchanged for methyl groups,[5] **Figure 3-2**.

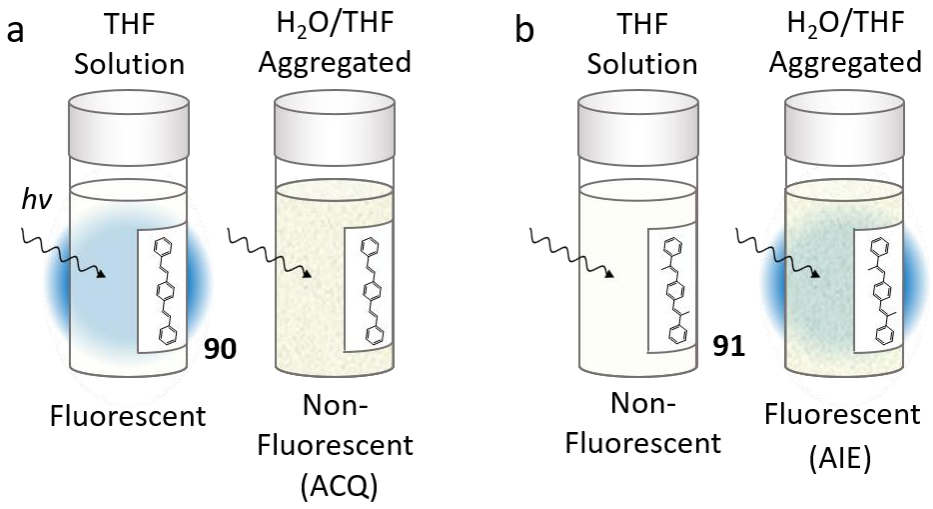


Figure 3-2 – Demonstration of (a) ACQ for 1,4-distyrylbenzene, and (b) AIE for 1,4-di[(E)-2-phenyl-1-propenyl]benzene. Aggregated solutions of these compounds are formed by diluting THF solution with H_2O.

The reason for the drastic transformation in properties can be ascribed to the change in crystal structure, which for 1,4-distyrylbenzene (**90**) is a face-to-face packing structure, with strong π-π stacking interactions which aids excimer formation and increases non-radiative decay routes.[6] However, the methylated derivative (**91**) adopts a non-planar conformation, and is indeed twisted out of the aromatic plane by about 40°. This minimises intermolecular interactions, and makes the compound emissive in the aggregated state.[4] It is therefore possible that the presence of the bulky carborane, regardless of the isomer, and the resulting aromatic deformation, is all that is needed to produce AIE.

Hence, in this chapter, optical studies of the three isomers of anthracenyl carborane and ***o*CbBDT** and ***o*CbNTP** are presented. Each compound is subjected to detailed optical studies in good solvent systems, bad solvent systems and in the solid state. Further, solution-based low-temperature PL studies are obtained for the isomeric carboranes. From this data, the PL properties of the anthracenyl carboranes are explained in terms of their structure, and the effect of rotational freedom on the PL of the *ortho*-carborane series is deduced.

AIE of aryl carboranes is examined in detail, and through scanning electron microscopy (SEM) the underlying gross structures of the aggregates are uncovered. Transmission electron microscopy (TEM) takes this further, revealing the microstructure of the aggregates and helping to explain the AIE phenomenon.

3.2 – Optical Studies of the Anthracenyl Carboranes

3.2.1 – UV-Vis and PL

To begin the investigation into the photoluminescence properties of the anthracenyl carboranes, UV-Vis spectroscopy and a steady-state PL study was performed on the compounds in THF solutions. The results are presented in **Figure 3-3**.

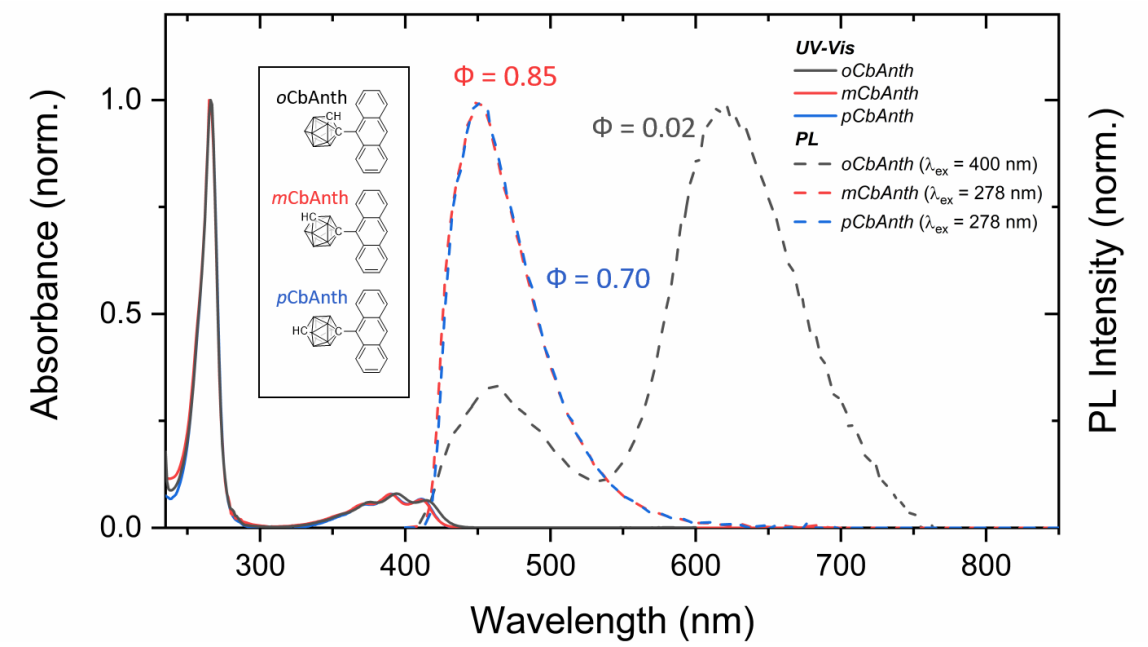


Figure 3-3 – UV-Vis and PL spectroscopy of the three isomers of anthracenyl carboranes in THF solutions, concentration = ca. 1 x 10^{-5} M, with quantum yields presented.

The UV-Vis of the isomers are strikingly similar to that of the parent anthracene,[7] which is not surprising; as discussed in the introduction, the parent carboranes are very weak absorbers of UV light. There are two clearly distinguishable parts, a high energy region centred at λ_{max} = 260 nm, and a second, vibronic region centred at λ_{max} = 390 nm. The two regions correspond to two separate states of electronic excitation. The first, high energy region is a π→π* (E-band) transition region, and the second is the lower energy π→π* (B-band) transition region.[8] The latter has a distinct vibronic shape, owing to the allowed Franck-Condon transitions. The differences between the vibrational sub-levels is likely due to the C-H bending vibration of anthracene, occurring at ca. 1443 cm^{-1}.[7]

The vibronic region is red-shifted relative to anthracene by approximately 25 nm, as a result of the electron-withdrawing carborane substituent narrowing the band gap (**Figure 2-7**). The absorbance of ***m*CbAnth** and ***p*CbAnth** isomers are virtually identical, but the vibronic region of ***o*CbAnth** is red-shifted by 4 nm. This subtle shift is likely a result of the stronger electron-withdrawing ability of *ortho*-

carborane relative to the other isomers, stabilising the LUMO and reducing the band gap to a greater degree. Note that in **Figure 2-7** the calculated band gap of the isomers is ca. 3.32 eV (373 nm), and all three are within 0.01 eV (ca. 1 nm), but this is the fundamental gap and not the measured optical band gap; in the latter case one must consider the binding energy of the electron-hole pair, which reduces the energy of the transition.[9] For this reason, and the shortcomings of the B3LYP functional, these calculations are not sensitive enough to predict such a small red-shift for ***o*CbAnth**. Such a phenomenon has however, also been observed for the analogous naphthyl carborane series.[1] The extinction coefficients of the three isomers are also very similar, as presented in **Appendix V**, and the value is slightly larger than that of the parent anthracene (dissolved in cyclohexane),[10] also a property seen for the naphthyl carborane series.

The isomers have similarities in their PL too. All three exhibit a vibronic emission centred at λ_{em} = 450 nm. However, ***o*CbAnth** also displays a long wavelength emission not observed in the other compounds. This peak is broad and featureless, which is often an indication of a delocalised excited state species. Whilst ***m*CbAnth** and ***p*CbAnth** are very efficient fluorophores (Φ = 0.85 and 0.70 respectively) in THF solution, the ***o*CbAnth** is barely emissive at all (Φ = 0.02).

The band shape of the vibronic emission follows the trend determined by the Franck-Condon principle, in which the vibronic absorption and emissive bands are mirror images of each other, **Figure 3-4**.

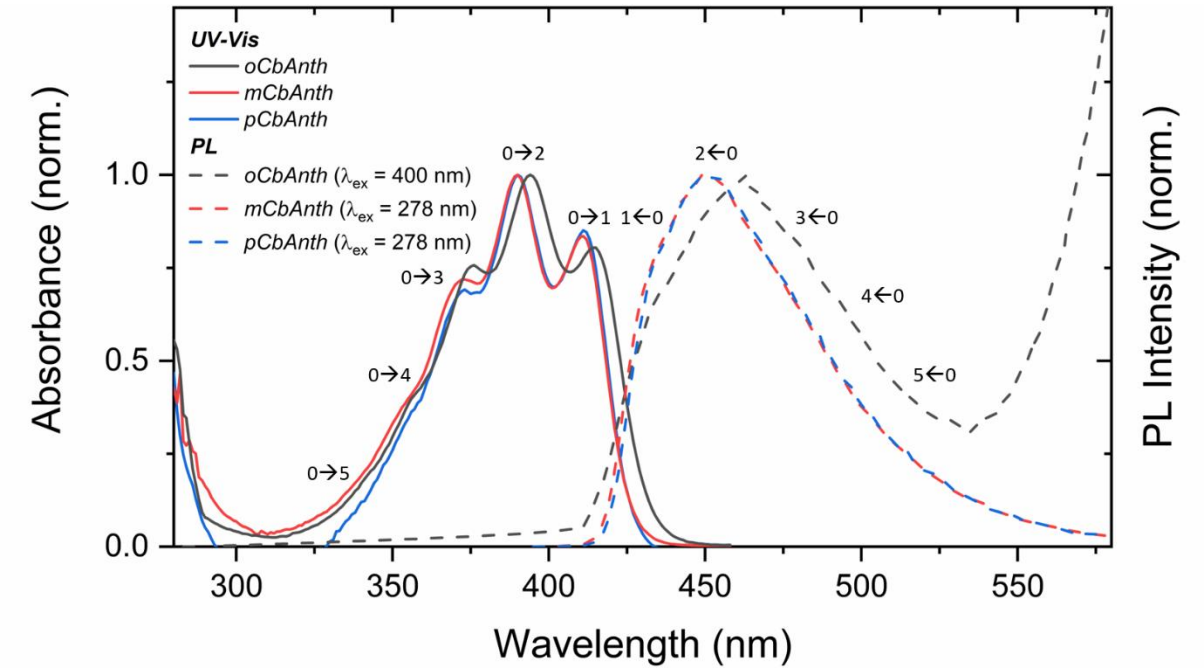


Figure 3-4 – Vibronic structures of absorbance and emissive band shapes, with electronic transitions labelled. The broader nature of the emissive peak is a result of larger slit widths used in PL measurements (>2 nm) compared with UV-Vis measurements (1 nm).

The emissive profile of the vibronic region is virtually identical to anthracene,[11] except slightly red-shifted in keeping with the red-shifted absorbance. Due to the same reasoning ***o*CbAnth** has a slightly lower energy vibronic emission. The lifetimes of these species, **Appendix V**. are also similar to those reported for the monomer emission of anthracene of ca. 5.7 ns.[12] This suggests that the vibronic emission from the carborane isomers originates from the anthracene moiety, with virtually no contribution from the cage, except some small electron withdrawing effects. Evidence supporting this hypothesis is provided by TD-DFT excitation and emission calculations, **Figure 3-5**.

3.2.2 – DFT/TD-DFT Calculated Emission Cycles

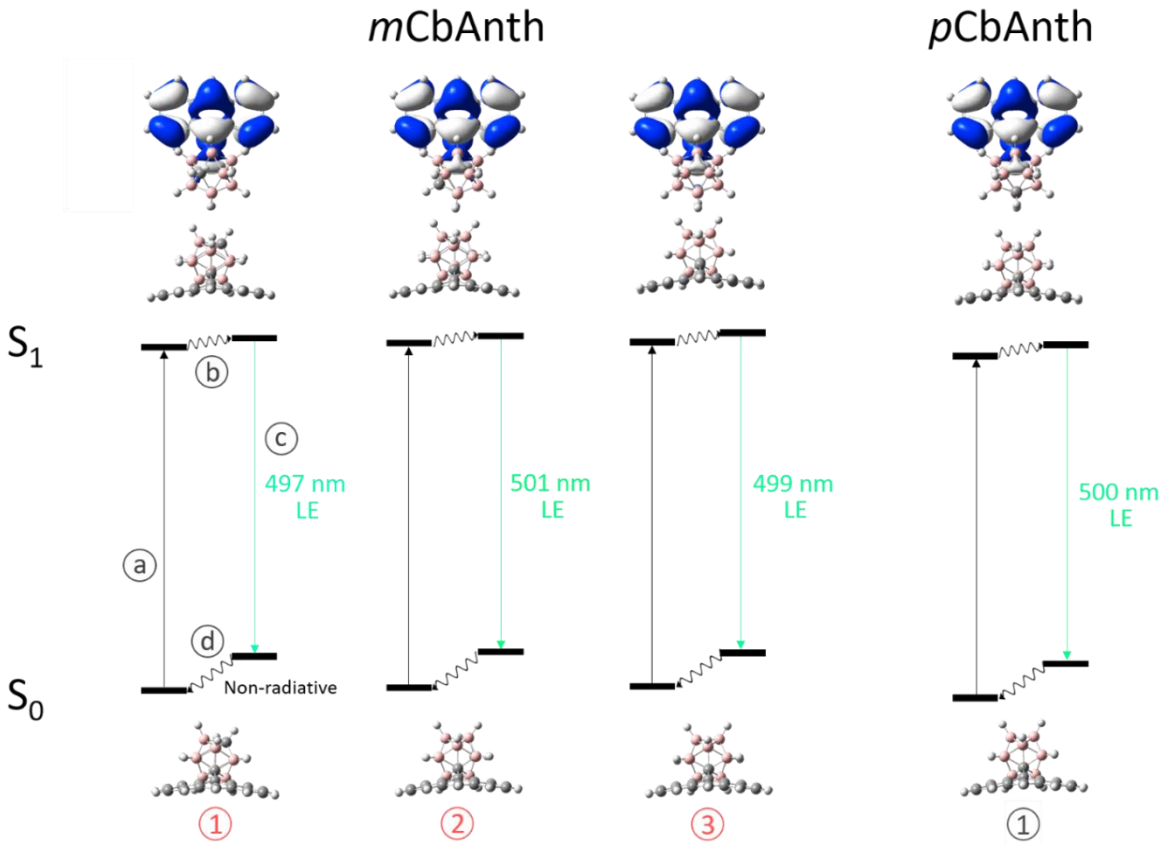


Figure 3-5 – DFT and TD-DFT (B3LYP/6-31G(d,p)//B3LYP/6-31G(d,p); solvent = THF) calculated emission cycle, with solvent relaxation, starting with each energy minima ground state geometry of ***m*CbAnth** and ***p*CbAnth**, as defined in **Figure 2-6**. Cycle steps are labels are (a) vertical excitation and optimisation, (b) solvent equilibration around the excited state geometry, (c) fluorescence, and (d) solvent equilibration around the ground state geometry. Emissive energies are labelled with wavelength, and the corresponding emission colours. Geometries of the optimised ground and excited states are presented, with the molecular orbitals for the S_1 excited state.

All energy minima ground states, as calculated in **Chapter 2**, were used as starting geometries in the absorption/emission cycles. The first step in the TD-DFT emissive cycle, using a THF, PCM solvent reaction field, was (a) a vertical excitation followed by relaxation (optimisation) of the excited state molecule. A frequency calculation was then performed to confirm that this was an energy minimum

geometry in the S_1 excited state. Step (b) allows for relaxation of the solvent force field around the new molecular geometry,[†] and example of this is presented in **Figure 3-6**.

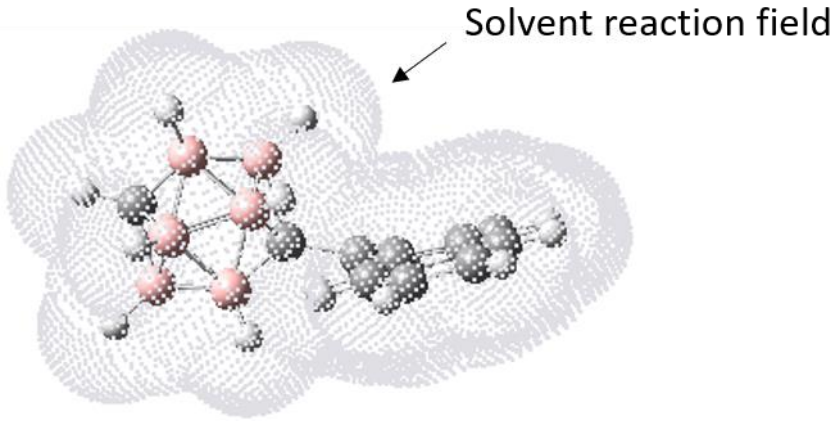


Figure 3-6 – DFT calculated (B3LYP/6-31G(d,p)) polarisation continuum model (PCM) solvent reaction field around the carborane molecule.

Step (c) relaxed the excited state molecule to the ground state but with non-equilibrium solvent, as fluorescence occurs on a timescale much faster than the rearrangement of solvent dipoles. Step (d) described the solvent rearrangement process, as the whole system decays back to the ground state and completing the cycle.

The emissive energies for ***m*CbAnth** and ***p*CbAnth** are remarkably similar, at ca. λ_{em} = 500 nm. In addition, the S_1 HOMO molecular orbitals are localised almost solely on the anthracene moiety, with only a slight contribution from the carborane. Such an emissive species is exactly what was hypothesised due to the vibronic nature of the high energy emission. Therefore, this emissive band can be confidently assigned to a LE from the anthracene.

For ***o*CbAnth** the situation is more complex, **Figure 3-7**.

[†] One would expect that solvent equilibration should reduce the energy of the excited state, and not increase it, as the solute and solvent dipole moments realign after excitation. The reason for the small energy increase in this case so far defies explanation but can be practically regarded as a quirk in the TD-DFT calculation. Importantly however, the same phenomenon occurs in all cases, so these calculations can still be regarded as a reasonable guide to emission energies as a function of carborane isomer and geometry.

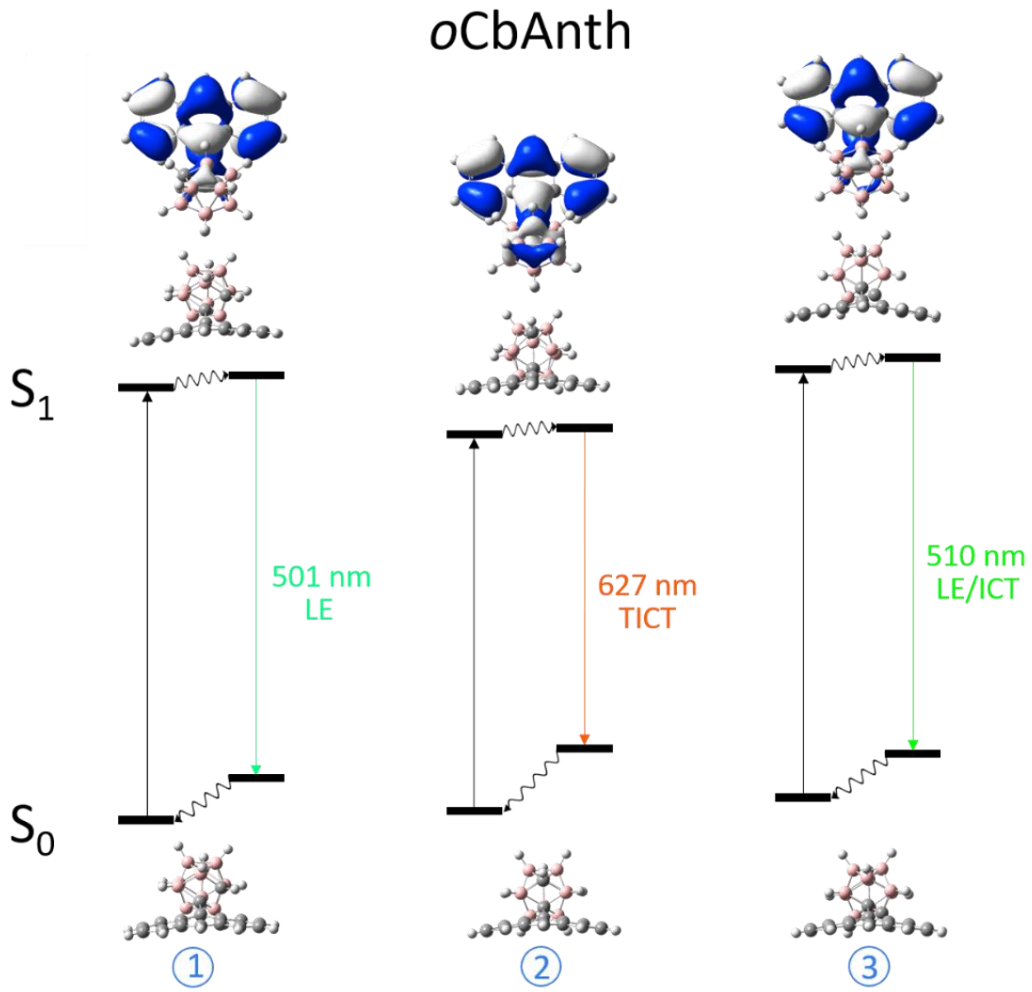


Figure 3-7 – DFT and TD-DFT (B3LYP/6-31G(d,p)//B3LYP/6-31G(d,p); solvent = THF) calculated emission cycle, with solvent relaxation, starting with each energy minima ground state geometry of ***o*CbAnth** as defined in **Figure 2-6**. Molecular orbitals of the S_1 excited state are displayed.

For the global ground state geometry, (1), the emission energy is identical to the LE of ***m*CbAnth** and ***p*CbAnth** isomers. The emissive energy is lower for ground state geometry (3), where there is a slightly larger contribution from the carborane. This is notable, as this emissive species is likely to be different from that which forms the LE; the C-C bond length is slightly larger for this state than the LE state (1.724 > 1.670 Å), suggesting it could be an ICT species. The full width half maximum (FWHM) of the LE of ***o*CbAnth** (**Figure 3-3**) is 5 nm larger than that of the *meta* and *para* isomers, suggesting that a second emissive state, such as an ICT state, may also be present in this region, but obscured by the dominant emissive peaks. This will be explored in detail later. Ground state geometry (2), with the C-C bond perpendicular to the aromatic plane, exhibits a significantly red-shifted emission, of λ_{em} = 627 nm, matching very well with the low energy emission in the PL spectrum. In the excited state, the C-C bond is significantly elongated relative to the ground state, and the molecular orbitals are delocalised around the cage. Based on this data one can confidently assign this peak to a TICT state.

The difference in the photoluminescence quantum yield between the isomers is stark. The quantum yield of anthracene is 0.23 (in cyclohexane), but the value is much higher when either *meta* or *para*-carboranes are attached. Fluorescence quenching for anthracene is mainly due to excimer formation,[13] therefore it seems likely that the bulky carborane reduces the likelihood of excimer formation in solution, thereby reducing non-radiative decay routes and boosting emission. The same is likely to be true for ***o*CbAnth**, however there the quantum yield is ca. x1000 times lower, so another non-radiative decay process must be at work. As discussed in **Chapter 1**, the highly elastic C-C bond can vibrate to dissipate energy, especially in TICT states.[1] For ***o*CbAnth** the TICT state is the lowest energy S_1 excited state species (**Figure 3-7**), therefore it seems likely that, through rotation of the carborane, most excited states will decay through this species, and the vast majority will decay non-radiatively through C-C bond vibration.

3.2.3 – PLE

One simple test of the theory can be obtained through photoluminescence excitation spectroscopy (PLE), which is an optical study complementary to PL. Whilst in PL the emissive wavelength is scanned as a function of excitation wavelength, in PLE the opposite is the case. The PLE of the three isomers of anthracenyl carborane are presented in **Figure 3-8**.

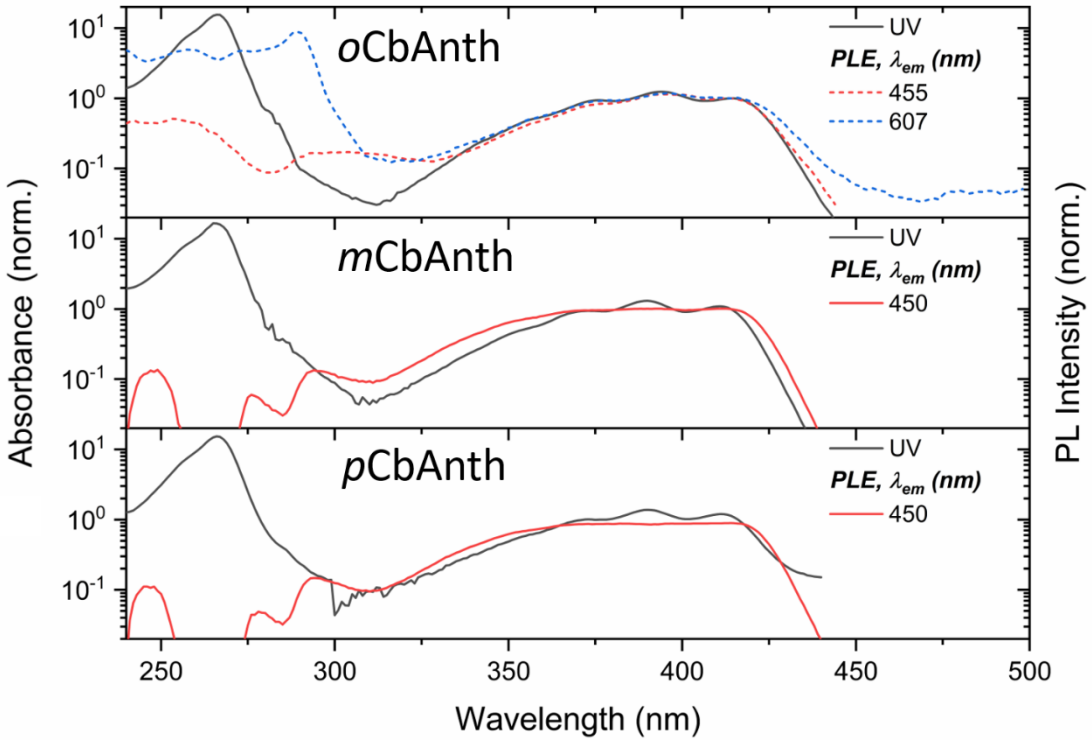


Figure 3-8 – UV-Vis, and PLE of emissive species for the three isomers of anthracenyl carborane.

For all emissive species the PLE faithfully follows the UV-Vis absorbance at the band edge. This suggests that the same excited states which decay radiatively to form the LE, can also decay via the TICT state, i.e. excited states localised on the anthracene unit can relax into the TICT state, and then decay radiatively or non-radiatively from this state. The PLE of the λ_{em} = 450 nm emission for ***m*CbAnth** and ***p*CbAnth** are indistinguishable, however the PLE for the same emission of ***o*CbAnth** is dissimilar in the high energy region. This gives some support to the argument that there may be two emissive species in this region of the PL spectrum (if it was just LE then the PLE should look the same as for the other isomers).

3.2.4 – Solvatochromic Studies

To investigate this further a solvatochromic PL study was undertaken, as presented in **Figure 3-9**.

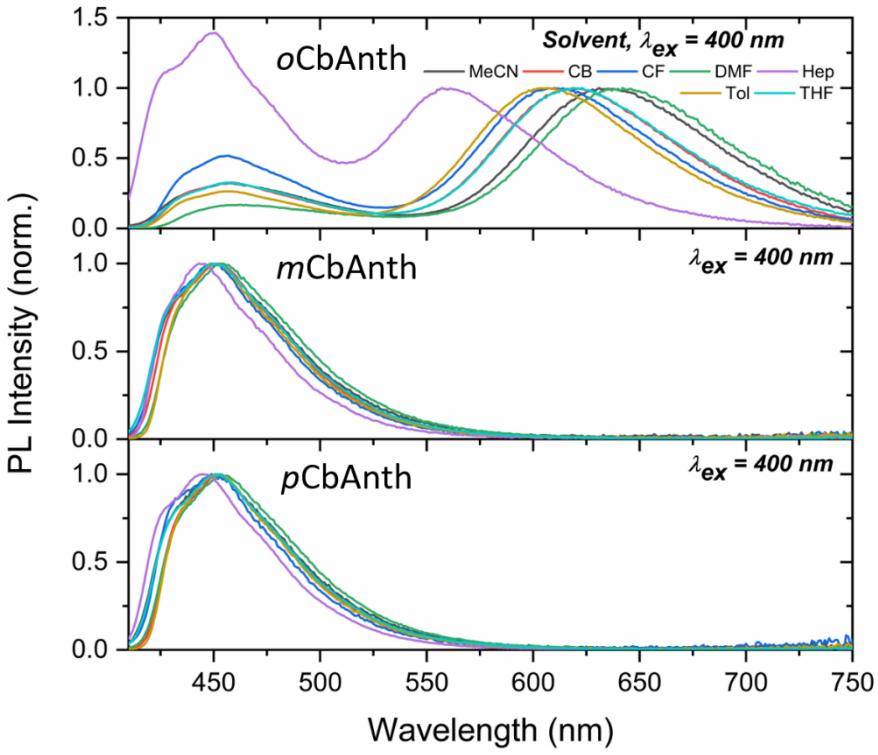


Figure 3-9 – Solvatochromic plots of anthracenyl *ortho*, *meta* and *para*-carboranes. Concentration = ca. 1 x 10^{-5} M. Non-normalised PL and PLE plots are presented in Appendix V.

The solvatochromic study demonstrates that there is virtually no change in the emission λ_{max} for ***m*CbAnth** and ***p*CbAnth**, and for the LE of ***o*CbAnth**. The band edge of the PLE, **Appendix V**, is also unchanged. The long wavelength emission for ***o*CbAnth** shows a significant change in λ_{max} as a function of solvent polarity, with a drastic blue-shift of the delocalised emission for the heptane solution. In addition, heptane is the only solvent in which the LE is larger than the long wavelength emission, and

the emission is also by far the most intense. This disparity, relative to the other solvents, suggests that the long wavelength emission for heptane may not result from the TICT species. This hypothesis was examined with the aid of a Lippert-Mataga plot, **Figure 3-10**.[14,15]

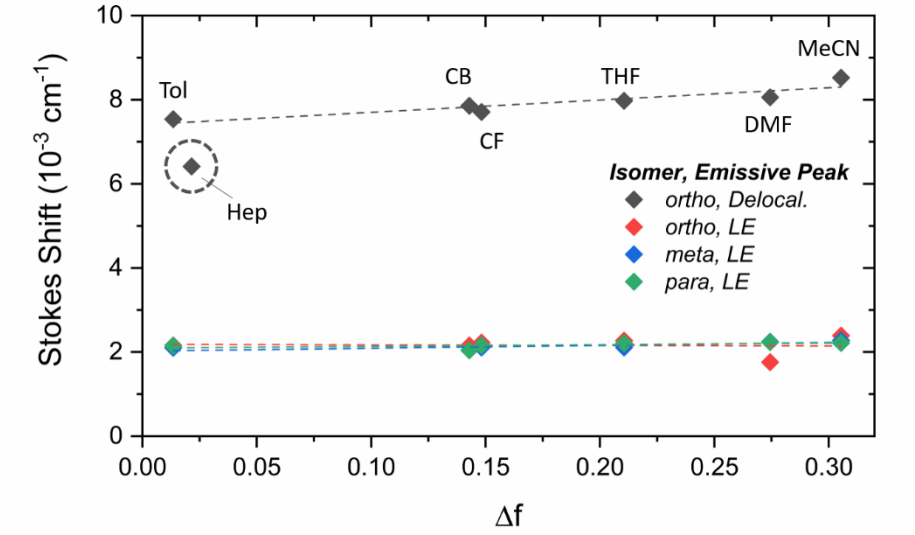


Figure 3-10 – Lippert-Mataga plots of the three isomers of anthracenyl carboranes.

Lippert-Mataga plots describe how the Stokes shift changes as a function of solvent properties. For excited states in which there is no (or very small) dipole moment change upon excitation, as in the case of locally excited species, the surrounding solvent shell remains unperturbed during the process. For charge transfer species there is a large dipole moment change upon excitation, so the solvent molecules will rearrange themselves to lower the energy of the chromophore-solvent system. Therefore, to a first approximation, locally excited species have a Stokes shift that is independent of solvent, whereas the Stokes shift of delocalised species will increase linearly with Δf. Δf is a solvent parameter based on, ε, the dielectric constant, and n, the refractive index. The Δf equation and relevant solvent parameters are presented in **Appendix VI**.

Figure 3-10 demonstrates that the LE of all three isomers is independent of solvent properties, as expected. It also shows that there is a positive linear correlation between the Stokes shift and Δf for the delocalised emission of ***o*CbAnth** in all solvents *except* heptane. This suggests that the delocalised emission observed for heptane is not as a result of the TICT species, as in the case of all other solvents. This matches the observation that the emission intensity is so much larger in for heptane solutions than all other solvents, as the TICT state is not formed, so non-radiative decay routes associated with the elongated C-C bond are quenched. We posit that the TICT state is highly unfavourable in heptane since this is the least polarisable of all the solvents studied, such that highly delocalised charge transfer states are unfavourable.

The delocalised emission in of ***o*CbAnth** in heptane likely occurs from one of two emissive species; an ICT state, or an excimer. As demonstrated previously, DFT calculations hint that an ICT state, with the carboranyl C-C bond approximately parallel to the aromatic plane, is a possible emissive species for this compound. These calculations are unimolecular, so by definition can give no indication of whether excimer states are possible.

3.2.5 – Concentration-Dependent PL

Excimers are concentration dependent, so a PL study spanning a large concentration range should show some indication of whether there are any bimolecular emissive species. Such a study is presented in **Figure 3-11**.

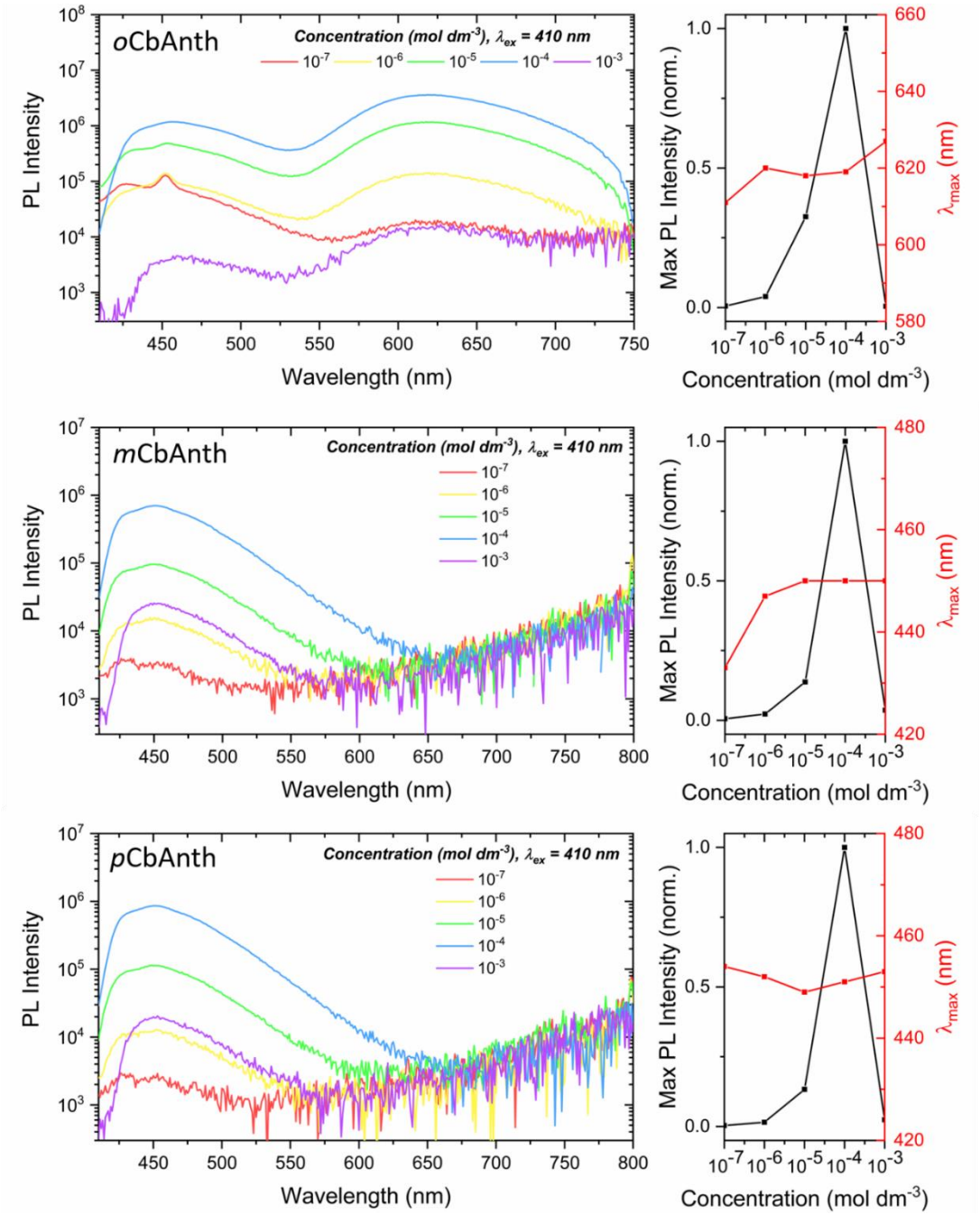


Figure 3-11 – Concentration dependent PL of the three isomers of anthracenyl carboranes in THF solution. The max PL intensity for ***o*CbAnth** relates to the TICT emission only.

There are comparisons to be drawn between the isomers from the concentration dependent PL study. First, the PL intensity increases linearly with concentration for the all isomers between a concentration of 10^{-7} and 10^{-4} M, but there is a drastic decrease for 10^{-3} M. There are several possible reasons for this phenomenon. It may be that aggregation begins to occur at concentrations >10^{-4} M, and PL emission intensity is diminished due to ACQ. Whilst this makes sense for the ***m*CbAnth** *and* ***p*CbAnth**, *ortho*-carboranyl TICT species are well known to aid AIE. One would therefore expect a PL intensity *increase*

for ***o*CbAnth** if aggregation was occurring. However, the PLE of the 10^{-3} M solution (**Appendix V**) is quite different to the other concentrations, for both the LE and TICT emissions. This is suggestive of a change in the environment of the molecules in solution, such as geometry changes or the formation excimers, exciplexes or aggregates.

It is also possible that the solutions are so concentrated at 10^{-3} M that most of the incident excitation beam is absorbed at a very small distance from entering the samples. Fluorescence then occurs in all directions, but the mask around the cuvette blocks most of the light emitted in this region from reaching the detector. This is a known problem for optical studies, and specialised cuvettes with short cavity pathlengths are on the market for precisely this reason. However, such cuvettes are expensive and were not used in this study. The fact that the PL properties of ***o*CbAnth** are so different to ***m*CbAnth** and ***p*CbAnth** isomers, yet the pattern of PL intensity as a function of concentration is almost identical for all of them, suggests that the dominant effect is not due to aggregation, but due to the experimental error associated with the cuvettes. Based on the PLE however, aggregation effects cannot be completely discounted.

The PLE of the concentration-dependent study also shows peaks at ca. λ_{ex} = 550 nm, which is an energy lower than that of the absorption onset. Similar, non-zero values are observed at ca. λ_{ex} = 500 nm in the solvatochromic study, and indeed in all *ortho*-carborane compounds discussed in this chapter. In some cases, it can be observed in the H_2O/THF (v/v) proportion studies too, especially in high H_2O solvent systems. This is a highly interesting phenomenon as it suggests that excited states can be formed without a $\pi \rightarrow \pi^*$ excitation. The unusual behaviour will be further explored in **Chapter 4**.

There is no substantial change in the λ_{max} of the emission of the isomers across all concentrations. This suggests that there are no concentration dependent emissive species for any of the isomers, at least over the concentration series studied. This is an important conclusion as it demonstrates that the delocalised emission for ***o*CbAnth** seen in heptane solution is not an excimer emission.

3.2.6 – Temperature-Dependent PL

It was then theorised that, if the delocalised emission for ***o*CbAnth** in heptane is an ICT species, there may be a temperature dependence for this emission. At low temperatures, the carborane rotates more slowly, as proved by the NMR study in **Figure 2-10**. Therefore, if rotation can be suitably slowed, emission may be more likely to occur from the (1) and (3) S_1 ground state geometries, as they cannot easily rotate into the TICT state and decay from there. In addition, reducing the thermal energy helps to eliminate vibrational non-radiative decay pathways, so it was suspected that at low temperature

the emission of all isomers would increase. As such, a temperature dependent PL was study was carried out on the three anthracenyl carborane isomers, **Figure 3-12**.

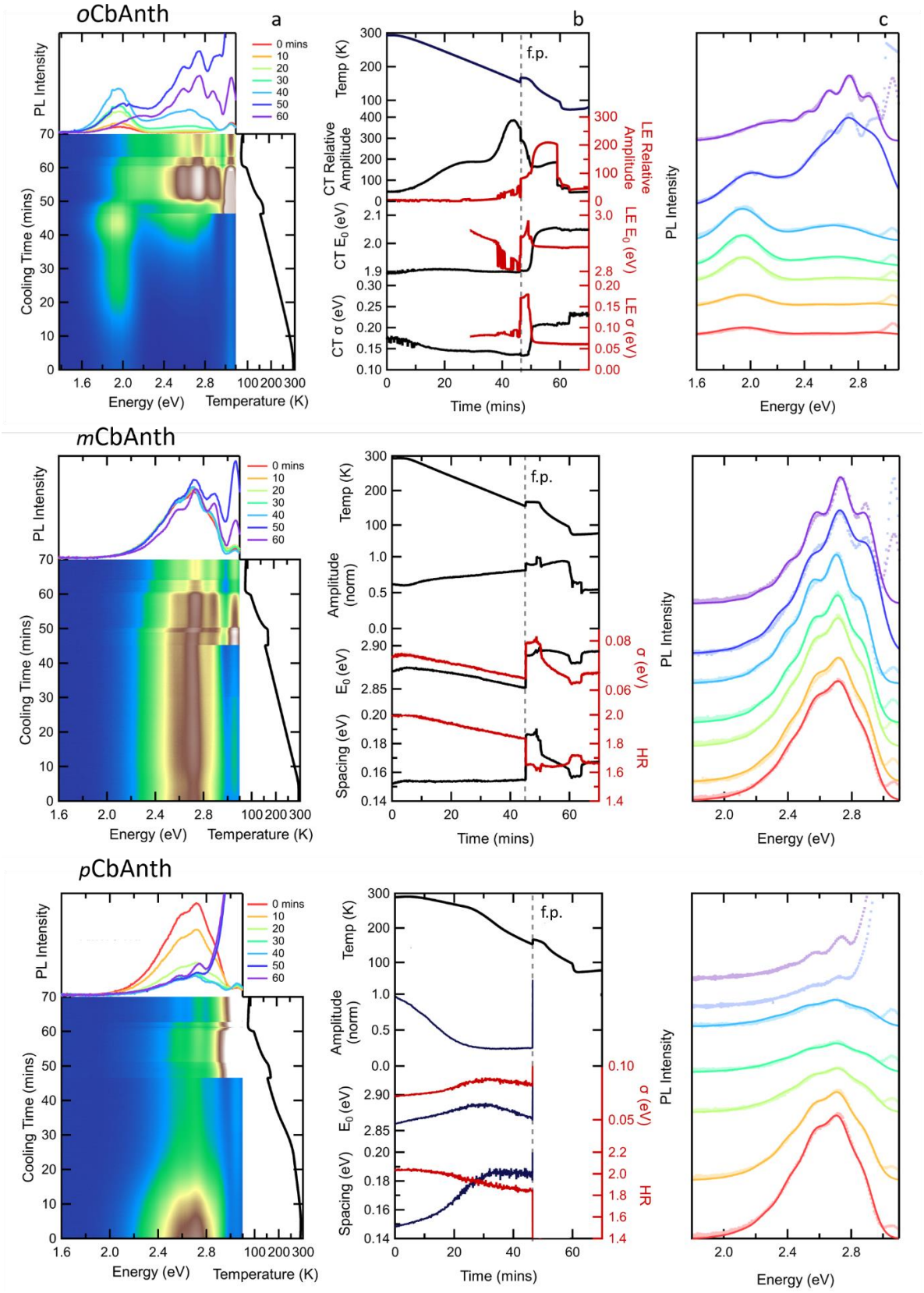


Figure 3-12 – (a) Temperature dependent PL for the three isomers of anthracenyl carboranes in THF solution (concentration = ca. 1 x 10^{-5} M), excitation energy = 3.1 eV (λ_{ex} = 400 nm). (b) Selected quantitative parameters extracted from the fitted dataset. Examples of the fitting are presented in (c). For more straightforward extraction of trends in emission, PL intensities are plotted as a function of energy. Data collection, fitting and presentation by Dr Matthew Dyson.

Of the three compounds studied, ***m*CbAnth** has perhaps the simplest temperature dependent PL. Upon cooling to the freezing point of the THF solvent (165 K), the amplitude of the vibronic emission slowly increases, which is consistent with a decrease in molecular vibration, and consequently the quenching of non-radiative decay routes. The Huang-Rhys (HR) parameter, which is proportional to the square of the equilibrium position offset, ΔQ_e (see **Figure 1-15**), also decreases in this temperature range, demonstrating that difference between the equilibrium geometries of the ground and excited states decreases upon cooling. The E_0 emissive energy maximum (energy equivalent of λ_{max}), and peak width (σ) also decrease with temperature; these, and the HR parameter, are all strongly related. The relationship between them is complex and beyond the scope of this study, however, their trends with temperature for ***m*CbAnth** are quite typical.[16] Below the freezing point of the solvent the situation changes significantly.[‡] There are stark differences in all the E_0, peak width and HR parameters upon freezing, which suggests there is a large geometric change. PL intensity slowly increases until ca. 100 K, where there is another phase transition in the solvent and emission intensity quickly drops off, before plateauing at a low intensity.

The data for just ***m*CbAnth** demonstrates some clearly complex phenomena, and there are some important observations to be garnered from the data. The main trend is that freezing of the solvent leads to geometric changes in the molecules. Moreover, similar geometric changes for the second phase transition of the solvent suggests that the formation of large aggregates is unlikely for this compound; if aggregates had formed it would be unlikely that changes in the surrounding solvent would have much of an effect on the geometry of the individual molecules inside the aggregates.

At time = 0 and just beyond, ***p*CbAnth** behaves virtually identically to ***m*CbAnth**, but upon cooling the PL intensity quickly decreases. This is precisely opposite to the *meta* isomer, and not easily interpreted. As explained above, due to a reduction in molecular vibration, most fluorophores will increase their emissive intensity as temperature is reduced. One theory as to why this is not the case for ***p*CbAnth** is that, upon cooling, the slower molecular movement allows for the formation of excimers, which can non-radiatively decay through π-π stacking interactions. The σ subtly increases as the PL intensity decreases, which could be an indication of a second emissive species in this region, such as an excimer state with a low quantum yield.

[‡] For all isomers, scattering of the excitation beam can be observed at high energies after the freezing of the solvent. Whilst efforts have been made (through fitting) to remove this, a degree of the artefact remains and somewhat distorts the quantitative parameter tracking. For ***p*CbAnth,** the emission below the freezing point of THF is so low the that no useful parameter tracking data can be presented.

Given that the *meta* and *para* isomers have almost indistinguishable behaviours, in all UV, PL and PLE data presented up to this point, it is highly intriguing that there should be such a difference. Assuming no experimental error, the difference could be ascribed to more planar conformation of the less sterically hindered *para* isomer. One could reasonably assume a flatter aromatic moiety would increase the likelihood of π-π stacked excimers. However, the data is far from conclusive.

The ***o*CbAnth** isomer has certainly the most dynamic changes in PL intensity as a function of temperature. Upon cooling, the LE starts at a low emissive intensity which is relatively unchanged until just above the freezing point. In the same temperature range, the TICT emission intensity increases, accompanied by a reduction in the σ. We ascribe this pattern of PL intensity as the normal suppression of non-radiative decay routes as molecular vibrations are suppressed at low temperature. As demonstrated in **Figure 3-7**, the TICT emission is the lowest energy excited state, and most of the excited states decay via this route, including locally excited states that would, in the case of ***m*CbAnth** or ***p*CbAnth,** likely decay radiatively via a LE. For this reason, the TICT state increases whilst the LE state appears temperature independent. Just before the freezing point of THF both the LE and the TICT emission increase sharply. This could be due to an increase in viscosity of the solvent as it approaches the freezing point, further reducing molecular vibration, and reducing non-radiative decay routes.

As in the cases of the other isomers, upon freezing the situation changes drastically. The LE intensity increases whilst the TICT emission decreases and, remarkably, there is a distinct blue-shift in the TICT emission. This we ascribe to a change from TICT emission, to the ICT emission as calculated in **Figure 3-7**, and seen in the heptane emission in **Figure 3-9**. The ICT state is less energetically favourable than the TICT state, therefore locally excited species are less likely to decay into this species, causing the rapid increase in LE intensity. Also, the geometry change associated with formation of the ICT state is less than that of the TICT state, which undergoes significant C-C bond elongation. It is therefore likely that ICT states can form back into LE states. This is somewhat supported by the slow increase in ICT emission upon further cooling, accompanied by a decrease in the rate of increase in the LE emission; low temperatures make ICT to LE species transition less likely, so a relatively larger proportion of excited states decay via the ICT state.

A second phase transition of the solvent occurs at 100 K, which is accompanied, as for ***m*CbAnth**, with a reduction in PL intensity, but with no real change in the other quantitative parameters. It is therefore possible that there is no significant change in the microstructure and photophysics of the carboranes

around this point, but perhaps more scattering of the excitation beam and detection signal, both contributing to a reduction in the observed PL intensity.

The question of why the TICT state is no longer favoured upon solvent freezing is an interesting one. We propose two reason for this phenomenon. First, it is likely that the solid microstructure around the carborane molecule strongly mechanically inhibits elongation of the C-C bond. Some support for this idea can be gained from closer inspection of the PL around 165 K. Freezing does not occur instantaneously, and solute molecules will tend to concentrate in isolated regions as the environment around them solidifies.[17] Or from the solvent perspective, areas with large concentrations of solute will solidify more slowly due to a local freezing point depression. Therefore, just below 165 K, there is a mixture of solute molecules mechanically locked in a frozen solvent matrix (where ICT emission and LE are promoted), and some which are still in solution (where TICT emission is promoted). The latter regions slowly solidify too, leading to the slow change of the E_0 from the TICT to ICT. A second possible reason for this phenomenon is that, upon freezing, the potential energy wells around each the ground state geometries are deeper, and indeed deepest around the global ground state geometry, where C-C bond is approximately parallel to the plane of the anthracene moiety. This will reduce carborane rotation and increase the proportion of ground state molecules in the global ground state geometry. Upon excitation rotation is similarly restricted, so these excited states will decay either via LE or ICT, but not TICT species. Note that, if the C-C bond is perpendicular to the aromatic plane in the global ground state, then TICT emission intensity would increase upon cooling, following this argument. One problem with this description is that the calculated ICT comes not from the global ground state geometry (1), which exhibits LE, but the (3) geometry as in **Figure 2-6**. However, this structure also has the C-C bond approximately parallel to the aromatic plane, and ICT states are well known to form from these states. It is therefore likely that ICT emission occurs from both geometries (1) and (3), and the ICT emission observed below the freezing point of the solvent occurs from the global ground state geometry.

To examine which of these arguments is most plausible, a second low temperature study was undertaken, but this time in chloroform, and at the precise concentration used in the NMR study of **Figure 2-8**. In the temperature range of 293 K – 213 K (which is above the freezing point of chloroform; 210 K) there is a clear indication of restricted rotation for these solutions, so if there is a rotational dependence on PL intensity, i.e. the second argument, such a study should demonstrate this. The data is presented in **Figure 3-13**.

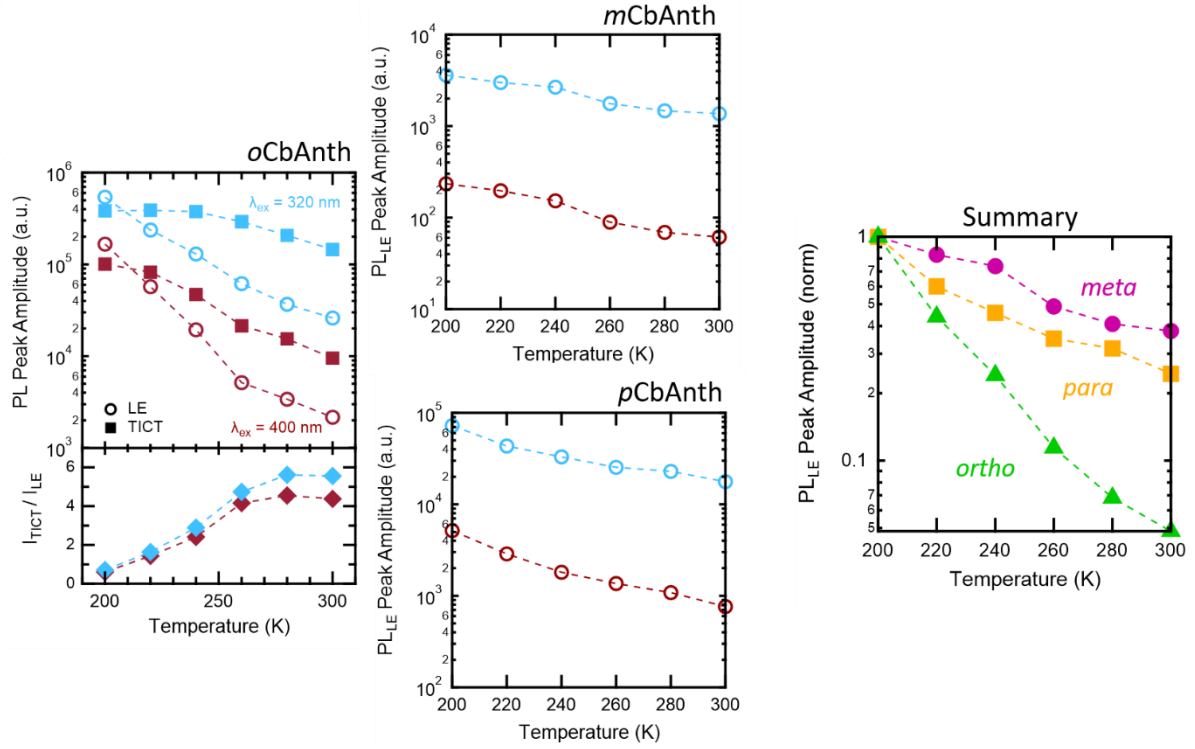


Figure 3-13 – Temperature dependent PL, cooling from 300-200 K, for the three isomers of anthracenyl carboranes in chloroform solution (concentration = 3 x 10^{-3} M). Raw PL spectra are presented in Appendix V. Data collection, fitting, and presentation by Dr Matthew Dyson.

The ***m*CbAnth** and ***p*CbAnth** isomers have a virtually identical temperature dependent PL; reducing temperature increases the emission. There is no obvious effect of aromatic deformation on PL, and interestingly ***p*CbAnth** does not decrease in PL intensity upon cooling, as observed in the THF study. This is curious as that phenomenon was tentatively explained through the formation of excimers which quench emission, but in this study the concentration is ca. x100 larger. One would expect excimer formation to be more likely as concentration is increased. Both THF and chloroform are good solvents for these compounds (both have Hildebrand parameters of approximately 9 $cal^{1/2}$ $cm^{-3/2}$),[18] but THF has a larger dielectric constant and so is more polarisable. It could therefore be the case that excimers of ***p*CbAnth** are able to form in THF and not chloroform, however more studies would be required to confirm this hypothesis.

Like the other isomers, the overall emission intensity of the ***o*CbAnth** increases upon cooling. Both the LE and TICT emission increase through the temperature range studied, but the latter at a slower rate. Whilst at room temperature the TICT emission dominates, at 200 K the two become approximately equal. This is a demonstration of restricted rotation affecting the PL profile; as the temperature is reduced and carborane rotation slows, a larger proportion of molecules sit in the deepest potential energy well, around the ground state geometry. This geometry has the C-C bond approximately

parallel to the plane of anthracene, where TICT is not possible, thus the proportion of TICT emissive states decreases as temperature decreases. As can be observed from the spectra in **Appendix V**, no ICT is clearly discernible. It is likely that such an emission is present but cannot be seen above the larger LE and TICT peaks.

Based on the two temperature dependent studies it appears that the PL of both ***m*CbAnth** and ***p*CbAnth** isomers are independent of carborane rotation. This is rational as the carborane, as demonstrated in **Figure 3-5**, exhibits essential no orbital contribution to the S_1 excited state. The PL of ***o*CbAnth** is affected by rotation, where restricting rotation reduces the number of excited states that decay through the TICT state and increase those which decay from LE or ICT. The effect is exacerbated when the solvent is frozen, where the environment around the carborane is restricted, increasing the potential energy barrier to rotation. Whilst it was proposed that C-C bond elongation may be restricted by the freezing of the solvent, there is no direct evidence for this, and the dynamics of PL are explained perfectly well without this assumption.

3.3 – Aggregation-Induced Emission

Following the various calculations and solvent, concentration and temperature dependent PL studies, the nature of the various emissive species for the anthracenyl carboranes is well understood. So far, aggregated states have been not been studied. The easiest method of inducing aggregation in solution is using a combination of THF (a good solvent) and H_2O (a bad solvent). First, solutions are made up in small volumes of THF, and large amounts of water are added in one portion. This instantaneously changes to solvent environment from good to bad and induces the formation of carborane aggregates. A study of PL intensity as a function of H_2O content in varying H_2O/THF (v/v) solvent proportions is presented in **Figure 3-14**.

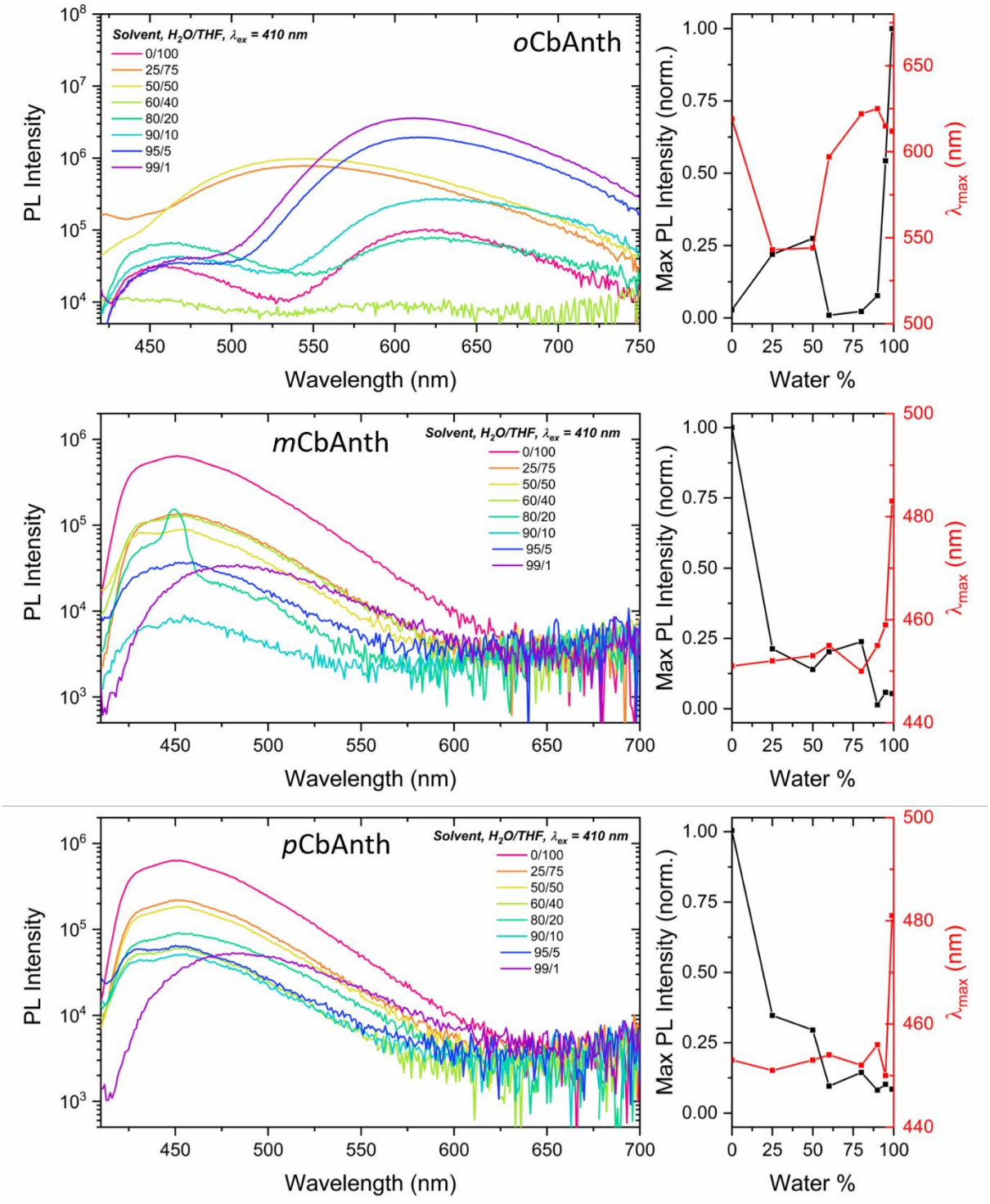


Figure 3-14 – H_2O/THF (v/v) solvent proportion dependent PL of the three isomers of anthracenyl carboranes in THF solution. Concentration = 1 x 10^{-5} M. λ_{ex} = 400 nm. The Max PL Intensity for ***o*CbAnth** relates to delocalised emission peak. Corresponding PLE is presented in Appendix V.

The ***o*CbAnth** isomer in THF solution exhibits both LE and TICT emission, and as H_2O proportions are increased up to H_2O/THF (v/v) 50/50 the PL intensity increases. This is accompanied by a blue-shift in the delocalised peak emission, which signifies the promotion of the ICT emission. Interestingly, this

ICT emission overlaps perfectly with that seen in THF at low temperature, **Appendix V**. Increasing H_2O proportions to 60/40 reduces the PL intensity to almost zero, but with a red-shift in the delocalised emission as the emissive species changes back to TICT. Further addition of H_2O beyond this increases the PL intensity with almost a power-law dependence, and the delocalised emission λ_{max} stays relatively constant. An increase in quantum yield generally coincides with longer excited state lifetimes; they can stay in the excited state before decaying as a result of fewer non-radiative decay pathways. Such an increase is observed when comparing the lifetimes of the TICT emission in THF and 99/1 H_2O/THF (v/v) solutions, (**Appendix V**). It should be noted however that whilst the fluorescent quantum yield increases, the extinction coefficient decreases (**Appendix V**). The photoluminescence intensity is a function of this, and so whilst the number of excited states decaying radiatively is larger in aggregated state of ***o*CbAnth**, the number of molecules in the excited states is lower.

From this study it is clear there are distinct phenomena occurring; (1) proportions of H_2O up to 50/50 favours ICT and increases emission intensity, and (2) beyond 50/50 the emission intensity drops to zero, before the TICT emission rises rapidly. The first phenomenon is likely to be a solvent effect, where all carborane molecules are still in solution, and the emission is affected by the changing solvent environment. H_2O is approximately twice as viscous as THF,[19] so carborane rotation is probably slowed somewhat and the ground state potential energy wells are deeper. This increases the likelihood of ICT emission, whilst simultaneously reducing TICT emission. The second phenomenon can be explained by first solvent effects and then aggregation. At the 60/40 solvent proportion, the THF concentration is low enough that fluorescence quenching by water begins to occur. It has been suggested that H_2O can aid the transition of a charge transfer species from a singlet to triplet state, and consequently a quenching of radiative singlet relaxation.[20] As the H_2O proportion is increased from this point, aggregates begin to form in increasing number.[§] The structure of these aggregates, explored later in this chapter, blocks the quenching affects of water from all but the surface carborane molecules, and so emission intensity beings to increase again. The aggregates also reduce the degrees of freedom for the fluorophores, thereby reducing non-radiative decay routes, and increasing TICT emission, boosting the quantum yield in a process known as AIE.

The ***m*CbAnth** and ***p*CbAnth** isomers are also interesting. Increasing H_2O content leads to a steady decline in emission intensity, probably as a result of the same fluorescence quenching H_2O argument above. But for very high H_2O proportions the PL red-shifts. The resulting emissive profile is devoid of the LE vibronic character, appearing broad and featureless. This peak is assigned to an excimer state

[§] These are generally large enough to make the solutions cloudy, and precipitation occurs in samples left for approximately one week. It is therefore important to use freshly prepared samples in the optical studies.

formed in the aggregated states of ***m*CbAnth** and ***p*CbAnth**. An almost identical excimer emission has been observed for solid-state anthracene at low temperature (77 K),[21] and room temperature after high pressure compression.[22] The time resolved data of the excimers, **Appendix V**, are, at least, consistent with reported anthracene excimers, however it must be noted that such species have a hugely variable lifetimes, from sub ns to > 100 ns.[23,24] There are several reported anthracenyl excimers depending on the relative geometry of the ring systems; the λ_{max} of this excimer is consistent with partially overlapping, approximately parallel, π-systems.[25] This precise geometry is present in the single-crystal XRD (see **Figure 2-4**), suggesting that the aggregates are highly ordered, and potentially even crystalline. This is explored later in the chapter. Excimer emission of anthracene in ambient conditions is rare, and it is intriguing that carboranes can induce such a property.[25]

The PLE of the H_2O/THF proportion studies of ***o*CbAnth** shows a change in the position of the absorption band edge as the proportion of H_2O increases. First a blue-shift is observed, followed by a scrambling of the vibronic fine structure and red-shift at up to 99/1. The first change is ascribed to a solvatochromic effect; note it does not appear for the PLE of the LE of the ***m*CbAnth** and ***p*CbAnth** isomers. The scrambling of the vibronic fine structure coincides with aggregate formation, suggesting it is caused by the presence of both solvated and aggregated molecules, each with their own subtly different absorption profiles according to their subtly different geometries. A further increase in H_2O content increases the proportion of carborane molecules in aggregates, forming a new fine structure with a slightly red-shifted absorbance.

The formation of aggregates is clearly a concentration dependent, it therefore seemed pertinent to understand this process. A study of concentration dependence on the PL intensity of ***o*CbAnth** in a H_2O/THF (v/v) 99/1 solution is presented in **Figure 3-15**.

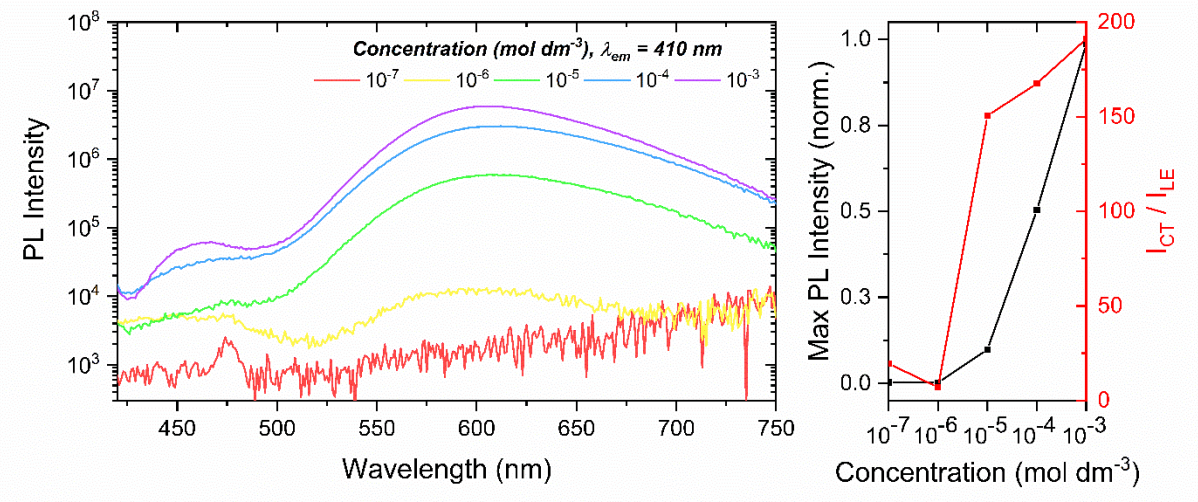


Figure 3-15 – Concentration dependent PL study of ***o*CbAnth** in H_2O/THF (v/v) 99/1 solvent. λ_{ex} = 410 nm

At very low concentrations (10^{-7} M) the emission is not discernible from the baseline. In THF solutions at this concentration, emission is observable (see **Figure 3-11**). This suggests that in the 99/1 solution the carboranes are not aggregated, but still in solution and excited states are quenched by H_2O. At 10^{-6} M, the LE and TICT emissions intensities are relatively equal, however the LE appears to tail off at higher wavelengths than the other concentrations. This is possibly due to the presence of ICT emission. At this concentration the carboranes are still in solution, however their numbers are such that, whilst most excited states are quenched by the action of H_2O, enough decay radiatively so that the signal can be observed. This is akin to the 60/40 emission for ***o*CbAnth** in **Figure 3-14**. At concentrations above 10^{-6} M, the TICT emission dominates, and the PL intensity increases linearly with concentration. This change signifies the formation of aggregates. The TICT emission intensity subtly increases relative to LE in this range. It is likely that at 10^{-5} M some molecules remain in solution as aggregation occurs, but in more concentrated samples the relative amount of solvated carboranes decreases relative to those in aggregates.

3.4 – Solution, Aggregated and Solid-State Emission

To better understand AIE and the excimer emission of the aggregates of ***m*CbAnth** *and* ***p*CbAnth** isomers, it was necessary to investigate the solid-state (polycrystalline) PL. The solid-state *is* an aggregated state, and the exact microstructure of this state is known from the crystal structure. The PL from THF, 99/1 H_2O/THF (v/v) solutions and the solid-state are presented in **Figure 3-16**.

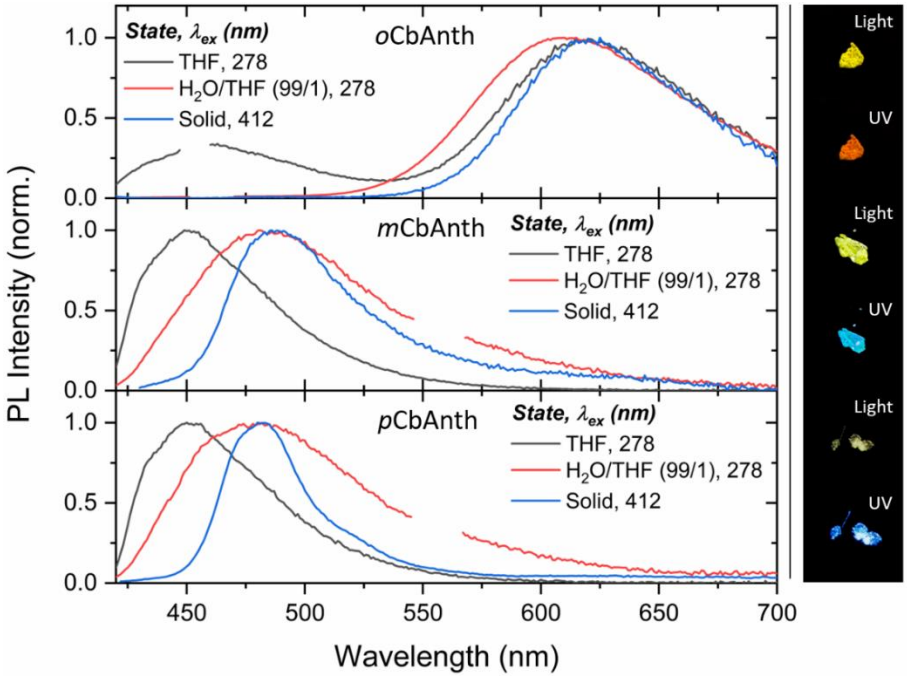


Figure 3-16 – PL of THF (concentration ca. 1 x 10^{-4} M) and H_2O/THF (v/v) 99/1 (concentration ca. 1 x 10^{-4} M) solutions, and the solid-state of the three isomers of anthracenyl carborane, with pictures of the solids states under white and UV light presented.

For each isomer, both aggregated states resemble one another. For the ***m*CbAnth** and ***p*CbAnth** isomers the aggregated states exhibit solely excimeric emission. Interestingly, the λ_{max} of the ***m*CbAnth** excimer emission is slightly red-shifted compared to ***p*CbAnth**. This could be due to two reasons. First, *meta* carborane is slightly more electron-withdrawing than the *para*-carborane, so it is possible the excimer state is more stabilised by the former, leading to a lower emissive energy. Second, structures of the excimers are slightly different, such that the π-overlap is larger for ***m*CbAnth**, creating a more stable excimer that decays radiatively with a lower energy. Given that the crystal structures of the two isomers are subtly different, this latter explanation appears more plausible. The quantum yield for the aggregated states are also similar, and much lower than in good solutions. It is likely that, whilst some excimers emit radiatively, π-π stacking also allows for many more non-radiative decay routes, causing ACQ and reducing the quantum yield.

For the ***o*CbAnth** the TICT emission dominates in both aggregated states and, notably, the quantum yield is similar for both. This strongly suggests that the microstructure of both states is similar, perhaps identical. The LE is virtually non-existent, which is as a result of ACQ, most likely due to π-π stacking (or excimer) non-radiative decay routes. It is therefore curious why the TICT emission is not also quenched. In the TICT state the molecular orbitals are localised heavily on the carborane. It appears that, due to the compact, spherical and σ-orbital bonding nature of the carborane, it cannot easily

form intermolecular bonding interactions. Therefore, once charge transfer occurs, and the charges are localised on the carboranes, there is essentially no non-radiative decay pathways, producing high quantum yields.

3.5 –Tricyclic Heteroaromatic *ortho*-Carboranes

3.5.1 – UV-Vis and PL

To investigate the effect of aromatic deformation and rotation barrier on PL, optical studies were undertaken for the ***o*CbBDT** and ***o*CbNTP** compounds synthesised in **Chapter 2**. The UV-Vis and PL spectra are presented in **Figure 3-17**.

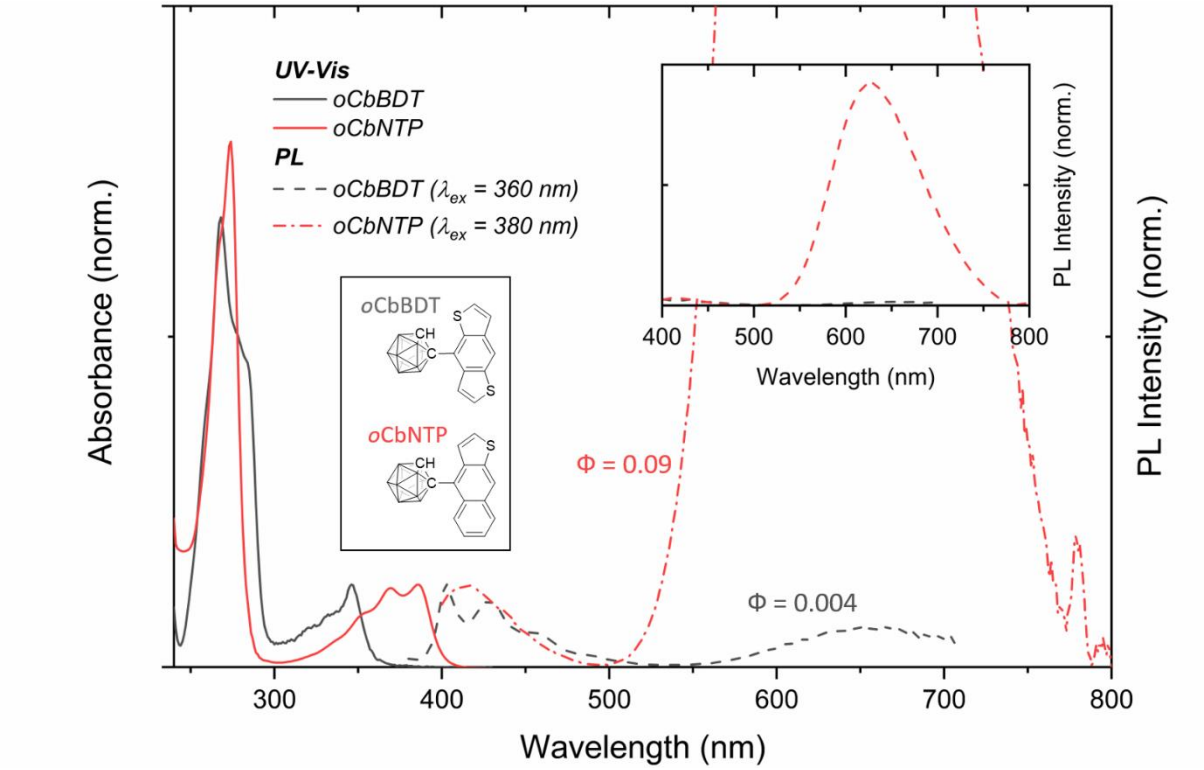


Figure 3-17 – UV-Vis and PL spectroscopy of ***o*CbBDT** and ***o*CbNTP** in THF solutions, concentration = ca. 1 x 10^{-5} M, with quantum yields presented.

Like the UV-Vis spectrum of the anthracenyl carboranes, both ***o*CbBDT** and ***o*CbNTP** exhibit a high energy π→π* (E-band), and a second lower energy π→π* (B-band) transition region, the latter of which shows vibronic character. The onset of absorption energy, equal to the optical band gap, increases on the order ***o*CbBDT** < ***o*CbNTP** < ***o*CbAnth**, which is consistent with increasing size of the delocalised π-system. The PL of these carboranes are also similar; all show a vibronic LE and a low energy delocalised emission. The Stokes shift for ***o*CbBDT** is significantly larger than the other

compounds, probably a result of greater vibrational relaxation in the excited state of the symmetrical BDT system. Similar phenomena has been observed for dithienothiophenes.[26] Notably, the ratio of the delocalised emission to the LE is significantly larger for the ***o*CbNTP** compound, associated with a much higher fluorescence quantum yield.

3.5.2 – Further Optical Studies

To understand the nature and underlying causes of the emission patterns observed for these compounds, a series of optical studies were undertaken. The concentration, H_2O/THF proportion-dependent and solvatochromic studies for ***o*CbBDT** are presented in **Figure 3-18**, with supporting data presented in **Appendix V**.

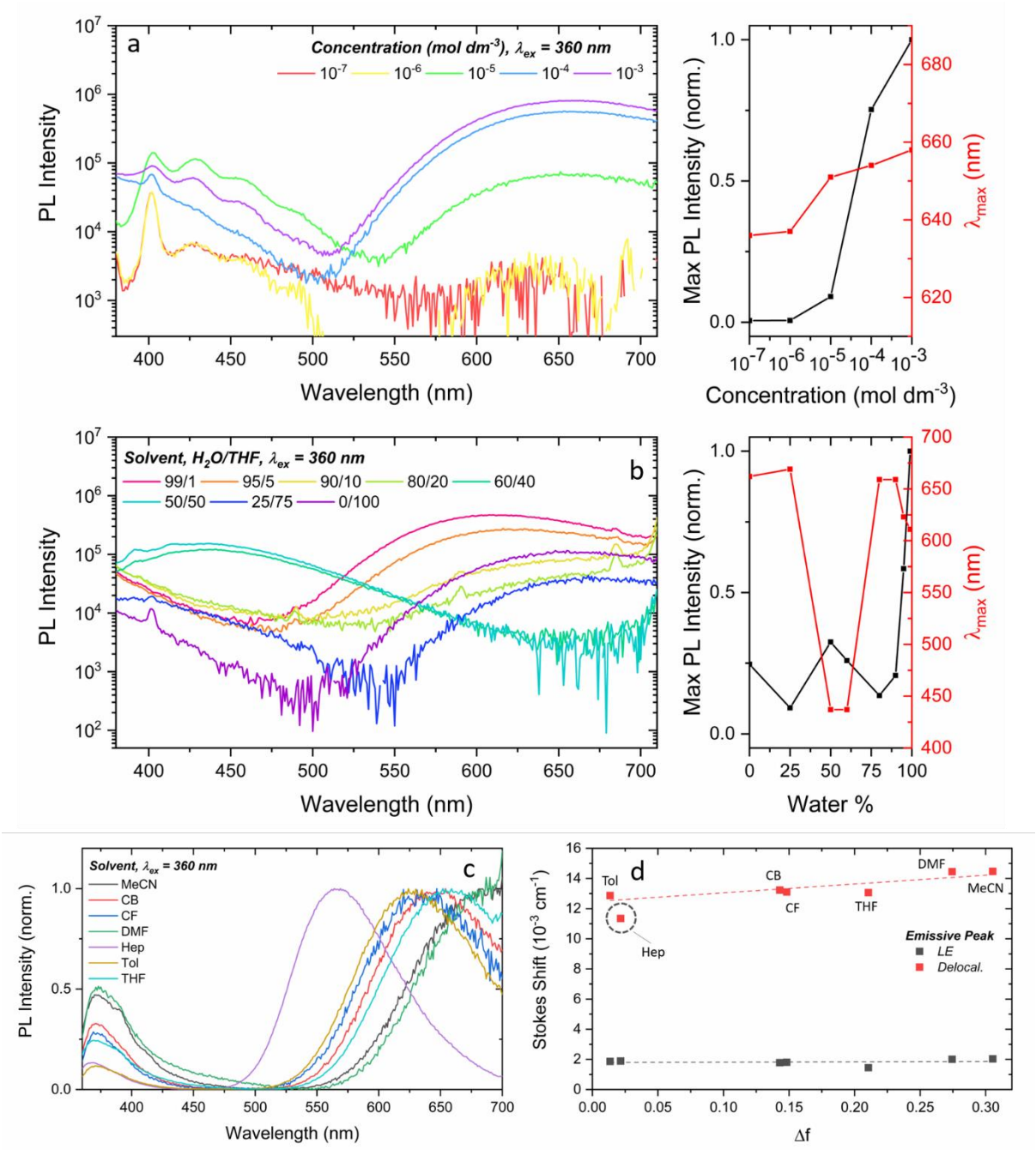


Figure 3-18 – Optical studies of ***o*CbBDT**; (a) concentration-dependent emission in THF, (b) solvent-dependent (relative proportions of H_2O/THF) emission, (c) solvent-dependent emission, and (d) Lippert-Mataga plot. In (a) and (b), λ_{max} refers to the delocalised emission. For solvent dependent plots concentration ca. 1 x 10^{-5} M.

The concentration-dependent PL study of ***o*CbBDT** is curious; whilst there is a general trend in PL intensity increase with increasing concentration, there is no dramatic reduction in PL intensity at high concentration (10^{-3} M). This is unlike the anthracenyl carboranes, where said reduction was attributed to absorption of the excitation beam at a very short distance inside the cuvette, such that fluorescence is blocked by the holder mask. The extinction coefficient of ***o*CbBDT** is approximately half that of the

anthracenyl carboranes, so it is likely that the excitation penetrates further inside the cuvette, and less of the fluorescence is blocked. This leads to an increase in PL intensity for 10^{-3} M relative to 10^{-4} M, but the difference does not follow a power law. This could be still a result of the mask blocking issue but, like ***o*CbAnth**, the PLE of the 10^{-3} M solution (**Appendix V**) differs from the other solutions. It could be that aggregation is occurring, causing the PLE changes and affecting the quantum yield, whilst not affecting the emissive band shape; the λ_{max} of the delocalised peak is essentially invariant as a function of concentration, suggesting that there is one emissive species responsible and it is unimolecular. Further studies would be required investigate this phenomenon.

Solvatochromism is also investigated and summarised in the Lippert-Mataga plot. The LE has a Stokes shift unaffected by solvent, whereas the delocalised emission clearly is. Like ***o*CbAnth**, ***o*CbBDT** in heptane produces an anomalous result. The delocalised emission in heptane is significantly blue-shifted relative to all other solvents. Such a blue-shift is indicative of a separate emissive species.

This is further corroborated with the variable H_2O/THF (v/v) solvent study; at zero and high H_2O proportions only the LE and delocalised emission are present, but at in-between proportions two delocalised species are present. The higher energy peak is assigned to ICT, whereas the low energy peak is assigned to TICT, in the same fashion as ***o*CbAnth**. The PL intensity also follows as similar pattern to the analogous anthracene derivative. The PL intensity initially reduces as H_2O proportions are increased, coinciding with a reduction in the LE and TICT, and an increase in the ICT. Upon the onset of aggregation, the TICT emission increases again, and the ICT emission decreases, leading to a large increase in emissive intensity. Interestingly, the PLE of the most aggregated states (**Appendix V**) have a long tail extending towards longer wavelengths, beyond the perceived band edge of the absorption. This is another example of the intriguing non $\pi \rightarrow \pi^*$ absorption, to be addressed in **Chapter 4**. The quantum yield of the aggregated states (99/1 H_2O/THF (v/v) and solid-state) are approximately ten times larger than in good solution, but it is still low (4%, **Appendix V**). This is significantly lower than the values observed for ***o*CbAnth**. Comparison between these compounds is difficult as the tricyclic fluorophores have inherent optical properties irrespective of the presence of the carborane. However, in aggregated states the dominant emissive species involves the carborane, so some structure-property relationships can be tentatively drawn. In **Chapter 2** it was observed that, upon rotation of the carborane, the BDT core flexes such that there are only three ground state geometries. It is also known that AIE is as a result of the diminishing non-radiative decay pathways as molecular degrees of freedom are reduced in aggregated states, i.e. the molecules are much less flexible. It is therefore possible that the low quantum yield value compared to ***o*CbAnth** is partly due to this increased flexibility. As such, one would expect ***o*CbNTP** to behave similarly.

The ***o*CbNTP** compound was subjected to the same optical studies as ***o*CbBDT**, with the important spectra presented in **Figure 3-19** and supporting data in **Appendix V**.

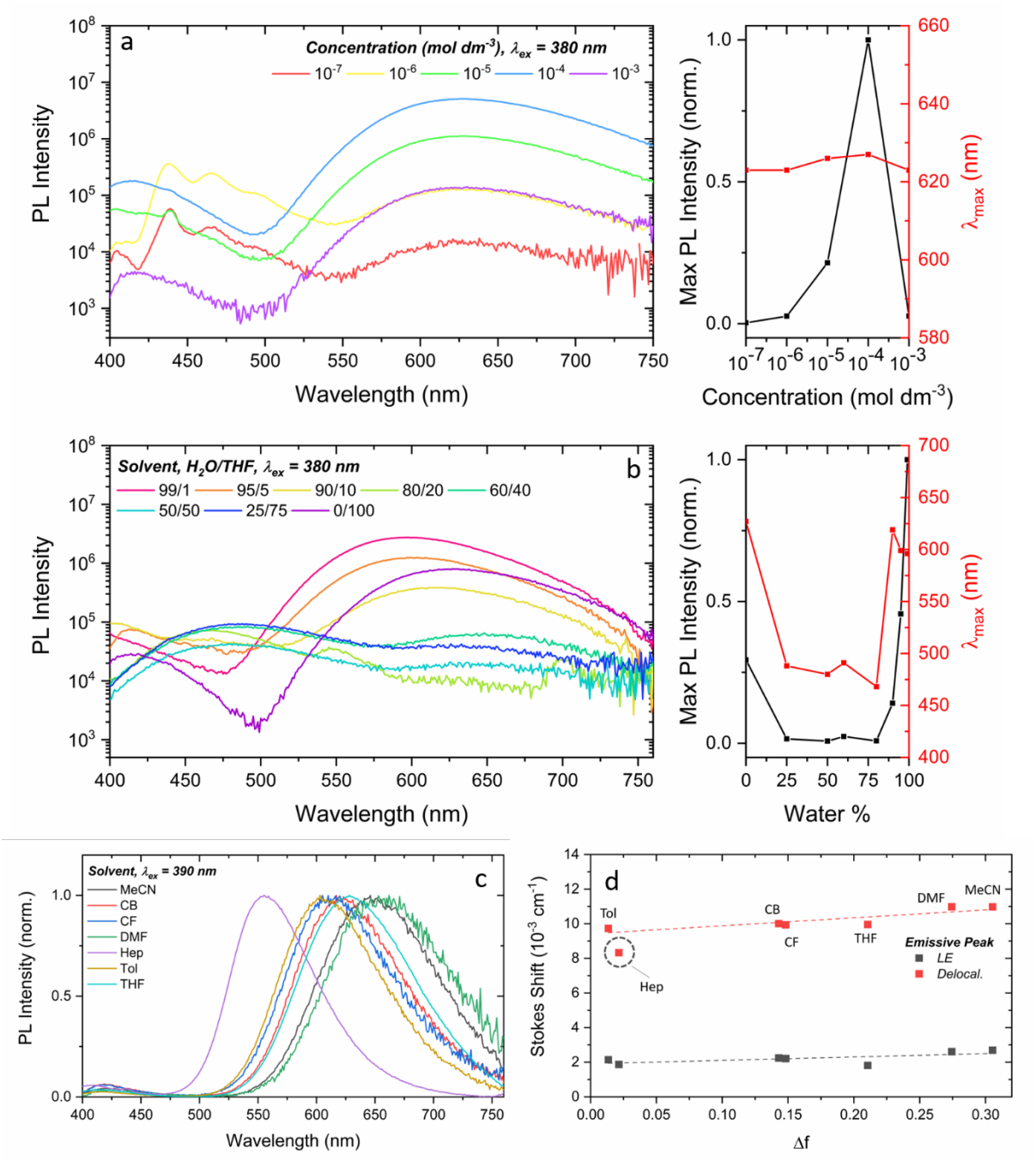


Figure 3-19 – Optical studies of ***o*CbNTP**; (a) concentration-dependent emission in THF, (b) solvent-dependent (relative proportions of H_2O/THF) emission, (c) solvent-dependent emission, and (d) Lippert-Mataga plot. In (a) and (b), λ_{max} refers to the delocalised emission. For solvent dependent plots concentration ca. 1 x 10^{-5} M.

All optical studies in **Figure 3-19** are strikingly like those of ***o*CbBDT** and ***o*CbAnth**. The concentration dependent study shows virtually no change in the λ_{max} of the delocalised emission, and there is a general trend of increased PL intensity with increasing concentration; the H_2O/THF (v/v) solvent study

shows ICT and TICT emission, simultaneously at ca. 50/50 proportions; and the solvatochromism study demonstrates ICT emission in heptane. It should be noted that in all the cases discussed for far, the heptane emission intensity is significantly larger than all other solvents. In good solvents, there TICT dominates, vibration of the elongated carboranyl C-C bond allows for an efficient non-radiative decay route. In heptane solution the ICT state does not have an elongated C-C bond, so no such decay route is possible. Therefore, the emissive quantum yield Is larger in this solvent.

The quantum yield of ***o*CbNTP** in both good solvents aggregated states are, as for ***o*CbBDT**, relatively low. This could again be due to the relatively large flexibility of the NTP ring system, during carborane rotation, compared to ***o*CbAnth**.

3.6 – The Nature of the Aggregation

Due to the similarity between the polycrystalline solid state, and 99/1 H_2O/THF (v/v) photoluminescence spectra of all carboranes presented in this chapter, and their quantum yields, it was theorised that the aggregates in the latter have a microstructure like that of the solid. This would require the aggregates to be highly ordered, and possibly even crystalline.

3.6.1 – DLS

To investigate the nature of the aggregates, and how these change as a function of H_2O and THF proportions, a dynamic light scattering (DLS) study was undertaken. DLS is a technique that uses light scattering to determine the sizes, and distribution profile, of microscopic solute particles in solutions. Suspensions are subjected to a laser light source, which then scatters in all directions as it bounces off the particles and hits a detector. The intensity of scattered light changes as a function of times as a result of the Brownian motion of the particles, and this dynamic information is used to generate the size information about the particles. Interestingly, these techniques were used by Albert Einstein to confirm the existence and size of atoms.[27] The various H_2O/THF (v/v) solutions of all isomers of anthracenyl carboranes were prepared as in the PL studies, and subjected to DLS as presented in **Figure 3-20**.

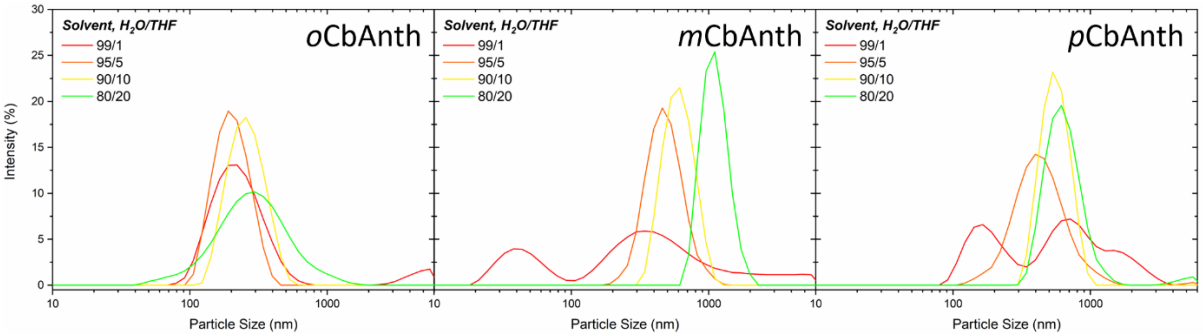


Figure 3-20 – DLS of the three isomers of anthracenyl carborane, in varying properties of H_2O/THF solutions. Concentrations = ca. 1 x 10^{-5} M.

Of all the solutions studied, only H_2O/THF 99/1, 99/5, 90/10, and 80/20 proportions gave a signal that aggregates were present. This is consistent with the PL for the ***o*CbAnth** isomer where the emission intensity begins to increase at H_2O proportions >60% (see **Figure 3-14**). Given that AIE does not occur for the ***m*CbAnth** or ***p*CbAnth** isomers no such comparison can be made, but the λ_{max} of both compounds similarly increases above >60% water proportions. The DLS data is therefore consistent with the PL data, with regards to at what solvent composition aggregates begin to form.

For all isomers there is a general trend for aggregate size to decrease as H_2O proportion increases, however there are large differences between the isomers. Whilst it is possible that these discrepancies are real, it must be noted that there are experimental issues associated with this DLS study. The first is that the cuvettes used in the machine are disposable plastic, and soluble in THF. Addition of water reduces the corrosion, but it is likely that the results are affected by this, especially for the higher THF proportion solvents. The input procedure was also not changed between solvents, which ideally would be the case; the SOP is calibrated against a known compound in a known solvent, so a solvent dependent study requires a new SOP for each H_2O/THF v/v studied. Instead of using many SOPs, it was decided using one for all samples would be preferable. Therefore, whilst the DLS study confirmed that aggregates are present in the samples that exhibit aggregation effects in their PL spectra, any analysis beyond this is unwise.

3.6.2 – SEM

A better way to assess the size and nature of the aggregates is via scanning electron microscopy (SEM). Using SEM one can view and measure the aggregates directly, which is a significant advantage over DLS methods, but with the disadvantage of it being a more laborious procedure. Solutions of all isomers were made-up, in the varying H_2O/THF (v/v) proportions as in the DLS study, in concentrations of 0.01% (ca. 3 x 10^{-4} M). These solutions were dropped on to cleaned glass slides and left to dry,

before being sputtered with silver, ready for SEM analysis. Selected pictures from the study are presented in **Figure 3-21**.

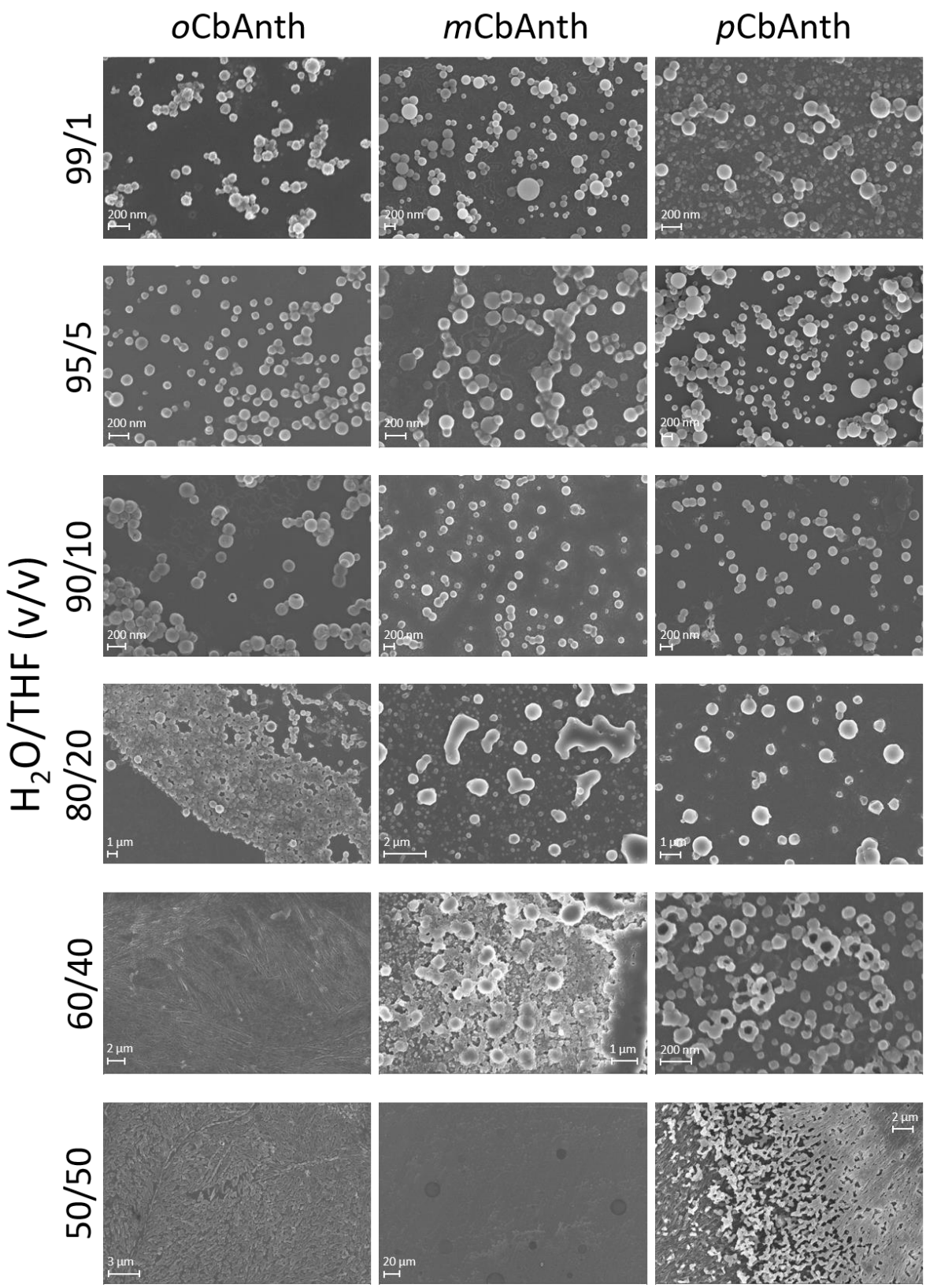


Figure 3-21 – SEM images (various magnifications) of the three isomers of anthracenyl carboranes in varying H_2O/THF proportions.

The SEM images clarify the nature of the aggregates; in the 99/1 H_2O/THF (v/v) proportions the aggregates form into nearly spherical nanoparticles. The nanoparticles are also present when the H_2O proportions are smaller, and it is hard to find differences between the images of 99/1 and 80/20 solvents. There are even nanoparticles in the 60/40 solutions (c.f. the DLS study where no such aggregates were observed), however the sphericity of the particles noticeably decreases as the H_2O proportion increases. At the same time the crystalline regions begin to grow, exemplified by the 60/40 ***m*CbAnth** isomer image, where nanoparticles lie on top of an ordered crystalline region, and the 50/50 image for all isomers where only crystalline regions are observed. These crystalline regions clearly were not present in solution but were solutions which crystallised upon evaporation of the solvent.

3.6.3 – Size-Distribution Analysis

Interestingly, the size of the nanoparticles varies hugely across the sample range. There are also numerous examples in which nanoparticles of the size of ca. 1 µm, and those of less than 100 nm are present within the same image. A second point of interest, not perceptible from **Figure 3-21**, but clear during the analysis, is the observation that the frequency of nanoparticles decreased as the proportion of H_2O in the solvent decreased; in the 99/1 solvent there were no regions that did not contain nanoparticles; in the 80/20 solvent there were some regions of nanoparticles but many more crystalline regions; and in the 50/50 solvent there were only crystalline regions. This led to the question of whether the changes in emission intensity observed upon aggregation, particularly in the highest H_2O proportions, were as a result of the concentration of nanoparticles (i.e. the proportion of carboranes in nanoparticles versus those in solution), or the size of nanoparticles, or both. To investigate this further, size distribution analysis of the nanoparticles was undertaken, and the data was extracted as demonstrated in **Figure 3-22**.

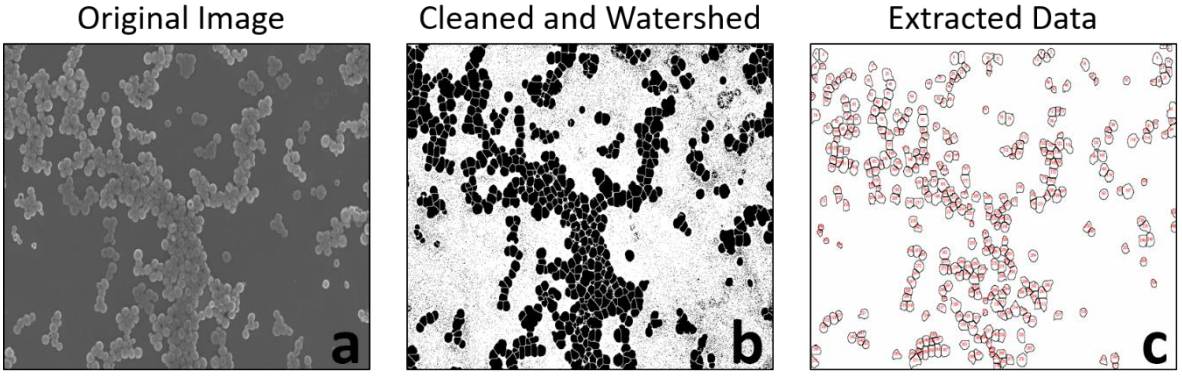


Figure 3-22 – Example of the cleaning and modification of SEM images to extract useable data. The contrast in (a) the original image is increased such that the individual nanoparticles can be isolated from clusters using a 'watershed' algorithm to form (b). Nanoparticles are then selected by roundness to remove remaining clusters, forming the data set in (c).

Using the watershed algorithm and roundness selection criterion is far from perfect, as many of the particles present in the original image are not present in the final dataset. However, given the large number of nanoparticles and the large number of images, this approach is the best available for such a large dataset. The resulting size (diameter) distribution analysis is presented in **Figure 3-23**, with the summary in **Figure 3-24**.

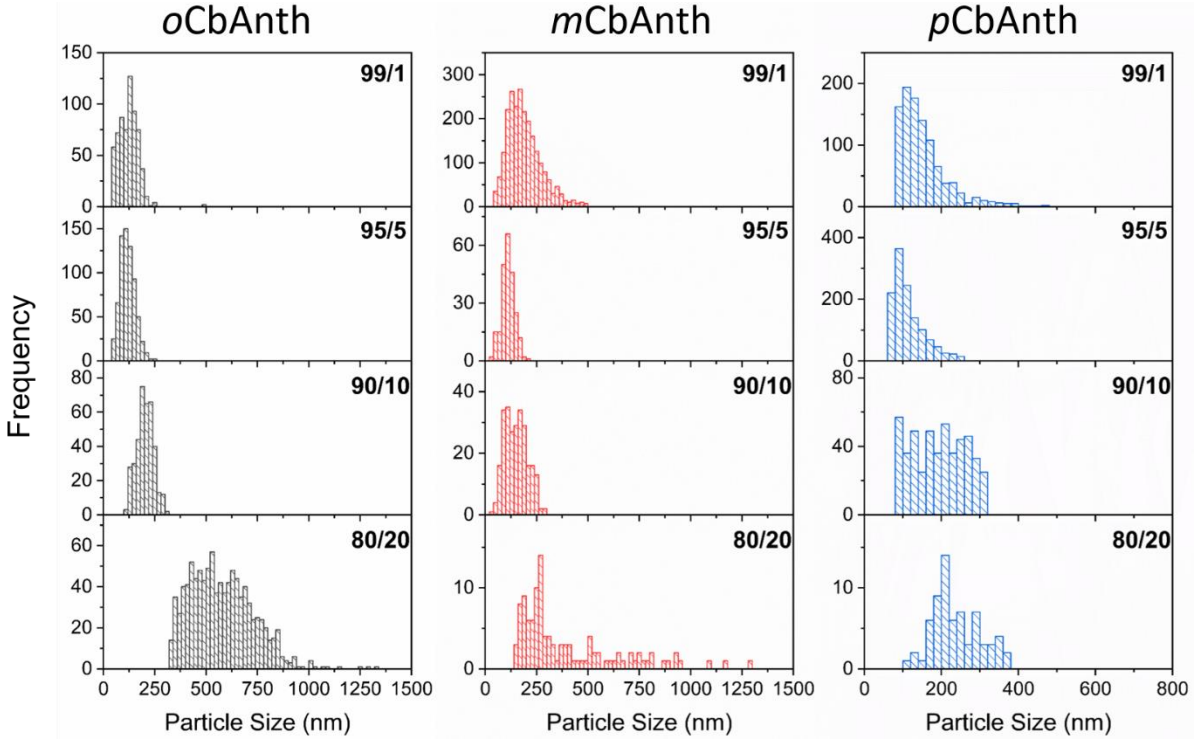


Figure 3-23 – SEM size distribution analysis of the three isomers of anthracenyl carborane in varying H_2O/THF (v/v) proportions.

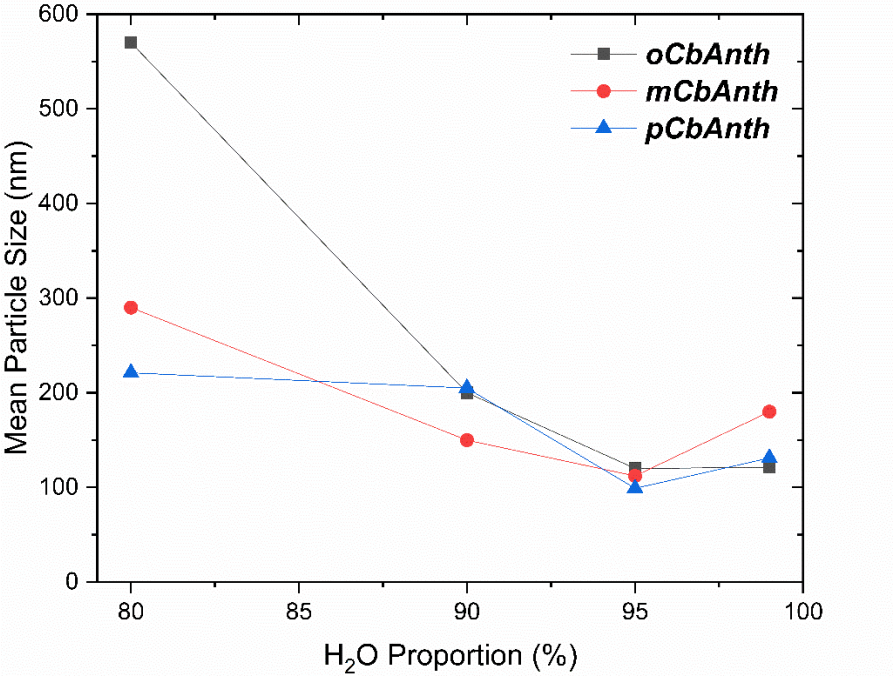


Figure 3-24 – Summary of the SEM size distribution analysis.

The size distribution analysis shows that there is a solvent dependence for nanoparticle size; as the H_2O proportion increases, the nanoparticle size decreases. The change in size is relatively modest however, except for ***o*CbAnth** which is reduced from ca. 600 nm to 100 nm over the solvent range studied. However, one must be cautious to draw too many conclusions from this as, whilst the sample size is reasonable in terms of data points (>1000 for each isomer), the magnification required to see these nanoparticles, and the lack of an automated data extraction process, requires that only a minute area of the whole sample can be studied. It is clear however, that at lower water proportions (<95%) the distribution of particle sizes increases, suggesting a more heterogenous particle formation process.

Whilst there is a clear trend in the size and size distribution of nanoparticles between the solvents, the question remains whether these effects are the underlying causes of the change in PL intensity, or simply the proportion of solutes in nanoparticles. This question can be answered by again examining the size distribution analysis.

The nanoparticles can be approximated as spheres, with volumes that scale with (0.5 x diameter)^3. A nanoparticle with a diameter of 100 nm therefore has 10^{-3} of the volume of a nanoparticle with a diameter of 1000 nm. When one considers all the carborane molecules in all nanoparticles, it is clear that most molecules will be in nanoparticles which are larger than the mean nanoparticle size of ca. 100 nm. This notion is exemplified in **Figure 3-25**.

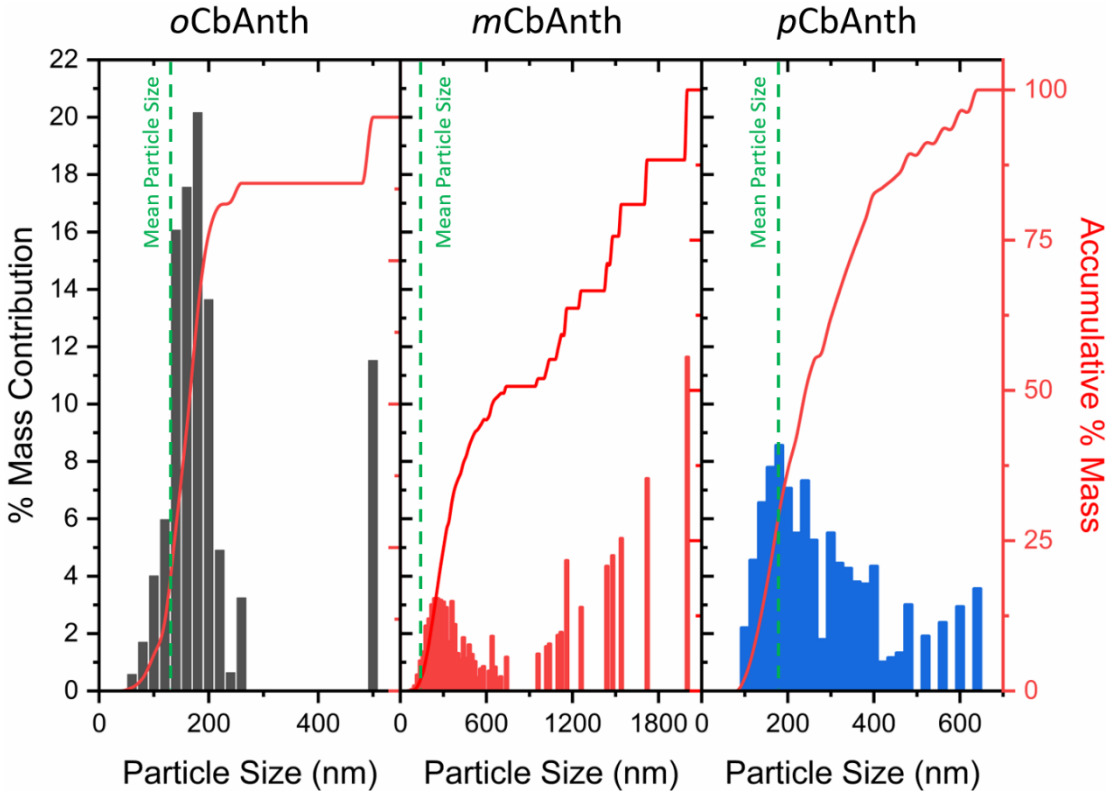


Figure 3-25 – Percentage mass contribution as a function of nanoparticle size for the three isomers of anthracenyl carborane in 99/1 H_2O/THF (v/v) solution.

One can see that for all three isomers, more than 50% of the mass contribution to all particles is present in particles larger than the mean nanoparticle size. Large particles (>1000 nm), of which there are very few (see **Figure 3-23**) have a huge impact on the overall accumulative mass. In fact, in the case of the ***m*CbAnth**, a single nanoparticle, in a dataset of 2347 particles, contains approximately 25% of the total mass of carboranes. This is important; it shows that the average carborane molecule will reside in a nanoparticle significantly larger than the mean nanoparticle size, and therefore PL intensity is less likely to be dependent on nanoparticle size. It can therefore be tentatively concluded that AIE is dependent on the concentration of total solute particles in nanoparticles, with a higher concentration in nanoparticles yielding larger emission intensities.

3.7 – Crystallinity of the Nanoparticles

3.7.1 – TEM and STEM

Based on the SEM data, nanoparticles are the cause of the AIE emission, but that is not the end of the story; the SEM data does not provide any details around the microstructure of the individual molecules in the nanoparticles, and particularly whether they are highly ordered or even crystalline,

as suggested by the similarity of the aggregated and solid-state emission spectra. To probe this, a transmission electron microscopy (TEM) and scanning transmission electron microscopy (STEM) was undertaken on the 99/1 H_2O/THF (v/v) solution of the ***o*CbAnth** (TEM is a highly time intensive technique, so only ***o*CbAnth** was studied, based on the assumption that its microstructure is representative of all anthracenyl carboranes). The solution was placed on a holey carbon film, and solvent evaporated before being placed in the spectrometer. A selection of the images is presented in **Figure 3-26**.

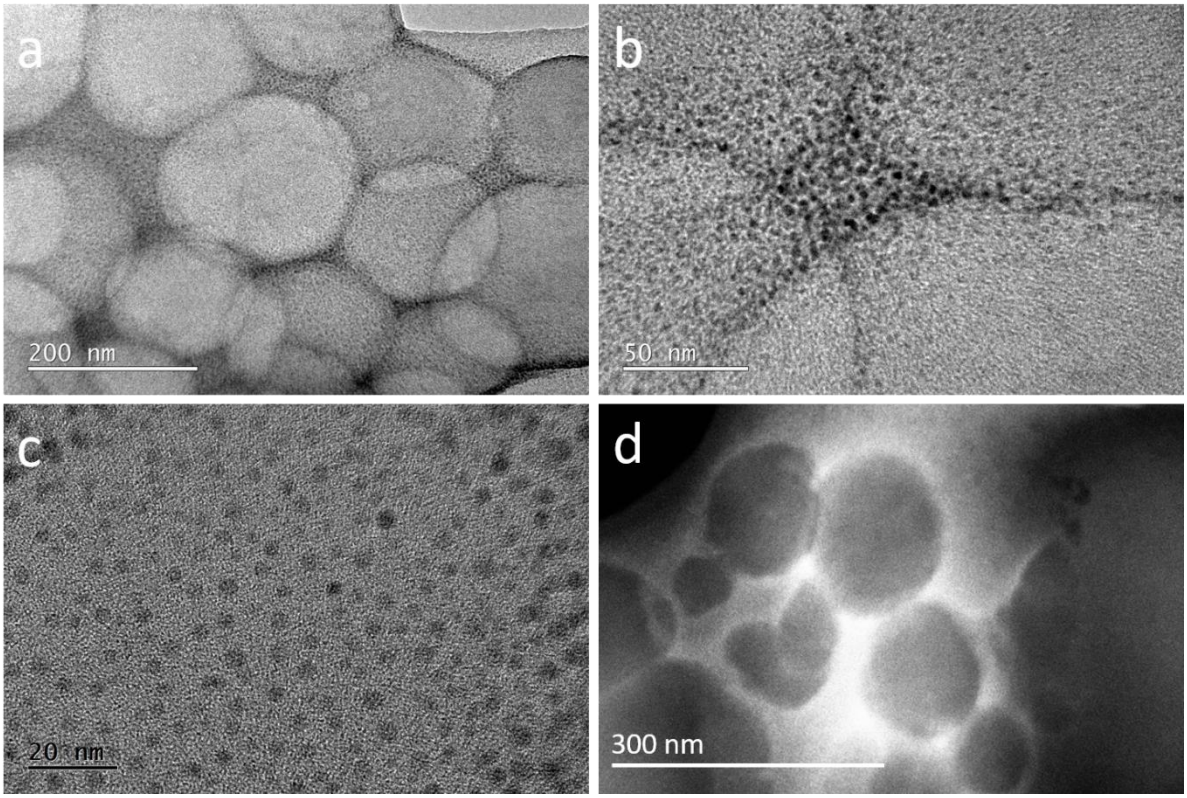


Figure 3-26 – TEM images of 99/1 H_2O/THF (v/v) solution of ***o*CbAnth**; (a) macroscopic view of a nanoparticle cluster, (b) edges of touching nanoparticle clusters, (c) magnified view of the surface of a nanoparticle, (d) annular dark-field STEM view of nanoparticle cluster.

Noticeable from the **Figure 3-26a** is that the nanoparticles appear transparent. This is simply a function of the electron beam interacting with atoms throughout the particle, and not just on the surface (as in SEM). In the magnified view (**Figure 3-26b** and **26c**) there a many perceptible darker 'dots' scattered throughout the nanoparticle with an approximate diameter of 5 nm, which appear in higher concentrations at the edges. The STEM view (**Figure 3-26d**) seems to correlate with this observation.

As suggested by its name, STEM is a technique where the TEM acts as an SEM. Using STEM, one can examine samples with annular dark-field imaging, where the machine takes the signal from outside of the principal beam, allowing for interferences to be detected. Spatial information is lost however, and

images appear more two-dimensional, as a projection of the real three-dimensions. What appears bright in the dark-field are signals which are diffracted significantly, whilst dark areas are transmitted without any scattering. One can therefore see that the surface of the nanoparticles seems to scatter more than the centres of the nanoparticles, which barely scatter at all. This suggests that the centres of the particles are less dense than the edges. At those edges, where the density of the small dark dots is larger, there is more interference, potentially caused by ordered crystal lattices.

For this to be true the dark dots would have to show crystallinity, and such an observation was made using TEM with a higher resolution electron gun. The images are presented in **Figure 3-27**.

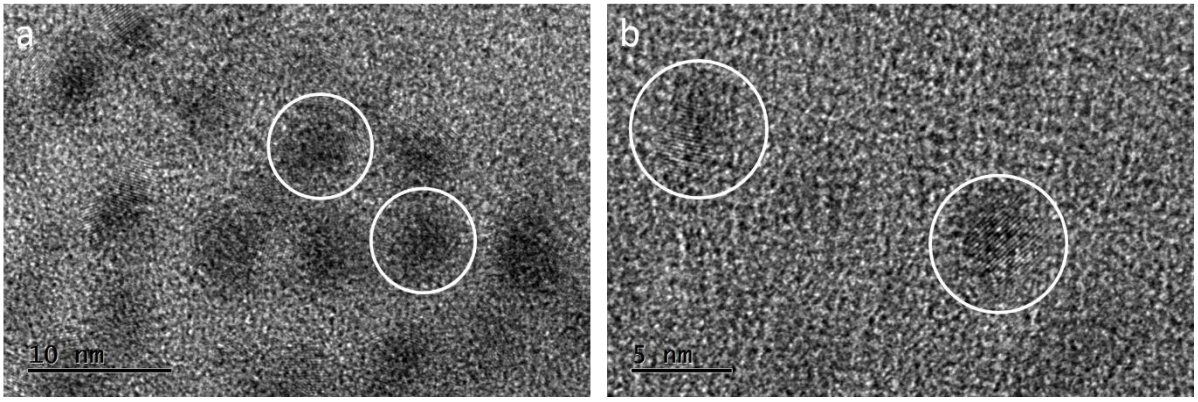


Figure 3-27 – High resolution TEM images of 99/1 H_2O/THF (v/v) solution of ***o*CbAnth**, with interferences circled.

From the high resolution TEM the black dots can be seen more clearly, and, in almost all instances, interference patterns can be observed. Such patterns are the mark of highly ordered, crystalline regions, and small particles of this nature are known as nanocrystals. However, the unit cell dimensions of ***o*CbAnth** are known from the crystal structure presented in **Chapter 2**, with the relevant data given in **Appendix II**. The values are: a = 1.596, b = 1.030, and c = 2.077 nm, which are clearly around an order of magnitude larger than the lattice fringes in **Figure 3-27**. This was initially troubling, however TEM images of methylene succinic acid films demonstrate a strikingly similar phenomenon.[28] Nanocrystals are observed with interference patterns, and lattice spacings of 0.21 nm, but unit cell dimensions of a = 0.546, b = 1.159, and c = 1.849 nm. These nanocrystals were unequivocally assigned to the acid, and it is therefore likely that the nanocrystals observed in **Figures 3-26** and **27** are indeed resulting from ***o*CbAnth**.

The coexistence of nanocrystals and nanoparticles have been observed for other, non-carboranyl, AIE-active compounds,[29–31] with the former occurring predominantly at lower H_2O fractions (~70%), and the latter at higher H_2O (>90%) fractions. The processes underlying the formation of the two aggregate morphologies is not well understood but, interestingly, AIE can result from either the crystalline,[29] or

amorphous types.[30,31] For all isomers in this study, the striking similarity between optical properties of the solid (polycrystalline) and 99/1 aggregate solutions make it highly likely that the nanocrystals contribute to the observed emissive properties, however, the coincidence of increasing of PL intensity with nanoparticle concentration makes it impossible to discount the their contribution without significant further investigation.

3.8 – Conclusions

The PL properties of the three isomers of anthracenyl carboranes were investigated with a range of concentration, solvatochromic, temperature, and H_2O/THF (v/v) proportion solvent studies. All isomers exhibit a high energy vibronic emission in good solvents, which was assigned to a LE from the anthracene chromophore. The peak position was identical for ***m*CbAnth** and ***p*CbAnth** isomers, but slightly red-shifted for the ***o*CbAnth** isomer, likely as a result of the more electron-withdrawing nature of the latter. The ***o*CbAnth** compound also displays a second, low emission in good solvents. Based on the broad and featureless presentation, as well as a Stokes shift which is solvent dependent, this peak was assigned to a delocalised emissive species. Concentration dependent studies all but rule out an excimer species, and DFT calculations aided the assignment of a TICT species being responsible for this emission. Interestingly, a significant blue-shift in this emission was observed for ***o*CbAnth** in heptane solvent, and the Stokes shift proves to be quite anomalous in a Lippert-Mataga plot. DFT calculations again contributed, suggesting a second emissive ICT state was formed when the carboranyl C-C bond was approximately in the plane of the anthracene core. Such an emissive state cannot undergo C-C bond elongation and relaxation, thus appears at higher energies than the TICT state.

Low temperature PL studies offered several insights. In THF solution ***m*CbAnth** was relatively unaffected by temperature, but the emission of ***p*CbAnth** was quenched upon cooling. This was tentatively assigned to the formation of excimers, perhaps aided by the more planar structure of ***p*CbAnth**. Experimental error, however, could not be ruled out. The temperature-dependent PL behaviour of the ***o*CbAnth** isomer was found to be much more complex. There was a general trend for an increase in both LE and TICT emission upon cooling, consistent with less molecular movement contributing to fewer non-radiative decay pathways. Upon freezing of the solvent, the TICT emission was replaced by an ICT emission along with an increase in the LE. This was attributed to more difficult rotation of the carborane, leading to a larger proportion of molecules residing in the ground state potential energy well, with the carboranyl C-C bond approximately perpendicular to the aromatic plane, promoting both LE and ICT. A similar study in chloroform solutions, in concentrations known to exhibit restricted carborane rotations, showed a general increase in PL with reduced temperature for

all isomers. For ***o*CbAnth** the LE increases at a faster rate than the TICT emission, again likely a result of the restricted rotation argument. There was, however, no discernible ICT emission in this solvent.

Proportional H_2O/THF (v/v) solvent studies demonstrated that aggregation was detrimental to the PL quantum yield of ***m*CbAnth** and ***p*CbAnth** isomers, and ACQ was occurring. However, in high H_2O solvents a new emissive species was observed. Based on the broad nature of this peak, and time-resolved data in comparison to literature, this peak was assigned to a rare anthracene excimer. Introduction of a bad solvent to THF solutions of ***o*CbAnth** first quenches TICT emission but promotes ICT emission. This was rationalised in terms of the quenching effects of H_2O, which occurred to a lesser extent for the less delocalised ICT species. At larger H_2O proportions AIE took place, leading to promotion of the TICT state and an overall increase in quantum yield. Almost identical emissive characteristics to the aggregated states, in both PL spectra and quantum yield, are observed in the polycrystalline solid-state for all isomers. It was therefore suggested the aggregates may have a large degree of ordering, perhaps even crystalline domains.

Optical studies of ***o*CbBDT** and ***o*CbNTP** demonstrated that their PL properties matched, to a great extent, the properties of ***o*CbAnth**. They both exhibited LE, whose peak position changed according to the aromatic chromophore (and due to the lack of significant carborane involvement in the emissive species), and TICT emission in good solvents. In heptane and in some H_2O/THF (v/v) proportions they showed ICT emission, and in high H_2O proportions AIE occurred. However, the quantum yield was still low relative to ***o*CbAnth**. It was theorised that this was due to the increased flexibility of the system, as a result of the reduced steric hinderance to rotation for these compounds.

Lastly, the nature of the aggregated states was investigated in detail. DLS measurements suggested aggregates formed in (in large enough number to be measured) in H_2O/THF (v/v) > 60/40. The data was not clear however, so SEM was used to image the aggregates directly. Highly spherical nanoparticles were observed, ranging from approximately 1 µm to < 100 nm in diameter. The size of the nanoparticles decreased somewhat with increased H_2O proportions; however the effect was small. It was considered more likely that the concentrations of nanoparticles was the main factor dictating the degree of AIE. Closer inspection of the nanoparticles through TEM analysis showed many < 10 nm particles which also exhibited electron interference patterns. With the aid of single crystal XRD data and literature precedence of such materials, these particles were suggested to be nanocrystals of ***o*CbAnth**. This explained the striking similarity between aggregated and polycrystalline emission behaviours; they are different macroscopic forms of the same underlying microstructures.

3.9 – Experimental

The H_2O/THF (v/v) solvent studies were achieved using the following method. The compound of interest was weighed out and dissolved in the desired proportion of THF, relative to a total volume of 10 mL. If the compound was difficult to dissolve it was subjected to sonication until solids were no longer observed. The desired proportion of H_2O was then added to the THF sample, via a syringe and in one portion, over the period of approximately 1 second. The resulting solution was then used directly in optical studies within 3 days.

Steady-state PL emission and excitation measurements were performed using a Horiba Scientific FluoroMax 4 spectrofluorometer. Solution measurements were performed using 1 cm path length quartz cuvettes. Solid-state PL, and PL quantum efficiency (PLQE) measurements were performed in the Horiba Quanta-Phi diffusely-reflecting integrating sphere attachment. PLQE was calculated using the methodology detailed by Ahn et al.[32] The setup was calibrated by testing fluorescence standards Rhodamine 6G and Fluorescein to ensure the accuracy and reliability of calculated PLQE values.

Solution time-resolved PL measurements were performed on THF and 99/1 H_2O/THF (v/v) ratio solutions in 1 cm quartz cuvettes. Measurements were carried out using a Horiba DeltaFlex time-correlated single photon counting (TCSPC) system, with a NanoLED excitation source, using a Spectral LED with 404 nm excitation wavelength. The time-range of the measurement was 100 ns. The IRF was recorded for each sample, using an aqueous sample of Ludox Colloidal Silica.

Continuous Temperature Dependent PL: PL spectra were recorded continuously in time, rather than waiting for temperature (controlled using a continuous flow cryostat (Oxford Instruments)) to stabilise between measurements as is typical, thus enabling the influence of cooling rate to be established. This necessitated continuous measurement of the solution temperature, achieved using a calibrated platinum Pt1000 resistive temperature sensor placed inside the solution, measured using a Keithley 2400 Source Measurement Unit. 1 ml of 1.5 x 10^{-4} M solution in THF inside a quartz cuvette was optically excited using a focussed 405 nm LED (Thorlabs), with emission detected by an Avantes CCD spectrometer via an optical fibre. Given the variation in PLQY, illumination intensity and exposure time were varied between samples to ensure an adequate signal to noise ratio while avoiding detector saturation. Spectra and temperature readings were recorded at 1s and 10s intervals respectively, enabling spectral changes to be associated with corresponding thermal signatures, such as exothermic solvent crystallisation. Spectra were fitted using a standard Franck Condon progression of Gaussian peaks, with a single broad Gaussian peak to represent the TICT and ICT transitions of the *ortho*-carborane isomer.

Additionally, PL spectra were acquired from 3 x 10^{-3} M solutions (similar to those of NMR measurements) at temperatures between 300 and 200 K using an Edinburgh Instruments FLSP920 double-monochromator spectrophotometer, with a 15 min stabilisation time. Excitation was at 320 and 420 nm; emission was collected in 2 nm increments with a 4 nm bandwidth - the exposure time was adjusted to ensure an adequate signal to noise ratio.

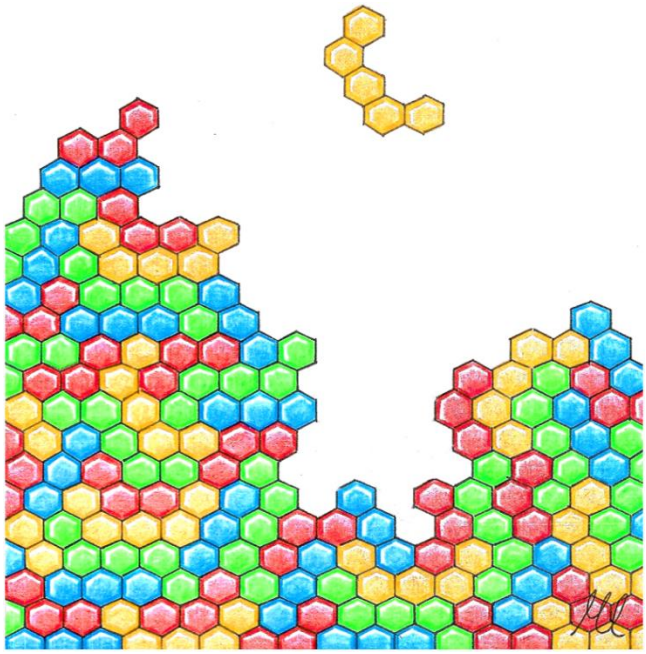
DFT and TD-DFT calculations were carried out using the software, basis set and functional as in **Chapter 2**, but in the THF solvent phase, using self-consistent reaction field (SCRF), and the default integral equation formalism variant PCM model. Non-equilibrium solvation was used in the fluorescence calculation cycle, as discussed in the main text.

Samples for SEM analysis were prepared using glass slides cut into approximately 1x1 cm squares, that were then cleaned with soap, water, and isopropanol, with the aid of sonication. 50 μL of H_2O/THF (v/v) carborane solution was added to the slides with the aid of a Gilson pipette, and left to dry in air at room temperature. The slides were then sputtered coated with silver using a Quorum Q15OR S sputter coater. Images were collected using a Zeiss Auriga Cross Beam SEM with an EHT voltage of 5.00 kV, at various magnification levels. Samples for TEM analysis were prepared similarly but using Agar Scientific holey carbon films on a mesh copper grid. Images were collected using a JOEL JEM-2100F TEM with an EHT voltage of 200 kV. SEM and TEM analysis was aided with the use of ImageJ imaging software.[33] The simulated electron diffraction spectrum was produced using CrystalDiffract 6 software.

3.10 – References

1 R. A. Harder, PhD Thesis, Durham University, 2012.
2 F. Bayrakçeken, O. J. Demir, L. Tunçyürek and İ. Ş. Karaaslan, *Spectrochimica Acta Part A: Molecular and Biomolecular Spectroscopy*, 2006, **65**, 27–31.
3 K.-R. Wee, Y.-J. Cho, J. K. Song and S. O. Kang, *Angew. Chem. Int. Ed.*, 2013, **52**, 9682–9685.
4 Y. Hong, J. W. Y. Lam and B. Z. Tang, *Chem. Soc. Rev.*, 2011, **40**, 5361–5388.
5 C. J. Bhongale, C.-W. Chang, C.-S. Lee, E. W.-G. Diau and C.-S. Hsu, *J. Phys. Chem. B*, 2005, **109**, 13472–13482.
6 H. Saigusa and E. C. Lim, *J. Phys. Chem.*, 1995, **99**, 15738–15747.
7 R. Norman. Jones, *Chem. Rev.*, 1947, **41**, 353–371.
8 L. D. S. Yadav, *Organic Spectroscopy*, Springer Science & Business Media, 2004.
9 J.-L. Bredas, *Materials Horizons*, 2014, **1**, 17–19.
10 M. Taniguchi and J. S. Lindsey, *Photochemistry and Photobiology*, 2018, **94**, 290–327.
11 N. Boens, W. Qin, N. Basarić, J. Hofkens, M. Ameloot, J. Pouget, J.-P. Lefèvre, B. Valeur, E. Gratton, M. vandeVen, N. D. Silva, Y. Engelborghs, K. Willaert, A. Sillen, G. Rumbles, D. Phillips, A. J. W. G. Visser, A. van Hoek, J. R. Lakowicz, H. Malak, I. Gryczynski, A. G. Szabo, D. T. Krajcarski, N. Tamai and A. Miura, *Anal. Chem.*, 2007, **79**, 2137–2149.
12 W. R. Ware and P. T. Cunningham, *J. Chem. Phys.*, 1965, **43**, 3826–3831.
13 E. A. Chandross and C. J. Dempster, *J. Am. Chem. Soc.*, 1970, **92**, 3586–3593.
14 N. Mataga, Y. Kaifu and M. Koizumi, *Bulletin of the Chemical Society of Japan*, 1956, **29**, 465–470.
15 E. Lippert, *Electrochemistry*, 1957, **61**, 962–975.
16 M. de Jong, L. Seijo, A. Meijerink and F. T. Rabouw, *Physical Chemistry Chemical Physics*, 2015, **17**, 16959–16969.
17 J. K. Thomas, *J. Phys. Chem. C*, 2014, **118**, 16380–16385.
18 C. M. Hansen, *The three dimensional solubility parameter and solvent diffusion coefficient: Their importance in surface coating formalation,* Danish Technical Press, 1967.
19 I. M. Smallwood, *Handbook of Organic Solvent Properties*, Wiley, 1996.
20 G. E. Dobretsov, T. I. Syrejschikova and N. V. Smolina, *BIOPHYSICS*, 2014, **59**, 183–188.
21 P. F. Jones and M. Nicol, *J. Chem. Phys.*, 1968, **48**, 5440–5447.
22 G. F. Moore, *Nature*, 1966, **212**, 1452.
23 P. K. Lekha and E. Prasad, *Chemistry - A European Journal*, 2010, **16**, 3699–3706.
24 H. Liu, L. Yao, B. Li, X. Chen, Y. Gao, S. Zhang, W. Li, P. Lu, B. Yang and Y. Ma, *Chem. Commun.*, 2016, **52**, 7356–7359.
25 M. Sugino, Y. Araki, K. Hatanaka, I. Hisaki, M. Miyata and N. Tohnai, *Crystal Growth & Design*, 2013, **13**, 4986–4992.
26 C.-Z. Wang, J.-H. Do, T. Akther, X. Feng, L. Horsburgh, M. R. J. Elsegood, C. Redshaw and T. Yamato, *Tetrahedron*, 2017, **73**, 307–312.
27 Carlo Rovelli, *Reality Is Not What It Seems*, Penguin, 2017.
28 S. Khan, A. Sharma, S. Ghoshal, S. Jain, M. K. Hazra and C. K. Nandi, *Chem. Sci.*, 2017, **9**, 175–180.
29 Y. Dong, J. W. Y. Lam, A. Qin, J. Sun, J. Liu, Z. Li, J. Sun, H. H. Y. Sung, I. D. Williams, H. S. Kwok and B. Z. Tang, *Chem. Commun.*, 2007, **0**, 3255–3257.
30 X. Zhang, Z. Chi, J. Zhang, H. Li, B. Xu, X. Li, S. Liu, Y. Zhang and J. Xu, *J. Phys. Chem. B*, 2011, **115**, 7606–7611.
31 X. Zhang, X. Zhang, B. Yang, M. Liu, W. Liu, Y. Chen and Y. Wei, *Polym. Chem.*, 2013, **5**, 356–360.
32 T.-S. Ahn, R. O. Al-Kaysi, A. M. Müller, K. M. Wentz and C. J. Bardeen, *Review of Scientific Instruments*, 2007, **78**, 086105.

33 C. A. Schneider, W. S. Rasband and K. W. Eliceiri, *Nature Methods*, 2012, **9**, 671–675.



Chapter 4 – The Synthesis, Structure and Properties of *ortho*-Carboranyl Non-Linear Acenes

4.1 – Introduction

In **Chapter 2**, it was demonstrated that attaching a carborane substituent to a tricyclic heterocycle can have a profound effect on the structure of the aromatic system. The, usually planar, structure is distorted such that end rings are bent away from the carborane, and the carboranes itself is shifted in the opposite direction, out of the plane. Understandably, the degree of deformation increases as the overlap between the Van der Waals radius of the carborane and aromatic also increases, and the effect is largest for *ortho*-carborane. These molecules are, somewhat surprisingly, stable, and so we questioned if it is possible to take this principle further, to make even more dramatically deformed carborane-aromatic systems. A logical extension of this work is to incorporate *ortho*-carborane into the bay area of phenanthrene and tetraphene compounds, **Figure 4-1**.

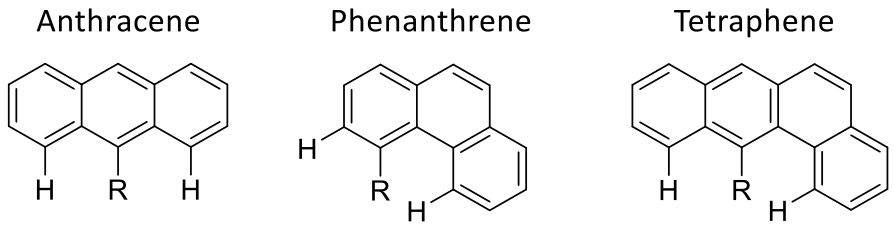


Figure 4-1 – The molecular structures of anthracene, phenanthrene and tetraphene with proximal protons to the substituent -R shown.

The substituent, -R, is situated in the most sterically hindered parts of the molecules. In anthracene, the nearby C-H bond are parallel to R, but in phenanthrene the proximal proton is actively directed towards the substituent. The same is true for tetraphene, however there is an additional 'anthracene-like' proton, further tightening the 'pocket' of space in which the substituent sits. It was theorised that, upon incorporation of the carborane at the -R position, aromatic deformation should increase on the order anthracene < phenanthrene < tetraphene, with the latter compound being a severely sterically strained molecule.

Also discovered in **Chapter 2,** was the property of restricted carborane rotation with increasing aromatic deformation. It was shown in the PL studies in **Chapter 3** that a reduction in carborane rotation increases quantum yield, but also that restriction of the carborane into the global ground state geometry, where the C-C bond is parallel to the aromatic plane, inhibits the efficient TICT radiative decay pathway. Therefore, if one can change this geometry, such that the C-C bond is perpendicular to the plane of the substituent, favouring TICT species formation, PL quantum yield should be increased in aggregated states. Such a ground state geometry can be achieved by substituting the carborane at the C(2) position, with a group that interacts favourably with the aromatic system; a phenyl group.

Intermolecular π-π stacking of adjacent aromatic groups has already been discussed intensively in this thesis, and it is a stabilising force. If phenyl-*ortho*-carborane is attached to an aromatic moiety, the geometry imposed by the architecture of the carborane is likely allow for π-overlap between the two delocalised ring systems. This will reduce the potential energy of the molecule, whilst simultaneously 'locking' the carborane in a geometry with the C-C bond perpendicular to the aromatic plane, favouring TICT species formation.

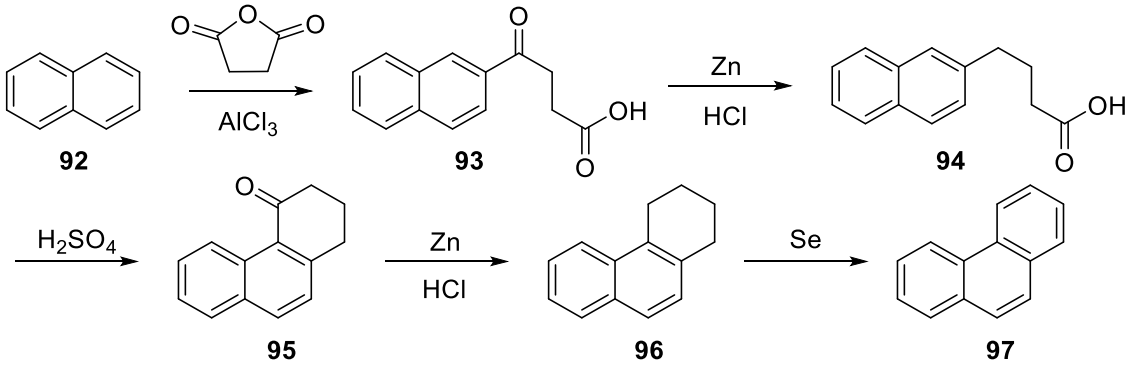
Hence, in this chapter, an investigation into the synthesis, structure, and PL properties of phenyl-*ortho*-carboranyl non-linear acenes is presented. By incorporating the bulky carborane into extremely sterically demanding positions, we aim to create the most sterically deformed aromatic carboranes

ever made. In addition, using a phenyl substituent at the C(2) position, we aim to tune the global ground state geometry of the molecules, such that the carboranyl C-C bond is perpendicular to the aromatic plane, aiding TICT emission. In this way we aim to boost the quantum yield in aggregated states, where AIE is as a result of highly efficient radiative TICT pathways.

4.2 – Synthesis

4.2.1 – Phenanthrene

Those most simple phenacene is phenanthrene, and there are many ways to synthesise it from readily available starting materials. The traditional reaction pathway is the Haworth synthesis from the early 20th century,[1] demonstrated in **Scheme 4-1**.

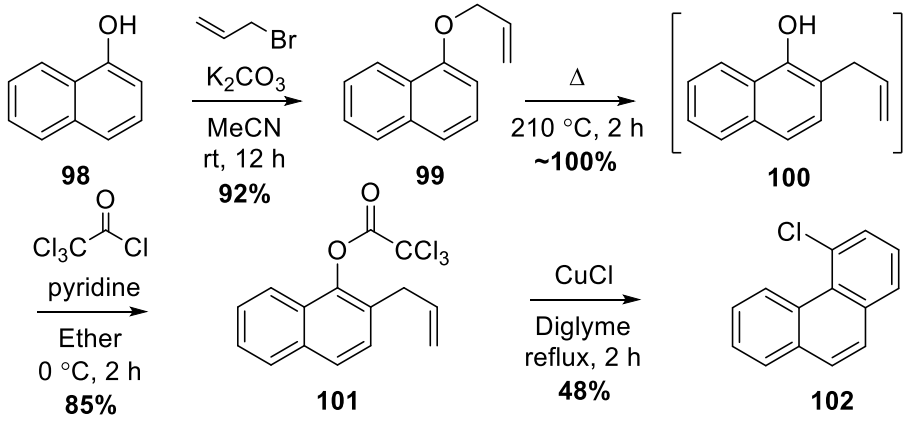


Scheme 4-1 – Haworth synthesis of phenanthrene.

Friedel-Crafts acylation of naphthalene (**92**) with succinic anhydride produces the ketone (**93**), which is reduced in a Clemmensen reaction to form the carboxylic acid (**94**). Acid-catalysed cyclisation forms the cyclic ketone (**95**), which is reduced to the cyclohexane derivative (**96**) and finally dehydrogenated with selenium to form phenanthrene (**97**).

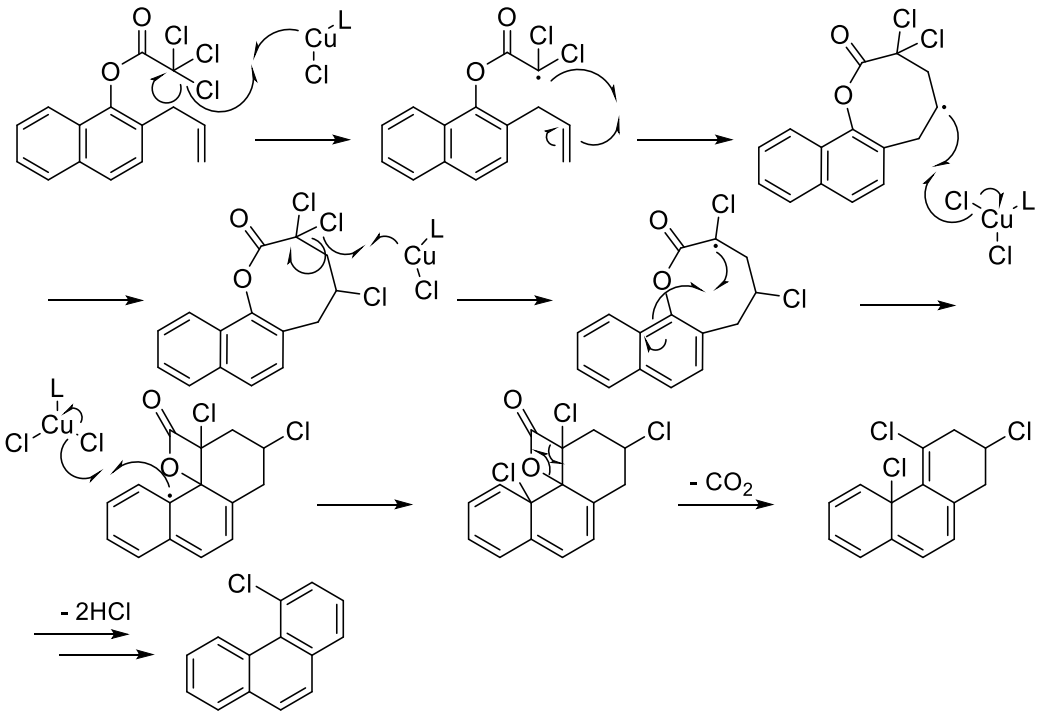
In order to introduce the carborane, either through decaborane/acetylene coupling or nucleophilic attack, selective functionalisation of the 4 position of phenanthrene must first take place (numbering nomenclatures of the acenes in this chapter are presented in **Appendix I**). This is problematic; the 4 and 5 positions have similar reactivities and in electrophilic substitution reactions, e.g. halogenation, disubstitution can occur.[2] Other reactions, such as bromination using $CuBr_2$ supported on alumina leads to regioselective reaction at the 9 position.[3] Monofluorination of phenanthrene at the 4 position *is* possible in a reaction with *N*-fluorobenzenesulfonimide, however this is a minor product only barely detectable in the reaction mixture.[4] To our knowledge, there is no reaction in which a phenanthrene

starting material can be selectivity monosubstituted at the 4 position. 4-Chlorophenanthrene can be conveniently synthesised however, through a naphthyl trichloroacetate, **Scheme 4-2**.



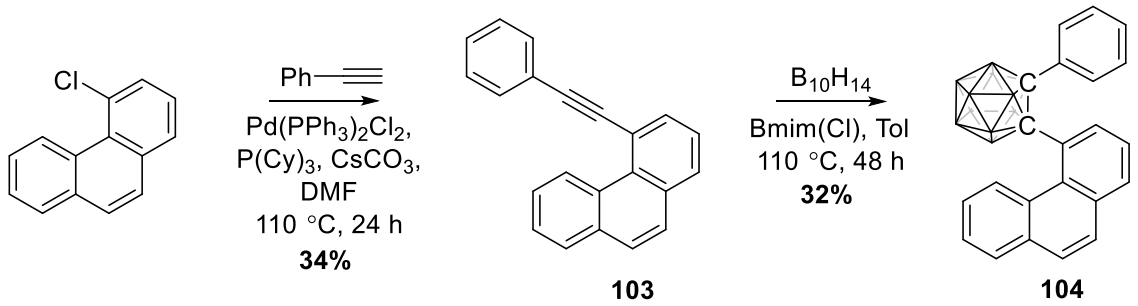
Scheme 4-2 – The synthesis of 4-chlorophenanthrene.

1-Naphthol (**98**) was allylated in conventional Williamson ether synthesis conditions, yielding 1-(allyloxy)naphthalene (**99**). Subsequent Claisen rearrangement at high temperature, followed by esterification with trichloroacetylchloride yielded the trichloroacetate (**101**). The transformation of **101** to 4-chlorophenanthene (**102**) takes place via an atom transfer radical cyclisation (ATRC), known as the Bull-Hutching-Quayle (BHQ) reaction. A proposed mechanism for this is presented in **Scheme 4-3**.[5,6]



Scheme 4-3 – A proposed mechanism for the BHQ reaction. L = solvent ligand.

The BHQ reaction generally leads to the desired PAH and a range of highly insoluble, black, polymeric products. As a result, the yields were relatively modest, however, purification by chromatography was simple; a silica plug eluted with a mixture of DCM and Pet. ether eluent yielded the directed product in high purity. The carborane product, 4-(2'-Ph-*ortho*-$C_2B_{10}H_{10}$)-phenanthrene (**Pho*o*CbPhen**) was then synthesised as in **Scheme 4-4**.

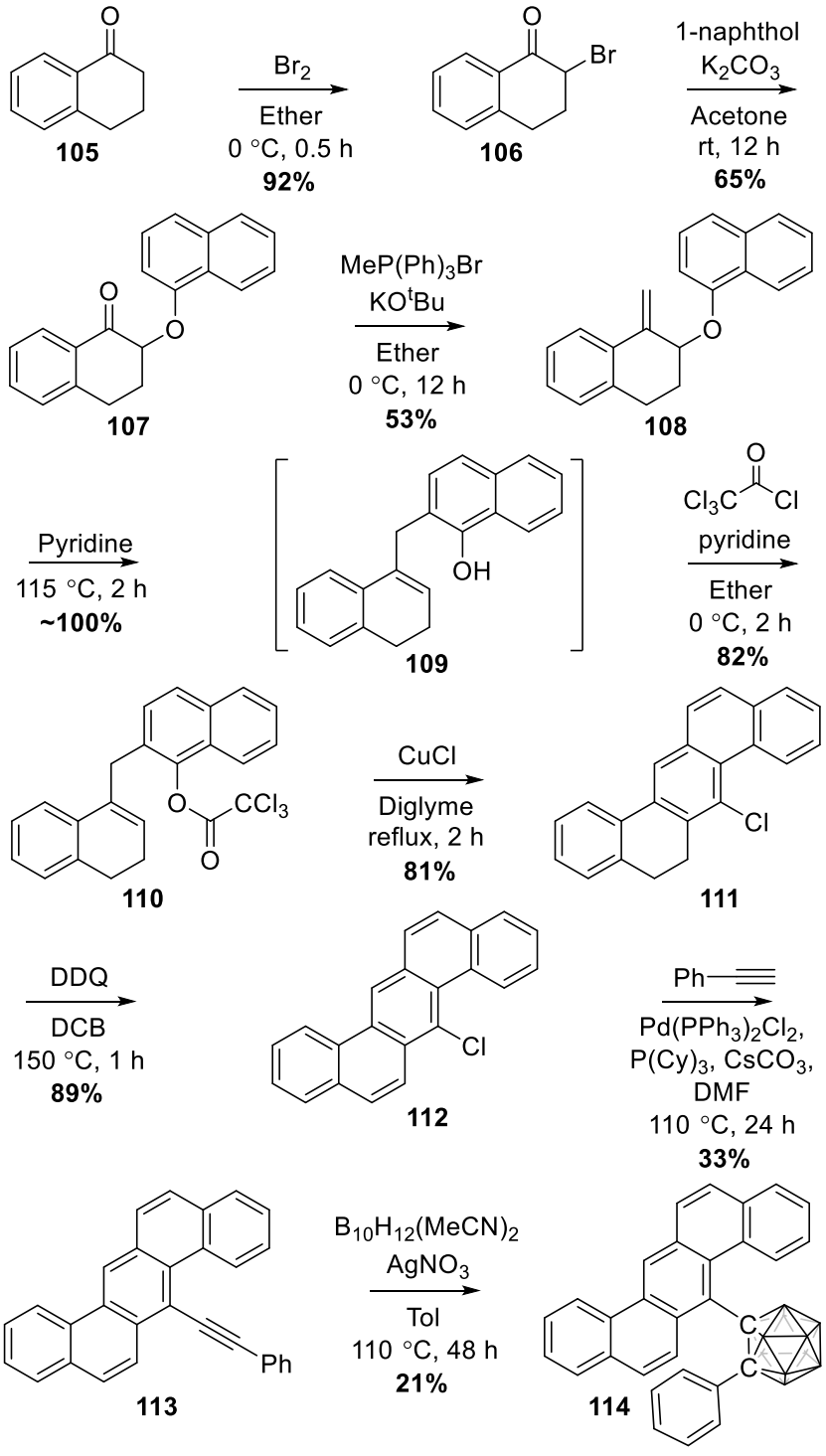


Scheme 4-4 – The synthesis of **Pho*o*CbPhen** from 4-chlorophenanthrene.

Copper-free Sonogashira coupling was employed to introduce the phenylacetylene groups forming **103**; it has been reported that the use of copper in these systems leads to direct alkyne/C-H coupling directly onto the PAH.[6] Whilst phenylacetylene was used for the reasons outlined in the introduction, it also has the added benefit of the product being an internal alkyne. The terminal alkynes described in **Chapter 2** were not stable over long timescales; the highly electron-rich alkynes react with oxygen quite readily. In contrast, these internal alkynes could be stored for long periods and recrystallised to form single-crystals suitable for XRD, as will be discussed later. Ionic-liquid promoted bmim(Cl) decaborane/acetylene coupling yields **Pho*o*CbPhen** in reasonable yield.

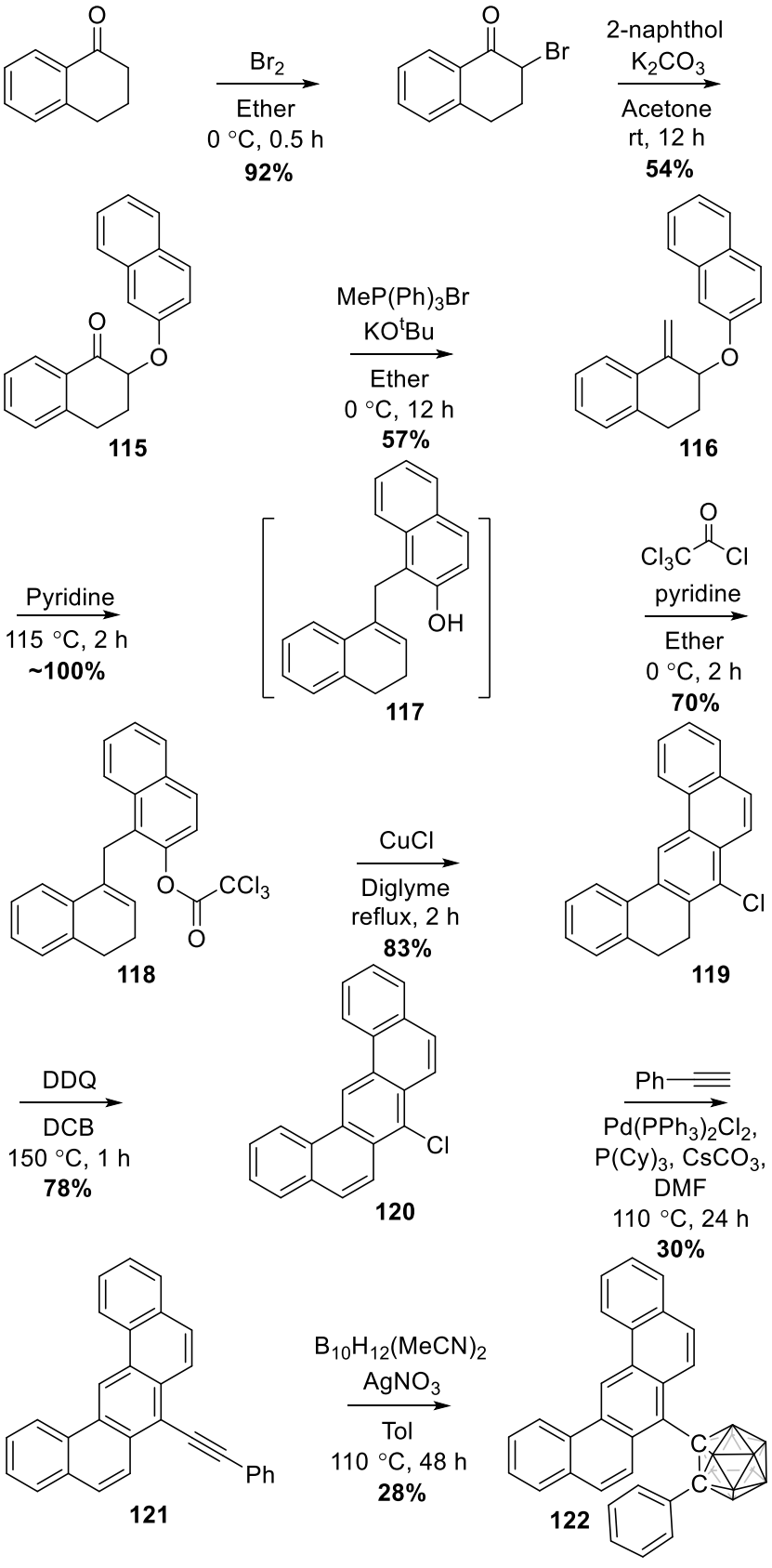
4.2.2 – Benzotetraphenes

Following the successful synthesis of **Pho*o*CbPhen**, attention turned to the tetraphene derivative. The desired chloro-tetraphene compound cannot be synthesised through the BHQ reaction, however, the more symmetrical benzo[*k*]tetraphene can.[6] The synthetic pathway to 7-chlorobenzo[*k*]tetraphene, and then to the carboranyl compound **Pho*o*CbBKT**, is slightly longer than in the phenanthrene case however, as presented in **Scheme 4-5**.



Scheme 4-5 – The synthesis of **Pho*o*CbBKT**.

Using precisely the same methodology, but exchanging 1-naphthol for 2-napthol, allowed for the synthesis of **Pho*o*CbBMT**. Whilst **Pho*o*CbBMT** is likely to exhibit similar aromatic deformation to the ***o*CbAnth** (due to being attached at the 7-position of benzo[*m*]tetraphene), it serves as a good comparison to **Pho*o*CbBKT** for optical studies. The synthesis is outlined in **Scheme 4-6**.



Scheme 4-6 – The synthesis of **Pho*C*bBMT**.

The synthesis of both **Ph*o*CbBKT** and **Ph*o*CbBMT** starts with bromination of 1-tetralone (**105**), yielding the 2-brominated product (**106**). **106** is a severe lachrymator and must be treated with caution. Williamson synthesis on the cyclic bromide forms the naphthol ether (**107** and **115**), and the synthesis then diverges from the analogous phenanthrene pathway for one step; a Wittig reaction using the methyl triphenyl phosphonium ylide installed the methylene group in place of the ketone (**108** and **116**). This creates the six-membered ring structure required for the Claisen rearrangement, making the hydroxyl intermediates (**109** and **117**) before the trichloroacetates (**110** and **118**) were formed from the esterification with trichloroacetylchloride. The BHQ reaction afforded the unsaturated benzotetraphenes (**111** and **119**) in good yield. **111** was a particularly interesting compound; the C(12) and C(13) protons produce precisely equivalent NMR singlets, where one would generally expect two doublets at different chemical shifts.[6] This reason for this has been proposed as being due to the lack of flexibility around the tethered biaryl bond.[6] A similar phenomenon has been observed for the analogous unsaturated 7,17-dichlorodinaphtho[1,2,-b:1',2'-k]chrysene precursor.[6] Aromatisation of **111** and **119** was achieved using 2,3-dichloro-5,6-dicyano-1,4-benzoquinone (DDQ), a reagent commonly used in dehydrogenative aromatisation reactions. Previous reports of this reaction with **111** in 1,2-dichlorobenzene (DCB) noted that the reaction mixture is intensely coloured, as a result of a charge-transfer complex between the benzo[*k*]tetraphene product (**112**) and DDQ, **Figure 4-2**.[6]

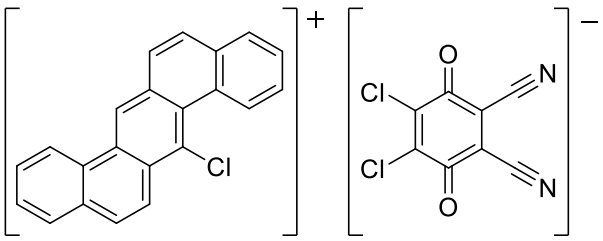


Figure 4-2 – The charge-transfer complex of 7-benzo[*k*]tetraphene and DDQ.

In discussion with the author of that work, it was decided that purification could likely be achieved by simple addition of methanol to the DCB solution. Methanol acts as a reducing agent on the acene, liberating it from the charge-transfer complex to yield **112**, which immediately precipitates from the polar solution. In this way purification became trivial and resulted in a much higher yield than reported. The same reaction and purification methodology isolated 7-chlorobenzo[*m*]tetraphene (**120**) in similarly good yield. Copper-free Sonogashira reactions with phenylacetylene yielded the internal alkynes (**113** and **121**) in a low yield, likely due to evaporation of the acetylene. These were then reacted with the decaborane/acetonitrile adduct in the presence of $AgNO_3$ to yield the carborane products **Ph*o*CbBKT** and **Ph*o*CbBMT** (**114** and **122** respectively). The yields of these reactions were low, but this is to be expected for these internal alkynes; the $AgNO_3$ method was chosen for this reason

as good yields have been reported for similar substrates, albeit not to quite the same degree of steric crowding around the triple-bond.[7]

4.3 – X-ray Crystallography

Recrystallisation of the acetylenes **113** and **121** yielded single-crystals suitable for XRD analysis, however **103** did not produce crystals good enough for diffraction. Crystal structures of **113** and **121** were obtained and are shown in **Figures 4-3** and **4-4**.

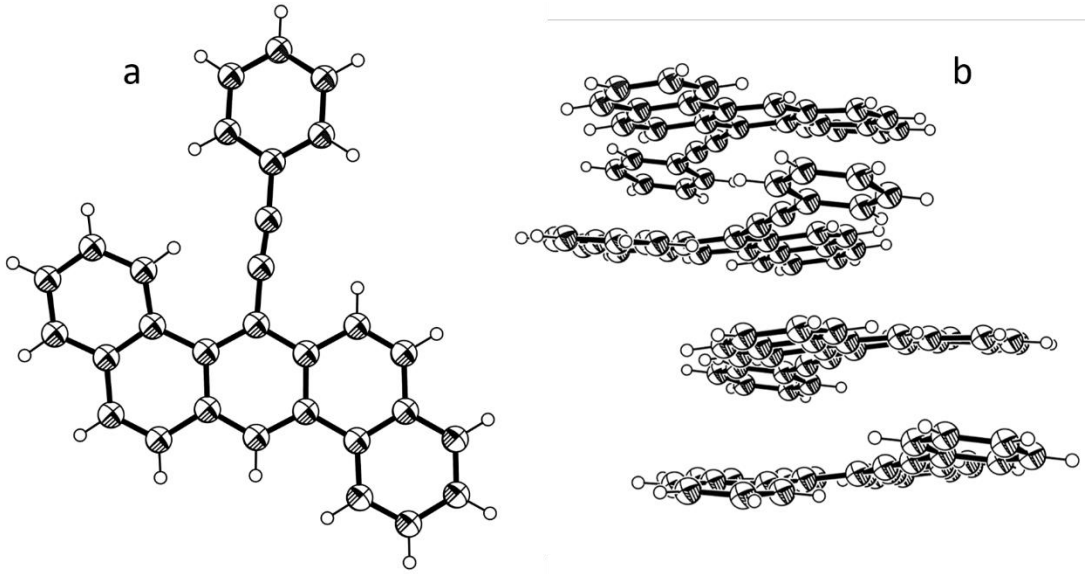


Figure 4-3 – ORTEPs of (a) the molecular structure, and (b) the packing, of 7-(phenylethynyl)-benzo[*k*]tetraphene (**113)**.

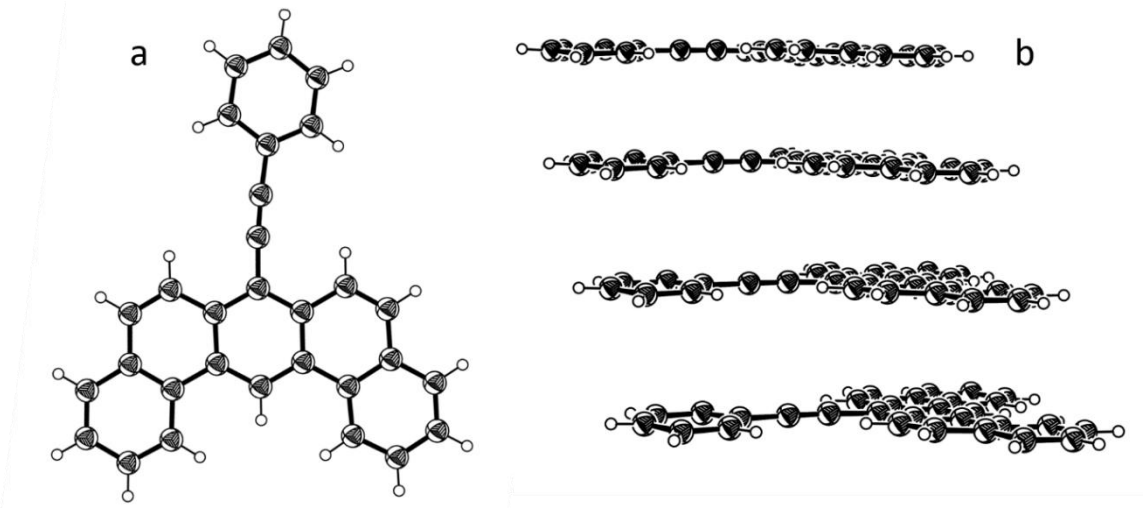


Figure 4-4 – ORTEPs of (a) the molecular structure, and (b) the packing, of 7-(phenylethynyl)-benzo[*m*]tetraphene (**121**).

Both **113** and **121** crystallise into the monoclinic, $P2_1/c$ space group. The molecular structure of **113** is notable for the non-linear triple-bonds; it is moved off the acetylene axis by the proximal C(8) proton. The aromatic is also slightly deformed away from planarity due to the crowded bay region. **121** is essentially planar, however, the acetylene is also slightly non-linear. Given that the molecule should be symmetrical about this bond, it is somewhat surprising that such a phenomenon occurs in this case. It is likely due to forces preserving favourable π-overlap between molecules in the packing arrangement. The packing of both compounds contains significant π-π stacking interactions between the aromatic cores, however, in the **113** case, these are better described as dimeric interactions.

Recrystallisation of **Ph*o*CbPhen**, **Ph*o*CbBKT**, and **Ph*o*CbBMT** from a biphasic solution of DCM and Pet. ether yielded single-crystal suitable for X-ray analysis. The crystal structures are presented in **Figures 4-5**, **4-6**, and **4-7**.

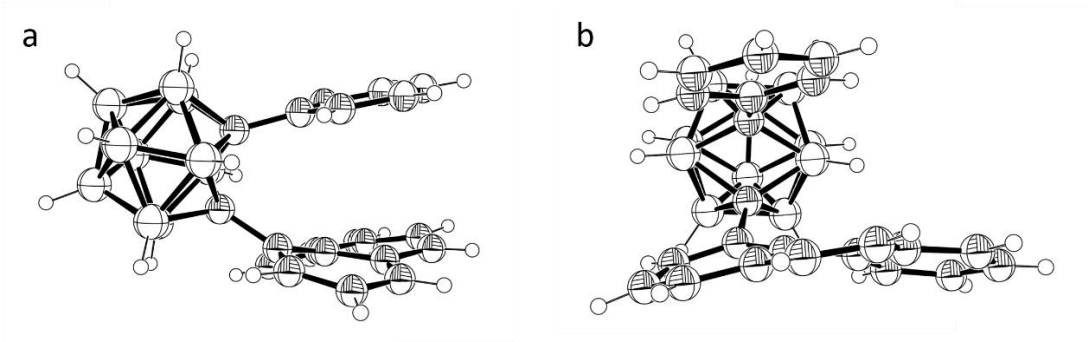


Figure 4-5 – ORTEPs of the molecular structure of **Ph*o*CbPhen** (a) along the molecular axis, and (b) perpendicular to the molecular axis. **Ph*o*CbPhen** crystallises with two independent molecules in the asymmetric unit, molecule (A) (**Table 4-1**) is presented here.

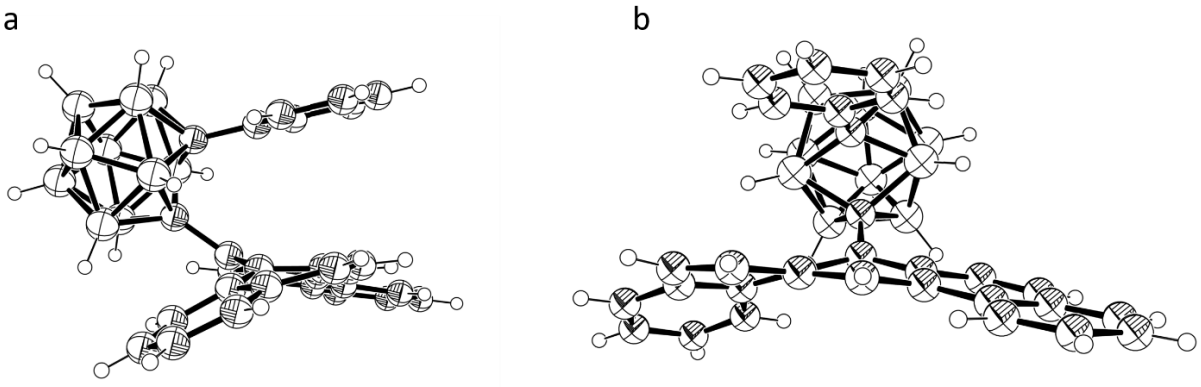


Figure 4-6 – ORTEPs of the molecular structure of **Ph*o*CbBKT** (a) along the molecular axis, and (b) perpendicular to the molecular axis. **Ph*o*CbBKT** crystallises with two independent molecules in the asymmetric unit, molecule (A) (**Table 4-1**) is presented here.

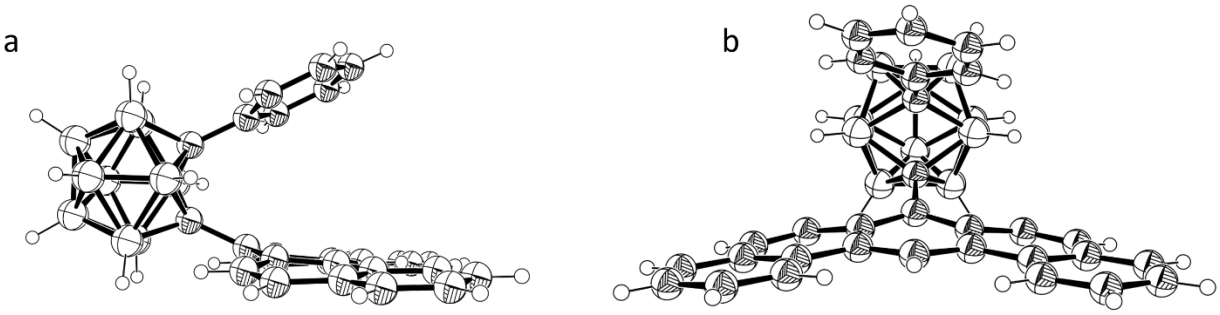


Figure 4-7 – ORTEPs of the molecular structure of **Pho*o*CbBMT** (a) along the molecular axis, and (b) perpendicular to the molecular axis.

Each structure exhibits significant deformation of the aromatic ring system, with the carborane bent out of the plane. In addition, the carboranyl C-C bond is perpendicular to the aromatic plane, with the phenyl group approximately planar to the phenacene. A more detailed account of these phenomena can be obtained **Table 4-1**, with reference to the deformation quantities described in **Appendix III**.

Compound	α (°)	β (°)	γ (°)	ϕ (°)	θ (°)	C(1)-C(2) Bond Length (Å)
Pho*o*CbPhen (A)	15.65	13.15	125.91	66.75	168.55	1.759
Pho*o*CbPhen (B)	14.77	10.88	126.21	70.72	169.27	1.769
Pho*o*CbBKT (A)	22.82	12.93	120.57	74.67	166.34	1.830
Pho*o*CbBKT (B)	23.37	13.95	120.02	77.68	166.30	1.827
Pho*o*CbBMT	17.19	6.47	-	86.29	170.46	1.817

Table 4-1 – Summary of the aromatic deformation quantities and carborane structural values of **Pho*o*CbPhen**, **Pho*o*CbBKT**, and **Pho*o*CbBMT**, as measured from single-crystal XRD data. Labels (A) and (B) refer to structurally independent molecules in the asymmetric unit.

The dihedral angle ϕ, a measure of the relative angle between the carboranyl C-C bond and the aromatic plane, ranges between ca. 70-90°. This geometry is imposed by favourable interactions between the phenyl group and the acene ring, with the distance between the two groups (**Appendix III**) ranging between 3.6-4.0 Å; perfectly in the range for favourable π-π stacking interactions. In addition, the θ angle is less than 180° which increases the overlap of the two aromatic groups further aiding the intramolecular bonding. Lastly, the carboranyl C-C bond length is, for all compounds, larger than the parent *ortho*-carborane. This is consistent with previous reports of *ortho*-carborane substituted with two bulky groups.[8]

The α and β quantities for **Pho*o*CbBMT** are similar to the anthracenyl carboranes, which is understandable given the, essentially identical, geometry around the carborane. For **Pho*o*CbPhen** the β is much larger, and for **Pho*o*CbBKT** both α and β angles are larger. In fact, **Pho*o*CbBKT** (B) has the highest deformation parameters of any carborane ever reported, with values on the order of cyclic 9,10-anthracenophanes, **Table 4-2**.

Compound	α (°)	β (°)	α + β (°)
[6](9,10)anthracenophane[9]	24.7	18.5	43.2
Pho*o*CbBKT (B)	**23.37**	**13.95**	**37.32**
Pho*o*CbBKT (A)	**22.82**	**12.93**	**35.75**
Pho*o*CbPhen(A)	**15.65**	**13.15**	**28.8**
9,10-Bis(2-phenyl-*ortho*-carborane)anthracene[10]	21.5	6.4	27.9
5,12-Bis(2-phenyl-*ortho*-carborane)tetracene[11]	20.2	7.2	27.4
Pho*o*CbPhen (B)	**14.77**	**10.88**	**25.65**
9-(2-phenyl-*ortho*-carborane)anthracene[12]	15.7	8.0	23.7
Pho*o*CbBMT	**17.19**	**6.47**	**23.66**
***o*CbAnth**	**13.6**	**7.2**	**20.8**
9-(2-trimethylsilyl-*ortho*-carborane)anthracene[12]	13.5	4.5	18.0
9-(2-methyl-*ortho*-carborane)anthracene[12]	13.4	4.5	17.9

Table 4-2 – Deformation angles α and β of carboranes in this thesis (in bold), in comparison to similarly deformed cyclic 9,10-anthracenophanes and carborane-containing acenes.

For **Pho*o*CbPhen** the C(5) proton pushes the carborane-phenanthrene bond away from perpendicularity, such that the γ angle increases by ca. 5°. A much smaller value is observed for **Pho*o*CbBKT**, likely because such a movement would push the carboranes closer to the C(6) proton.

The intermolecular bonding in these compounds is also of interest and presented in **Figure 4-8**.

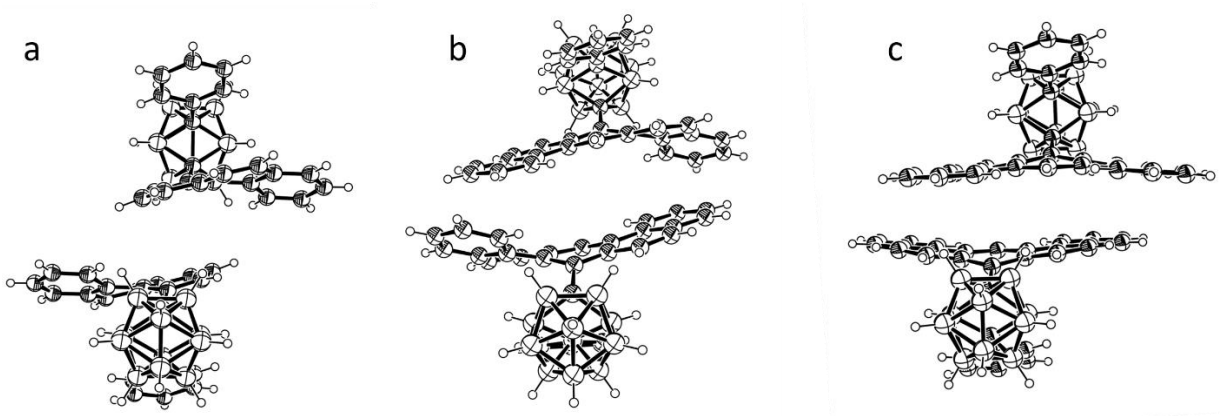


Figure 4-8 – ORTEPs of the dimerisation of (a) **Pho**CbPhen, (b) **Pho**CbBKT, (c) **Pho**CbBMT, in the crystal packing.

In the crystal packing of the carborane compounds, each show dimerisation of the aromatic cores. Intermolecular bonding occurs on the opposite side to which the carborane resides; clearly the bulky moiety precludes the close proximity required to achieve π-π stacking on the other side.

4.4 – Calculations

Given the large potential energy barrier to rotation observed in carboranes in **Chapter 2**, it seemed pertinent to carry out a similar study on the, more sterically hindered, carboranes in this Chapter. Potential energy and carboranyl C-C bond length as a function of dihedral rotation is presented in **Figure 4-9**.

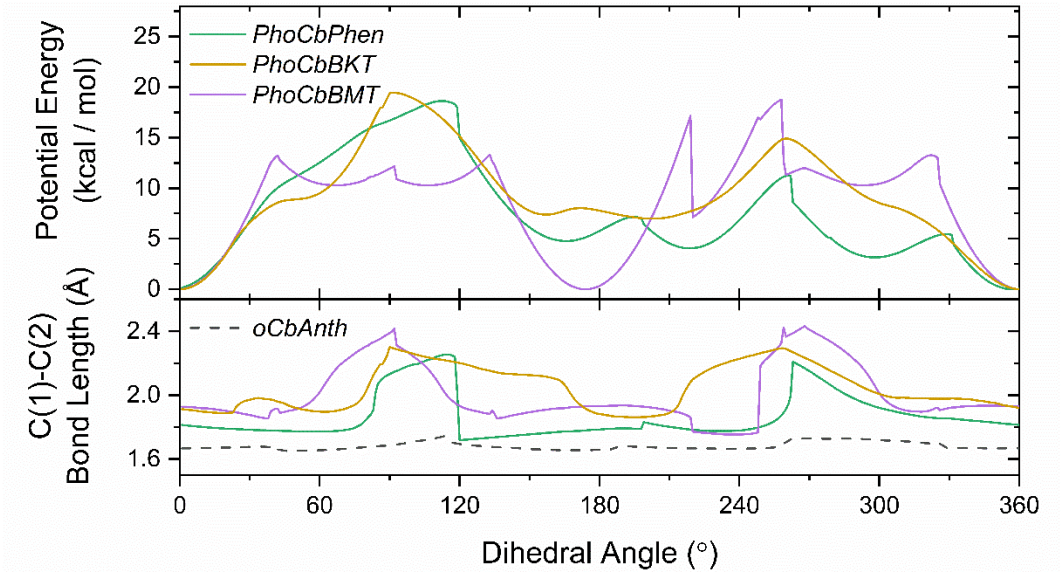


Figure 4-9 – DFT (B3LYP/6-31G(d,p); gas phase) calculated potential energy surface and C(1)-C(2) bond lengths of **Pho**CbPhen, **Pho**CbBKT and **Pho**CbBMT, as a function of dihedral angle at 1° intervals, relative to the ground state energy of each. The arbitrarily defined 0° state is the global ground state geometry. Dihedral rotation for **Pho**CbPhen, **Pho**CbBKT and **Pho**CbBMT occurs in the direction of the C(5), C(6) and C(8) atoms respectively.

The potential energy curve of **Ph*o*CbBMT** exhibits global energy minima at both 0° and ca. 180°. This is due to the plane symmetry of benzo[*m*]tetraphene perpendicular to the molecular axis, and that the aromatic ring system flips when the carboranes rotates, akin to ***o*CbBDT** and ***o*CbNTP** in **Figure 2-17**. Due to this, it is somewhat surprising that the PES is not quite symmetrical about the centre. This is likely an experimental error; the resolution of the calculations is 1° and given that the second energy minimum does not occur at precisely 180°, the geometries calculated in the second half of the PES are slightly different than those in the first half.

The energy barrier to rotation is large for all the carboranes, approximately 5 kcal / mol larger than the barrier to rotation for ***o*CbAnth** (**Figure 2-5**). The barriers for **Ph*o*CbPhen** and **Ph*o*CbBKT** are also slightly higher than **Ph*o*CbBMT**, coinciding with rotation towards the phenanthryl proton. Clearly however, the presence of the phenyl group has a larger effect on the overall barrier to rotation than the presence of the structure of the phenacene. Interestingly, the C-C bond length changes drastically during rotation for all the carboranes studied, to a much greater degree than ***o*CbAnth** which contains no such phenyl group. Increases in C-C bond length coincides with significant increases in the PES, which suggests that the steric interactions between the carboranes and the large aromatic moieties are minimised by increasing the space between them. Bond lengths of ca. 2.3-2.4 Å are usually observed in TICT species, so it is surprising that such phenomena are observed in the ground state.

4.5 – Optical Studies of the Carboranyl Non-Linear Acenes

To begin the investigation into the photoluminescence properties of the carboranyl non-linear acenes, UV-Vis spectroscopy and a simple PL study was carried out on the compounds in THF solutions. The results are presented in **Figure 4-10**.

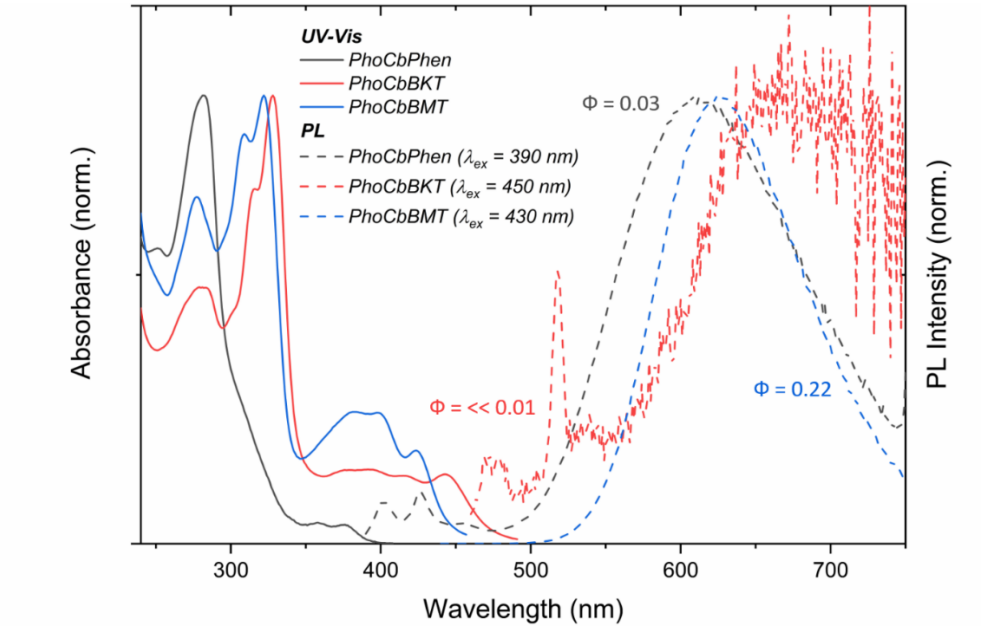


Figure 4-10 – UV-Vis and PL spectroscopy of **Pho*o*CbPhen**, **Pho*o*CbBKT** and **Pho*o*CbBMT** in THF solutions, normalised to the largest peaks. Concentration = ca. 1 x 10^{-4} M, with quantum yields presented.

The UV-Vis of all three compounds show similar behaviour to the carboranes presented in **Chapter 3**, in that the spectra resemble to parent acene compounds,[6] but red-shifted at the band-edge. This is due, as noted in earlier chapters, to the fact that the carborane is itself a very poor absorber of UV light, so the overall shape of the spectrum remains unchanged, however the electron-withdrawing nature of *ortho*-carborane does slightly 'pull' the absorbance to lower energies. Each compound demonstrates a high energy π→π* (E-band) region, and a lower energy π→π* (B-band) region, the latter of which shows a vibronic character, representative of Franck-Condon electronic transitions.

The PL of these compounds are intriguing, as only **Pho*o*CbPhen** exhibits a clear LE, which is a mirror image of the absorption at higher wavelengths. **Pho*o*CbBKT** shows some evidence of LE, and **Pho*o*CbBMT** has no LE at all. Each compound has a large, long-wavelength featureless emission which dominates the PL spectra and increases subtly with the size of the aromatic region. The differences in quantum yield for the compounds are stark and **Pho*o*CbBKT** is virtually non-emissive in THF solution. The reasons for this are not entirely clear; it is possible that excimers of **Pho*o*CbBKT** form in solution (such dimers form in the solid-state as demonstrated in **Figure 4-8**) which allow for non-radiative decay routes. It is also possible that the increase in carboranyl C-C bond length during rotation allows for non-radiative relaxation of ICT states, however, based on the DFT data, one would expect this to also be true for **Pho*o*CbPhen** and **Pho*o*CbBMT**, but both compounds have an appreciable emission in solution. Similarly, all compounds show dimerisation in the solid-state. The patterns in emission intensity do follow the same trends in the degree to which the carboranes are bent out of the aromatic plane; larger degrees

of deformation lead to lower quantum yields. It is possible that this has some impact on the PL, such as if larger deformation allows for greater C-C bond elongation and non-radiative decay via this route, however, on the available evidence it is not possible to definitively explain these phenomena.

4.5.1 – Optical properties of Ph*o*CbPhen

A summary of the concentration, H_2O/THF proportion-dependent and solvatochromic studies for **Ph*o*CbPhen** are presented in **Figure 4-11**, with supporting data presented in **Appendix VII**.

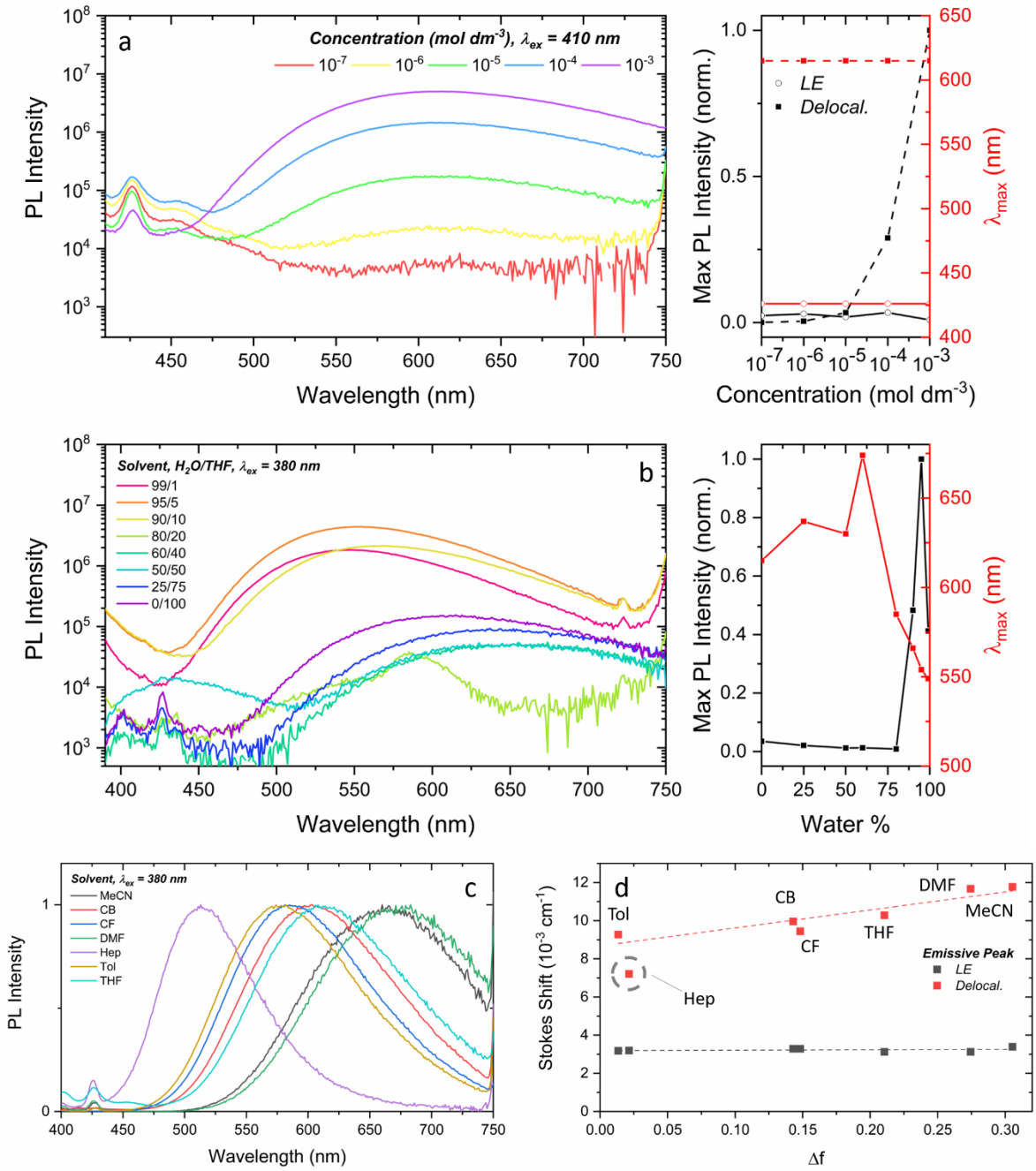


Figure 4-11 – Optical studies of **Pho*CbPhen**; (a) concentration-dependent emission in THF, (b) solvent-dependent (relative proportions of H_2O/THF) emission, (c) solvent-dependent emission, and (d) Lippert-Mataga plot. In (b), λ_{max} refers to the delocalised emission. For solvent dependent plots concentration ca. 1 x 10^{-5} M.

The concentration-dependent study in **Figure 4-11a** reveals a phenomenon not observed in the carborane compounds in **Chapter 3**; the long-wavelength emission decreases in intensity, relative to the LE, as the concentration is decreased. Neither the λ_{max} of the LE or long-wavelength emission changes as a function of concentration. This data suggests that the long-wavelength emission observed for **Pho*CbPhen** results from a non-unimolecular excited state species, such as an excimer or an exciplex. A similar phenomenon is observed in **Chapter 5**, where the emission is probed with

detailed temperature-dependent optical studies. Based on the similarities between that investigation and the observations made from the concentration study, it seems likely that the low-energy emission for **Ph*o*CbPhen** in good solution results from an excimer species, however more detailed study would be required to confidently assert this.

The H_2O/THF proportion solvent study in **Figure 4-11b** demonstrates trends that are subtly different to those that have been observed for similar compounds in **Chapter 3**. Small amounts of H_2O in the solvent actually red-shift the emission, relative to THF solutions. This is probably a result of the more polar solvent environment changing the structure of the excimer species, such that it emits at lower energies. At 80/20 H_2O/THF v/v, emission intensity reaches a minimum, and there is no evidence of the excimer species. Increasing water content beyond this leads to a new emissive peak, centred at λ_{max} = 550 nm, coupled with a drastic increase in PL intensity. Based on the investigations into aggregation in **Chapter 3**, one can confidently assign this emission to AIE, and the excited state to a TICT species. A reduction in the PL intensity at 99/1 H_2O/THF v/v seems therefore seems somewhat anomalous, however, from the counterpart UV-Vis study (**Appendix VII**) it is observed that the absorption intensity also decreases in this solvent. The likely explanation, therefore, is that a reduction in PL intensity is as a result of a lower absorption, however the quantum yield remains unchanged or even increases, as would be expected with more solute material in nanoparticles, as highlighted in **Chapter 3**.

It is also worth noting that **Ph*o*CbPhen** shows no evidence of ICT emission **Figure 4-11b**, however the solvatochromic study and Lippert-Mataga plot in **Figures 4-11c** and **d** do suggest heptane can produce such an emissive species. The emission is significantly blue-shifted relative to low-energy emissive species in the other solvents, and the heptane data point in the Lippert-Mataga plot appears anomalous relative to the positive linear correlation for all other solvents. This correlation demonstrates the delocalised nature of the long-wavelength emission, whilst the lack of any variation in Stokes shift with solvent for the vibronic emission supports the LE designation.

The PLE of **Ph*o*CbPhen** concentration-dependent study, as well as the H_2O/THF proportion solvent study, show something quite intriguing; there appears to be some excitation wavelengths which lead to PL, that are beyond the band-edge of the absorbance, **Figure 4-12**.

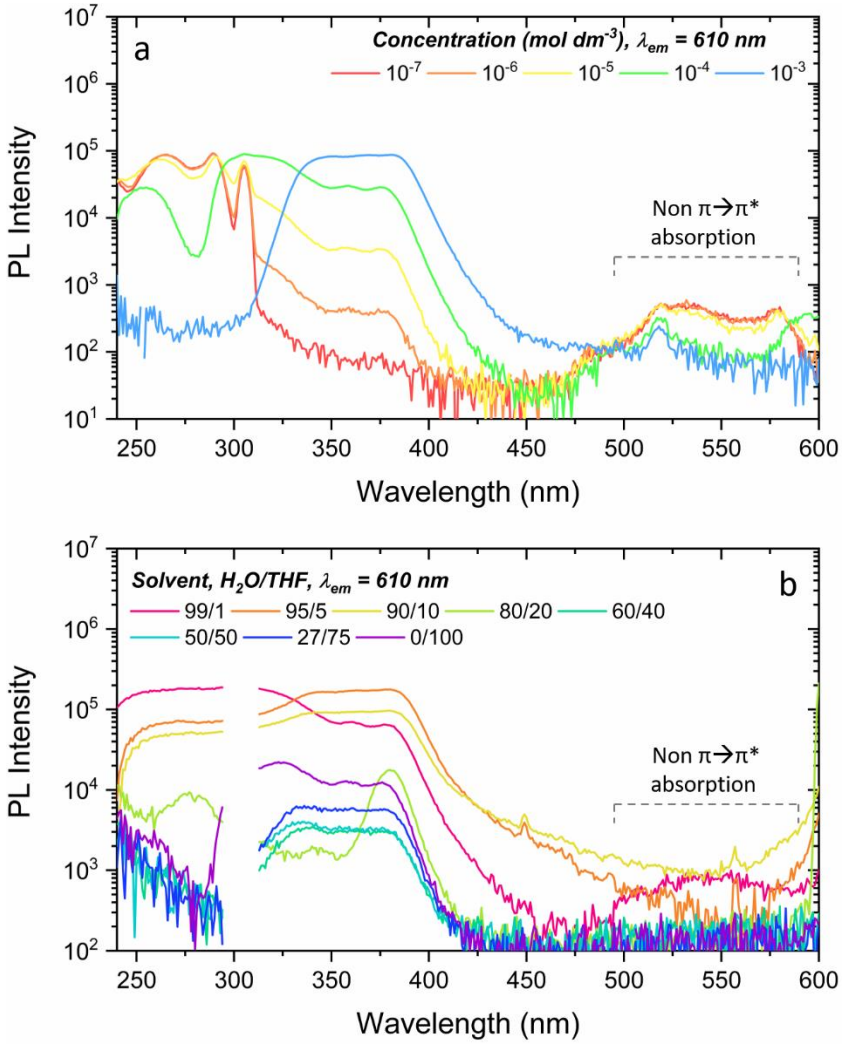


Figure 4-12 – (a) Concentration-dependent (in THF), and (b) solvent-dependent (relative proportions of H_2O/THF), PLE of **Pho*o*CbPhen**, with non π→π* absorbance regions labelled. Concentration in (b) ca. 1 x 10^{-5} M.

The UV-Vis spectra of **Pho*o*CbPhen** from the various optical studies in **Appendix VII** appear to have a band-edge at ca. 420 nm, which varies slightly according to the specific solvent conditions. However, in **Figure 4-12a** and **b** there are clearly wavelengths showing absorbance which are red-shifted significantly relative to the UV-Vis absorbance. These regions of the PLE have a very low intensity, and so it is likely that whilst the absorbance appears to be zero in these regions, there is some absorbance which is not visible above the baseline noise.* Note that if this was not the case then excitation in these regions would cause PL without any absorption, which, to the best of our knowledge, is not physically possible.

* Due to the nature of the instruments used, the PLE spectroscopy is a much more sensitive measurement than UV-Vis spectroscopy.

As discussed in **Chapter 1**, ICT and TICT states are known to form first through excitation of the aromatic region to which the carboranes is attached, and then charge transfer occurs. The low-energy PLE regions of **Ph*o*CbPhen** are, however, red-shifted relative to the onset of the absorption of the vibronic region of the absorbance. This means that excitation wavelengths in these regions are of too low energy to form the S_1 excited state of the aromatic local oscillator, i.e. conventional $\pi \rightarrow \pi^*$ transitions require much higher energy. Photoexcitation of carboranes also requires significantly higher energies.[13] Therefore, these very low energy transitions observed in the PLE are likely due to direct ground state to ICT state transitions.

As ICT states do not have an elongated carboranyl C-C bond, c.f. TICT states, the geometry of ICT states can also be achieved in the ground state. Therefore, a small number of molecules in solution at any time are in a ground state geometry identical to the ICT geometry and there is a non-zero dipole-moment allowing for the vertical excitation into the S_1 excited state. Following this transition, the ICT states can either decay radiatively as ICT states, or rotate into TICT states, or decay non-radiatively. Notably, in **Figure 4-12b**, the 99/1 H_2O/THF v/v PLE shows non $\pi \rightarrow \pi^*$ absorption, but the solution emits solely via a TICT species. These ideas are explored further in **Chapter 5**.

4.5.2 – Optical Properties of Ph*o*CbBKT

A summary of the concentration and H_2O/THF proportion-dependent studies for **Ph*o*CbBKT** are presented in **Figure 4-13**, with supporting data presented in **Appendix VII** (the compound proved poorly emissive in a range of good solvents so solvatochromic data is not presented).

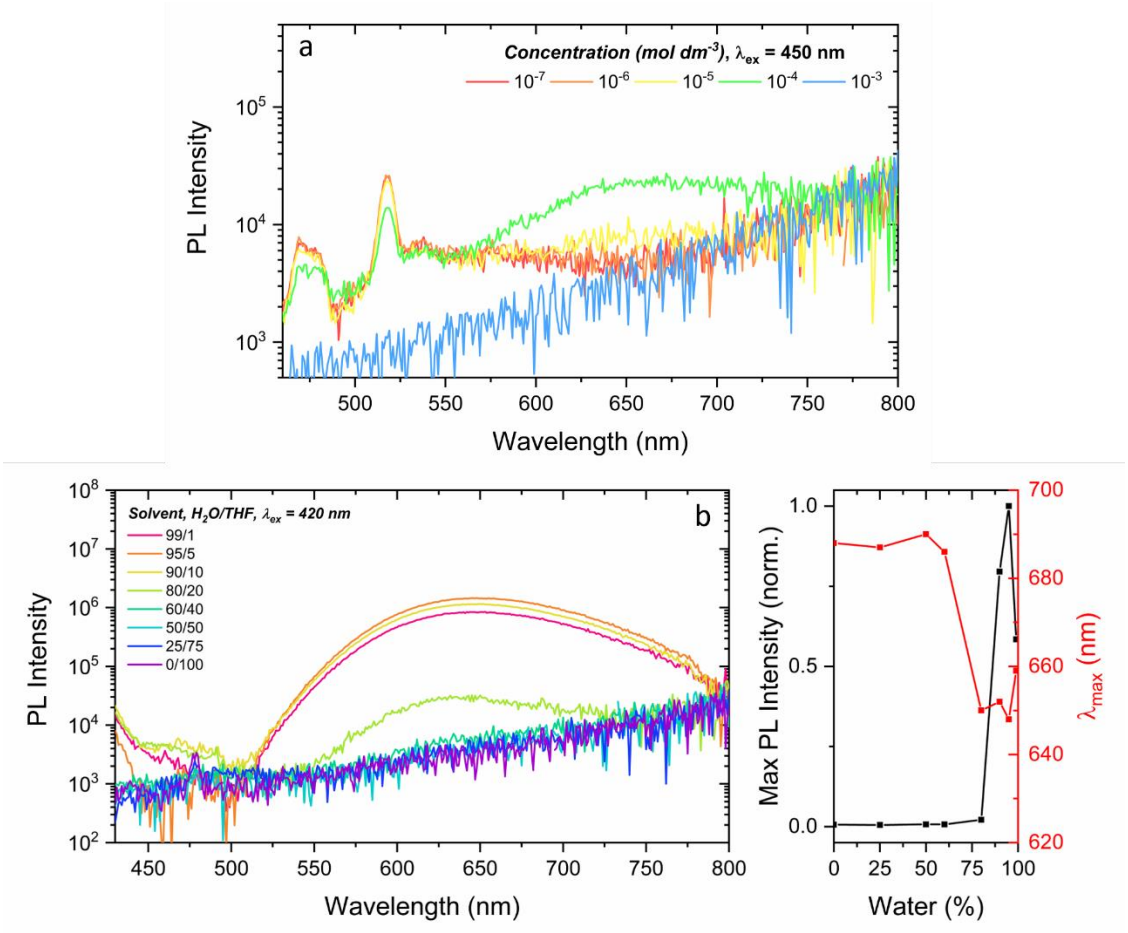


Figure 4-13 – Optical studies of **Pho*CbBKT**; (a) concentration-dependent emission in THF, (b) solvent-dependent (relative proportions of H_2O/THF) emission. For (b) concentration ca. 1 x 10^{-5} M.

The concentration study in **Figure 4-13a** demonstrates that **Pho*CbBKT** is extremely weakly emissive in solution at all the concentrations studied. The LE remains relatively constant from 10^{-7}-10^{-4} M, but a long-wavelength emissive peak arises with increasing concentration. At 10^{-3} M the solution becomes completely non-emissive, which is likely a result of the problems with mask blocking PL as discussed in **Chapter 3**. The nature of the long-wavelength emission is not immediately obvious, but a similar peak can be observed in the H_2O/THF v/v study in **Figure 4-13b**. At low H_2O proportion solvents, the emission is extremely low, but increases dramatically beyond 60/40, with the rise of a broad, delocalised emission at λ_{max} = 650 nm. This is clearly AIE, and the excited state responsible is the TICT species. Of all the compounds considered in this thesis, **Pho*CbBKT** is probably the best example of an AIE-active material; it is essentially non-emissive in good solvents but emits very well when aggregated (details of the quantum yield in all states can be found in **Appendix VII**). Unlike **Pho*CbPhen**, **Pho*CbBKT** shows no clear evidence of non π-π* transitions in the PLE, however there are two points of note with regards to this. First, the emission in good solvents is so low that the both the PL and PLE are very noisy, and so very small peaks cannot be observed above the baseline. Second, for the high-proportion

H_2O solvents where the emission is excellent, and so such small PLE peaks could be observed, the spectrum ends at λ_{ex} = 600 nm. This is because the instrument used has a correction factor that is only calibrated between 240-600 nm. For **Ph*o*CbPhen**, the non π-π* transitions are observed at energies very close to the TICT emission which, for **Ph*o*CbBKT**, is beyond 600 nm. Therefore, it is possible that such transitions are possible for this compound but were not observed due to experimental limitations.

4.5.3 – Optical Properties of Ph*o*CbBKT

A summary of the concentration and H_2O/THF proportion-dependent studies for **Ph*o*CbBKT** are presented in **Figure 4-14**, with supporting data presented in **Appendix VII**.

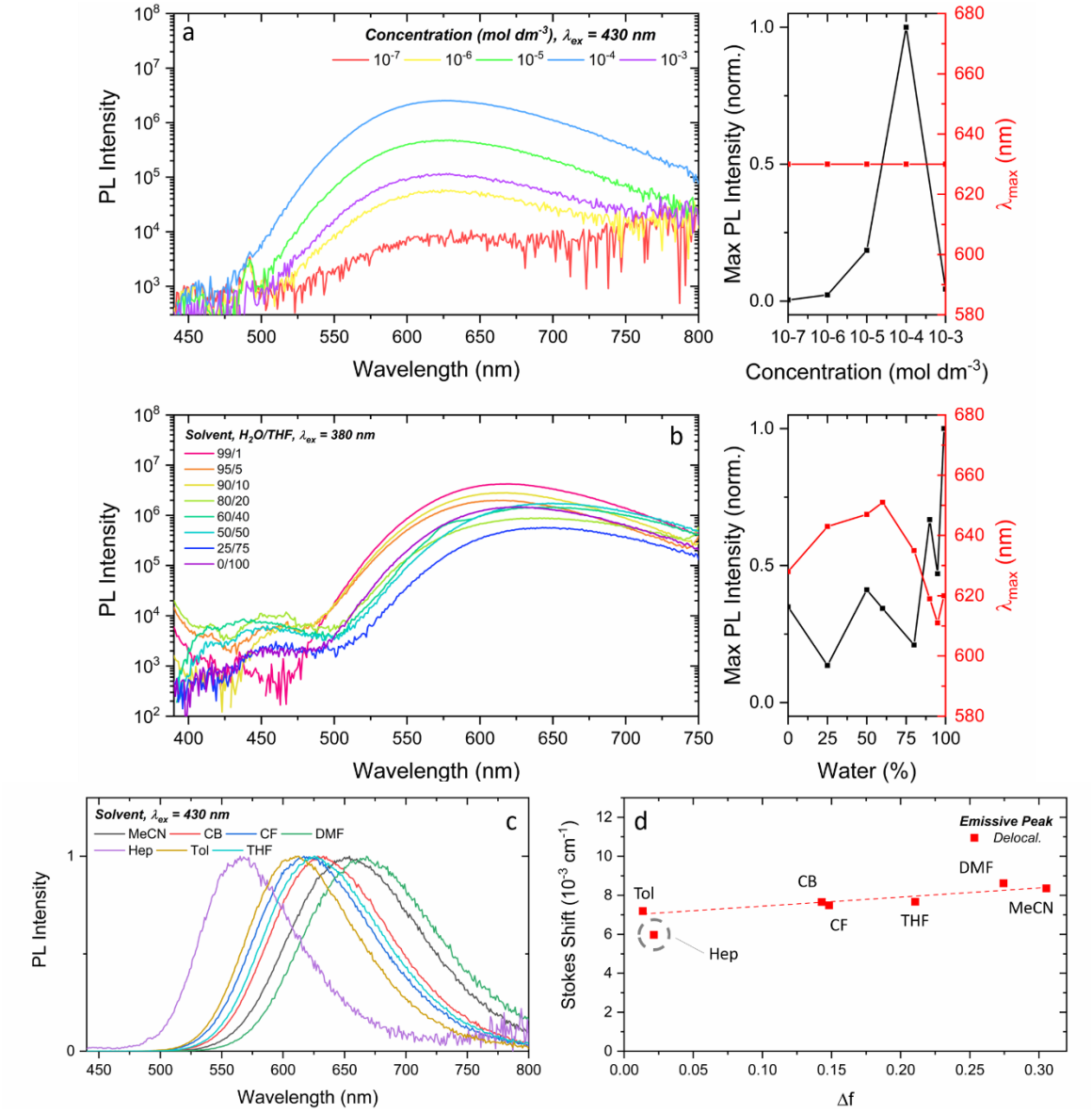


Figure 4-14 – Optical studies of **Pho*C*bBMT**; (a) concentration-dependent emission in THF, (b) solvent-dependent (relative proportions of H_2O/THF) emission, (c) solvent-dependent emission, and (d) Lippert-Mataga plot. In (b), λ_{max} refers to the delocalised emission. For solvent dependent plots concentration ca. 1 x 10^{-5} M.

The concentration study in **Figure 4-14a** shows no discernible LE for **Pho*C*bBKT**, which is unlike all other carboranes considered in this thesis. One explanation for this is that the charge transfer process is highly efficient, such that no LE occurs. It could also be that the locally excited states that do not undergo ICT decay non-radiatively, such as through excimer formation. As shown in **Figure 4-10**, the quantum yield of **Pho*C*bBKT** in THF solution is relatively high, so it is likely that the non-radiative decay pathways are not that efficient. Based on the available data however, it is difficult to determine the structure property relationship. The TICT emission increases with concentration with a power-law dependence, suggesting there are no concentration-dependent non-radiative decay pathways. The

10^{-3} M concentration decreases in intensity due to the experimental errors discussed previously in **Chapter 3**.

The H_2O/THF study in **Figure 4-14b** shows no ICT emission for **Pho*o*CbBKT**, as is true for all the carboranes in this Chapter. The λ_{max} of the emission varies subtly as the H_2O proportion is increased, but the difference between 0/100 and 99/1 v/v is minimal. This suggests the TICT species is the only emissive species in this study. PL intensity increases dramatically at high H_2O proportions, indicative of AIE. The solvatochromism study demonstrates that ICT emission is possible for **Pho*o*CbBKT** in heptane solvent; once again, this is the only solvent that appears anomalous in the Lippert-Mataga plot.

The quantum yields of **Pho*o*CbPhen**, **Pho*o*CbBKT**, and **Pho*o*CbBMT** in solution and solid state are given in **Table 4-3**.

State	Φ		
	Pho*o*CbPhen	Pho*o*CbBKT	Pho*o*CbBMT
THF	0.03	<<0.01	0.22
99/1 H_2O/THF v/v	0.50	0.11	0.44
Solid	0.51	0.38	0.50

Table 4-3 – Quantum yields for **Pho*o*CbPhen**, **Pho*o*CbBKT**, and **Pho*o*CbBMT** in solution and aggregated states.

The quantum yields show a general trend, for all isomers, of increasing from solutions to aggregated solutions and the solid-state. This is due to AIE. In the solid-state all molecules can be considered aggregated but, as discovered in **Chapter 3**, not all molecules in the aggregated solutions are contained within aggregated microstructures. Therefore, for these types of molecules, one should always expect the solid-state to have a slightly higher quantum yield relative to aggregated solutions. Notably, the quantum yields of these compounds are all larger than the *ortho*-carborane compounds in **Chapter 3**. This is consistent with the hypothesis that the phenyl-group will help 'lock' the carborane into a geometry which aids TICT emission, and therefore increase quantum yield. However, the nature of the aromatics is different, and so one must be cautious in drawing structure-property relationships based on this data. Further investigations could focus on this by comparing the quantum yield of *ortho*-carboranyl-acenes with their phenyl-*ortho*-carborane counterparts. It is clear however, particularly with regards to **Pho*o*CbBKT**, that introduction of the phenyl group is not sufficient to produce good quantum yields in good solutions; it is likely that the molecules have enough flexibility to make overcome the 'locking' effect in these conditions.

4.6 – Conclusions

A series of phenyl-*ortho*-carborane substituted non-linear acenes have been designed and synthesised, via a chloro-acene derivatives themselves formed through an improved literature procedure utilising the BHQ cyclisation reaction. Three compounds were formed, **Ph*o*CbPhen**, **Ph*o*CbBKT,** and **Ph*o*CbBMT**, and single-crystal XRD was performed on each of these, and (for the latter two) their acetylene precursors too. Whilst the acetylenes were found to be mostly planar, they demonstrated some degree of deformation about the triple-bond, suggesting that these are strained alkynes and possibly aiding the decaborane coupling reaction. For the carboranes the situation was quite different; each exhibited significant deformation of the aromatic core. In fact, both **Ph*o*CbPhen** and **Ph*o*CbBKT** were measured to have the largest α and β angles of any carborane previously reported, and for the latter these angles were on the order of cyclic 9,10-anthracenophanes. For all compounds the C-C bond in the solid-state was found to be approximately perpendicular to the aromatic plane, aided by intramolecular π-π stacking interactions between the phenyl and acene substituents on the carborane.

DFT calculations probing the effect of dihedral rotation of the carborane showed significant increases in the potential energy during rotation, larger than those observed for non-phenyl-*ortho*-carboranes. This restriction in carborane rotation, coupled with the ground state geometry with the C-C bond perpendicular to the aromatic plane was hypothesised to aid TICT emission. The calculations also demonstrated that the carboranyl C-C bond stretches during rotation of these highly sterically congested structures. This was unexpected and highlighted that the bond is flexible in the ground state, and not just the excited state.

Optical studies of **Ph*o*CbPhen** demonstrated both LE and a long-wavelength delocalised emission, and a concentration study in THF suggested that the latter results from a non-unimolecular species, which we attribute to an excimer. In aggregated states a different emissive species dominates, coupled with a large increase in PL intensity. This AIE was attributed to a TICT excited state. The PLE of these studies also showed an intriguing excitation peak at energies lower than the vibronic absorption of the UV-Vis spectrum. This was attributed to a direct ground state to ICT state vertical excitation, i.e. excitation of **Ph*o*CbPhen** into the ICT state without first exciting the phenanthrene core, and then a charge transfer process. To the best of our knowledge such a phenomenon has never been reported for carborane compounds.

Ph*o*CbBKT was found to be essentially non-emissive in all good solutions, notably with a lack of LE; the hallmark of PAH photoluminescence. A non-radiative excimer decay pathway was proposed as a

reason for this, however the data did not definitively prove this. In aggregated solutions a TICT emission was observed, with good quantum yield, showing **Ph*o*CbBKT** to be the best of example of an AIE-active molecule of all the compounds in this thesis. **Ph*o*CbBMT** behaved similarly in optical studies, with no significant LE being observed in any state. The compound does, however, emit with reasonable quantum yield in good solutions as a result of TICT emission. The exact reasons for this difference between **Ph*o*CbBKT** and **Ph*o*CbBMT** are not clear, as it is hard to extricate the influence of the specific aromatic systems from the effect of the carborane-induced deformation on the system. However, the lack of LE for both suggests some non-radiative decay pathway associated with this excited state species is present for both compounds, but the latter can decay into a TICT state more efficiently, such that radiative emission can occur before all LE states return to the ground state. More detailed optical studies, such as low-temperature PL could be used to probe these ideas.

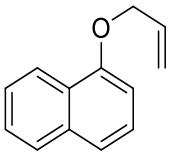
Lastly, the quantum yield in all compounds in this Chapter in the solid-state are larger than the *ortho*-carboranyl compounds in **Chapter 3**. This finding is in-line with the hypothesis that steric-induced restriction of the rotation of the carborane, when the C-C bond is perpendicular to the aromatic plane in the global ground state geometry, will help to increase the quantum yield in aggregated states. However, to solidify this structure-property relationship, further investigations are required.

4.7 – Experimental

Materials and characterisation techniques for this Chapter are identical to those described in **Chapter 2**. Steady-state PL was carried out as described in **Chapter 3**.

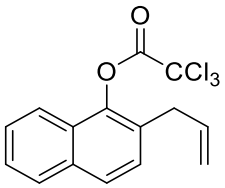
Warning: Exposure to PAH-containing substances increases the risk of cancer in humans.[14] **Replication of these syntheses should be proceeded with caution.**

1-(Allyloxy)naphthalene[6] (99)



Allyl bromide (17.99 mL, 208 mmol) was added to a suspension of 1-naphthol (15.00 g, 104 mmol) and K_2CO_3 (43.13 g, 312 mmol) in dry acetonitrile (300 mL) and stirred overnight at room temperature. The inorganic components were separated by vacuum filtration and washed with diethyl ether (300 mL). The filtrate was washed with water (5 x 200 mL), brine (2 x 200 mL) and dried over $MgSO_4$. Solvent was removed *in vacuo* yielding the *title compound* as a yellow oil (17.63 g, 95.7 mmol, 92%), which was subsequently used without further purification. ^{1}H NMR (400 MHz, $CDCl_3$) δ 8.45-8.40 (1H, m), 7.91-7.85 (1H, m) 7.62-7.39 (4H, m), 6.86 (1H, d, *J* = 7.8 Hz), 6.30-6.19 (1H, m), 5.62 (1H, dd, *J* = 17.2, 1.5 Hz), 5.41 (1H, dd, *J* = 10.6, 1.5 Hz) 4.76 (2H, d, *J* = 5.1 Hz) ppm. ^{13}C NMR (100 MHz, $CDCl_3$) δ 154.6, 134.9, 133.6, 127.8, 126.7, 126.1, 126.0, 125.5, 122.4, 120.7, 117.6, 106.4, 69.2 ppm. HRMS (EI^+) $C_{13}H_{12}O$ requires 184.0888, found 184.0879.

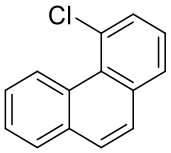
2-Allyl-1-(2,2,2-trichloroacetyl)naphthalene[6] (101)



1-(Allyloxy)naphthalene (15.00 g, 81.4 mmol) was heated under argon, with stirring, for 2 h at 210 °C, after which the heating was removed and the brown oil was allowed to cool to room temperature. Dry diethyl ether (300 mL) and pyridine (9.00 mL, 111 mmol) were added, the solution was cooled to 0 °C and trichloroacetyl chloride (12.50 mL, 111 mmol) was added dropwise. The mixture was stirred for 2 h then allowed to warm to room temperature. The brown solution was poured into a slurry of ice-water (200 g) and $NaHCO_3$ (5 g), washed with water (2 x 100 mL), saturated aq. NH_4Cl (3 x 100 mL), water (3 x 100 mL), brine (2 x 100 mL), and dried over $MgSO_4$. Solvent was removed *in vacuo* yielding the *title compound* as an orange solid (22.81 g, 69.2 mmol, 85%), which was subsequently used without further purification. m.p. 68-70 °C. ^{1}H NMR (400 MHz, $CDCl_3$) δ 7.91-7.84 (2H, m), 7.80 (1H, d, *J* = 8.5 Hz), 7.60-7.48 (2H, m) 7.41 (1H, d, *J* = 8.5 Hz) 6.03-5.91 (1H, m), 5.16 (1H, m), 5.13 (1H, t, *J* = 1.5 Hz) 3.52 (2H, m) ppm. ^{13}C NMR (100 MHz, $CDCl_3$) δ 160.7, 143.8, 135.4, 133.9, 128.8, 128.4, 128.0,

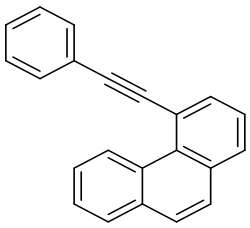
127.7, 127.6, 126.6, 120.6, 117.4, 34.6 ppm. HRMS (APCI) $C_{15}H_{11}Cl_3O_2$ requires 328.9897, found 328.9897.

4-Chlorophenanthrene[6] (102)



2-Allyl-1-(2,2,2-trichloroacetyl)naphthalene (4.00 g, 12.1 mmol) was dissolved in dry diglyme (4 mL) and the solution was purged with argon for 20 mins. Cuprous chloride (5 mol%, 60 mg, 0.61 mmol) was added and the mixture was purged with argon for a further 20 mins before being heated to reflux for 2 h, or until HCl gas emission ceased. The mixture was cooled, loaded directly onto a flash chromatography column and eluted with 1:9 DCM:Pet. ether. The product fractions were left to slowly evaporate, yielding the *title compound* as a white crystalline solid (1.24 g, 5.83 mmol, 48%). m.p. 59 °C. ^{1}H NMR (400 MHz, $CDCl_3$) δ 10.59-10.50 (1H, m), 8.16 (1H, dd, *J* = 7.3, 1.4 Hz), 7.98-7.92 (2H, m), 7.80 (2H, m), 7.70-7.63 (3H, m) ppm. ^{13}C NMR (100 MHz, $CDCl_3$) δ 134.6, 133.6, 133.4, 131.1, 130.2, 128.8, 128.3, 127.8, 127.3, 126.7, 126.6, 126.1, 120.2, 98.1 ppm. HRMS (EI^+) $C_{14}H_9Cl$ requires 212.0393, found 212.0402.

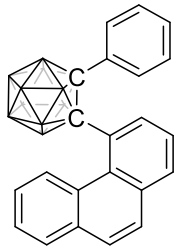
4-(Phenylethynyl)phenanthrene (103)



4-Chlorophenanthrene (2.00 g, 9.40 mmol), cesium carbonate (3.06 g, 9.40 mmol), bis(triphenylphosphine)palladium(II) dichloride (10 mol%, 660 mg, 0.94 mmol) tri(cyclohexyl)phosphine (20 mol%, 527 mg, 1.88 mmol) and phenylacetylene (4.13 mL, 37.6 mmol) were added to a flask charged with dry DMF (30 mL), and the mixture was purged with argon before being heated to 110 °C overnight. After cooling to room temperature, the mixture was added directly to a silica plug (Pet. ether), which was eluted first with Pet. ether, then 1:5 DCM:Pet. ether to eluted the crude product. Solvent was removed *in vacuo* and the crude product was subjected to column chromatography Pet. ether eluent, yielding the *title compound* as colourless crystals (893 mg, 3.20 mmol, 34%). m.p. 72-73 °C. ^{1}H NMR (400 MHz, $CDCl_3$) δ 10.40 (1H, dd, *J* = 8.3, 0.8 Hz), 7.98 (1H, dd, *J*

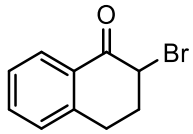
= 7.4, 1.4 Hz), 7.91 (2H, td, *J* = 8.3, 1.4 Hz), 7.75 (2H, m), 7.72-7.62 (4H, m), 7.57 (1H, t, *J* = 7.6 Hz), 7.48-7.38 (3H, m) ppm. ^{13}C NMR (100 MHz, $CDCl_3$) δ 135.2, 133.5, 133.4, 131.7, 131.1, 130.1, 130.0, 128.9, 128.7, 128.2, 127.7, 127.2, 126.6, 126.3, 125.9, 124.1, 119.6, 95.2, 92.8 ppm. HRMS (EI^+) $C_{22}H_{14}$ requires 278.1096, found 278.1103.

4-(2-phenyl-1,2-dicarbadodecaboran-1-yl)phenanthrene (104)



4-(Phenylethynyl)phenanthrene (286 mg, 1.03 mmol) and decaborane (377 mg, 3.09 mmol) were added to a vigorously stirring flask charged with a biphasic mixture of bmim(Cl) (162 mg, 0.93 mmol) and dry toluene (10 mL), and the mixture was heated to reflux for 48 h. After cooling the solvent was removed *in vacuo* and the crude product was subjected to column chromatography with hexane eluent, yielding the *title compound* as bright green crystals (131 mg, 0.33 mmol, 32%). Crystals suitable for X-ray diffraction analysis were grown by slow evaporation of a biphasic solution of DCM and hexane. m.p. 184 °C. ^{1}H NMR (400 MHz, $CDCl_3$) δ 8.77 (1H, d, *J* = 8.2 Hz), 8.28 (1H, dd, *J* = 7.7, 1.2 Hz), 7.77 (1H, dd, *J* = 8.0, 1.2 Hz), 7.60 (1H, ddd, *J* = 8.0, 7.0, 1.2 Hz), 7.48 (1H, ddd, *J* = 8.0, 7.0, 1.2 Hz), 7.42 (1H, d, *J* = 8.6 Hz), 7.38 (1H, dd, *J* = 7.7, 1.0 Hz), 7.30 (1H, t, *J* = 7.7 Hz), 7.04 (1H, d, *J* = 8.6 Hz), 6.94 (1H, m), 6.67-6.61 (2H, m), 6.50-6.44 (2H, m), 4.29-1.51 (10H, br) ppm. ^{11}B NMR (128 MHz, $CDCl_3$) δ -0.68, -1.85, -2.60, -3.78, -9.74, -10.90 ppm. ^{13}C NMR (100 MHz, $CDCl_3$) δ 139.6, 133.3, 133.2, 133.0, 132.6, 130.4, 130.2, 129.9, 129.5, 127.8, 127.6, 127.0, 126.9, 126.8, 124.1, 123.4, 90.9, 89.3 ppm. HRMS (EI^+) $C_{22}B_{10}H_{24}$ requires 396.2916, found 396.2908. ATR-IR (*v* cm^{-1}) 3061, 2593 (B-H) br, 2556 (B-H) br, 2210, 2166, 2051, 1978, 1919, 1604, 1492, 1446, 1257, 1332, 1074, 1019, 1003, 880, 792, 778, 744, 718, 705, 685.

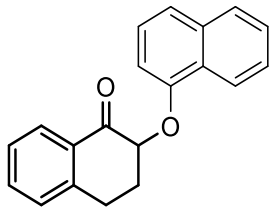
2-Bromo-1-tetralone[6] (106)



Note: this compound is a severe lachrymator and should be treated with caution.

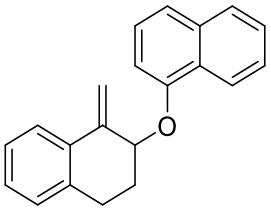
To a stirring solution of 1-tetralone (18.20 mL, 137 mmol) in dry diethyl ether (100 mL) cooled to 0 °C, was added bromine (7.02 mL, 137 mmol) dropwise over 5 mins, and the mixture was stirred for a further 30 mins. Ice water (100 mL) was added to the reaction, followed by sat. sodium sulfite solution (100 mL). The organic layer was separated, washed with water (3 x 100 mL), brine (100 mL), dried over $MgSO_4$. Solvent was removed *in vacuo* to yield the *title compound* as a brown oil (28.37 g, 126 mmol, 92%) which was subsequently used without further purification. ^{1}H NMR (400 MHz, $CDCl_3$) δ 8.09 (1H, dd, *J* = 8.0, 1.4 Hz), 7.52 (1H, td, *J* = 7.6, 1.4 Hz), 7.35 (1H, t, *J* = 8.0 Hz), 7.28 (1H, d, *J* = 7.6 Hz), 4.73 (1H, dd, *J* = 5.1, 3.8 Hz), 3.32 (1H, ddd, *J* = 17.1, 9.8, 4.8 Hz), 2.92 (1H, dt, *J* = 17.1, 4.4, Hz), 2.59-2.41 (2H, m) ppm. ^{13}C NMR (100 MHz, $CDCl_3$) δ 190.9, 143.3, 134.4, 130.3, 129.1, 129.0, 127.4, 50.8, 32.3, 26.5 ppm. HRMS (EI^+) $C_{10}H_9BrO$ requires 223.9837, found 223.9824.

2-(Naphthalene-1'-yloxy)-1-tetralone[6] (107)



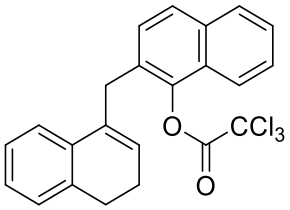
To a stirring suspension of 1-naphthol (14.79 g, 103 mmol) and K_2CO_3 (28.37 g, 205 mmol) in dry acetone (300 mL) was added 2-bromo-1-tetralone (23.12 g, 103 mmol) at room temperature, in one portion, and the mixture was stirred overnight. The inorganic material was removed by vacuum filtration, washed with acetone, and the organic fractions were concentrated *in vacuo*. The brown residue was dissolved in diethyl ether (300 mL), washed with NaOH solution (1.0 M, 3 x 100 mL), water (3 x 100 mL), brine (100 mL) and dried over $MgSO_4$. Solvent was removed in *vacuo* to afford the *title compound* as a light brown solid (19.31 g, 67.0 mmol, 65%). m.p. 95-97 °C. ^{1}H NMR (400 MHz, $CDCl_3$) δ 8.37-8.30 (1H, m), 8.09 (1H, dd, *J* = 8.0, 1.0 Hz), 7.85-7.77 (1H, m), 7.58-7.44 (4H, m), 7.41-7.34 (2H, m), 7.32 (1H, d, *J* = 7.6 Hz), 6.98 (1H, d, *J* = 7.6 Hz), 5.15 (1H, dd, *J* = 10.4, 5.2 Hz), 3.35-3.13 (2H, m), 2.70-2.54 (2H, m) ppm. ^{13}C NMR (100 MHz, $CDCl_3$) δ 195.0, 154.3, 143.6, 135.0, 134.2, 132.3, 129.0, 128.4, 127.8, 127.3, 126.7, 122.6, 121.6, 107.8, 79.7, 30.4, 27.8 ppm. HRMS (EI^+) $C_{20}H_{16}O_2$ requires 288.1150, found 288.1147.

2'-(Naphthalene-1'-yloxy)-1-methylene-2,3,4-trihydronaphthalene[6] (108)



To a vigorously stirring suspension of 2-(Naphthalene-1'-yloxy)-1-tetralone (15.00 g, 52.0 mmol) in dry diethyl ether (200 mL) was added a ylide solution freshly prepared from the addition of methyltriphenylphosphonium bromide (28.17 g, 78.9 mmol) and KO^{t}Bu (8.85 g, 78.9 mmol) to a solution of dry diethyl ether (200 mL) at 0 °C, which had been left stirring for 30 mins. The resulting bright yellow mixture was left stirring overnight, then the inorganic material was removed via suction filtration through celite. The filtration was concentrated *in vacuo* and dry loaded onto a silica plug which was eluted with Pet. ether until a yellow colour appeared in the filtrate, after which eluent was changed to 1:9 DCM:Pet. ether. The yellow filtrate fractions were combined and left to evaporate slowly yielding the *title compound* as bright yellow crystals (7.89 g, 27.6 mmol, 53%). m.p. 101-102 °C. ^{1}H NMR (400 MHz, $CDCl_3$) δ 8.21 (1H, d, J = 8.2 Hz), 7.79 (1H, d, J = 8.0 Hz), 7.64 (1H, dd, J = 8.0, 1.4 Hz), 7.49-7.29 (4H, m), 7.26-7.16 (3H, m), 6.97 (1H, d, J = 7.5 Hz), 5.65 (1H, s), 5.36, (1H, s), 5.24 (1H, dd, *J* = 7.8, 3.2 Hz), 3.21 (1H, dt, *J* = 17.0, 6.4 Hz), 3.0 (1H, dt, *J* = 17.0, 6.4 Hz), 2.44-2.27 (2H, m) ppm. ^{13}C NMR (100 MHz, $CDCl_3$) δ 154.1, 143.3, 136.2, 135.0, 134.2, 129.2, 128.4, 127.8, 126.9, 126.6, 126.6, 126.1, 125.5, 125.5, 122.7, 120.9, 110.4, 107.9, 77.7, 29.7, 27.3 ppm. HRMS (EI$^+$) $C_{21}H_{18}O_2$ requires 286.1358, found 286.1360.

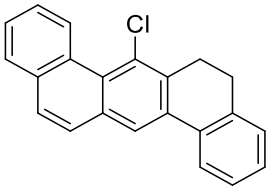
2'-((3,4-Dihydronaphthalen-1-yl)methyl)naphthalen-1'-trichloroacetate[6] (110)



A solution of 2'-(Naphthalene-1'-yloxy)-1-methylene-2,3,4-trihydronaphthalene (19.00 g, 66.3 mmol) in pyridine (18.7 mL, 232 mmol) was heated in an inert atmosphere, with stirring, for 2 h at 115 °C after which the solution was allowed to cool to room temperature. The residue was dissolved with dry diethyl ether (300 mL), cooled to 0 °C and trichloroacetyl chloride (8.84 mL, 79.0 mmol) was added dropwise. The mixture was stirred for 2 h then allowed to warm to room temperature. The brown solution was poured into a slurry of ice-water (200 g) and $NaHCO_3$ (5 g), washed with water (2 x 100

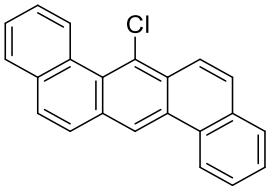
mL), saturated aq. NH_4Cl (3 x 100 mL), water (3 x 100 mL), brine (2 x 100 mL), and dried over $MgSO_4$. Solvent was removed *in vacuo* yielding the *title compound* as a brown solid (23.5 g, 54.4 mmol, 82%) which was subsequently used without further purification. m.p. 125 °C (decomp.). ^{1}H NMR (400 MHz, $CDCl_3$) δ 7.94 (1H, d, *J* = 8.4 Hz), 7.89 (1H, d, *J* = 8.0 Hz), 7.76 (1H, d, *J* = 8.4 Hz), 7.60 (1H, t, *J* = 7.6 Hz), 7.54 (1H, t, *J* = 7.6 Hz), 7.42 (1H, d, *J* = 8.4 Hz), 7.28-7.10 (4H, m), 5.85 (1H, t, *J* = 4.0 Hz) 3.94 (2H, s), 2.84 (2H, t, *J* = 7.8 Hz), 2.40-2.29 (2H, m) ppm. ^{13}C NMR (100 MHz, $CDCl_3$) δ 160.6, 144.0, 136.8, 134.9, 133.8, 133.6, 128.9 128.9, 128.8, 128.4, 127.9, 127.7, 127.6, 127.6, 127.3, 126.8, 126.6, 123.1, 120.5, 90.1, 33.3, 28.5, 23.6 ppm. HRMS (EI$^+$) $C_{23}H_{17}Cl_3O_2$ requires 430.0294, found 430.0309.

7-Chloro-5,6-dihydrobenzo[*k*]tetraphene[6] (111)



2'-((3,4-Dihydronaphthalen-1-yl)methyl)naphthalen-1'-trichloroacetate (4.00, 9.26 mmol) was dissolved in dry diglyme (5 mL) and the solution was purged with argon for 20 mins. Cuprous chloride (5 mol%, 46 mg, 0.463 mmol) was added and the mixture was purged for a further 10 mins before being heated to reflux for 2 h, or until HCl gas emission ceased. After cooling to room temperature, the crude mixture was subjected to column chromatography using 1:9 DCM:Pet. ether, and the *title compound* was isolated as a beige solid (2.36 g, 7.50 mmol, 81%). m.p. 133-134 °C. ^{1}H NMR (400 MHz, $CDCl_3$) δ 9.92 (1H, d, *J* = 8.1, 1.8 Hz), 8.18 (1H, s), 7.93 (1H, d, *J* = 7.6 Hz), 7.91-7.87 (1H, m), 7.72 (2H, s), 7.68-7.60 (2H, m), 7.42-7.34 (1H, m), 7.34-7.31 (2H, m), 3.38 (2H, dd, *J* = 8.6, 5.7 Hz), 3.00 (2H, dd, *J* = 8.6, 5.7 Hz) ppm. ^{13}C NMR (100 MHz, $CDCl_3$) δ 137.9, 136.5, 134.3, 134.1, 134.0, 133.8, 131.0, 130.0, 128.9, 128.5, 128.4, 128.3, 128.0, 127.6, 127.5, 127.5, 127.0, 126.0, 124.9, 123.1, 29.0, 27.4 ppm. HRMS (EI$^+$) $C_{22}H_{15}Cl$ requires 314.0862, found 314.0857.

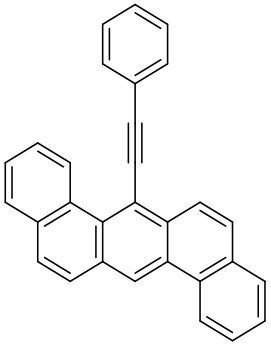
7-Chlorobenzo[*k*]tetraphene[6] (112)



2,3-Dichloro-5,6-dicyano-1,4-benoquinone (DDQ) (10.0 g, 44.0 mmol) was added to a stirring solution of 7-chloro-5,6-dihydrobenzo[*k*]tetraphene (6.00 g, 19.1 mmol) in dry dichlorobenzene (150 mL) and

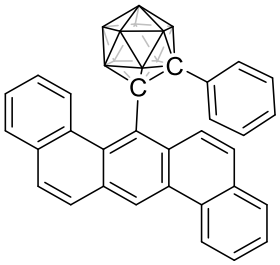
the mixture was heated to 150 °C for 1 h before being allowed to cool to room temperature. Methanol (300 mL) was added and the beige precipitate formed was collected via vacuum filtration, washed with water until the filtrate turned clear, then methanol. Drying yielded the *title compound* as light-brown microcrystals (5.32 g, 39.2 mmol, 89%). m.p. 181 °C. ^{1}H NMR (400 MHz, $CDCl_3$) δ 10.00-9.95 (2H, m), 9.07 (2H, s), 8.84 (2H, dd, *J* = 8.2, 0.6 Hz), 8.63 (2H, dd, *J* = 9.6, 0.6 Hz), 7.97-7.84 (4H, m), 7.78-7.64 (5H, m) ppm. ^{13}C NMR (100 MHz, $CDCl_3$) δ 134.2, 132.8, 131.9, 130.1, 130.1, 130.0, 129.8, 128.9, 128.9, 128.6, 128.0, 127.9, 127.7, 127.6, 127.0, 127.0 126.2, 124.4, 123.5, 122.2 ppm. HRMS (EI^+) $C_{22}H_{13}Cl$ requires 312.0706, found 312.0714.

7-(Phenylethynyl)benzo[*k*]tetraphene (113)



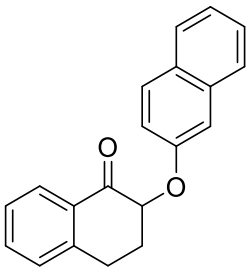
7-Chlorobenzo[*k*]tetraphene (500 mg, 1.60 mmol), cesium carbonate (520 mg, 1.60 mmol), bis(triphenylphosphine)palladium(II) dichloride (10 mol%, 113 mg, 0.16 mmol) tri(cyclohexyl)phosphine (20 mol%, 90 mg, 0.32 mmol) and phenylacetylene (0.71 mL, 4.17 mmol) were added to a flask charged with dry DMF (7 mL), and the mixture was purged with argon before being heated to 110 °C overnight. After cooling to room temperature, the mixture was added directly to a silica plug (Pet. ether), which was eluted first with Pet. ether, then 1:5 DCM:Pet. ether to elute the crude product. Solvent was removed *in vacuo* and the crude product was subjected to column chromatography Pet. ether eluent, yielding the *title compound* as light-orange crystals (200 mg, 0.53 mmol, 33%). Crystals suitable for X-ray diffraction analysis were grown by evaporation from a biphasic solution of DCM and hexane. m.p. 177-178 °C. ^{1}H NMR (400 MHz, $CDCl_3$) δ 10.53 (1H, d, J = 8.0 Hz), 9.10 (1H, s), 8.84 (1H, d, J = 8.0 Hz), 8.80 (1H, d, J = 9.3 Hz), 7.98-7.79 (6H, m), 7.77-7.64 (5H, m), 7.54-7.43 (3H, m) ppm. ^{13}C NMR (100 MHz, $CDCl_3$) δ 133.8, 133.5, 132.1, 131.7, 131.5, 130.4, 130.1, 129.0, 129.0, 128.9, 128.8, 128.7, 128.3, 128.3 127.7, 127.6, 127.6, 127.3, 126.3, 125.8, 124.2 123.9, 123.3, 116.9, 101.9, 91.0 ppm. HRMS (EI^+) $C_{30}H_{18}$ requires 378.1409, found 378.1415.

7-(2-Phenyl-1,2-dicarbadodecaboran-1-yl)benzo[*k*]tetraphene (114)



Decaborane (237 mg, 1.94 mmol) was stirred into dry acetonitrile (0.4 mL) and heated to 60 °C for 2 h, after which the mixture was cooled and diluted with dry toluene (10 mL). 7-(Phenylethynyl)benzo[*k*]tetraphene (221 mg, 0.58 mmol) and $AgNO_3$ (9 mg, 0.051 mmol) were added, and the mixture was heated to reflux for 48 h, after which solvent was removed *in vacuo*, and the residue was subjected to column chromatography with hexane eluent. Recrystallization by evaporation of the column fractions product yielded the title compound as red crystals (61 mg, 0.12 mmol, 21%). Crystals suitable for X-ray diffraction analysis were grown by slow evaporation of a biphasic solution of DCM and hexane. m.p. 268-270 °C. ^{1}H NMR (400 MHz, $CDCl_3$) δ 9.23 (1H, d, J = 9.6 Hz), 8.58-8.52 (1H, m), 8.52 (1H, d, J = 8.0 Hz), 8.31 (1H, s), 7.96-7.90 (1H, m), 7.87 (1H, d, J = 9.6 Hz), 7.82 (1H, dd, J = 8.0, 1.1 Hz), 7.70-7.63 (3H, m), 7.53 (1H, ddd, J = 8.0, 7.6, 1.1 Hz), 7.50 (1H, d, J = 8.6 Hz), 7.10 (1H, m), 7.08 (1H, d, J = 8.6 Hz), 6.64 (2H, t, J = 7.6 Hz), 6.16 (2H, d, J = 7.6 Hz) 4.46-1.11 (10H, br) ppm. ^{11}B NMR (128 MHz, $CDCl_3$) δ 0.61, -0.47, -1.87, -3.10, -9.57 ppm. ^{13}C NMR (100 MHz, $CDCl_3$) δ 137.1, 136.1, 134.1, 131.8, 131.2, 131.1, 130.8, 130.7, 130.6, 130.6, 130.0, 129.9, 128.9, 128.8, 128.7, 127.8, 127.7, 127.6, 127.0, 126.7, 126.5, 124.9, 124.7, 123.9, 123.7, 122.7, 96.9, 92.2 ppm. HRMS (MALDI-ToF) $C_{30}B_{10}H_{28}$ requires 497.3, found 497.3. ATR-IR (*v* cm^{-1}) 3784, 2549 (B-H) br, 2218, 2040, 1953, 1602, 1486, 1446, 1258, 1147, 1068, 1029, 884, 825, 795, 749, 689, 663.

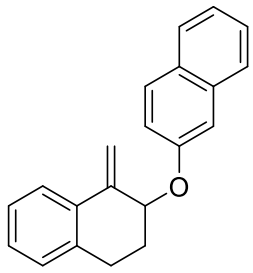
2-(Naphthalene-2'-yloxy)-1-tetralone[6] (115)



To a stirring suspension of 2-naphthol (14.79 g, 103 mmol) and K_2CO_3 (28.37 g, 205 mmol) in dry acetone (300 mL) was added 2-bromo-1-tetralone (23.12 g, 103 mmol) at room temperature in one portion and the mixture was stirred overnight. The inorganic material was removed by vacuum

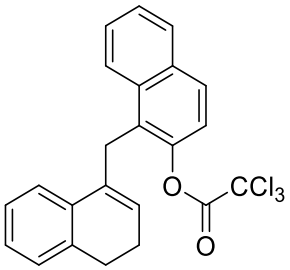
filtration and washed with acetone, and the organic fractions were concentrated *in vacuo*. The brown residue was dissolved in diethyl ether (300 mL), washed with NaOH solution (1.0 M, 3 x 100 mL), water (3 x 100 mL), brine (100 mL) and dried over $MgSO_4$. Solvent was concentration *in vacuo*, methanol (100 mL) was stirred into the brown residue and the solution was cooled to -78 to afford the *title compound* as a light brown precipitate (16.03 g, 55.6 mmol, 54%). m.p. 107-108 °C. ^{1}H NMR (400 MHz, $CDCl_3$) δ 8.09 (1H, dd, J = 8.0, 1.0 Hz), 7.77 (2H, d, J = 9.2 Hz), 7.71 (1H, d, J = 8.2 Hz), 7.54, (1H, td, J = 7.6, 1.2 Hz), 7.43 (1H, ddd, J = 7.6, 6.7, 1.2 Hz), 7.39-7.25 (5H , m), 5.13 (2H, dd, J = 11.5, 4.5 Hz), 3.30-3.14 (2H, m), 2.66-2.56 (1H, m), 2.55-2.42 (1H, m) ppm. ^{13}C NMR (100 MHz, $CDCl_3$) δ 195.1, 156.3, 143.6, 134.7, 134.2, 132.2, 129.8, 129.7, 129.0, 128.3, 128.0, 127.3, 127.2, 126.7, 124.3, 119.5, 109.6. 79.2, 30.2, 27.9 ppm. HRMS (EI^+) $C_{20}H_{16}O_2$ requires 288.1150, found 288.1156.

2'-(Naphthalene-2'-yloxy)-1-methylene-2,3,4-trihydronaphthalene[6] (116)



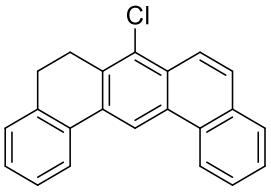
To a vigorously stirring suspension of 2-(naphthalene-2'-yloxy)-1-tetralone (15.00 g, 52.0 mmol) in dry diethyl ether (300 mL) was added a ylide solution freshly prepared from the addition of methyltriphenylphosphonium bromide (28.17 g, 78.9 mmol) and KO^{t}Bu (8.85 g, 78.9 mmol) to a solution of dry diethyl ether (300 mL) at 0 °C, which had been left stirring for 30 mins. The resulting bright yellow mixture was left stirring overnight, then the inorganic material was removed via suction filtration through celite. The filtration was concentrated *in vacuo* and dry loaded onto a silica plug (Pet. ether) which was eluted with Pet. ether, after which eluent was changed to 1:9 DCM:Pet. ether and these filtrate fractions were combined and left to evaporate slowly yielding the *title compound* as white crystals (8.49 g, 29.6 mmol, 57%). m.p. 86-88 °C. ^{1}H NMR (400 MHz, $CDCl_3$) δ 7.80 (2H, t, J = 8.2 Hz), 7.74 (1H, d, J = 8.2 Hz), 7.68 (1H, dd, J = 7.5, 1.7 Hz), 7.48 (1H, ddd, J = 8.0, 6.8, 1.1 Hz), 7.37 (1H, ddd, J = 8.0, 6.8, 1.1 Hz), 7.32-7.18 (5H, m), 5.69 (1H, s), 5.37 (1H, s), 5.22 (1H, dd, J = 8.1, 3.7 Hz), 3.20 (1H, dt, *J* = 17.0, 6.4 Hz), 3.00 (1H, dt *J* = 17.0, 6.4 Hz), 2.44-2.26 (2H, m) ppm. ^{13}C NMR (100 MHz, $CDCl_3$) δ 156.2, 143.1, 136.2, 134.8, 133.8, 129.7, 129.5, 129.2, 128.4, 128.0, 127.1, 126.6, 125.5, 124.1, 120.0, 110.5, 110.3, 109.9, 77.2, 29.5, 27.1 ppm. HRMS (EI^+) $C_{21}H_{18}O_2$ requires 286.1358, found 286.1364.

1’-((3,4-Dihydronaphthalen-1-yl)methyl)naphthalen-1’-trichloroacetate[6] (118)



A solution of 2’-(naphthalene-2’-yloxy)-1-methylene-2,3,4-trihydronaphthalene (16.30 g, 56.9 mmol) in pyridine (16.0 mL, 199 mmol) was heated in an inert atmosphere, with stirring, for 2 h at 115 °C, after which the heating was removed and the solution was allowed to cool to room temperature. The residue was dissolved with dry diethyl ether (300 mL), cooled to 0 °C and trichloroacetyl chloride (8.00 mL, 71.49 mmol) was added dropwise. The mixture was stirred for 2 h then allowed to warm to room temperature. The brown solution was poured into a slurry of ice-water (200 g) and $NaHCO_3$ (5 g), washed with water (2 x 100 mL), saturated aq. NH_4Cl (3 x 100 mL), water (3 x 100 mL), brine (2 x 100 mL), and dried over $MgSO_4$. Solvent was removed *in vacuo* yielding the *title compound* as a light brown solid (22.0 g, 39.8 mmol, 70%) which was subsequently used without further purification. m.p. 80-82 °C (decomp.). ^{1}H NMR (400 MHz, $CDCl_3$) δ 7.95-7.86 (3H, m), 7.56-7.47 (4H, m), 7.32 (1H, s), 7.19 (2H, m), 5.19-5.14 (1H, m), 4.18 (2H, m), 2.68 (2H, t, *J* = 8.1 Hz), 2.11-2.02 (2H, m) ppm. ^{13}C NMR (100 MHz, $CDCl_3$) δ 161.1, 147.1, 137.0, 135.7, 133.6, 133.3, 129.0, 129.0, 127.9, 127.4, 127.3, 126.8, 126.6, 126.4, 125.1, 122.3, 120.2, 111.0, 109.9, 90.0, 28.5, 28.4, 23.4 ppm. HRMS (EI^+) $C_{23}H_{17}Cl_3O_2$ requires 430.0294, found 430.0316.

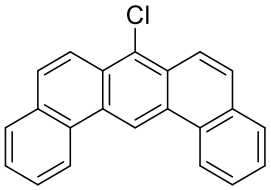
7-Chloro-5,6-dihydrobenzo[*m*]tetraphene[6] (119)



1’-((3,4-Dihydronaphthalen-1-yl)methyl)naphthalen-1’-trichloroacetate (4.00, 9.26 mmol) was dissolved in dry diglyme (5 mL) and the solution was purged with argon for 20 mins. Cuprous chloride (5 mol%, 46 mg, 0.463 mmol) was added and the mixture was purged for a further 10 mins before being heated to reflux for 2 h, or until HCl gas emission ceased. After cooling to room temperature, the crude mixture was subjected to column chromatography using 1:9 DCM:Pet. ether, and the *title compound* was isolated as a beige solid (2.42 g, 7.69 mmol, 83%). m.p. 93-95 °C. ^{1}H NMR (400 MHz,

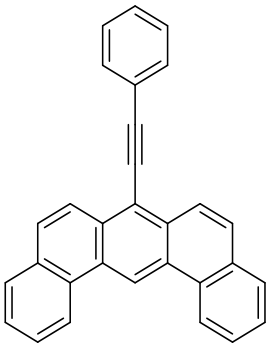
$CDCl_3$) δ 9.03 (1H, s), 8.79 (1H, d, *J* = 8.3 Hz), 8.28 (1H, d, *J* = 9.2 Hz), 8.04 (1H, d, *J* = 7.7 Hz), 7.92 (1H, dd, *J* = 7.7, 1.4 Hz), 7.83 (1H, d, *J* = 9.2 Hz), 7.74-7.67 (1H, m), 7.64 (1H, ddd, *J* = 7.7, 7.4, 1.3 Hz), 7.46-7.39 (1H, m), 7.35-7.32 (2H, m), 3.30 (2H, dd, *J* = 8.7, 5.4 Hz), 2.99 (2H, dd, *J* = 8.7, 5.4 Hz) ppm. ^{13}C NMR (100 MHz, $CDCl_3$) δ 138.1, 134.7, 134.6, 134.4, 132.2, 130.6, 130.5, 129.3, 129.1, 129.1, 128.6, 128.5, 128.4, 127.6, 127.3, 127.3, 124.9, 123.3, 123.1, 116.9, 28.9, 26.9 ppm. HRMS (EI^+) $C_{22}H_{15}Cl$ requires 314.0868, found 314.0857.

7-Chlorobenzo[*m*]tetraphene[6] (120)



2,3-Dichloro-5,6-dicyano-1,4-benoquinone (DDQ) (6.74 g, 29.7 mmol) was added to a stirring solution of 7-chloro-5,6-dihydrobenzo[*m*]tetraphene (4.05 g, 12.9 mmol) in dry dichlorobenzene (120 mL) and the mixture was heated to 150 °C for 1 h before being allowed to cool to room temperature. Methanol (200 mL) was added and the grey precipitate formed was collected via vacuum filtration, washed with water until the filtrate turned clear, then methanol. Drying yielded the *title compound* as light-grey microcrystals (3.13 g, 23.2 mmol, 78%). m.p. 239-240 °C. ^{1}H NMR (400 MHz, $CDCl_3$) δ 10.03 (1H, s), 9.00 (2H, d, J = 8.3 Hz), 8.44 (2H, d, J = 9.3 Hz), 7.95 (2H, dd, J = 7.7, 1.3 Hz), 7.87 (2H, d, J = 9.3 Hz), 7.78 (2H, ddd, J = 8.3, 7.0, 1.2 Hz), 7.69 (2H, ddd, J = 7.7, 7.0, 1.2 Hz) ppm. ^{13}C NMR (100 MHz, $CDCl_3$) δ 132.1, 130.6, 129.7, 129.2, 129.1, 128.4, 127.8, 127.7, 123.5, 123.3, 115.8 ppm. HRMS (EI^+) $C_{22}H_{13}Cl$ requires 312.0706, found 312.0710.

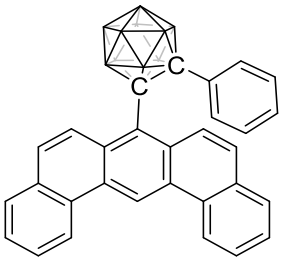
7-(Phenylethynyl)benzo[*m*]tetraphene (121)



7-Chlorobenzo[*m*]tetraphene (500 mg, 1.60 mmol), cesium carbonate (520 mg, 1.60 mmol), bis(triphenylphosphine)palladium(II) dichloride (10 mol%, 113 mg, 0.16 mmol)

tri(cyclohexyl)phosphine (20 mol%, 90 mg, 0.32 mmol) and phenylacetylene (0.71 mL, 4.17 mmol) were added to a flask charged with dry DMF (7 mL), and the mixture was purged with argon before being heated to 110 °C overnight. After cooling to room temperature, the mixture was added directly to a silica plug (Pet. ether), which was eluted first with Pet. ether, then 1:5 DCM:Pet. ether to elute the crude product. Solvent was removed *in vacuo* and the crude product was subjected to column chromatography Pet. ether eluent, yielding the *title compound* as light-orange crystals (182 mg, 0.48 mmol, 30%). Crystals suitable for X-ray diffraction analysis were grown by evaporation from a biphasic solution of DCM and hexane. m.p. 256-258 °C. ^{1}H NMR (400 MHz, $CDCl_3$) δ 10.08 (1H, s), 9.03 (2H, d, J = 8.1 Hz), 8.60 (2H, d, J = 9.2 Hz), 7.96 (2H, dd, J = 8.1, 1.2 Hz), 7.88 (2H, d, J = 9.2 Hz), 7.84-7.75 (4H, m), 7.69 (2H, ddd, J = 8.1, 7.0, 1.2 Hz), 7.52-7.41 (3H, m) ppm. ^{13}C NMR (100 MHz, CDCl3) δ 132.4, 132.2, 132.1, 130.1, 129.2, 128.9, 128.8, 127.6, 127.4, 125.6, 123.2, 117.4, 100.7, 86.9 ppm. HRMS (EI^+) $C_{30}H_{18}$ requires 378.1409, found 378.1410.

7-(2-Phenyl-1,2-dicarbadodecaboran-1-yl)benzo[*m*]tetraphene (122)



7-(Phenylethynyl)benzo[*m*]tetraphene (182 mg, 0.48 mmol) and decaborane (242 mg, 1.98 mmol) were added to a vigorously stirring flask charged with a biphasic mixture of bmim(Cl) (103 mg, 0.59 mmol) and dry toluene (10 mL), and the mixture was heated to reflux for 48 h. After cooling the solvent was removed *in vacuo* and the crude product was subjected to column chromatography with hexane eluent, yielding the *title compound* as orange crystals (92 mg, 0.13 mmol, 28%). Crystals suitable for X-ray diffraction analysis were grown by slow evaporation of a biphasic solution of DCM and hexane. m.p. 281-283 °C. ^{1}H NMR (400 MHz, $CDCl_3$) δ 9.63 (1H, s), 8.91 (2H, d, *J* = 9.6 Hz), 8.68 (2H, d, *J* = 7.8 Hz), 7.89 (2H, dd, *J* = 7.3, 1.7 Hz), 7.74 (2H, d, *J* = 9.6 Hz), 7.72-7.63 (4H, m), 6.82 (1H, tt, *J* = 7.3, 1.1 Hz), 6.51-6.46 (2H, m), 6.42-6.36 (2H, m), 4.34-1.62 (10H, br) ppm. ^{11}B NMR (128 MHz, $CDCl_3$) δ 0.92, -0.06, -1.86, -3.17, -8.45, -9.52, -10.59 ppm. ^{13}C NMR (100 MHz, $CDCl_3$) δ 133.6, 131.1, 130.4, 130.3, 130.0, 129.1, 128.6, 127.7, 127.5, 127.4, 126.7, 125.4, 123.2, 121.2, 120.7, 95.1, 91.0 ppm. HRMS (MALDI-ToF) $C_{30}B_{10}H_{28}$ requires 497.3, found 497.3. ATR-IR (*v* cm^{-1}) 3856, 3736, 3672, 2599 (B-H) br, 2173, 2050, 2014, 1982, 1491, 1386, 1257, 1165, 1073, 1035, 884, 831, 793, 743, 690, 665.

4.8 – References

1 R. D. Haworth, *J. Chem. Soc.*, 1932, 2717–2720.

2 S. Grimme, C. Mück-Lichtenfeld, G. Erker, G. Kehr, H. Wang, H. Beckers and H. Willner, *Angew. Chem. Int. Ed.*, 2009, **48**, 2592–2595.

3 Y. Ma, C. Song, W. Jiang, Q. Wu, Y. Wang, X. Liu and M. B. Andrus, *Org. Lett.*, 2003, **5**, 3317–3319.

4 G. I. Borodkin, I. R. Elanov and V. G. Shubin, *Russ J Org Chem*, 2010, **46**, 1317–1322.

5 J. A. Bull, PhD Thesis, University of Manchester, 2008.

6 M. Little, PhD Thesis, University of Manchester, 2014.

7 A. Toppino, A. R. Genady, M. E. El-Zaria, J. Reeve, F. Mostofian, J. Kent and J. F. Valliant, *Inorg. Chem.*, 2013, **52**, 8743–8749.

8 R. A. Harder, PhD Thesis, Durham University, 2012.

9 Y. Tobe, S. Saiki, N. Utsumi, T. Kusumoto, H. Ishii, K. Kakiuchi, K. Kobiro and K. Naemura, *J. Am. Chem. Soc.*, 1996, **118**, 9488–9497.

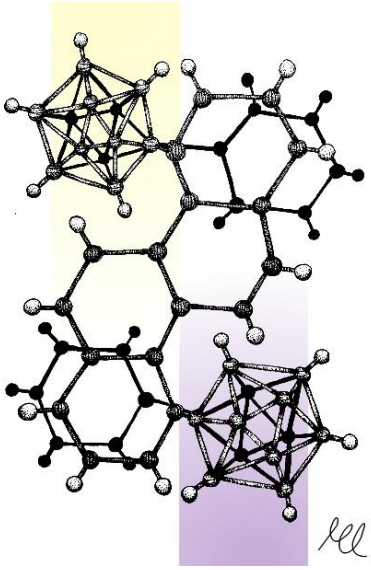
10 H. Naito, Y. Morisaki and Y. Chujo, *Angew. Chem. Int. Ed.*, 2015, **54**, 5084–5087.

11 H. Naito, K. Nishino, Y. Morisaki, K. Tanaka and Y. Chujo, *Chem. Asian J.*, 2017, **12**, 2134–2138.

12 H. Naito, K. Nishino, Y. Morisaki, K. Tanaka and Y. Chujo, *J. Mater. Chem. C*, 2017, **5**, 10047–10054.

13 H. Kunkely and A. Vogler, *Inorganica Chimica Acta*, 2004, **357**, 4607–4609.

14 Boström Carl-Elis, Gerde Per, Hanberg Annika, Jernström Bengt, Johansson Christer, Kyrklund Titus, Rannug Agneta, Törnqvist Margareta, Victorin Katarina and Westerholm Roger, *Environmental Health Perspectives*, 2002, **110**, 451–488.



Chapter 5 – Carborane-Induced Excimer Emission of Twisted bis-*ortho*-Carboranyl Chrysene

5.1 – Introduction

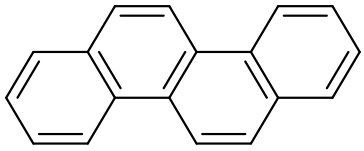
In **Chapter 3**, ***m*CbAnth** and ***p*CbAnth** were shown to exhibit excimer emission in the aggregated and solid-state. Excimer emission from anthracene is relatively rare, especially in nominal conditions (i.e. not at pressure or very low temperature). The appearance of excimers for these molecules was ascribed to the carborane changing the degree of intermolecular bonding, either through deformation of the aromatic system, or physical perturbation of the π-π stacks due to the bulky nature of the moiety. Unlike the parent anthracene, excimers of these anthracenyl carborane dimers do not non-radiatively decay so readily, resulting in increased radiative emission. Interestingly, the λ_{max} of these excimers were not identical; ***m*CbAnth** is slightly red-shifted relative to ***p*CbAnth**. It is possible that the carboranes are somewhat electronically involved in the excimer species and, accordingly, the more electron-withdrawing *meta*-carborane stabilises the excited state to a slightly greater degree than *para*-carborane. However, it is perhaps more likely that the subtle differences in emissive energy are due to the variation in aromatic system overlap; a known structure-property relationship.[1–3] In these

cases, therefore, whilst the carboranes affect excimer emission, they likely do not participate electronically in the excimer species.

Ortho-carborane has also been shown, to a very limited extent, to aid excimer emission. When disubstituted with two naphthyl donor groups, the imposed proximity of the aryl systems allows for an overlap of the aromatic wavefunctions, such that dimerization occurs readily when one naphthalene is in the excited state.[4] In other cases where *ortho*-carborane has been attached to pyrene, the bulky carborane moiety was found not to inhibit the π-π stacking required for pyrene excimer formation.[5–7] Again however, in these few cases the carborane can be considered essentially electronically isolated from the aromatic excimer species, save for some electron-withdrawing inductive effects.

In **Chapter 4**, it was discovered that **Ph*o*CbPhen** exhibited a novel, concentration-dependent, low energy emissive peak in solution. Concentration dependence for an emission is characteristic of non-unimolecular emissive species, and interestingly no other compound in the chapter exhibited such a phenomenon. Phenanthrene does not normally show excimer emission in solution due to the low stabilisation energy for excimer formation,[8] but it can be observed in solid films at λ_{max} = 450 nm. The concentration-dependent **Ph*o*CbPhen** emission is at much lower energy, suggesting that, if the emissive species responsible is an excimer, then the electronic structure is likely very different to the conventional phenanthrene excimer, and may contain significant electronic contribution from *ortho*-carborane.

To explore whether the possible excimer inducing properties of *ortho*-carborane, attention was focused on chrysene (**123**), a polycyclic aromatic hydrocarbon named after the Greek work for gold, 'chrysos', in recognition of the gold crystals into which it forms.* Chrysene is a nonlinear tetracyclic ring system, as depicted in **Figure 5-1**.



123

Figure 5-1 – The molecular structure of chrysene.

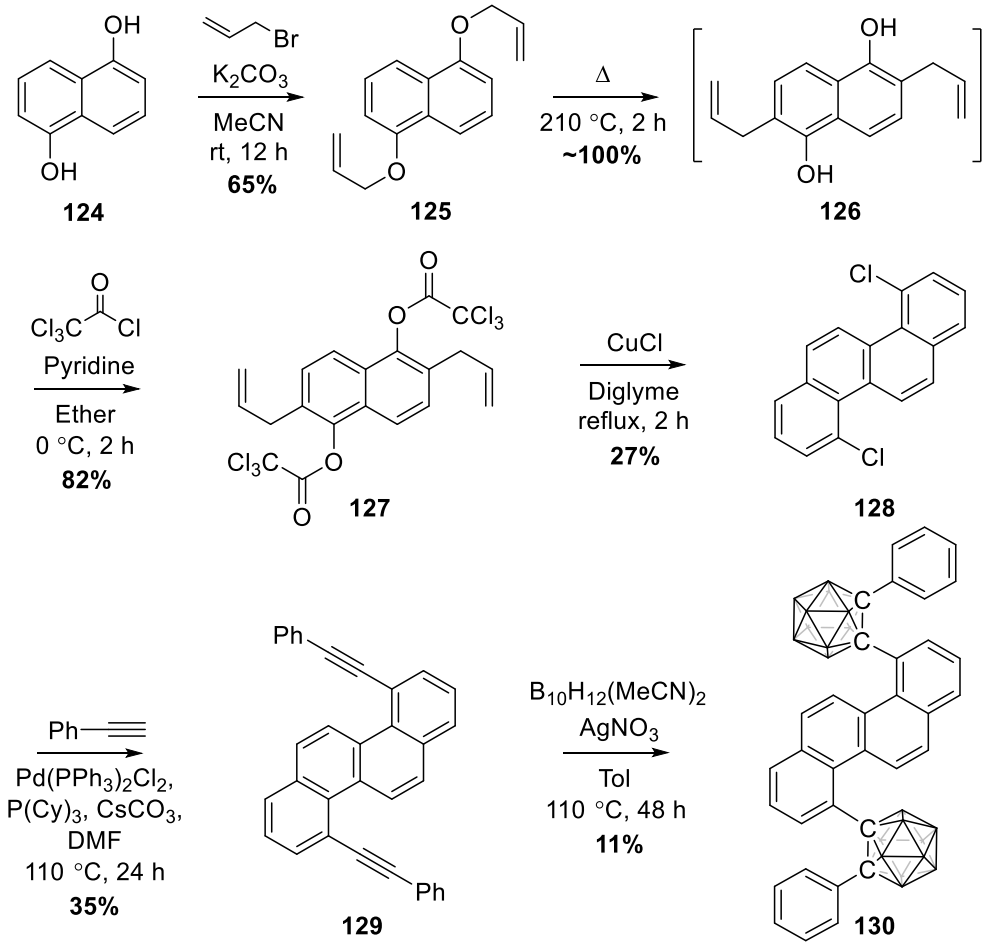
* Incidentally the gold colour is due to a tetracene impurity, and pure samples are colourless.

Chrysene is notable amongst PAHs for its lack of excimer emission. For decades it was thought chrysene could only form excimers in the solid state, following morphology changes at very high pressure.[9,10] Only recently have these excimers been observed in solution, requiring supramolecular DNA scaffolds to force chrysene units sufficiently close together in a face-to-face orientation such that excimer formation can occur.[11]

Inspired by these results, we planned to incorporate two phenyl-*ortho*-carboranes into the bay areas of chrysene (**Appendix I**), theorising that the bulky carboranes would cause aromatic deformation to such an extent that π-delocalization would be inhibited. As a consequence, the intermolecular repulsion potential would be lowered, conceivably allowing chrysene monomers to approach one another and support dimer formation.[9] Also, as in **Chapter 4**, we proposed that the π-π interactions between the phenyl group of the carborane and chrysene would help to 'lock' the carboranyl C-C bond perpendicular to the aromatic plane in a geometry favourable for TICT, and in doing so add to the growing class of severely twisted, multi-emissive luminescent materials.[12]

5.2 – Synthesis

4,10-bis(2-phenyl-*ortho*-carboranyl)-chrysene (**Ph*o*Cb$_2$Chry**) (**130**) is synthesised according to the procedure in **Scheme 5-1**.



Scheme 5-1 – The synthesis of **PhoCb_2Chry**.

The synthetic procedure began with 1,5-dihydroxynaphthalene (**124**), a cheap intermediate product used in the preparation of dyestuffs, and proceeded in much the same manner as the in the synthesis of the phenacenes in **Chapter 4**.[13] Williamson ether synthesis of conditions were used for the allylation to yield 1,5-bis(allyloxy)naphthalene (**125**), and Claisen rearrangement to the diol (**126)** was achieved at high temperature under argon. **126** is highly unstable, and rapidly oxidises in air to from a quinone,[14] therefore the neat mixture was immediately diluted with ether, and pyridine, then trichloroacetylchloride was added at 0 °C. Esterification proceeded well to yield the, relatively stable, trichloroacetate (**127**). A double BHQ benzannulation reaction yielded 4,10-dichlorochrysene (**128**), and copper-free Sonogashira coupling with phenyacetylene formed the bis-acetylene product (**129**). Coupling with decaborane was first attempted using the bmim(Cl) procedure. This did produce the desired carborane product (**130**), but in very low yield (~2%). As discussed in **Chapter 1**, coupling of decaborane and internal alkynes is generally difficult and low-yielding, and so forming bis-carborane products in this fashion is doubly challenging. Silver (I) mediated decaborane/acetylene couplings have produced good yields for internal alkynes,[15] and so this method was trialled using $AgNO_3$ as the

Lewis acid. The reaction still produced a relatively low yield (11%); the main by-products of these reactions were various non-*closo*-carboranyl chrysenes, suggesting mechanistically that the cage closure step did not proceed efficiently, likely as a result of the severely congested environment around the alkyne. The yield was, however, satisfactory in terms of isolating enough material for characterisation and optical studies.

5.3 – X-ray Crystallography

Both the **Pho*C*b$_2$Chry** product and the bis-phenylacetylene product **129,** are novel compounds, and as such, they were recrystallised by slow evaporation of a biphasic solution DCM and hexane to afford single-crystals suitable for XRD analysis. Crystal structures were obtained and are shown in **Figure 5-2** and **5-3**, with the intermolecular bonding interactions for **Pho*C*b$_2$Chry** pictured in **Figure 5-4**.

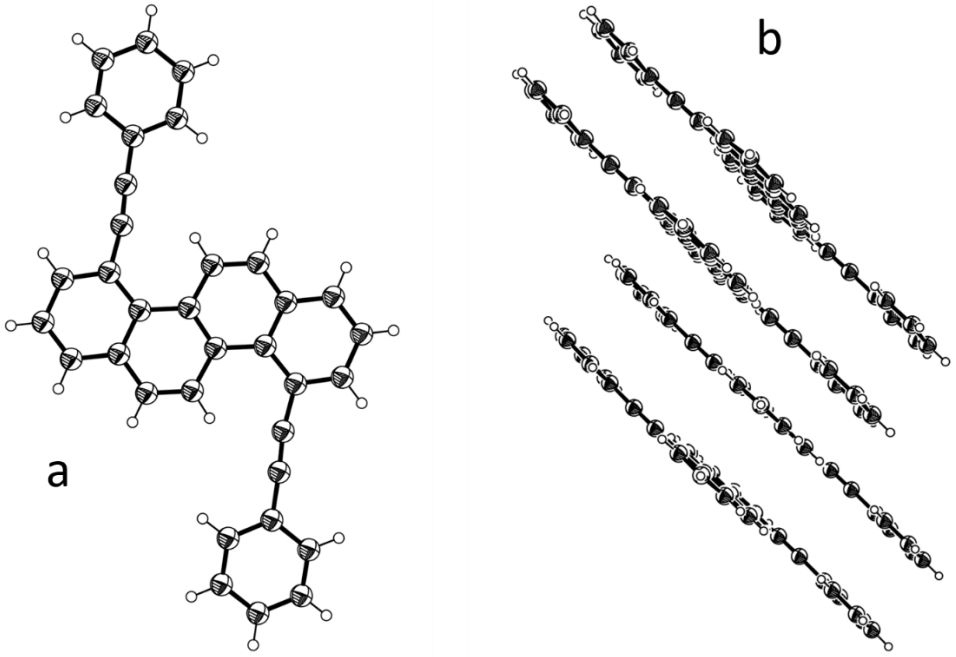


Figure 5-2 – ORTEPs of (a) the molecule structure, and (b) the packing, of bis-phenylacetylene compound **124**.

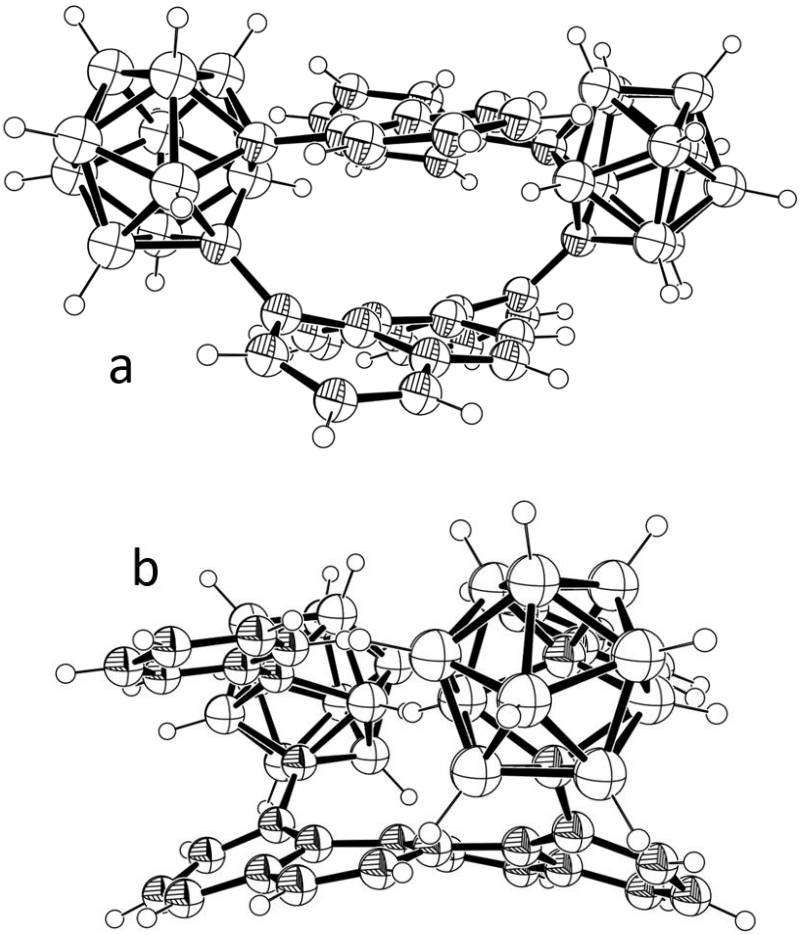


Figure 5-3 – ORTEPs of **PhoCb_2Chry** along (a) the molecular axis, and (b) perpendicular to the molecular axis.

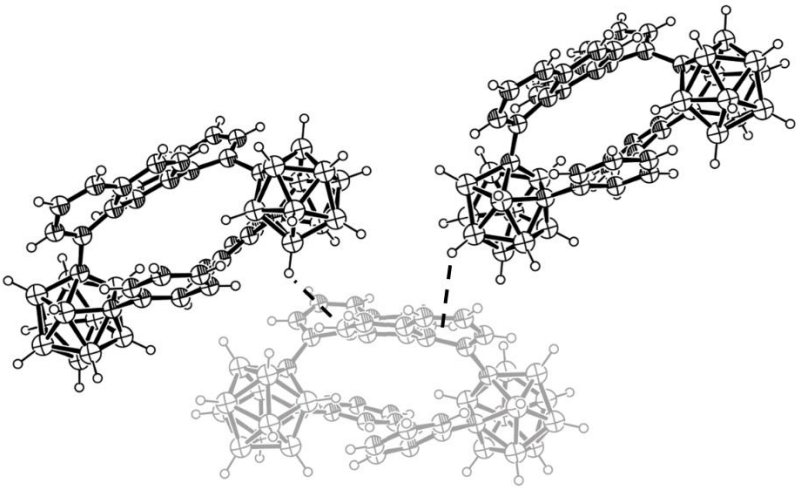


Figure 5-4 – The intermolecular hydrogen-bonding interactions between each chrysene core, and the carboranes of two neighbouring molecules.

The bis-phenylacetylene **129** crystallised into the monoclinic, $P2_1/c$ space group. Interestingly, the molecular structure deviates from what one may expect; the alkyne groups are not linear (i.e. ≠ 180°). Both alkynes are slightly pushed ca. 10° away from linearity by proximal protons in the bay region. Strained alkynes, particularly cycloalkynes, are generally much more reactive than their linear counterparts,[16] so this property may, in fact, be beneficial for reactions with decaborane. Clearly however, this is counterbalanced with the considerable steric crowding around the acetylene, which greatly reduces the ability of decaborane to fuse with the acetylene. The molecule is essentially planar, and the chrysene moieties stack in the packing arrangement, facilitated by favourable π-π overlap between neighbouring molecules.

The carborane compound **Ph*o*Cb$_2$Chry** crystallised into the orthorhombic, Pbca space group. The incorporation of the carboranes results in significant distortion of the usually planar chrysene core, affording a highly asymmetrically distorted ring system with α and β angles on the order of **Ph*o*CbPhen**. Steric interactions between the carboranes and the protons (and carbon atoms) in the in the bay area of chrysene leads to the dramatic twisting. Both carboranes are situated out-of-the-plane, and on the same side, of the chrysene core, and the C-C bond is perpendicular to the chrysene plane. This is due to the phenyl group 'locking' the carborane in the perpendicular orientation to the aromatic core, as observed for the phenacenes in **Chapter 4**. The region of space between the carboranes is also highly congested due to the phenyl substituents. These interact with each other, favouring twisting of the groups in order to reduce their steric interactions. Simultaneously, these groups are stabilised by the intramolecular π-π stacking interactions with the end rings of the chrysene, which favours an arrangement planar to the molecular axis. The opposing forces resolve with the carboranes being distinctly inequivalent, as demonstrated by the aromatic deformation parameters in **Appendix III**. The carboranyl C-C bond lengths are significantly larger than the parent *ortho*-carborane, which is a common phenomenon for such systems substituted with two bulky groups.[17]

Unlike the carboranyl phenacenes in **Chapter 4**, **Ph*o*Cb$_2$Chry** does not exhibit dimerisation of the aromatic cores in the packing arrangement. The non-carborane side of the chrysene cores are flanked by carboranes from two separate molecules, which hydrogen bond intermolecularly with the end rings of the aromatic, as demonstrated in **Figure 5-4**.

5.4 – Calculations

PhoCb_2Chry is the only compound studied in this thesis which contains two carborane compounds, and the single-crystal XRD clearly demonstrates that they sterically interact with one another. The question of how this interaction changes as a function of carboranes rotation is an intriguing one. In **Chapters 2** and **4** these calculations were carried out in the gas phase, however in this study we aimed to consider the effect of the solvent using a PCM solvation model. In addition, given that the precise solid-state structure of **PhoCb_2Chry** is known, is seemed pertinent to consider how the crystal packing effects the carborane rotation, and therefore the distribution of ground state geometries. This was achieved using a two-layer own N-layer integrated molecular orbital + molecular mechanics (ONIOM) method, in which one **PhoCb_2Chry** molecule is treated with high-level DFT, and the nearest neighbour molecules are also considered in the calculation, but with a lower-level molecular mechanics (MM) degree of theory. The structure of the system is presented in **Figure 5-5**.

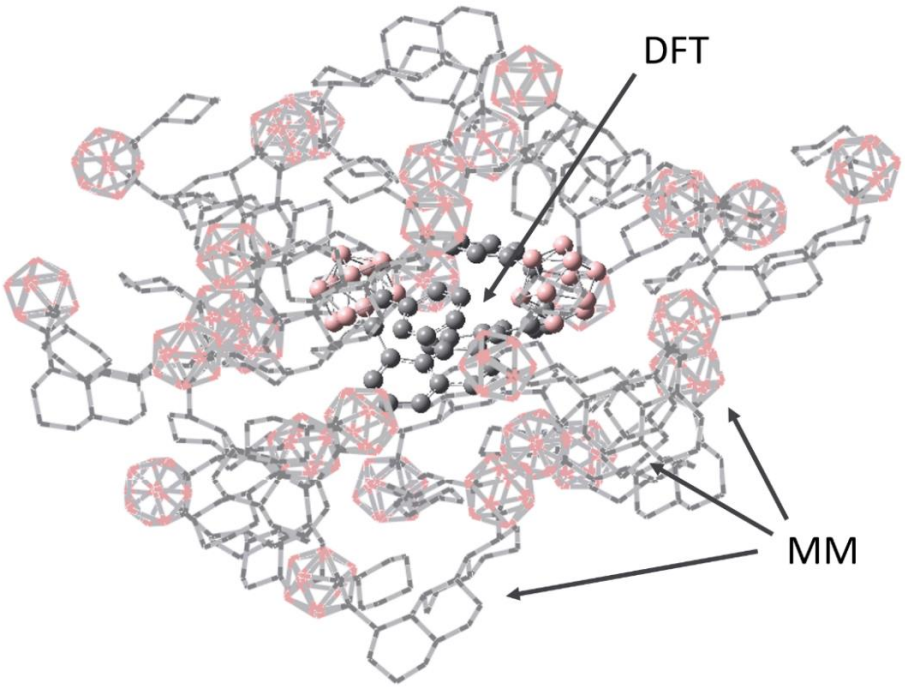


Figure 5-5 – The ONIOM model used in the solid-state dihedral calculations. The skeletal structured **PhoCb_2Chry** molecules are treated with MM, whilst the centre molecule is treated with high-level DFT. Packing is as observed from single crystal XRD. Protons removed for clarity

Using these methodologies, the PES for **PhoCb_2Chry**, as a function of carborane (A) rotation, is presented in **Figure 5-6**.

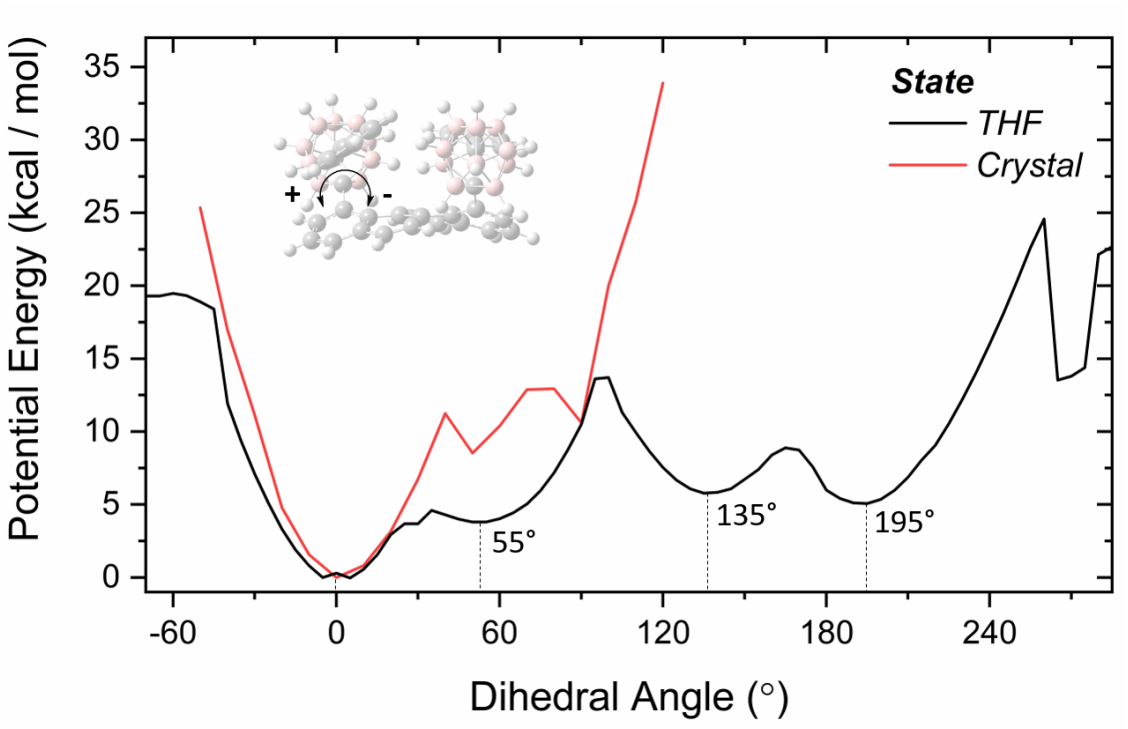


Figure 5-6 – DFT calculated (ωB97XD/6-31G(d)) PES of **PhoCb_2Chry** as a function of carborane (A) rotation, in THF (PCM solvation method) and solid-state (two-layer ONIOM method). Rotation occurs in a positive or negative direction, as depicted, from the global found state arbitrarily assigned the 0° dihedral angle. Calculations are performed at 5° intervals for the THF calculations, and 10° intervals for the solid-state. Minimum energy geometries are labelled.

The PES in THF shows that rotation of the carborane towards the centre of the molecule greatly increases potential energy. This is understandable as it brings both the phenyl groups in close proximity, and rotates the carborane towards the C(5) proton. Rotation away from the centre of the molecule also leads to an increase in potential energy, however there are energy minima geometries at 55°, 135°, 195° dihedral orientations, in addition to the global ground state geometry at 0°. The 55° and 135° geometries correspond to the carboranyl C-C bond approximately planar, and the 0° and 195° geometries approximately perpendicular, to the aromatic plane. There is another energy minimum at ca. 270° however the potential energy barriers on either side of the geometry are extremely high, so the number of molecules in this state is likely to be very low.

The PES in the solid-state similarly has the global ground state geometry at the 0° dihedral angle. Rotation of the carborane in the positive or negative direction rapidly increases the potential energy of the system, and there are no, real, energy minima in the space calculated. Indeed, rotation of 60° in the negative direction, or 120° in the positive direction, produces potential energies on the order of BINOL; a molecule with a steric-induced axis of chirality at room temperature.[18] It is therefore likely that, in the solid state, rotation is restricted to the 180° region calculated in the solid state, which

contains only one energy minimum geometry, with the C-C bond perpendicular to the aromatic plane, ideal for TICT species formation.

These calculations only probe the rotation of a single carborane as including a second carborane, forming a three-dimensional PES, would be take prohibitively long to calculate. However, using the energy minima geometries in **Figure 5-6**, one can calculate the emissive energies for all the ground state geometries considering both carboranes. The calculations proceeded as in the process described in **Figure 3-5**, and the emissive energies are presented in **Table 5-1**.

Cb (2) Dihedral Angle (°) \ Cb (1) Dihedral Angle (°)	0	55	135	195
0	698	455	474	296
55	-	392	474	440
135	-	-	345	345
195	-	-	-	500

Emissive Energy (nm)

Table 5-1 – DFT (ωB97XD/6-31G(d); solvent = THF) calculated emissive energies of **PhoCb_2Chry** as a function of carborane dihedral rotation. The energies in the visible spectrum are coloured according to their wavelength.

The 0°, 0° geometry is notably distinct to the other geometries; the emission is of a very low energy. This is suggestive of carborane involvement in the excited state species. The other geometries produce a range of high energy emissions, which are likely a result of LE from the chrysene moiety. Moreover, the changes in the degree of deformation, and therefore the degree of aromaticity, of the ring system as the carborane rotates lead to subtle changes in the nature of the local oscillator, which leads to somewhat different LE emissive energies. The calculated molecular orbitals of the geometries considered are presented in **Figure 5-7**.

As expected from the long wavelength emission of the 0°, 0° geometry, the carborane has significant involvement in the frontier orbitals of the S_1 excited state species. Interestingly, unlike ***o*Cb_2BDT** (**Figure 2-21**), there is no evidence of a bis-TICT state (where both carboranes have an elongated C-C bond in the optimised S_1 excited state). In this geometry the C-C bond lengths of Cb (1) and Cb (2) are 2.341 and 1.757 Å respectively. This is not surprising; for ***o*Cb_2BDT** both carboranes are attached at the *para*-positions on the same benzene ring, however, whilst the carboranes are spatially close in **PhoCb_2Chry**, they are separated by two benzene rings, which are also arranged non-linearly. Electronic communication between the carboranes is therefore difficult. This idea is supported by the CV of these compounds which in the case of ***o*Cb_2BDT** shows four distinct reduction and oxidation peaks,

suggesting a stabilising effect of one carborane on the reductive potential on the other,[19] but in the case of **Ph*o*Cb$_2$Chry** shows only two peaks (**Appendix IV**), suggesting the carboranes are electronically isolated.

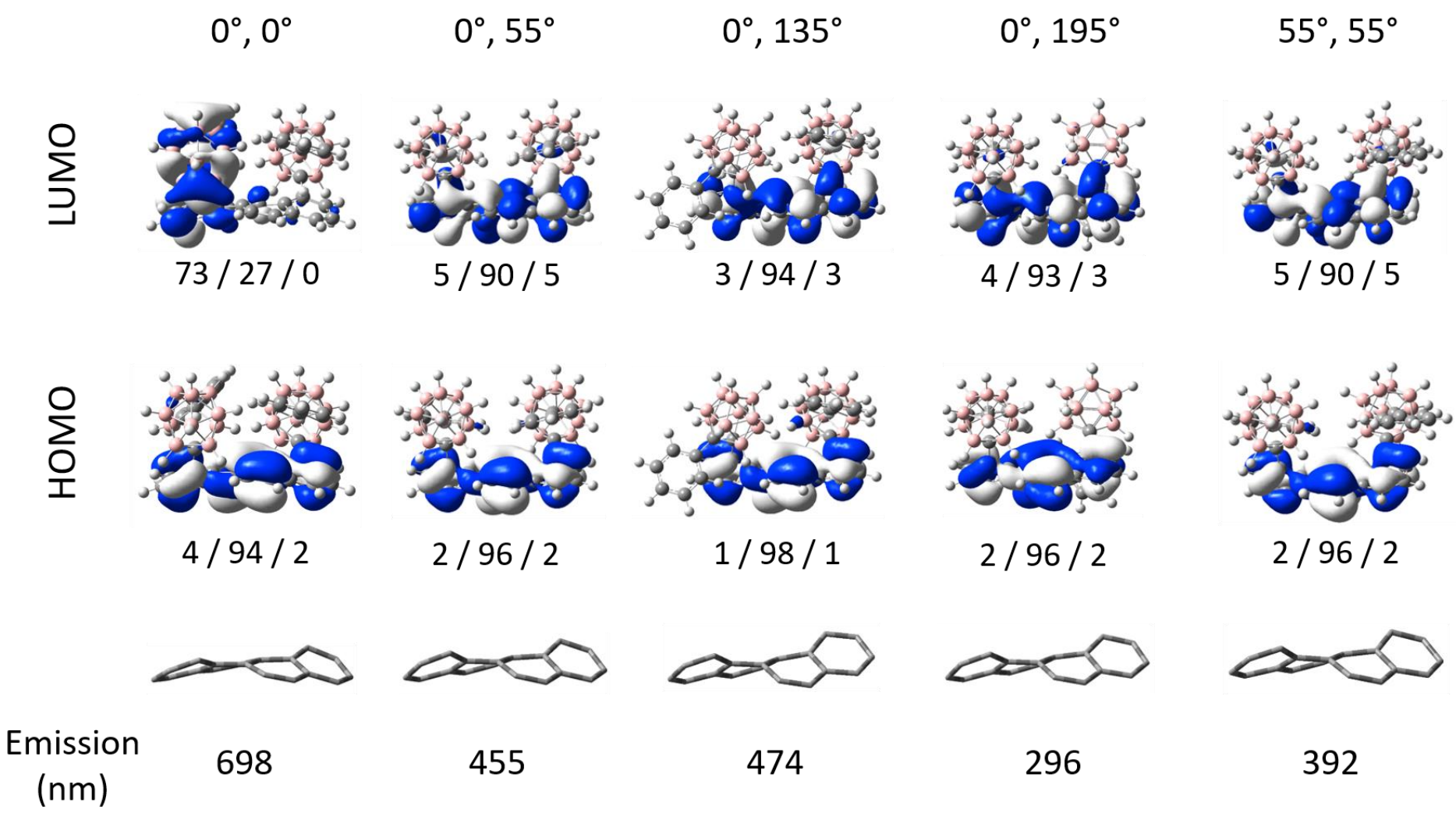


Figure 5-6 – Caption overleaf.

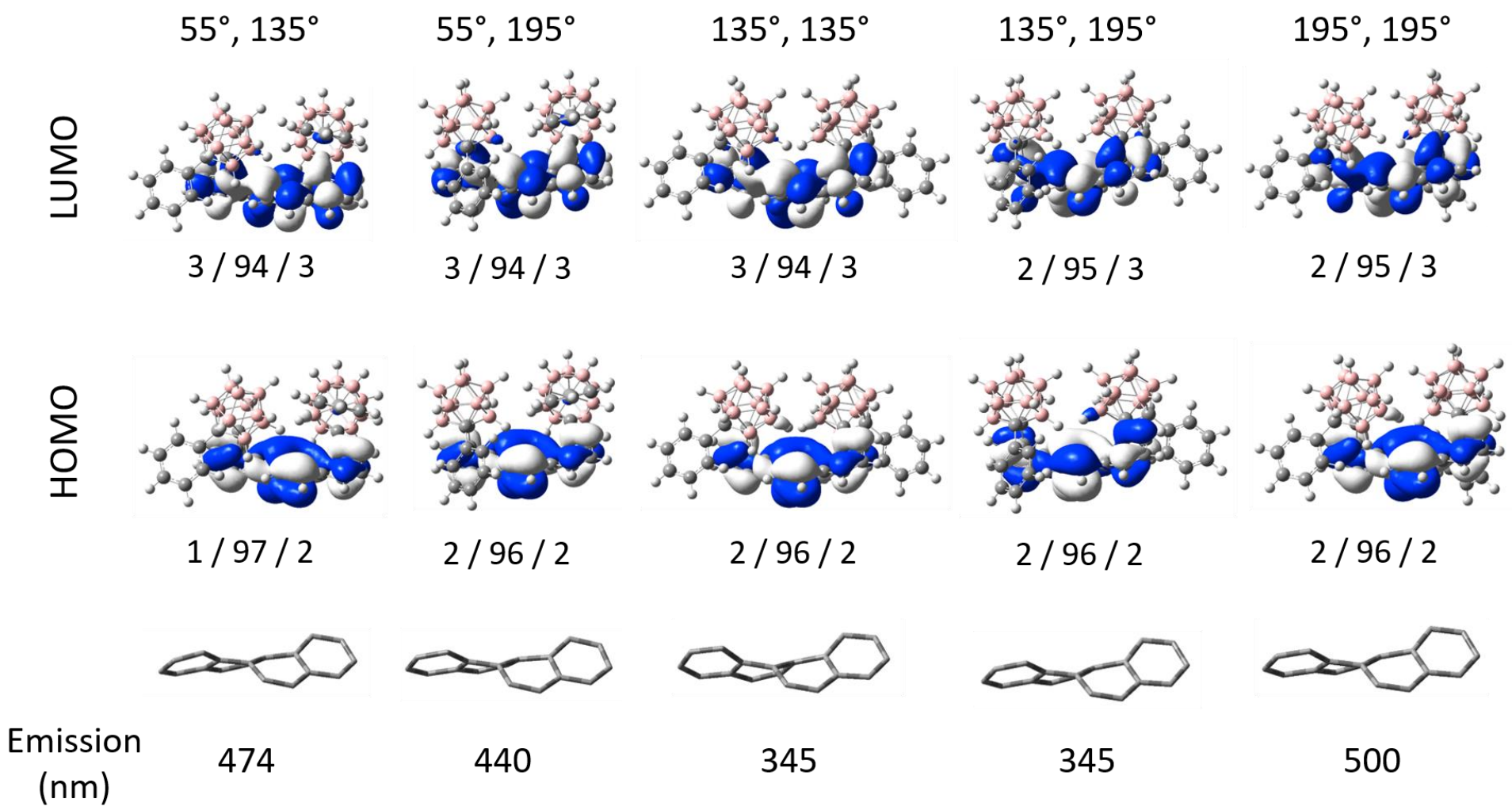


Figure 5-7 – TD-DFT (ωB97XD/6-31G(d); solvent = THF) calculated geometries, molecular orbitals, and relative Cb (1) / chrysene / Cb (2) contributions to the HOMO and LUMO of the S_1 excited state, with emissive energies provided. The skeletal structure of the chrysene moiety is pictured with carborane groups and protons moved for clarity.

There is no evidence of charge transfer in any of the other carborane geometries, where excited states are localised on the chrysene moiety. The emissive wavelengths vary, as does the degree of aromatic deformation, however no causal relationship is clear (one may expect larger deformation to yield smaller delocalised excited states of higher energy, and accordingly, higher energy emission).

The 0°, 195° geometry is curious, as an emissive wavelength of 296 nm is significantly higher than the other LE. It is possible that such an emission could occur from the phenyl moiety, and for such an emissive species one would expect the excited state to be localised, almost entirely in that region. However, the electron density of the HOMO and LUMO are both spread over the chrysene ring system. This geometry can therefore be considered something on an anomaly in the calculations.

5.5 – Optical Studies of PhoCb_2Chry

5.5.1 – UV-Vis and PL

To begin the investigation into the photoluminescence properties of the **PhoCb_2Chry**, UV-Vis spectroscopy and PL was carried out on the compound in THF solution. The results are presented in **Figure 5-8**.

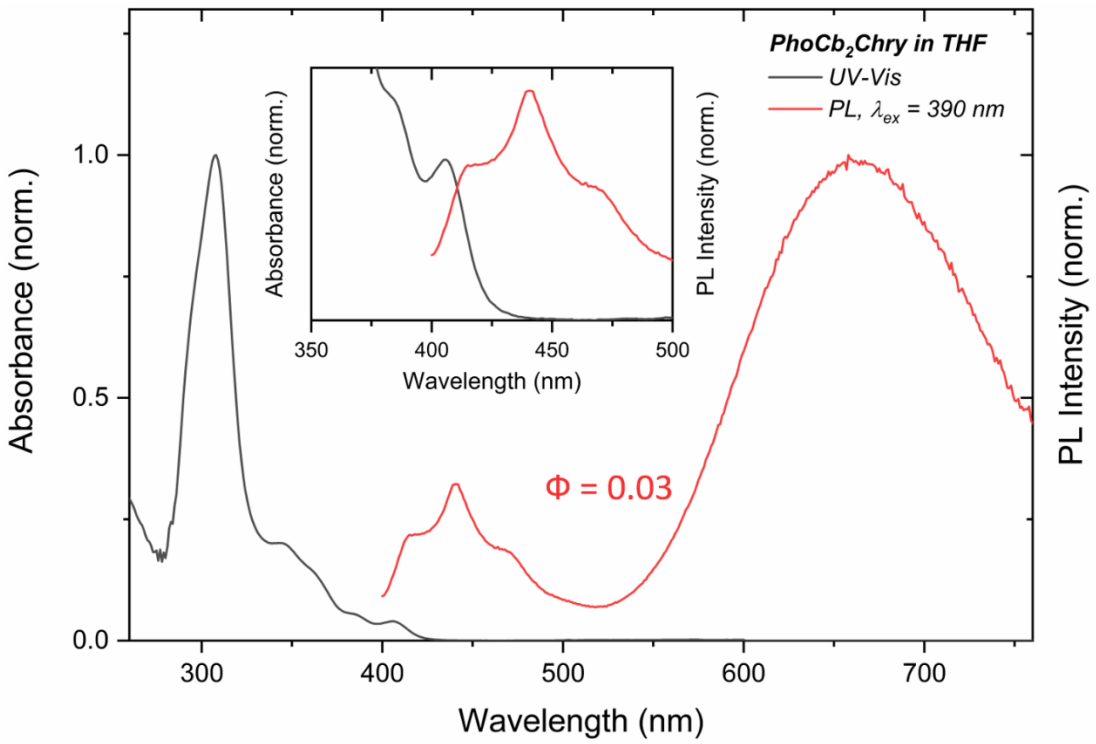


Figure 5-7 – UV-Vis and PL spectroscopy of **PhoCb_2Chry** in THF solution, concentration = ca. 1 x 10^{-4} M, with quantum yield presented. The inset depicts the vibronic region of the UV-Vis and PL, normalised to those peaks.

The UV-Vis of **Ph*o*Cb$_2$Chry** is dominated by the chrysene moiety. This is because *ortho*-carborane is weakly absorbing, and the phenyl group attached to it absorbs at a higher energy than that measured (ca. 255 nm).[20] Like the carboranes in **Chapter 3** and **4**, the absorption occurs in two main bands, the high energy $\pi \rightarrow \pi^*$ (E-band) transition region, and a second, lower energy $\pi \rightarrow \pi^*$ (B-band) transition region. The latter is very complex; this reflects the complex vibrational modes associated with the large, non-linear chrysene region.

This vibronic region is mirrored in the PL, with a small Stokes-shift, suggestive of a LE from the chrysene core. The PL also contains a low energy emission centred at λ_{max} = 655, which is broad and featureless, characteristics of a delocalised emission. The TRES PL (**Appendix VIII**) supports this identification; the vibronic emission has an excited state lifetime of 0.18 ns and the delocalised emission a much longer lifetime of 3.3 ns. Longer lifetimes for delocalised emissive species have been a notable characteristic of the carborane molecules in **Chapters 3** and **4**. Similarly, as for all the *ortho*-carborane compounds in this thesis, the overall quantum yield for **Ph*o*Cb$_2$Chry** in THF is rather low.

During the preliminary investigations into the optical properties of **Ph*o*Cb$_2$Chry**, it was noticed that the emission of the compound in THF was highly dependent on the excitation wavelength, **Figure 5-9**.

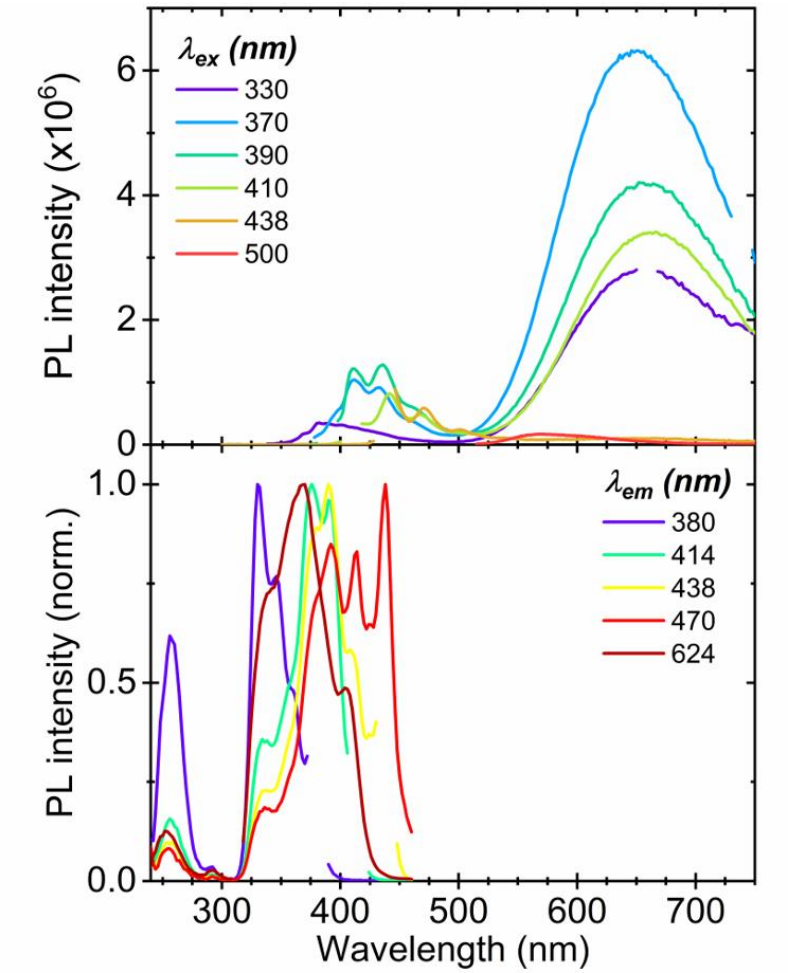


Figure 5-8 – (a) PL, and (b) normalised PLE, of **PhoCb_2Chry** in THF (1 x 10^{-4} M) at various excitation wavelengths.

Both the LE and delocalised emission are excitation dependent, but the LE is particularly noteworthy. For most systems such as these, whilst the intensity of the LE is generally excitation dependent, the shape of the emission is consistent. However, for **PhoCb_2Chry**, both the intensity *and* the band shape change with the excitation wavelength. There are also two clear emissive bands, the LE and a delocalised emission as in **Figure 5-8**, however, λ_{ex} = 500 nm reveals another emission peak centred at λ_{max} = 580 nm. In addition, the PLE is also highly variable and the λ_{em} = 470 nm is particularly curious as the band-edge of the PLE is red-shifted relative to the UV-Vis spectrum.

5.5.3 – PL and PLE

To probe these phenomena further, a two-dimensional PL/PLE study was undertaken at 1 nm resolution, as presented in **Figure 5-10**.

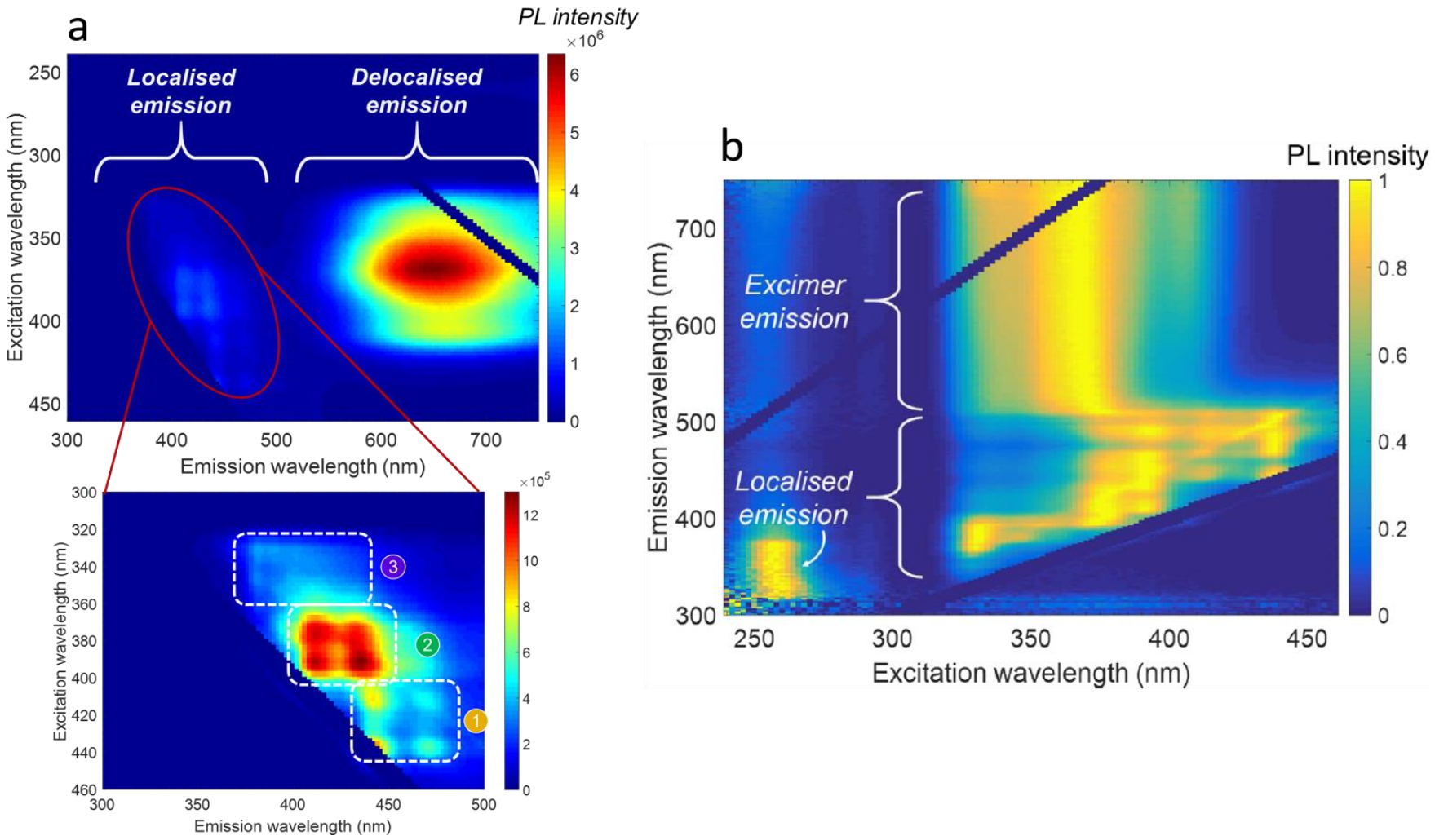


Figure 5-9 – (a) 2D photoluminescence emission map and (b) photoluminescence excitation map (each slice along the y axis corresponds to a normalised PLE diagram), of **PhoCb$_2$Chry** in THF (concentration = 1 x 10^{-4} M). Data removed at one and two-times the excitation wavelength. At least three sets of correlated absorption and emission peaks are identified, with 0-0 PL vibronic emission peaks centred at 380, 410, 440 nm. Data collection, analysis and presentation by Dr Nathan Cheetham.

From the 2D emission map it is clear that there are three sets of correlated absorption and emission peaks. These can be ascribed to the changing degrees of deformation of the chrysene core, according to relative dihedral angles of the carboranes. The subtly different chrysene geometries each absorb and emit uniquely, as demonstrated in the DFT study in **Figure 5-7**, such that both the excitation and emission spectra vary. There is a general trend of the excitation spectrum band edge to red-shift as the vibronic emission red-shifts, i.e. the Stokes shift remains essentially constant. This is unsurprising given the excited state species responsible is locally excited.

In **Figure 5-10**, there is some evidence of the λ_{max} = 560 nm peak observed in **Figure 5-9**, as the delocalised emissive species appears to blue-shift slightly at excitations of ca. 375 nm, relative to higher or lower excitation energies. In **Chapter 3** a similar observation was made; a dominant, delocalised TICT species was occasionally accompanied by another broad, featureless emission of higher energy, which was assigned to an ICT emissive species. In **Chapter 4** it was demonstrated that an ICT species can be formed directly from the ground state, and such a phenomenon can be observed in the PLE, where the excitation spectrum continues to energies lower than the vibronic region of the UV-Vis. This is similarly observed for the λ_{max} = 560 nm peak, **Figure 5-11**.

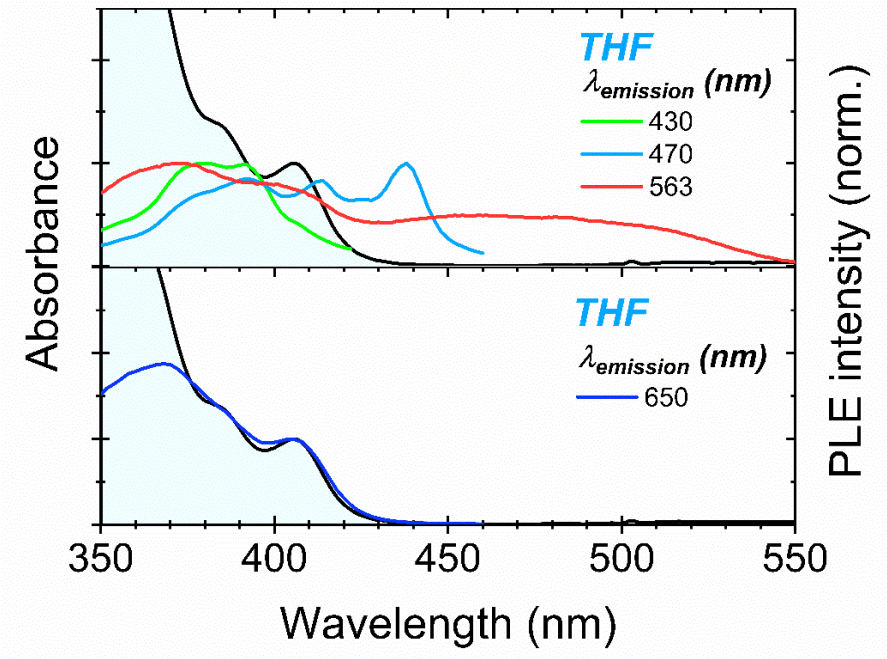


Figure 5-10 – UV-Vis absorption (shaded blue) and selected normalised PLE of **PhoCb$_2$Chry** in THF. Solution concentrations ca. 10^{-4} M.

The PLE of both the 470 nm and 563 nm emissive peaks appear to continue beyond the band-edge of the UV-Vis absorption spectrum, c.f. the to 650 nm emissive peak which follows the band-edge of the

absorption almost perfectly. However, it must be noted that these PLE are normalised; the 470 nm PLE spectrum is likely contained within the absorption, but the absorption is extremely low in this region, so the fine details of the PLE are not clearly seen in the UV-Vis spectrum. The λ_{em} = 470 nm PLE has a vibronic structure, suggesting that the emission is due to the chrysene local oscillator, supporting this idea. The λ_{em} = 563 nm PLE spectrum extends far beyond the absorption however, and contains no vibronic structure, which suggests that the excited state species cannot be restricted to just the chrysene moiety. This is likely an ICT species, and the PLE in the low energy region represents a direct ground state to ICT vertical excitation, as also seen in **Chapter 4**. However, whilst the transition must occur in this fashion, it is conceivable that the emission is a TICT species and not an ICT species. It is possible that ICT states are formed with the carborane C-C bond parallel to the aromatic plane but, following this, rotation occurs in the excited state such that the C-C bond becomes perpendicular to the aromatic plane and, following relaxation through elongation of this bond, the emission occurs via a TICT species. This idea will be addressed later in the Chapter.

5.5.4 – The Nature of the Delocalised Emission

The excited state character of **PhoCb_2Chry** can be investigated by solvatochromism with the aid of a Lippert-Mataga plot, as shown in **Appendix VIII**. The samples of the compound in good solvents follow a positive linear trend in Stokes shift with the Δf parameter for the long wavelength peak at ca. 660 nm, characteristic of a charge-transfer nature. Poor solvent solutions of **PhoCb_2Chry** do not conform to this trend, most likely due to the occurrence of local aggregation.[21] For these cases, it is possible there is no longer one dominant emission species, rather two similarly contributing and competing emissions as evidenced by broadened emissive peaks. Finally, the Stokes shift for the LE emission is virtually independent of solvent quality, further supporting that this is indeed emission originating from the chrysene core.

For **PhoCbPhen** in **Chapter 4**, it was noted that the concentration dependent study demonstrated an intriguing phenomenon; the delocalised emission seemed to be change in intensity, relative to the LE, depending on the concentration of the solution. It was theorised that non-unimolecular excited-state species, such as an excimer, may be responsible for the emissive peak. A similar study was carried out for **PhoCb_2Chry**, **Figure 5-12**.

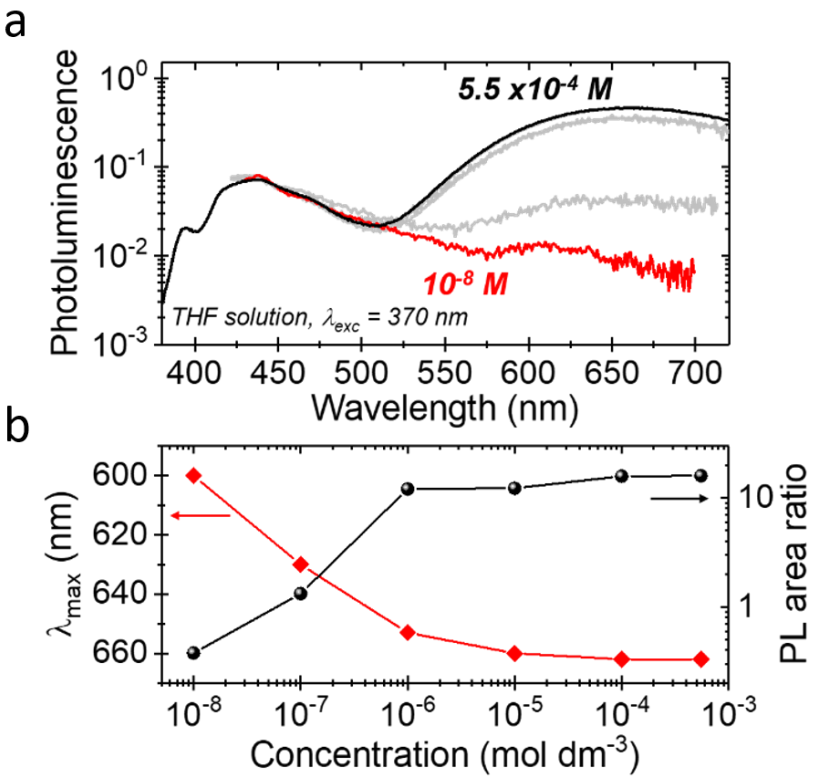


Figure 5-11 – Concentration dependent emission of **PhoCb_2Chry** in THF; (a) normalized PL spectra following 370 nm excitation, and (b) λ_{max} of long wavelength peak and long wavelength to LE PL area ratio, as a function of concentration.

Figure 5-12a outlines the effect of varying concentration on the emission of **PhoCb_2Chry** in THF. Of interest here is the stark reduction in the 660 nm peak, relative to the LE peak, below a critical concentration of ~10^{-6} M. At a concentration of 10^{-8} M, the 660 nm peak has all but disappeared, while a small amount of blue-shifted emission (**Figure 5-12b**) remains. We attribute this to the 580 nm emissive species, which appears to be present in tiny amounts, **Figure 5-9**. The 660 nm emission is consistent with an excited state dimerization process where, above a critical concentration (ca. 10^{-6} M), emission from the excimer dominates, whilst below this most excited state relaxation occurs prior to excimer formation.

Further support for an excimer explanation of these phenomena can be obtained from a temperature dependent study in chlorobenzene, **Figure 5-13**.

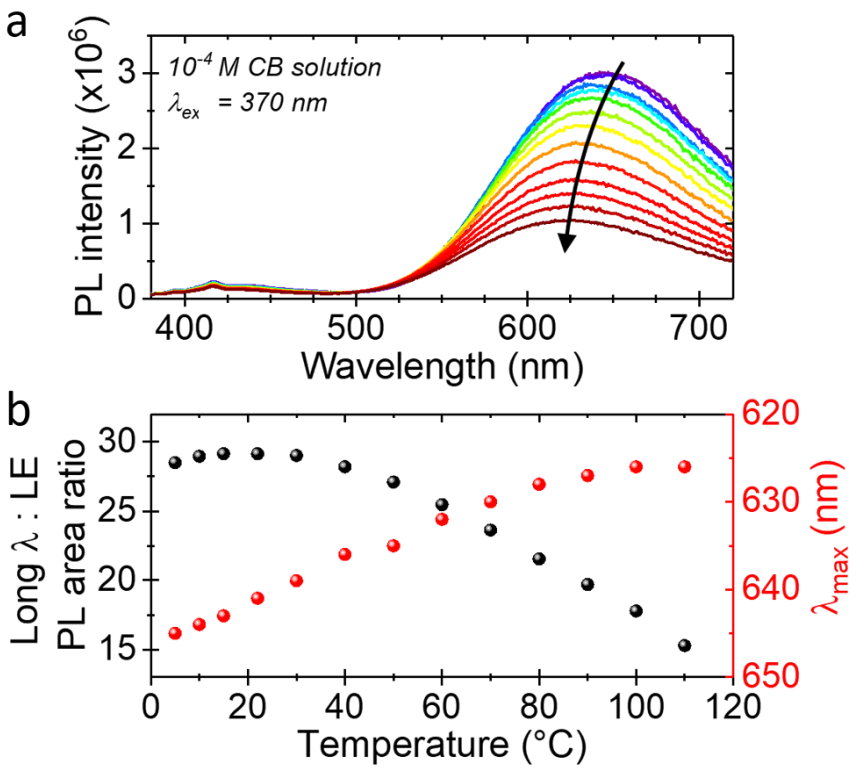


Figure 5-12 – (a) PL of **PhoCb_2Chry** in chlorobenzene, and (b) long λ:LE area ratio and λ_{max}, as a function of temperature (> R.T.).

At temperatures above those where excimer formation is a diffusion-controlled process, further temperature increase is known to reduce excimer emission;[22] an increasingly larger proportion of the molecules in solution have the activation energy to separate from the excimer, back into unimolecular species. In **Figure 5-13**, at temperatures from 5 °C and up to 25 °C, the delocalised emission increases relative to the LE. This is due to the monomer/excimer system being diffusion controlled, and an increase in temperature allows for more molecular collisions on the timescales of the unimolecular excited states, and so more excimers to form. Further increases in temperature cause the delocalised emission of **PhoCb_2Chry** decreases, and the λ_{max} blue-shifts. This is the high temperature regime as described above, and the excimers return to unimolecular ICT species, which emit at high energies.

On this basis, and supported by evidence from the concentration PL and solvatochromism study, we attribute the 660 nm emission to an excimer species formed from a ground state and an excited molecule of **PhoCb_2Chry**; the first time excimer emission has been observed in a chrysene based small molecule.[9,11,23]

The novelty and significance of this excimer can be further appreciated by comparing the degree of Stokes shift from the peak emission (λ_{max} = 660 nm) of **PhoCb_2Chry** with that of the pristine chrysene

excimer (λ_{max} = 475 nm).[11] Given the severe twisting of the chrysene backbone and steric hinderance induced by carboranyl groups, the excimer of **PhoCb_2Chry** is distinct to that previously observed, not solely originating from a dimer of the chrysene core. Rather, the lower energy emission points to a more electronically delocalized excimer species, consistent with dimerization where at least one of the molecules exhibits ICT character, with delocalization across the chrysene core onto the carboranyl groups.

5.5.5 – AIE

To understand the effect of aggregation on the excimer species, a variable H_2O/THF v/v study was undertaken, with the results presented in **Figure 5-14**.

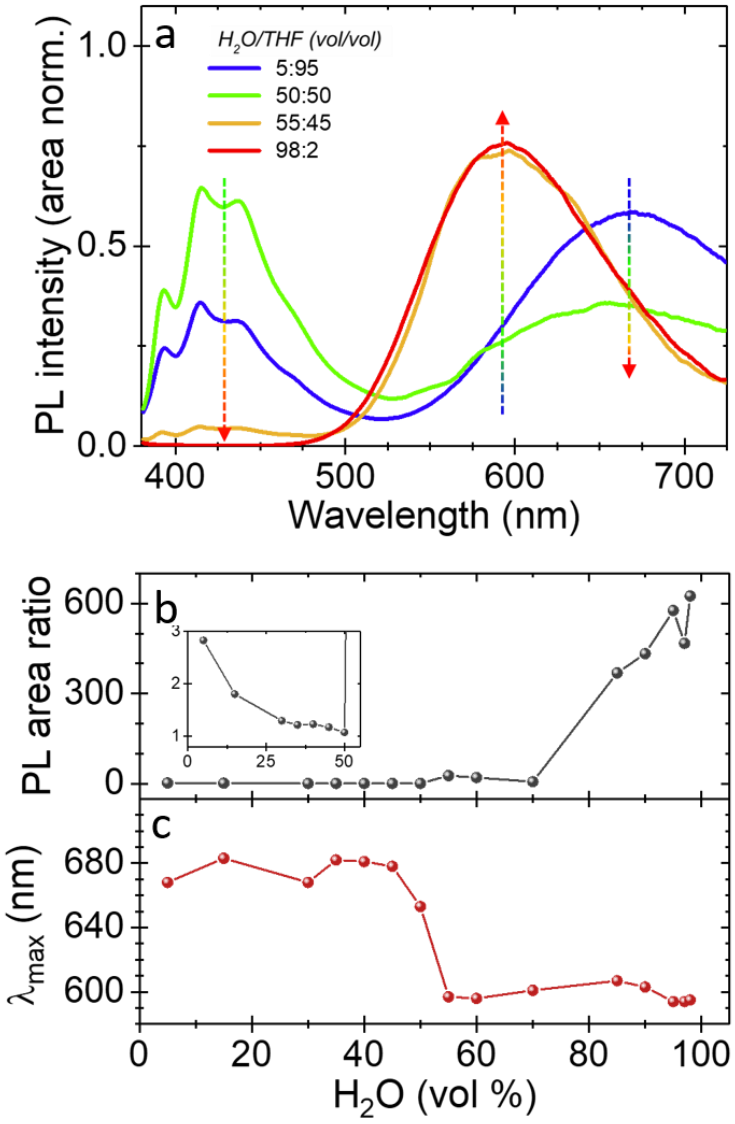


Figure 5-13 – PL of **PhoCb_2Chry** (a) in a range of varying H_2O/THF v/v, (b) PL area ratio, and (c) long-wavelength emission λ_{max} (c) as a function of H_2O volume.

At low H_2O proportions the PL of **Pho*Cb*$_2$Chry** appears identical to that in THF solution. At 50/50 H_2O/THF v/v the LE has increased relative to lower H_2O proportions, and the excimer emission decreases in intensity. This can be ascribed to the ability of water to quench delocalised excited states, as discussed in **Chapter 3**. The excimer emission also blue-shifts slightly, and further increases in the volume of H_2O in the solvent exacerbate this effect, until the λ_{max} = ca. 600 nm. This is the appearance of a non-excimer delocalised emission, and its occurrence coincides with a huge increase in PL intensity. The change in emission over the study is stark, and perhaps demonstrated most clearly in **Figure 5-15**.



Figure 5-14 – Solutions of **Pho*Cb*$_2$Chry** with varying H_2O/THF compositions, under UV excitation at 365 nm. From left to right, H_2O/THF v/v = 0/100, 25/75, 50/50, 80/20, 90/10, 95/5 and 99/1.

The dramatic increase in PL intensity is likely due to aggregation of the carborane molecules, and so can be described as AIE. Based on calculations and analysis of optical studies in **Chapter 3** and **4,** where AIE was universally attributed to carboranyl TICT states, we attribute the λ_{em} = 600 nm peak also to a TICT species.

5.5.6 – Temperature-Dependent PL

Further evidence for the TICT nature of the AIE can be found in the low-temperature PL data, **Figures 5-16** and **5-17**. For both the temperature-dependent PL in THF, and $CHCl_3$ solution, cooling from room temperature results in a reduction in the excimer emission. As demonstrated in the heated chlorobenzene study in **Figure 5-13**, in this temperature regime, excimer emission is diffusion controlled. Therefore, reducing the energy in the system also reduces the number of excimers which form on the time-scale of the excited states and, accordingly, emission intensity decreases. At the freezing point of both solvents there is a dramatic blue-shift in emission, with an increase in emission intensity, precisely replicating the results of the variable H_2O/THF v/v study (**Figure 5-14**). These

changes occur over a very small temperature range, reflecting the complexities of solvent freezing in these systems (discussed in **Chapter 3**).

Once all the solvent has frozen there is no change in the emissive λ_{max}, reflecting that there is only one emissive species present. At extremely low temperatures (10 K) it is reasonable to assume that the system is of sufficiently low energy that carborane rotation is 'turned-off', and that effectively all molecules are in the global ground state geometry, in which the carboranes have their C-C bond perpendicular to the aromatic plane; ideal for TICT emission. Based on these optical studies the ca. 600 nm emission can be confidently assigned to a TICT species.

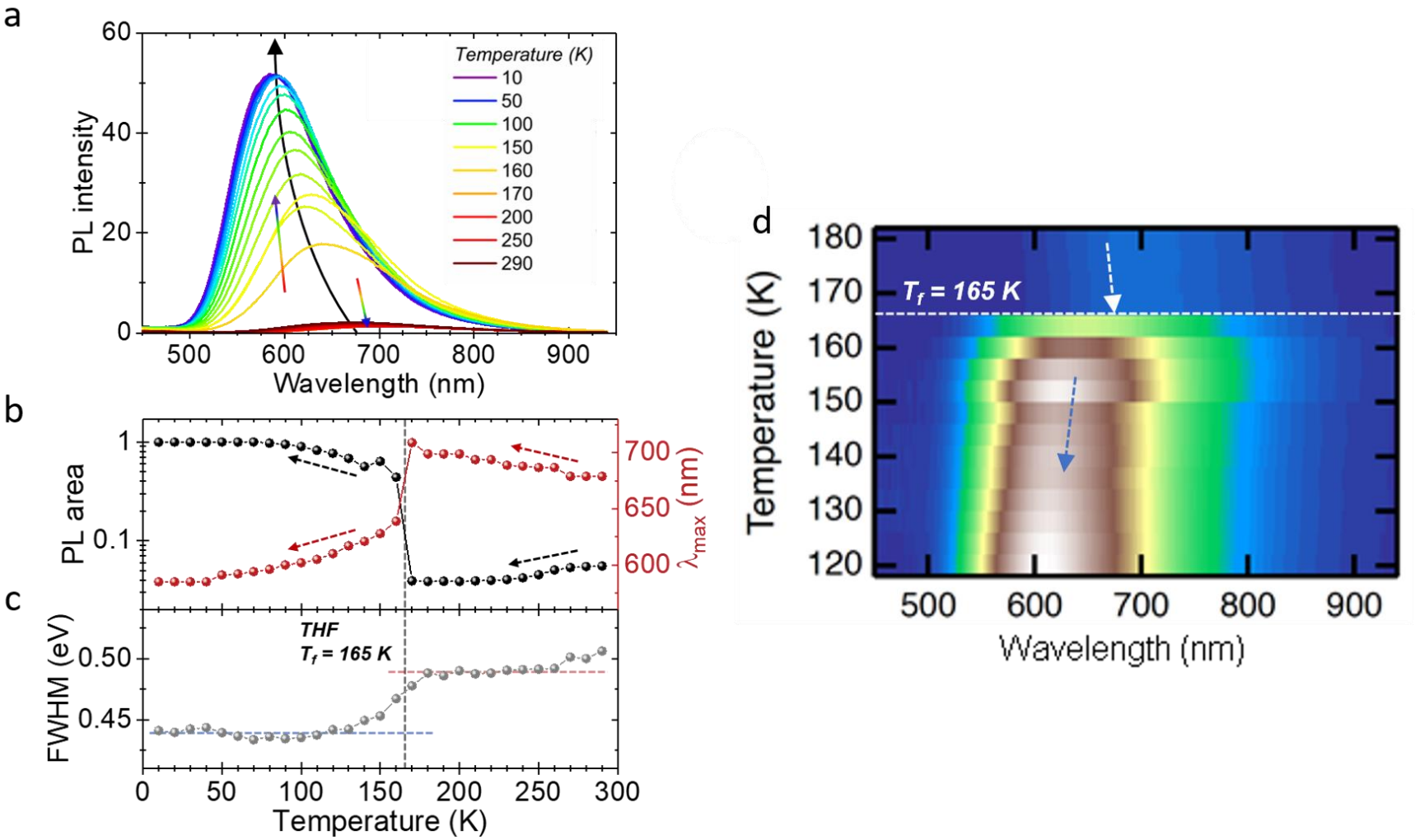


Figure 5-15 – PL of **PhoCb$_2$Chry** (a) in THF, (b) PL area ratio and long wavelength emission λ_{max}, (c) full width half maximum (FWHM), and (d) as a 2D contour map, as a function of temperature, where PL intensity increases from purple to orange. Concentration ca. 10^{-4} M.

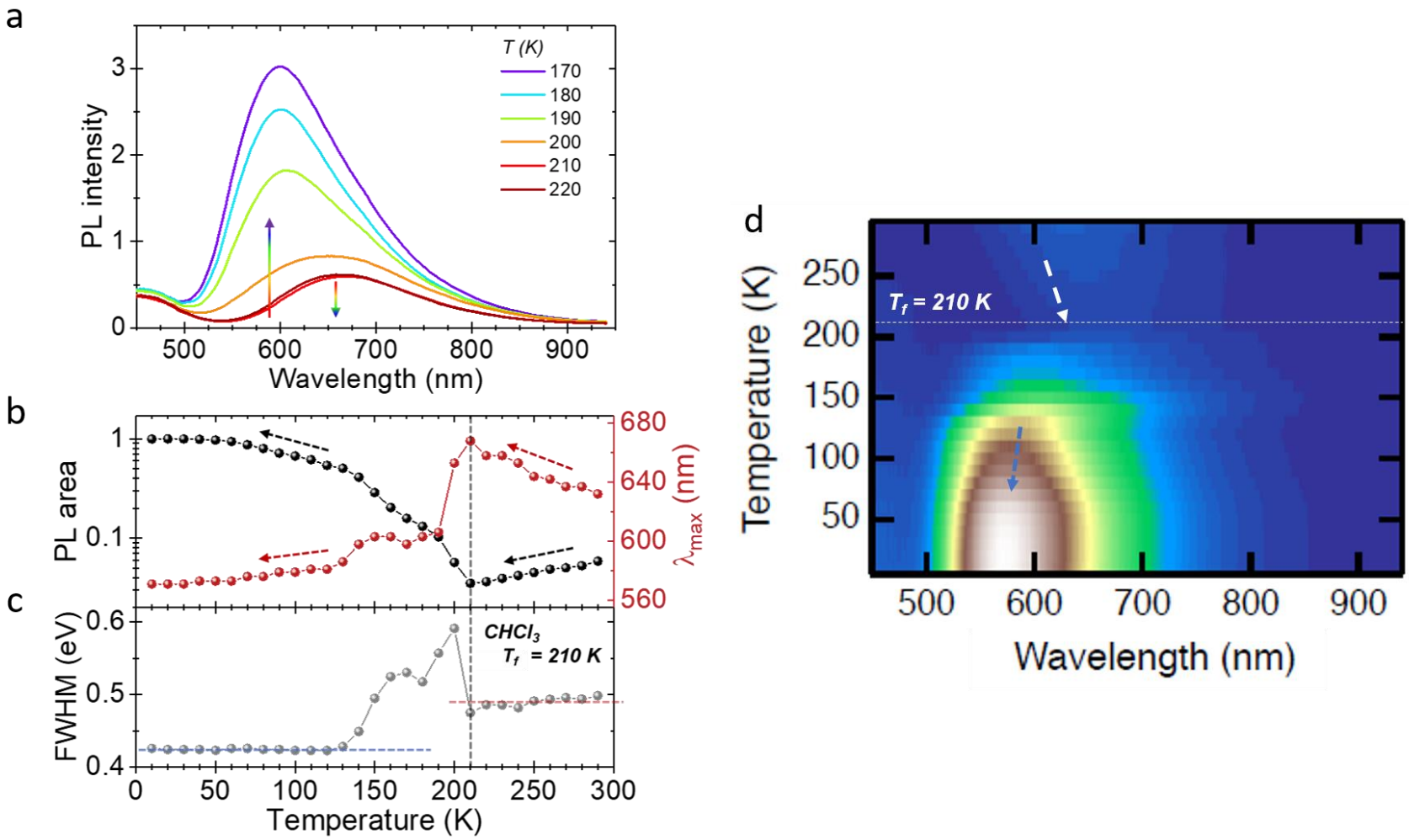


Figure 5-16 – PL of **PhoCb_2Chry** (a) in $CHCl_3$, (b) PL area ratio and long wavelength emission λ_{max}, (c) full width half maximum (FWHM), and (d) as a 2D contour map, as a function of temperature, where PL intensity increases from purple to orange. Concentration ca. 10^{-4} M.

5.5.7 – Comparison of Solution, Aggregated, and Low-Temperature PL

It is notable that, unlike for the other carboranyl acenes discussed in this thesis, **Pho*Cb*$_2$Chry** does not seem to exhibit any ICT emission. This is likely due to the significant barriers to rotation of the carboranes, causing most states to reside in the global ground state geometry, with the C-C bond perpendicular to the aromatic plane. Support for this idea can be garnered from comparison of the PL of **Pho*Cb*$_2$Chry** in good solutions, aggregated state, and in frozen solvent media at very low temperatures, **Figure 5-18**, with a summary of the data presented in **Table 5-2**.

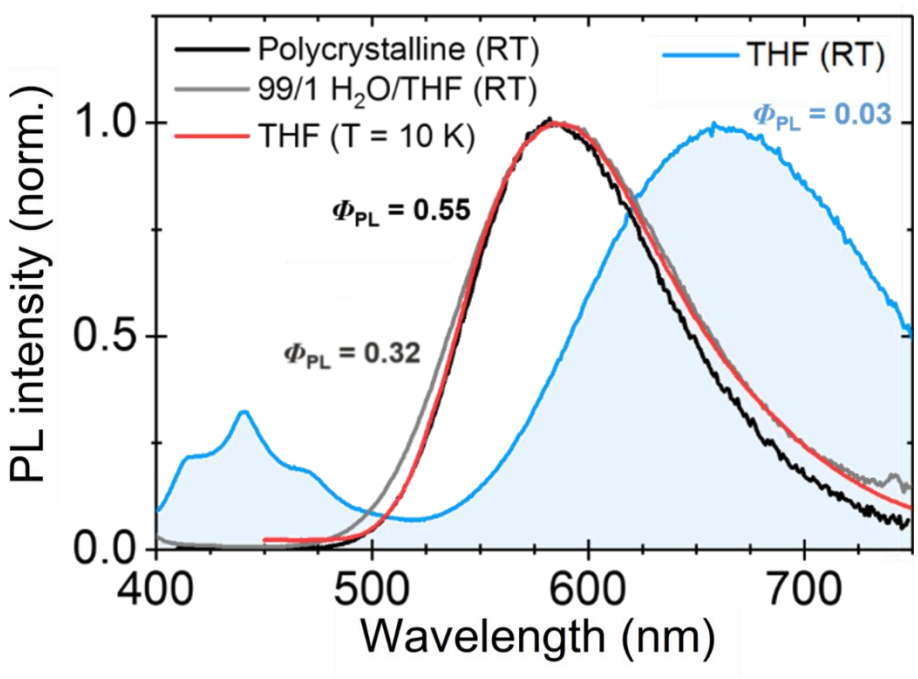


Figure 5-17 – Normalized PL spectra of **Pho*Cb*$_2$Chry** in THF (λ_{ex} = 390 nm); in 99/1 H_2O/THF v/v (λ_{ex} = 390 nm); in the solid-state (λ_{ex} = 385 nm); and in THF at low temperature (10 K, λ_{ex} = 400 nm). All solution concentrations ca. 10^{-4} M.

Condition	λ_{em} (nm)	Φ	τ (ns)
THF	436 657	0.03 0.03	0.18 ± 0.1 3.3 ± 0.1
99/1, H_2O/THF (v/v)	585	0.32	23 ± 1
Solid-state	583	0.55	17 ± 2

Table 5-2 – Summary of the PL, PL quantum efficient and TRES PL data for **Pho*Cb*$_2$Chry**. TRES data for the polycrystalline condition was carried out on a film sample.

The crystalline, 99/1 H_2O/THF, and THF (10 K) spectra are almost identical, and the aggregated states have similar quantum yield values, and excited state lifetimes (TRES data is presented in **Appendix**

VIII); both of which are extremely long for singlet emission from an organic fluorophore.[24] This is persuasive evidence that they all represent the same emissive, TICT, species. They also are essentially identical to the PL from the λ_{ex} = 500 nm in THF solution, **Figure 5-9**. The PLE of this species demonstrates a direct ground-state to ICT transition, however only a TICT emission is observed. The explanation of this phenomenon is that the ICT states which are formed quickly relax into TICT states, with C-C bond elongation. This must be either because the carboranes already have their C-C bond perpendicular to the aromatic plane, or that they have their C-C bond parallel to the aromatic plane, then rotate into the TICT geometry in the excited state. Given that no ICT emission is observed in any of the optical studies of **Ph*o*Cb$_2$Chry**, it seems most likely that the former is true, and direct ground state to ICT excitation, in which the carboranes have their C-C bond perpendicular to the aromatic plane, is possible.

5.6 – Conclusions

A new bis-*ortho*-carboranyl based chrysene derivative, **Ph*o*Cb$_2$Chry**, has been designed and synthesised, via a dichloro-chrysene compound itself formed through a BHQ cyclisation reaction. Single-crystal XRD demonstrated that the molecule was severely twisted, exhibiting some of the highest α and β deformation angles of any reported carborane-containing compound. In addition, both carboranes have their C-C bonds approximately perpendicular to the aromatic plane, 'locked' into this position with the aid of intramolecular π-π stacking between the phenyl rings and chrysene core. Optical studies in good solvents revealed a complex, multi-emissive profile, containing both LE and delocalised emission as evidenced by solvatochromism studies. The LE was found to be highly excitation-dependent, with at least three sets of correlated absorption and emission peaks. TD-DFT calculations suggested that these variations were due to the relative carboranes geometries, affecting the degree of deformation of the chrysene core, which varies the size of the locally excited state, and therefore the emissive wavelengths.

The nature of the delocalised emission in good solvents was initially ambiguous; TD-DFT calculations suggested a TICT emission could produce such low-energy emissions, however the peak proved to be reduced in intensity, relative to the LE, as the concentration was reduced. TICT species are unimolecular, but a concentration dependence points towards an excimer or exciplex excited state species. Temperature-dependent PL demonstrated that the delocalised emission decreases as the temperature is raised above approximately room temperature, and if the temperature is reduced below room temperature. This is a demonstration of two temperature-dependent regimes, which is a hallmark of excimer emission; first the diffusion-controlled excimer formation at low temperature, and second the increasing ability of dimers to dissociate at high temperature. On this basis the long-wavelength emission in good solvents was attributed to excimer emission. This excimer is significantly red-shifted relative to previously observed excimers of chrysene (which are themselves quite rare). It was therefore suggested that, significantly, the carborane must be electronically involved in the excited state. This is the first time such an excimer has been reported.

Ph*o*Cb$_2$Chry was found to exhibit AIE in aggregated H_2O/THF v/v solvents and in the solid state, with exceedingly long singlet excited state lifetimes and with good quantum yield. The emissive peak was, however, blue-shifted relative to the excimer emission. The same emissive peak, accompanied with a large increase in PL intensity, it observed in frozen solvent media at cryogenic temperatures. It was proposed that, at these temperatures, and due to the significant barriers to carborane rotation as calculated using DFT methods, essentially all molecules will be present in the ground-state geometry

in which the C-C bond is perpendicular to the aromatic plane. Precisely this geometry produced a TICT emission in TD-DFT calculations, and so the AIE was attributed to the TICT excited state. Notably, no ICT emission was observed in any of the optical studies for **PhoCb_2Chry**, however a directly ground state to ICT excitation can be observed from the PLE. Therefore, all ICT states that decay radiatively, do so via the TICT state, i.e. for **PhoCb_2Chry** all ICT states relax into TICT states. It is possible that ICT states are formed when the C-C bond is approximately parallel to the aromatic plane, and then rotate into TICT states, but it seems much more likely that these ICT states form by direct excitation from the ground state when the C-C bond is perpendicular to the plane.

5.7 – Experimental

Materials and characterisation techniques for this Chapter are identical to those described in **Chapter 2**. Steady-state PL was carried out as described in **Chapter 3**.

Solution time-resolved PL: Solution time-resolved photoluminescence measurements were performed on THF and 99/1 H_2O/THF v/v ratio solutions in 1 cm quartz cuvettes. The excitation source was a 379 nm laser excitation source, pulsed at 10 MHz and focused onto the solution with a x20 microscope objective. Resulting photoluminescence was focused into a Chromex 250 IS imaging spectrograph coupled to a Hamamatsu C4334 Streakscope detector. The time-range of the measurement was 20 and 200 ns for the THF and 99/1 H_2O/THF solutions respectively. The streak-camera setup allowed for collection of full emission spectra (400-680 nm, 3 nm spectral resolution) at every time point, which were subsequently integrated as a function of time to obtain PL kinetic traces of different emission regions.

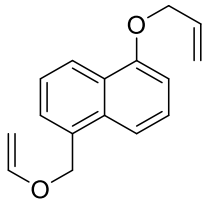
Film time-resolved PL: Thin films were prepared by spin-coating a 5 mg mL^{-1} chlorobenzene solution of **PhoCb_2Chry** on VWR Plain Micro Slides using a Laurell Model WS-650-23 spin coater under nitrogen atmosphere, with a 1000 rpm spin speed and 2 min spin time. Film time-resolved photoluminescence measurements were carried out on a Horiba Scientific DeltaFlex TCSPC system, with a PPD 650 picosecond photon detection module and an IBH NanoLED 404 nm pulsed diode excitation source. The time-range of the measurement was 100 ns, and PL kinetic traces were collected at 580 and 650 nm with 2 nm spectral resolution.

Temperature dependent photoluminescence measurements were performed on **PhoCb_2Chry** in solution, held in a 1 mm path length fused silica cuvette. Samples were inside a helium filled gas cooled closed-cycle cryostat, with spectra recorded at 10 K increments. The sample temperature was held constant via for 5 minutes prior to each measurement, enabling the sample to reach thermal equilibrium. The excitation wavelength was 400 nm, produced using a monochromated supercontinuum light source, with a long pass filter at 450 nm to attenuate the scattered excitation beam. Emitted light was collected perpendicular to excitation and focused into a 100 µm diameter optical fibre. An Andor SR-163 spectrometer was then used to disperse the emitted light onto a CCD (Andor i-Dus), with the signal averaged over 50 accumulations of 0.1 s exposure to reduce noise. A dark background was subtracted from all spectra before correcting with a calibration file derived from a known light source to account for both detector response and that of the long pass filter. No changes aside from temperature were made to the optical configuration between measurements.

Computational studies were carried out using Gaussian G09 rev. d01 and GaussView 5.0.9 visualization software. DFT calculations were accomplished using an ω tuned ωB97XD functional, with the tuning performed according to the methodology described by Körzdörfer and Brédas, and a 6-31G(d) basis set.[25] Molecular mechanics (MM) calculations were carried out using a universal force field (UFF) model. Solvent was modelled using a self-consistent reaction field (SCRF) approach using the polarisable continuum model. For solid state calculations a multilayer ONIOM model was used; high-level was treated with DFT and low-level with MM, with electronic embedding. Where appropriate, energy minima were identified following geometry optimisation and frequency calculations returning zero imaginary frequencies.

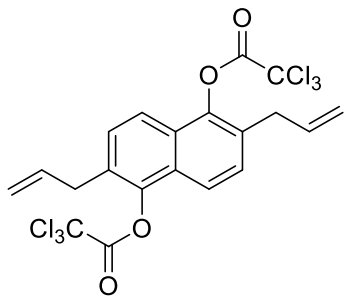
Warning: Exposure to PAH-containing substances increases the risk of cancer in humans.[26] **Replication of these syntheses should be proceeded with caution.**

1,5-Bis(allyloxy)naphthalene[14] (125)



Allyl bromide (32.19 mL, 375 mmol) was added to a suspension of 1,5 dihydroxynaphthalene (25.00 g, 156 mmol) and K_2CO_3 (51.75 g, 375 mmol) in dry acetonitrile (400 mL) and stirred overnight at room temperature. The inorganic components were separated by vacuum filtration and washed with diethyl ether (300 mL), the filtrate was washed with water (5 x 200 mL), brine (2 x 200 mL) and dried over $MgSO_4$. The solution was concentrated in vacuo and poured into methanol (300 mL) cooled to -78 °C. The precipitate was collected, washed with methanol and dried yielding the *title compound* as a light brown solid (24.46 g, 101 mmol, 65%). m.p. 90-92 °C. ^{1}H NMR (400 MHz, $CDCl_3$) δ 7.90 (2H, d, *J* = 8.6 Hz), 7.36 (2H, dd, *J* = 8.6, 7.7 Hz), 6.85 (2H, d, *J* = 7.7 Hz), 6.18 (2H, ddt, *J* = 17.2, 10.6, 5.0 Hz), 5.52 (2H, dd, *J* = 17.2, 1.6 Hz), 5.34 (2H, dd, *J* = 10.6, 1.6 Hz), 4.72 (4H, dt, *J* = 5.0, 1.6 Hz) ppm. ^{13}C NMR (100 MHz, $CDCl_3$) δ 154.5, 133.7, 127.2, 117.7, 114.9, 106.2, 69.3 ppm. HRMS (EI^+) $C_{16}H_{16}O_2$ requires 240.1150, found 240.1153.

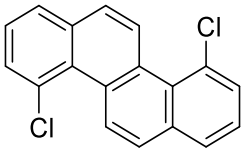
2,6-Diallyl-1,5-bis(2,2,2-trichloroacetyl)naphthalene[14] (127)



1,5-Bis(allyloxy)naphthalene (15.00 g, 62.5 mmol) was heated in an inert atmosphere, with stirring, for 2 h at 210 °C, after which the heating was removed and the orange-brown solid was allowed to cool to room temperature. Dry diethyl ether (300 mL) and pyridine (12.00 mL, 150 mmol) were added, the solution was cooled to 0 °C and trichloroacetyl chloride (16.74 mL, 150 mmol) was added dropwise. The mixture was stirred for 2 h then allowed to warm to room temperature. The brown solution was poured into a slurry of ice-water (200 g) and $NaHCO_3$ (5 g), washed with water (2 x 100 mL), saturated aq. NH_4Cl (3 x 100 mL), water (3 x 100 mL), brine (2 x 100 mL), and dried over $MgSO_4$. Solvent was removed in vacuo yielding the *title compound* as a yellow-brown solid (27.23 g, 51.3

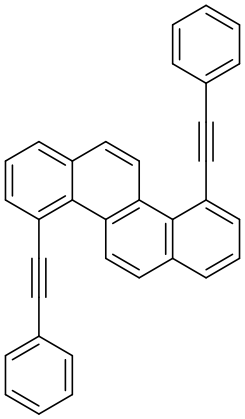
mmol, 82%) which was subsequently used without further purification. m.p. 132-133 °C. ^{1}H NMR (400 MHz, $CDCl_3$) δ 7.82 (2H, d, *J* = 8.6 Hz), 7.49 (2H, d, *J* = 8.6 Hz), 6.01-5.85 (2H, m), 5.17-5.04 (4H, m), 3.55-3.48 (4H, m) ppm. ^{13}C NMR (100 MHz, $CDCl_3$) δ 160.6, 140.0, 134.9, 129.7, 120.2, 89.8, 34.4 ppm. HRMS (EI^+) $C_{20}H_{14}Cl_6O_4$ requires 527.9023, found 527.9045.

4,10-Dichlorochrysene[14] (128)



2,6-Diallyl-1,5-bis(2,2,2-trichloroacetyl)naphthalene (4.00 g, 7.53 mmol) was dissolved in dry diglyme (4 mL) and the solution was purged with argon for 20 mins. Cuprous chloride (5 mol%, 37 mg, 0.38 mmol) was added and the mixture was purged with argon for a further 20 mins before being heated to reflux for 2 h, or until HCl gas emission ceased. The mixture was cooled, loaded directly onto a flash chromatography column and eluted with 1:9 DCM:Pet. ether. The product fractions were left to slowly evaporate, yielding the *title compound* as light-gold microcrystals (604 mg, 2.03 mmol, 27%). m.p. 159-161 °C. ^{1}H NMR (400 MHz, $CDCl_3$) δ 9.52 (2H, d, *J* = 9.1 Hz),7.90 (2H, dd, *J* = 7.8, 1.3 Hz), 7.85 (2H, d, *J* = 9.1 Hz), 7.76 (2H, dd, *J* = 7.8, 1.3Hz), 7.53 (2H, t, *J* = 7.8 Hz) ppm. ^{13}C NMR (100 MHz, $CDCl_3$) δ 134.9, 131.8, 130.1, 130.2, 127.9, 127.8, 126.9, 126.8, 125.3 ppm. HRMS (EI^+) $C_{18}H_{10}Cl_2$ requires 296.0160, found 296.0154.

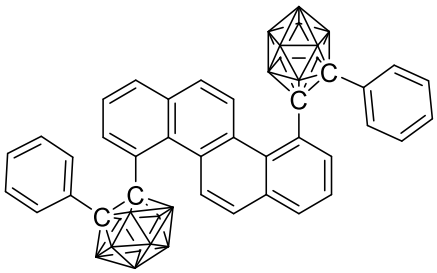
4,10-Bis(phenylethynyl)chrysene (129)



4,10-Dichlorochrysene (500 mg, 1.68 mmol), cesium carbonate (0.55 g, 1.68 mmol), bis(triphenylphosphine)palladium(II) dichloride (10 mol%, 118 mg, 0.17 mmol) tri(cyclohexyl)phosphine (20 mol%, 96 mg, 0.34 mmol) and phenylacetylene (0.74 mL, 6.73 mmol)

were added to a flask charged with dry DMF (7 mL), and the mixture was purged with argon before being heated to 110 °C overnight. After cooling to room temperature, the mixture was added directly to a silica plug (Pet. ether), which was eluted first with Pet. ether, then 1:5 DCM:Pet. ether to eluted the crude product. Solvent was removed in vacuo and the yellow oil was subjected to column chromatography with 1:19 DCM:Pet. ether, yielding the *title compound* as bright-green crystals (254 mg, 0.60 mmol, 35%). Crystals suitable for X-ray diffraction analysis were grown by slow evaporation of a biphasic solution of DCM and hexane. m.p. 184 °C. ^{1}H NMR (400 MHz, $CDCl_3$) δ 10.30 (2H, d, *J* = 9.1 Hz) 8.05-7.96 (6H, m), 7.69 (4H, m), 7.62 (2H, td, *J* = 7.7, 0.4 Hz), 7.48-7.38 (6H, m) ppm. ^{13}C NMR (100 MHz, $CDCl_3$) δ 135.1, 133.4, 131.7, 130.6, 130.2, 129.7, 128.9, 128.8, 126.5, 126.0, 125.7, 124.1, 120.1, 95.2, 92.7 ppm. HRMS (EI^+) $C_{34}H_{20}$ requires 428.1565, found 428.1579.

4,10-Bis(2-phenyl-1,2-dicarbadodecaboran-1-yl)chrysene (130)



Bmim(Cl) Method:

1 (250 mg, 0.58 mmol) and decaborane (138 mg, 1.13 mmol) were added to a vigorously stirring flask charged with a biphasic mixture of bmim(Cl) (59 mg, 0.34 mmol) and dry toluene (10 mL), and the mixture was heated to reflux for 72 h. After cooling the solvent was removed in vacuo and the crude orange oil was subjected to column chromatography with 1:19 DCM:Pet. ether, yielding 2 as bright yellow microcrystals (7 mg, 0.02 mmol, 2%).

$AgNO_3$ method:

Decaborane (552 mg, 6.96 mmol) was dissolved in a stirring solution of dry CH_3CN (1 mL) and the mixture was heated to 60 °C for 1 h. After cooling the mixture was diluted with dry toluene (10 mL), 4,10-bis(phenylethynyl)chrysene (750 mg, 1.74 mmol) and $AgNO_3$ (14 mg) were added, and the mixture was heated to reflux for 4 days. After cooling the solvent was removed in vacuo and the crude orange oil was subjected to column chromatography with 1:19 DCM:Pet. ether, yielding 2 as bright yellow microcrystals (127 mg, 0.19 mmol, 11%). Crystals suitable for X-ray diffraction analysis were grown by slow evaporation of a biphasic solution of DCM and hexane. m.p. >350 °C. ^{1}H NMR (400 MHz,

$CDCl_3$) δ 8.45 (2H, d, *J* = 8.8 Hz), 8.35 (2H, dd, *J* = 7.8, 1.0 Hz), 7.48 (2H, dd, *J* = 7.8, 1.0 Hz), 7.36 (2H, t, *J* = 7.8 Hz), 7.19 (2H, ddt, *J* = 7.5, 7.5, 1.6 Hz) 7.09 (2H, d, *J* = 8.8 Hz), 7.00 (4H, ddt, *J* = 8.8, 7.5, 1.6 Hz), 6.77-6.72 (4H, m), 4.01-1.59 (20H, br) ppm. ^{11}B NMR (128 MHz, $CDCl_3$) δ -0.91, -2.14, -3.17, -6.80, -10.14 ppm. ^{13}C NMR (100 MHz, $CDCl_3$) δ 139.8, 132.6, 132.5, 131.8, 131.4, 131.3, 130.4, 130.4, 129.8, 128.3, 126.7, 124.8, 122.2, 90.5, 89.0 ppm. MS (MALDI-ToF) $C_{34}B_{20}H_{40}$ requires 665.5, found 665.5. ATR-IR (ν cm^{-1}) 3195, 2636 (B-H) br, 2564 (B-H) br, 2259, 2162, 1269, 1951, 1395, 1447, 1263, 1073, 1017 856, 837, 774, 751, 730, 685.

5.8 – References

1 A. M. Philip, S. K. Manikandan, A. Shaji and M. Hariharan, *Chemistry – A European Journal*, 2018, **24**, 18089–18096.

2 Y. Gao, H. Liu, S. Zhang, Q. Gu, Y. Shen, Y. Ge and B. Yang, *Phys. Chem. Chem. Phys.*, 2018, **20**, 12129–12137.

3 J. Hoche, H.-C. Schmitt, A. Humeniuk, I. Fischer, R. Mitrić and M. I. S. Röhr, *Phys. Chem. Chem. Phys.*, 2017, **19**, 25002–25015.

4 H. Tricas, M. Colon, D. Ellis, S. A. Macgregor, D. McKay, G. M. Rosair, A. J. Welch, I. V. Glukhov, F. Rossi, F. Laschi and P. Zanello, *Dalton Trans.*, 2011, **40**, 4200–4211.

5 K. Nishino, H. Yamamoto, K. Tanaka and Y. Chujo, *Org. Lett.*, 2016, **18**, 4064–4067.

6 K. Nishino, H. Yamamoto, K. Tanaka and Y. Chujo, *Asian J. Org. Chem.*, 2017, **6**, 1818–1822.

7 X. Wu, J. Guo, J. Zhao, Y. Che, D. Jia and Y. Chen, *Dyes and Pigments*, 2018, **154**, 44–51.

8 H. Masuhara, F. C. D. Schryver, N. Kitamura and N. Tamai, *Microchemistry: Spectroscopy and Chemistry in Small Domains*, Newnes, 2012.

9 J. B. Birks, *Chemical Physics Letters*, 1967, **1**, 304–306.

10 H. W. Offen, *The Journal of Chemical Physics*, 1966, **44**, 699–703.

11 O. Khorev, C. D. Bösch, M. Probst and R. Häner, *Chemical Science*, 2014, **5**, 1506–1512.

12 Z. Yang, Z. Mao, Z. Xie, Y. Zhang, S. Liu, J. Zhao, J. Xu, Z. Chi and M. P. Aldred, *Chem. Soc. Rev.*, 2017, **46**, 915–1016.

13 United States, US4973758A, 1990.

14 M. Little, PhD Thesis, University of Manchester, 2014.

15 A. Toppino, A. R. Genady, M. E. El-Zaria, J. Reeve, F. Mostofian, J. Kent and J. F. Valliant, *Inorg. Chem.*, 2013, **52**, 8743–8749.

16 J. Dommerholt, F. P. J. T. Rutjes and F. L. van Delft, *Top Curr Chem (Cham)*, , DOI:10.1007/s41061-016-0016-4.

17 R. A. Harder, PhD Thesis, Durham University, 2012.

18 J. M. Brunel, *Chem. Rev.*, 2005, **105**, 857–898.

19 A. V. Marsh, Masters Thesis, Imperial College London, 2015.

20 M. Taniguchi and J. S. Lindsey, *Photochemistry and Photobiology*, 2018, **94**, 290–327.

21 D. W. Cho and D. W. Cho, *New J. Chem.*, 2014, **38**, 2233–2236.

22 M. Aoudia, M. A. J. Rodgers and W. H. Wade, *J. Phys. Chem.*, 1984, **88**, 5008–5012.

23 U. E. Wegner, R. L. Kroes, A. P. Kulshreshtha and T. Mookherji, *Journal of Luminescence*, 1971, **4**, 134–136.

24 J.-L. Bredas and S. R. Marder, *The WSPC Reference on Organic Electronics: Organic Semiconductors: (In 2 Volumes)Volume 1: Basic ConceptsVolume 2: Fundamental Aspects of Materials and Applications*, World Scientific, 2016.

25 T. Körzdörfer and J.-L. Brédas, *Acc. Chem. Res.*, 2014, **47**, 3284–3291.

26 Boström Carl-Elis, Gerde Per, Hanberg Annika, Jernström Bengt, Johansson Christer, Kyrklund Titus, Rannug Agneta, Törnqvist Margareta, Victorin Katarina and Westerholm Roger, *Environmental Health Perspectives*, 2002, **110**, 451–488.

Conclusions and Further Work

Conclusions

In **Chapter 1**, a review of the carborane literature was undertaken, from the first reports of the synthesis of icosahedral carboranes in the classified rocket fuel laboratories of the US, to the state-of-the-art carborane research examining the luminescent properties of many carborane derivatives. The latter was identified as an area ripe for research; whilst great strides had been made towards understanding the carborane luminescence structure property relationships, there was found to be confusion in the literature regarding ICT and TICT states, and how they relate to AIE. In addition, much of the current carborane research was found to focus on *ortho*-carborane, with the luminescence of *meta* and *para*-carborane left relatively unexplored. It was in these areas that the aims of the thesis were set out and explored in the following chapters.

In **Chapter 2**, the three carboranyl isomers of 9-anthracenyl carborane were synthesised and characterised in detail. Through single crystal XRD, it was found that all exhibited notable deformation of the aromatic backbone due to carborane incorporation, and that this increased on the order of *para* < *meta* < *ortho*-carborane. Computational calculations demonstrated that carborane rotation should be restricted in the same order, and temperature-dependent NMR evidence showed this experimentally. Further, it was shown, through study of the synthesised *ortho*-carboranyl NTP and BDT compounds, that the barrier to carborane rotation can be tuned by varying the groups proximal to the carborane.

In **Chapter 3**, the optical properties of the carboranes synthesised in the previous chapter were analysed. The *meta* and *para*-carboranes were found to have an efficient high-energy fluorescence in solution, as a result of the LE from the anthracene moiety. The *ortho*-carboranes exhibited the same LE, accompanied by a lower-energy emission that was assigned to TICT species. Due to this species, and the non-radiative decay route associated with vibration of the carboranyl C-C bond, the luminescence efficiency of these compounds was significantly lower than for *meta* and *para*-carboranes. Temperature-dependent PL studies for the anthracenyl-carboranes revealed that the luminescence of *meta* and *para* isomers were relatively unaffected by temperature. For the *ortho* isomer however, the PL was found to be strongly temperature dependent. Intriguingly, below the freezing point of the solvent the TICT emission decreased rapidly, accompanied by the appearance of

a new delocalised species at higher energy. This was assigned to an ICT species, in which the carboranyl C-C bond is approximately parallel to the aromatic plane (as in the ground state), appearing when the rotational decay route to the TICT species is shunted at low temperature. In H_2O/THF 99/1 (v/v) aggregated states luminescence of all compounds changed drastically. *Meta* and *para* species exhibited a delocalised excimer species, accompanied by a reduction in PL efficiency, but all *ortho* species demonstrated AIE, associated with an increase in TICT emission. Interestingly, for all compounds the solid-state emission was virtually indistinguishable to the aggregated solvent species. The nature of the aggregation in the latter was investigated with SEM and TEM, revealing ca. 100 nm – 1 µm amorphous nanoparticles, and ca. 5 nm nanocrystals. Given that the nanocrystals have a microstructure similar to the solid state, it was suggested that AIE must result from these aggregates, but AIE from the nanoparticles could not be discounted.

In **Chapter 4**, a series of phenyl-*ortho*-carborane substituted non-linear PAHs were designed and synthesised. Single crystal XRD revealed that, for all molecules, incorporation of the carborane into highly sterically congested areas of these compounds resulted in severely deformed aromatic cores, with the benzo[*k*]tetraphene derivative exhibiting the largest α and β deformation angles ever reported for any carborane species. In addition, the carboranyl C-C bond lay approximately perpendicular to the aromatic plane, as a result of the favourable interactions between the bulky phenyl group and the aromatic core. Calculated barriers to rotation for the carboranes were also found to be extremely high. The optical properties of these compounds were studied in detail, with each exhibiting LE and TICT emission in solution with relatively low emissive efficiently. ICT states were observed for these compounds, and these could be occupied by direct excitation, i.e. without first exciting the aromatic moiety and charge transfer taking place; the first time such a phenomenon has been observed for a carborane compound. In aggregated states, each compound demonstrated AIE, associated with an increase in TICT emission, aided by the perpendicular C-C carboranyl ground state geometries, and the high rigidity of the molecules.

In **Chapter 5**, a bis-phenyl-*ortho*-carboranyl-chrysene compound was designed and synthesised, with the goal of inducing a rare chrysene excimer. Single crystal XRD revealed severe aromatic deformation of the chrysene core, with both carboranes situated significantly out of the aromatic plane, and with their C-C bond approximately perpendicular to it. The luminescence in solution was found to be very complex, with a highly excitation dependent LE attributed to the various, calculated, ground state geometries of the carboranes. The molecule also exhibited a low energy emission which was found to be concentration and temperature dependent (increased with increased concentration, and decreased with increasing temperature respectively), indicative of an excimer excited state species.

The low energy nature of this excimer was unlike any other reported chrysene excimer and was found to be both the first for chrysene in solution not requiring a supramolecular scaffold, and the first excimer to involve a carborane in the excited state. The molecule was also found to exhibit AIE, aided, like the molecules in **Chapter 4**, by the high rigidity and perpendicular carboranyl C-C bond ground state geometry of the molecule.

Further Work

A logical extension of the severely deformed carborane-containing aromatics presented in this thesis is, simply, to make them more deformed. One candidate for this is a structural isomer of **Ph*o*CbBMT**, where the carborane is incorporated not at C(7) positions, but at the C(14) position. With the carborane flanked on *both* sides by phenanthrene-like groups, it is likely that this molecule, if stable, would beat **Ph*o*CbBKT** to be the most deformed carborane-containing aromatic system. This is not just an academic exercise; it is important to find the limit of structures which can incorporate carboranes to form stable molecules. Notably, during the course of this work, a limit to disubstitution of *ortho*-carborane with aromatic molecules was uncovered. Whilst dinaphthyl-*ortho*-carborane is a known compound, dianthracenyl-*ortho*-carborane is not a product from the reaction of decaborane and the appropriate acetylene (using the currently known methods), and 1-anthracenyl-2-naphthyl-*ortho*-carborane similarly could not be isolated. Clearly, decaborane will not react with all acetylenes, and so the ability to predict what structures are possible to form, before attempting synthesis, would be very useful.

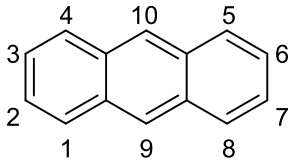
The effect of restricted carborane rotation on PL was studied extensively in this thesis, and in **Chapter 4** and **5**, phenyl groups were introduced to *ortho*-carborane to further increase molecular rigidity through favourable phenyl/acene π-π stacking interactions. Whilst there is little doubt, from the single-crystal XRD data, that these interactions exist, and that they enforce a perpendicular geometry for the carboranyl C-C bond relative to the aromatic plane, the PL in good solutions of these molecules varied significantly. The exact consequence of these interactions was difficult to probe, given that the nature of the acenes also varied across the series. Therefore, in order to investigate the specific effects of the introduction of phenyl groups to the PL of these systems, *ortho*-carborane derivatives of the phenyl-*ortho*-carborane compounds presented in this thesis could be synthesised. Whilst there are clearly other confounding variables to consider in such a study (e.g. the ground state C-C bond lengths are likely to differ), comparison of the two series is likely to yield much stronger structure-property relationships. These may form guiding principles in the design and synthesis of more efficient *ortho*-carborane containing fluorophores.

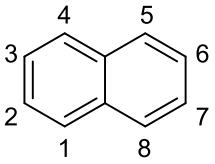
In **Chapter 4** and **5**, it was proposed that excimers involving aromatic systems, in which the delocalised region extended onto *ortho*-carborane, were possible. The exact structures of these excimers were not explored, but such an investigation using computational methods is plausible. One would require two molecules in which one is in the S_1 excited state (treated with TD-DFT), whilst the other is in the ground state (treated with DFT), and the molecules would be allowed to interact. Such a methodology is far from trivial, but the molecular orbitals may provide an insight into the delocalised nature of these excimer species. Moreover, as noted in the **Chapter 1**, incorporating the carborane into large delocalised systems for their electron-withdrawing characteristics (e.g. for OFETs) has been very challenging, so a greater understanding of instances where this *is* possible may provide useful insights for organic electronic applications.

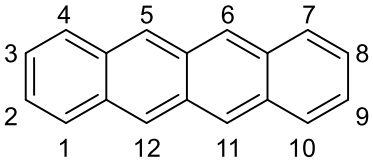
Many of the compounds discussed in this thesis are good to excellent light-emitters, especially in aggregated states, and the range of emissive wavelengths spans the whole of the visible spectrum. One such application of these materials therefore is OLEDs. The *meta* and *para*-carborane compounds may be of greater use here as they tend to emit at lower wavelengths (due to the lack of emissive charge-transfer states), in the blue-region. As discussed in **Chapter 1**, blue-emitting fluorophores often suffer from stability problems owing to the high-energy excited state required to achieve that emissive wavelengths. Carboranes are known to stabilise such species, so incorporating ***m*CbAnth** and ***p*CbAnth** into OLEDs with the aim of achieving stable, blue-light emission could prove fruitful. In addition, some of the compounds in this thesis have extremely excitation-dependent emissive properties; when excited at λ_{max} = 370 nm, **Ph*o*Cb$_2$Chry** emits blue and red-light, but when excited at λ_{max} = 500 nm the same compound emits green-light, i.e. it is a multi-emissive compound. One can imagine a single carborane-compound that emits across the whole light-spectrum as a white-light emitter. Such properties would clearly be useful for OLED devices.

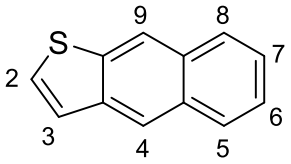
Lastly, all the carborane compounds in this thesis could be tested in neutron scintillator devices. As discussed in the introduction, the high boron density of carboranes make them well suited to such devices, however there are very few reports of their use in these applications. The reasons for this are transparent; carboranes are very expensive, and sources of fast-neutrons (i.e. synchrotrons) are few and far between. The upshot of these factors is that, for groups with appropriate resources and expertise in these areas, this field is ripe for research.

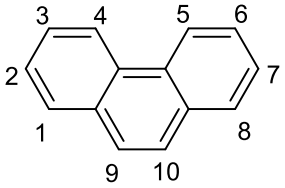
Appendix I – Page of Numbered Structures

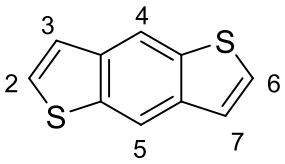


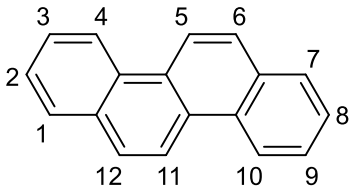


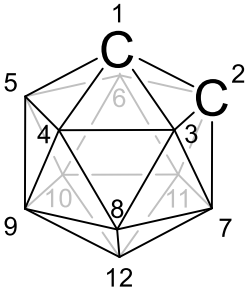


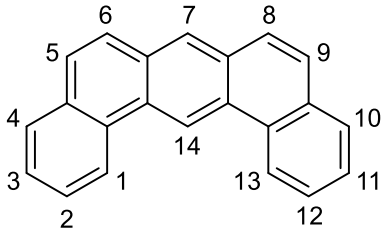


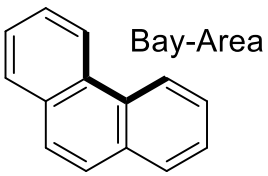


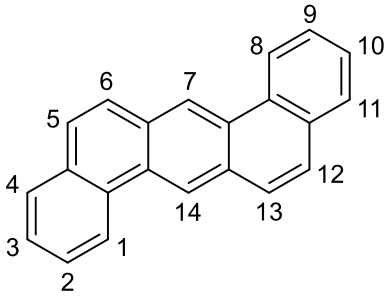












Appendix II – Crystal Data and Structure Refinement

ORTEP drawings of single crystal XRD data are presented with 50% ellipsoids, using the ellipsoid element style given below. Crystal data and structure refinement for all XRD data in this thesis is also provided.



Figure II-1 – Element styles of the ORTEP drawings presented in this thesis.

1-(9'-anthracenyl)-*para*-$C_2B_{10}H_{11}$		
Formula	$C_{16}H_{20}B_{10}$	
Formula weight	320.42	
Temperature	173(2) K	
Diffractometer, wavelength	Agilent Xcalibur 3 E, 0.71073 Å	
Crystal system, space group	Monoclinic, $P2_1/c$	
Unit cell dimensions	a = 20.9642(13) Å	α = 90°
	b = 7.2780(4) Å	β = 106.099(7)°
	c = 11.7069(7) Å	γ = 90°
Volume, Z	1716.17(19) $Å^3$, 4	
Density (calculated)	1.240 Mg/m^3	
Absorption coefficient	0.061 mm^{-1}	
F(000)	664	
Crystal colour / morphology	Green thin plates	
Crystal size	0.62 x 0.38 x 0.02 mm^3	
q range for data collection	2.976 to 28.189°	
Index ranges	-20<=h<=27, -9<=k<=5, -15<=l<=8	
Reflns collected / unique	5807 / 3449 [R(int) = 0.0214]	
Reflns observed [F>4s(F)]	2705	
Absorption correction	Analytical	
Max. and min. transmission	0.999 and 0.982	
Refinement method	Full-matrix least-squares on F2	
Data / restraints / parameters	3449 / 0 / 235	
Goodness-of-fit on F2	1.029	
Final R indices [F>4s(F)]	R1 = 0.0494, wR2 = 0.1194	
R indices (all data)	R1 = 0.0678, wR2 = 0.1292	
Largest diff. peak, hole	0.228, -0.286 $eÅ^{-3}$	
Mean and maximum shift/error	0.000 and 0.000	

1-(9'-anthracenyl)-*meta*-$C_2B_{10}H_{11}$		
Formula	$C_{16}H_{20}B_{10}$	
Formula weight	320.42	
Temperature	173(2) K	
Diffractometer, wavelength	Agilent Xcalibur 3 E, 0.71073 Å	
Crystal system, space group	Monoclinic, P21/n	
Unit cell dimensions	a = 8.9388(4) Å	α = 90°
	b = 10.1290(5) Å	β = 97.158(4)°
	c = 18.9719(8) Å	γ = 90°
Volume, Z	1704.35(13) Å^3, 4	
Density (calculated)	1.249 Mg/m^3	
Absorption coefficient	0.062 mm^{-1}	
F(000)	664	
Crystal colour / morphology	Light green tablets	
Crystal size	0.66 x 0.42 x 0.14 mm^3	
□ range for data collection	2.658 to 28.206°	
Index ranges	-10<=h<=11, -13<=k<=12, -24<=l<=12	
Reflns collected / unique	5817 / 3393 [R(int) = 0.0254]	
Reflns observed [F>4□(F)]	2685	
Absorption correction	Analytical	
Max. and min. transmission	0.993 and 0.972	
Refinement method	Full-matrix least-squares on F2	
Data / restraints / parameters	3393 / 0 / 235	
Goodness-of-fit on F2	1.032	
Final R indices [F>4□(F)]	R1 = 0.0517, wR2 = 0.1279	
R indices (all data)	R1 = 0.0668, wR2 = 0.1406	
Largest diff. peak, hole	0.247, -0.283 eÅ^{-3}	
Mean and maximum shift/error	0.000 and 0.000	

1-(9'-anthracenyl)-*ortho*-$C_2B_{10}H_{11}$		
Formula	$C_{16}H_{20}B_{10}$	
Formula weight	320.42	
Temperature	173(2) K	
Diffractometer, wavelength	Agilent Xcalibur 3 E, 0.71073 Å	
Crystal system, space group	Orthorhombic, Pbca	
Unit cell dimensions	a = 15.9576(5) Å	α = 90°
	b = 10.3037(3) Å	β = 90°
	c = 20.7746(5) Å	γ = 90°
Volume, Z	3415.82(17) Å^3, 8	
Density (calculated)	1.246 Mg/m^3	
Absorption coefficient	0.061 mm^{-1}	
F(000)	1328	
Crystal colour / morphology	Yellow blocks	
Crystal size	0.64 x 0.45 x 0.21 mm^3	
□ range for data collection	2.549 to 28.176°	
Index ranges	-11<=h<=19, -13<=k<=12, -16<=l<=27	
Reflns collected / unique	7783 / 3448 [R(int) = 0.0223]	
Reflns observed [F>4□(F)]	2730	
Absorption correction	Analytical	
Max. and min. transmission	0.988 and 0.979	
Refinement method	Full-matrix least-squares on F2	
Data / restraints / parameters	3448 / 0 / 235	
Goodness-of-fit on F2	1.029	
Final R indices [F>4□(F)]	R1 = 0.0487, wR2 = 0.1244	
R indices (all data)	R1 = 0.0645, wR2 = 0.1386	
Largest diff. peak, hole	0.302, -0.273 eÅ^{-3}	
Mean and maximum shift/error	0.000 and 0.000	

1-(4'-benzo[1,2-*b*;4,5-*b'*]dithiophenyl)-*ortho*-$C_2B_{10}H_{11}$		
Formula	$C_{12}H_{16}B_{10}S_2$	
Formula weight	332.47	
Temperature	173(2) K	
Diffractometer, wavelength	Agilent Xcalibur PX Ultra A, 1.54184 Å	
Crystal system, space group	Monoclinic, P21/c	
Unit cell dimensions	a = 7.0366(2) Å	α = 90°
	b = 9.8201(4) Å	β = 96.026(3)°
	c = 23.1446(9) Å	γ = 90°
Volume, Z	1590.47(10) Å^3, 4	
Density (calculated)	1.388 Mg/m^3	
Absorption coefficient	2.878 mm^{-1}	
F(000)	680	
Crystal colour / morphology	Colourless platy needles	
Crystal size	0.34 x 0.17 x 0.01 mm^3	
□ range for data collection	3.841 to 73.894°	
Index ranges	-8<=h<=8, -8<=k<=11, -27<=l<=28	
Reflns collected / unique	5157 / 3046 [R(int) = 0.0394]	
Reflns observed [F>4□(F)]	2347	
Absorption correction	Analytical	
Max. and min. transmission	0.971 and 0.615	
Refinement method	Full-matrix least-squares on F2	
Data / restraints / parameters	3046 / 90 / 242	
Goodness-of-fit on F2	1.076	
Final R indices [F>4□(F)]	R1 = 0.0553, wR2 = 0.1381	
R indices (all data)	R1 = 0.0752, wR2 = 0.1524	
Largest diff. peak, hole	0.550, -0.330 eÅ^{-3}	
Mean and maximum shift/error	0.000 and 0.000	

1-(4'-naphtho[2,3-*b*]thiophenyl)-*ortho*-$C_2B_{10}H_{11}$		
Formula	$C_{14}H_{18}B_{10}S$	
Formula weight	326.44	
Temperature	173(2) K	
Diffractometer, wavelength	Agilent Xcalibur 3 E, 0.71073 Å	
Crystal system, space group	Monoclinic, P21/n	
Unit cell dimensions	a = 10.9189(4) Å	α = 90°
	b = 11.1440(3) Å	β = 96.026(3)°
	c = 14.1536(5) Å	γ = 90°
Volume, Z	1658.82(10) Å^3, 4	
Density (calculated)	1.307 Mg/m^3	
Absorption coefficient	0.186 mm^{-1}	
F(000)	672	
Crystal colour / morphology	Pale yellow blocks	
Crystal size	0.66 x 0.54 x 0.34 mm^3	
□ range for data collection	2.663 to 28.205°	
Index ranges	-12<=h<=14, -14<=k<=9, -18<=l<=12	
Reflns collected / unique	5404 / 3333 [R(int) = 0.0158]	
Reflns observed [F>4□(F)]	2805	
Absorption correction	Analytical	
Max. and min. transmission	0.948 and 0.926	
Refinement method	Full-matrix least-squares on F2	
Data / restraints / parameters	3333 / 0 / 226	
Goodness-of-fit on F2	1.053	
Final R indices [F>4□(F)]	R1 = 0.0458, wR2 = 0.1239	
R indices (all data)	R1 = 0.0550, wR2 = 0.1319	
Largest diff. peak, hole	0.398, -0.348 eÅ^{-3}	
Mean and maximum shift/error	0.000 and 0.000	

4-bromo-benzo[1,2-*b*;4,5-*b'*]dithiophene		
Formula	$C_{10}H_5BrS_2$	
Formula weight	269.17	
Temperature	173(2) K	
Diffractometer, wavelength	Agilent Xcalibur 3 E, 0.71073 Å	
Crystal system, space group	Monoclinic, P21	
Unit cell dimensions	a = 9.3796(12) Å	α = 90°
	b = 3.9654(5) Å	β = 93.336(11)°
	c = 12.5455(14) Å	γ = 90°
Volume, Z	465.83(10) Å^3, 2	
Density (calculated)	1.919 Mg/m^3	
Absorption coefficient	4.801 mm^{-1}	
F(000)	264	
Crystal colour / morphology	Colourless needles	
Crystal size	0.74 x 0.07 x 0.02 mm^3	
□ range for data collection	2.639 to 28.165°	
Index ranges	-9<=h<=11, -3<=k<=5, -16<=l<=15	
Reflns collected / unique	2659 / 1582 [R(int) = 0.0423]	
Reflns observed [F>4□(F)]	1338	
Absorption correction	Analytical	
Max. and min. transmission	0.919 and 0.397	
Refinement method	Full-matrix least-squares on F2	
Data / restraints / parameters	1582 / 1 / 119	
Goodness-of-fit on F2	1.033	
Final R indices [F>4□(F)]	R1 = 0.0659, wR2 = 0.1614	
R indices (all data)	R1 = 0.0762, wR2 = 0.1739	
Absolute structure parameter	0.46(4)	
Largest diff. peak, hole	1.204, -1.790 eÅ^{-3}	
Mean and maximum shift/error	0.000 and 0.000	

4-(2'-Ph-*ortho*-$C_2B_{10}H_{10}$)-phenanthrene		
Formula	$C_{22}H_{24}B_{10}$	
Formula weight	396.51	
Temperature	173(2) K	
Diffractometer, wavelength	Agilent Xcalibur 3 E, 0.71073 Å	
Crystal system, space group	Triclinic, P-1	
Unit cell dimensions	a = 10.9407(5) Å	α = 109.144(4)°
	b = 13.8980(6) Å	β = 91.991(4)°
	c = 16.4885(8) Å	γ = 110.785(4)°
Volume, Z	2181.68(19) Å3, 4	
Density (calculated)	1.207 Mg/m^3	
Absorption coefficient	0.061 mm^{-1}	
F(000)	824	
Crystal colour / morphology	Colourless blocks	
Crystal size	0.53 x 0.45 x 0.23 mm^3	
□ range for data collection	2.574 to 28.126°	
Index ranges	-13<=h<=12, -16<=k<=18, -21<=l<=14	
Reflns collected / unique	12562 / 8575 [R(int) = 0.0165]	
Reflns observed [F>4□(F)]	6677	
Absorption correction	Analytical	
Max. and min. transmission	0.991 and 0.977	
Refinement method	Full-matrix least-squares on F2	
Data / restraints / parameters	8575 / 0 / 578	
Goodness-of-fit on F2	1.031	
Final R indices [F>4□(F)]	R1 = 0.0480, wR2 = 0.1124	
R indices (all data)	R1 = 0.0670, wR2 = 0.1250	
Largest diff. peak, hole	0.265, -0.236 eÅ^{-3}	
Mean and maximum shift/error	0.000 and 0.000	

7-(phenylethynyl)-benzo[*k*]tetraphene		
Formula	$C_{30}H_{18}$	
Formula weight	378.44	
Temperature	173(2) K	
Diffractometer, wavelength	Agilent Xcalibur PX Ultra A, 1.54184 Å	
Crystal system, space group	Monoclinic, P21/c	
Unit cell dimensions	a = 13.8344(4) Å	α = 90°
	b = 18.7503(5) Å	β = 92.262(2)°
	c = 7.37898(18) Å	γ = 90°
Volume, Z	1912.60(9) Å^3, 4	
Density (calculated)	1.314 Mg/m^3	
Absorption coefficient	0.567 mm^{-1}	
F(000)	792	
Crystal colour / morphology	Yellow platy needles	
Crystal size	0.30 x 0.24 x 0.02 mm^3	
□ range for data collection	3.197 to 73.748°	
Index ranges	-17<=h<=15, -20<=k<=22, -9<=l<=6	
Reflns collected / unique	6331 / 3678 [R(int) = 0.0251]	
Reflns observed [F>4□(F)]	2677	
Absorption correction	Analytical	
Max. and min. transmission	0.988 and 0.900	
Refinement method	Full-matrix least-squares on F2	
Data / restraints / parameters	3678 / 0 / 271	
Goodness-of-fit on F2	1.028	
Final R indices [F>4□(F)]	R1 = 0.0477, wR2 = 0.1197	
R indices (all data)	R1 = 0.0683, wR2 = 0.1381	
Largest diff. peak, hole	0.251, -0.199 eÅ^{-3}	
Mean and maximum shift/error	0.000 and 0.000	

7-(2'-Ph-*ortho*-$C_2B_{10}H_{10}$)-benzo(*k*)tetraphene		
Formula	$C_{30}H_{28}B_{10}$	
Formula weight	496.62	
Temperature	173(2) K	
Diffractometer, wavelength	Agilent Xcalibur 3 E, 0.71073 Å	
Crystal system, space group	Monoclinic, P21/c	
Unit cell dimensions	a = 20.6054(7) Å	α = 90°
	b = 12.8214(4) Å	β = 96.661(3)°
	c = 20.2210(8) Å	γ = 90°
Volume, Z	5306.1(3) Å^3, 8	
Density (calculated)	1.243 Mg/m^3	
Absorption coefficient	0.065 mm^{-1}	
F(000)	2064	
Crystal colour / morphology	Orange blocks	
Crystal size	0.41 x 0.17 x 0.13 mm^3	
□ range for data collection	2.576 to 28.328°	
Index ranges	-20<=h<=26, -12<=k<=16, -26<=l<=14	
Reflns collected / unique	18892 / 10564 [R(int) = 0.0269]	
Reflns observed [F>4□(F)]	6998	
Absorption correction	Analytical	
Max. and min. transmission	0.993 and 0.985	
Refinement method	Full-matrix least-squares on F2	
Data / restraints / parameters	10564 / 0 / 721	
Goodness-of-fit on F2	1.025	
Final R indices [F>4□(F)]	R1 = 0.0653, wR2 = 0.1577	
R indices (all data)	R1 = 0.1042, wR2 = 0.1881	
Largest diff. peak, hole	0.477, -0.254 eÅ^{-3}	
Mean and maximum shift/error	0.000 and 0.000	

7-(phenylethynyl)-benzo[*m*]tetraphene		
Formula	$C_{30}H_{28}B_{10}$	
Formula weight	496.62	
Temperature	173(2) K	
Diffractometer, wavelength	Agilent Xcalibur 3 E, 0.71073 Å	
Crystal system, space group	Monoclinic, P21/c	
Unit cell dimensions	a = 20.6054(7) Å	α = 90°
	b = 12.8214(4) Å	β = 96.661(3)°
	c = 20.2210(8) Å	γ = 90°
Volume, Z	5306.1(3) $Å^3$, 8	
Density (calculated)	1.243 Mg/m^3	
Absorption coefficient	0.065 mm^{-1}	
F(000)	2064	
Crystal colour / morphology	Orange blocks	
Crystal size	0.41 x 0.17 x 0.13 mm^3	
□ range for data collection	2.576 to 28.328°	
Index ranges	-20<=h<=26, -12<=k<=16, -26<=l<=14	
Reflns collected / unique	18892 / 10564 [R(int) = 0.0269]	
Reflns observed [F>4□(F)]	6998	
Absorption correction	Analytical	
Max. and min. transmission	0.993 and 0.985	
Refinement method	Full-matrix least-squares on F2	
Data / restraints / parameters	10564 / 0 / 721	
Goodness-of-fit on F2	1.025	
Final R indices [F>4□(F)]	R1 = 0.0653, wR2 = 0.1577	
R indices (all data)	R1 = 0.1042, wR2 = 0.1881	
Largest diff. peak, hole	0.477, -0.254 $eÅ^{-3}$	
Mean and maximum shift/error	0.000 and 0.000	

7-(2'-Ph-*ortho*-$C_2B_{10}H_{10}$)-benzo(*m*)tetraphene		
Formula	$C_{30}H_{28}B_{20}$, CH_2Cl_2	
Formula weight	581.55	
Temperature	173(2) K	
Diffractometer, wavelength	Agilent Xcalibur PX Ultra A, 1.54184 Å	
Crystal system, space group	Triclinic, P-1	
Unit cell dimensions	a = 11.6340(6) Å	α = 105.701(6)°
	b = 12.1182(9) Å	β = 95.845(5)°
	c = 12.9972(8) Å	γ = 116.863(7)°
Volume, Z	1519.11(19) $Å^3$, 2	
Density (calculated)	1.271 Mg/m^3	
Absorption coefficient	2.067 mm^{-1}	
F(000)	600	
Crystal colour / morphology	Yellow blocks	
Crystal size	0.37 x 0.19 x 0.12 mm^3	
□ range for data collection	3.659 to 73.718°	
Index ranges	-8<=h<=14, -15<=k<=11, -14<=l<=16	
Reflns collected / unique	8650 / 5803 [R(int) = 0.0261]	
Reflns observed [F>4□(F)]	4403	
Absorption correction	Analytical	
Max. and min. transmission	0.874 and 0.717	
Refinement method	Full-matrix least-squares on F2	
Data / restraints / parameters	5803 / 0 / 361	
Goodness-of-fit on F2	1.042	
Final R indices [F>4□(F)]	R1 = 0.0574, wR2 = 0.1553	
R indices (all data)	R1 = 0.0725, wR2 = 0.1700	
Largest diff. peak, hole	0.384, -0.335 $eÅ^{-3}$	
Mean and maximum shift/error	0.000 and 0.000	

4,10-bis(phenylethynyl)-chrysene		
Formula	$C_{34}H_{20}$	
Formula weight	428.50	
Temperature	173(2) K	
Diffractometer, wavelength	Agilent Xcalibur PX Ultra A, 1.54184 Å	
Crystal system, space group	Monoclinic, P21/c	
Unit cell dimensions	a = 4.04196(17) Å	α = 90°
	b = 24.5247(9) Å	β = 100.033(4)°
	c = 11.0878(4) Å	γ = 90°
Volume, Z	1082.30(7) Å^3, 2	
Density (calculated)	1.315 Mg/m^3	
Absorption coefficient	0.567 mm^{-1}	
F(000)	448	
Crystal colour / morphology	Yellow plates	
Crystal size	0.42 x 0.29 x 0.04 mm^3	
□ range for data collection	3.605 to 73.718°	
Index ranges	-3<=h<=4, -27<=k<=30, -11<=l<=13	
Reflns collected / unique	4257 / 2096 [R(int) = 0.0306]	
Reflns observed [F>4□(F)]	1625	
Absorption correction	Analytical	
Max. and min. transmission	0.978 and 0.859	
Refinement method	Full-matrix least-squares on F2	
Data / restraints / parameters	2096 / 0 / 154	
Goodness-of-fit on F2	1.041	
Final R indices [F>4□(F)]	R1 = 0.0455, wR2 = 0.1111	
R indices (all data)	R1 = 0.0613, wR2 = 0.1259	
Largest diff. peak, hole	0.192, -0.178 eÅ^{-3}	
Mean and maximum shift/error	0.000 and 0.000	

4,10-bis(2'-Ph-*ortho*-$C_2B_{10}H_{10}$)$_2$-chrysene		
Formula	$C_{34}H_{40}B_{20}$	
Formula weight	664.86	
Temperature	173(2) K	
Diffractometer, wavelength	Agilent Xcalibur PX Ultra A, 1.54184 Å	
Crystal system, space group	Orthorhombic, Pbca	
Unit cell dimensions	a = 15.6347(2) Å	α = 90°
	b = 14.20177(17) Å	β = 90°
	c = 32.3610(4) Å	γ = 90°
Volume, Z	7185.43(16) Å^3, 8	
Density (calculated)	1.229 Mg/m^3	
Absorption coefficient	0.436 mm^{-1}	
F(000)	2752	
Crystal colour / morphology	Yellow blocks	
Crystal size	0.15 x 0.13 x 0.07 mm^3	
□ range for data collection	3.932 to 73.783°	
Index ranges	-19<=h<=17, -17<=k<=16, -21<=l<=39	
Reflns collected / unique	14223 / 6970 [R(int) = 0.0349]	
Reflns observed [F>4□(F)]	5518	
Absorption correction	Analytical	
Max. and min. transmission	0.975 and 0.953	
Refinement method	Full-matrix least-squares on F2	
Data / restraints / parameters	6970 / 0 / 487	
Goodness-of-fit on F2	1.043	
Final R indices [F>4□(F)]	R1 = 0.0443, wR2 = 0.1098	
R indices (all data)	R1 = 0.0636, wR2 = 0.1200	
Largest diff. peak, hole	0.215, -0.191 eÅ^{-3}	
Mean and maximum shift/error	0.000 and 0.000	

Appendix III – Aromatic Deformation Parameters

A description and summary of the carborane-induced aromatic deformation quantities are presented below:

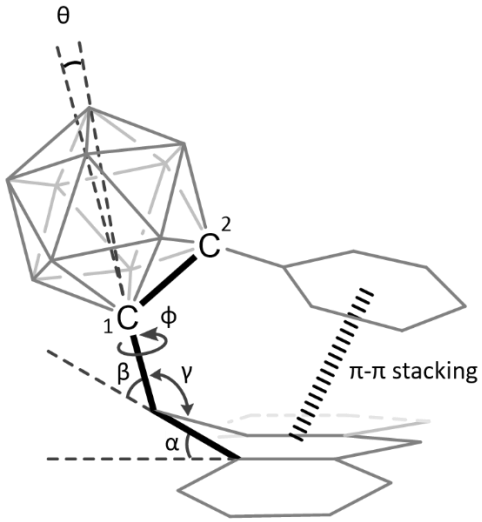


Figure III-1 – Definition of the carborane-induced aromatic deformation quantities.

Compound	α (°)	β (°)	γ (°)	ϕ (°)	θ (°)	C(1)-C(2) Bond Length (Å)	π-π distance (Å)
1-(9'-anthracenyl)-*ortho*-$C_2B_{10}H_{11}$	13.39	7.28	-	22.26	172.13	1.664	-
1-(9'-anthracenyl)-*meta*-$C_2B_{10}H_{11}$	14.89	5.65	-	-	175.68	-	-
1-(9'-anthracenyl)-*para*-$C_2B_{10}H_{11}$	13.33	5.62	-	-	176.90	-	-
1-(4'-benzo[1,2-*b*;4,5-*b'*]dithiophenyl)-*ortho*-$C_2B_{10}H_{11}$	6.79	1.14	120.78	14.59	175.45	1.665	-
1-(4'-naphtho[2,3-*b*]thiophenyl)-*ortho*-$C_2B_{10}H_{11}$	11.07	4.27	120.16	22.79	172.58	1.663	-
4-(2'-Ph-*ortho*-$C_2B_{10}H_{10}$)-phenanthrene (A)	15.65	13.15	125.91	66.75	168.55	1.759	3.638
4-(2'-Ph-*ortho*-$C_2B_{10}H_{10}$)-phenanthrene (B)	14.77	10.88	126.21	70.72	169.27	1.769	4.090
7-(2'-Ph-*ortho*-$C_2B_{10}H_{10}$)-benzo(*k*)tetraphene (A)	22.82	12.93	120.57	74.67	166.34	1.830	3.674
7-(2'-Ph-*ortho*-$C_2B_{10}H_{10}$)-benzo(*k*)tetraphene (B)	23.37	13.95	120.02	77.68	166.30	1.827	3.606
7-(2'-Ph-*ortho*-$C_2B_{10}H_{10}$)-benzo(*m*)tetraphene	17.19	6.47	-	86.29	170.46	1.817	3.996
4,10-bis(2'-Ph-*ortho*-$C_2B_{10}H_{10}$)$_2$-chrysene (1)	15.52	19.49	126.08	71.11	169.52	1.772	3.920
4,10-bis(2'-Ph-*ortho*-$C_2B_{10}H_{10}$)$_2$-chrysene (2)	17.50	13.48	124.85	71.69	168.44	1.761	3.780

Table III-1 – Summary of the aromatic deformation quantities and carborane structural values, as measured from single-crystal XRD data. Labels (A) and (B) refer to structurally independent molecules in the asymmetric unit, and (1) and (2) refer to the two carboranes within the one chrysene molecule. The quantity γ presented is the larger of the two possible γ angles.

Appendix IV – Cyclic Voltammetry

CV traces of the aryl carboranes in this these are presented in **Figure IV-1**, with selected data presented in **Table IV-1** and **IV-2**. Compounds are labelled: (a) 9-(1'-*ortho*-$C_2B_{10}H_{11}$)-anthracene, (b) 4-(1'-*ortho*-$C_2B_{10}H_{11}$)-BDT, (c) 4-(1'-*ortho*-$C_2B_{10}H_{11}$)-NTP, (d) 1-(4'-phenanthrenyl)-2-phenyl-*ortho*-$C_2B_{10}H_{10}$, (e) 1-(7'-benzo[m]tetraphenyl)-2-phenyl-*ortho*-$C_2B_{10}H_{10}$, (f) 1-(7'-benzo[k]tetraphenyl)-2-phenyl-*ortho*-$C_2B_{10}H_{10}$, (g) 4,10-(1'-(2''-phenyl)-*ortho*-$C_2B_{10}H_{10})_2$chrysene. Note, *meta* and *para*-carboranes in general are not stable towards electrochemical reduction.

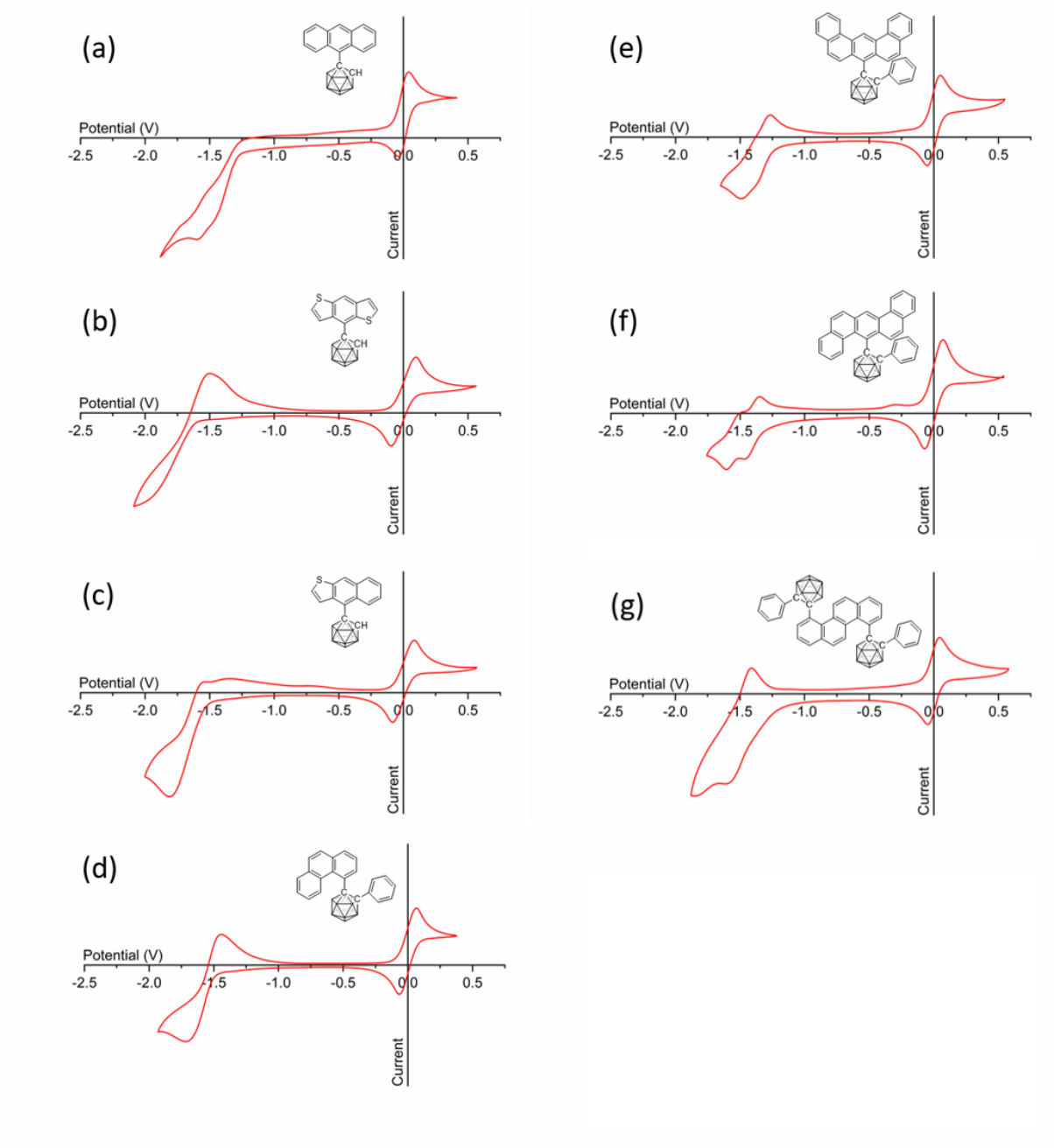


Figure IV-1 – CV traces of aryl carboranes.

Compound	E (Red_1) cathodic (V)	E (Red_1) anodic (V)	$E_{1/2}$ (Red_1) (V)	Red_1 p-p (mV)	E (Red_2) cathodic (V)	E (Red_2) anodic (V)	$E_{1/2}$ (Red_2) (V)	Red_2 p-p (mV)	$E_{1/2}$ (Red_1-Red_2) (mV)
(a)	-1.46	-1.29	-1.38	170	-1.63	-1.51	-1.57	120	195
(b)[a]	-1.80	-1.61	-1.71	190	-	-	-	-	-
(c)[a]	-1.72	-1.52	-1.62	200	-	-	-	-	-
(d)[a]	-1.62	-1.50	-1.56	120	-	-	-	-	-
(e)	-1.36	-1.24	-1.30	120	-1.48	-1.39	-1.44	0.09	135
(f)	-1.44	-1.31	-1.38	130	-1.62	-1.52	-1.57	0.10	195
(g)	-1.80	-1.52	-1.66	280	-1.88	-1.7	-1.79	0.18	130

[a] The two redox processes overlap and are indistinguishable.

[b] This compound exhibits four redox processes; row two contains data for Red_3 and Red_4.

Table IV-1 – Reduction and oxidation potentials for various aryl *ortho*-carboranes in 0.1 M NBu_4PF_6 in dry DCM, at 100 mV / s sweep speed, using a platinum working electrode, Pt counter electrode and an Ag/AgCl (Ag/Ag^+) reference electrode with ferrocene as internal reference at 0 V.

Compound	HOMO (eV)
(a)	-2.94
(b)	-2.60
(c)	-2.68
(d)	-2.78
(e)	-3.04
(f)	-2.96
(g)	-2.53

Table IV-2 – HOMO levels of the aryl *ortho*-carboranes.

Appendix V – Optical Data from Chapter 3

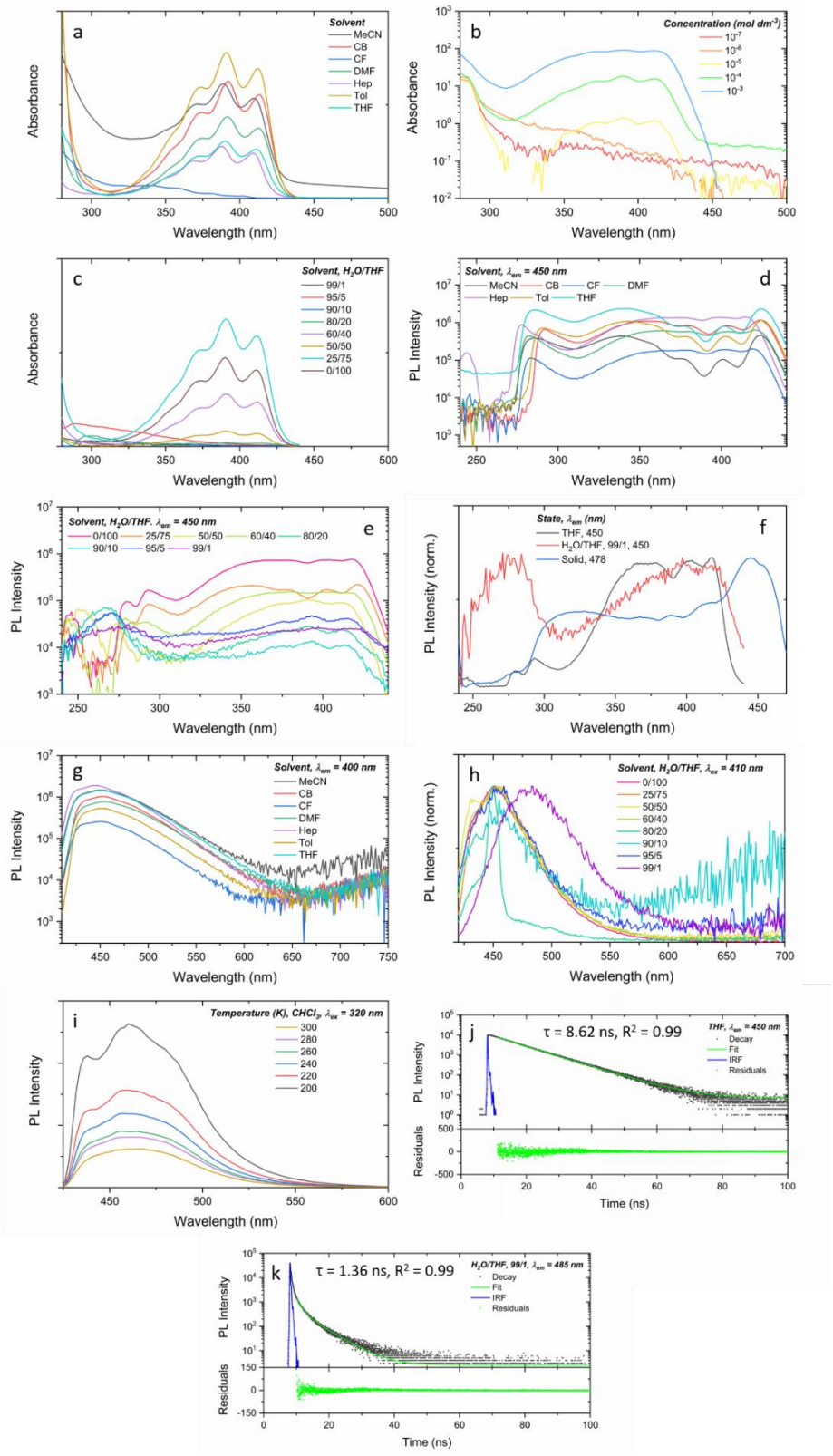


Figure V-1 – Optical studies of ***p*CbAnth**. (a) Solvent-dependent UV-Vis; (b) concentration-dependent UV-Vis; (c) H_2O/THF (v/v) solvent-dependent UV-Vis; (d) solvent-dependent PLE; (e) H_2O/THF (v/v) solvent-dependent PLE; (f) THF, 99/1 H_2O/THF (v/v) and solid-state PLE; (g) solvent-dependent PL (non-norm.); (h) H_2O/THF (v/v) solvent-dependent PL (norm.); (i) temperature-dependent PL (chloroform); (j) time-resolved PL in THF; (k) time-resolved PL in 99/1 H_2O/THF (v/v) solution.

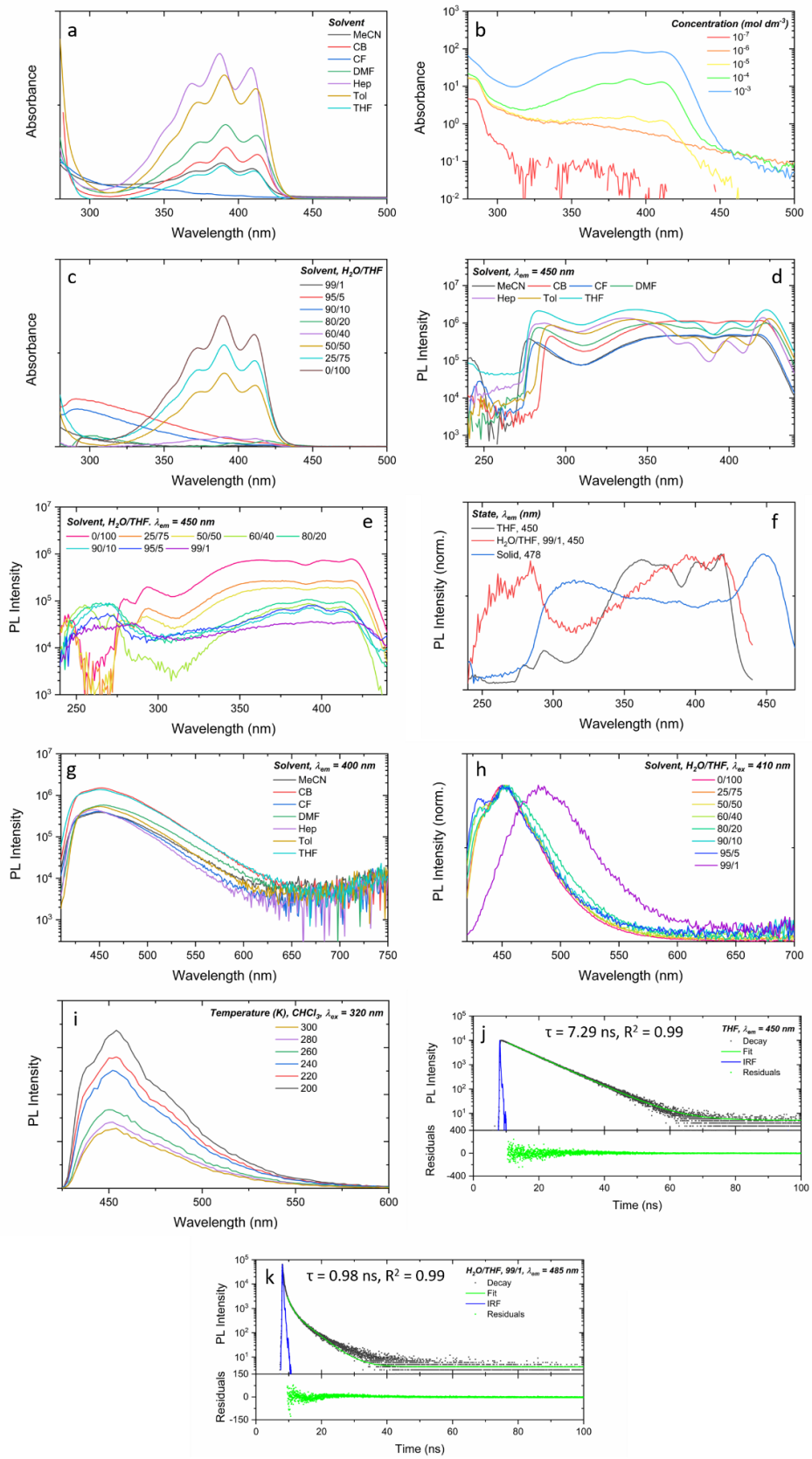
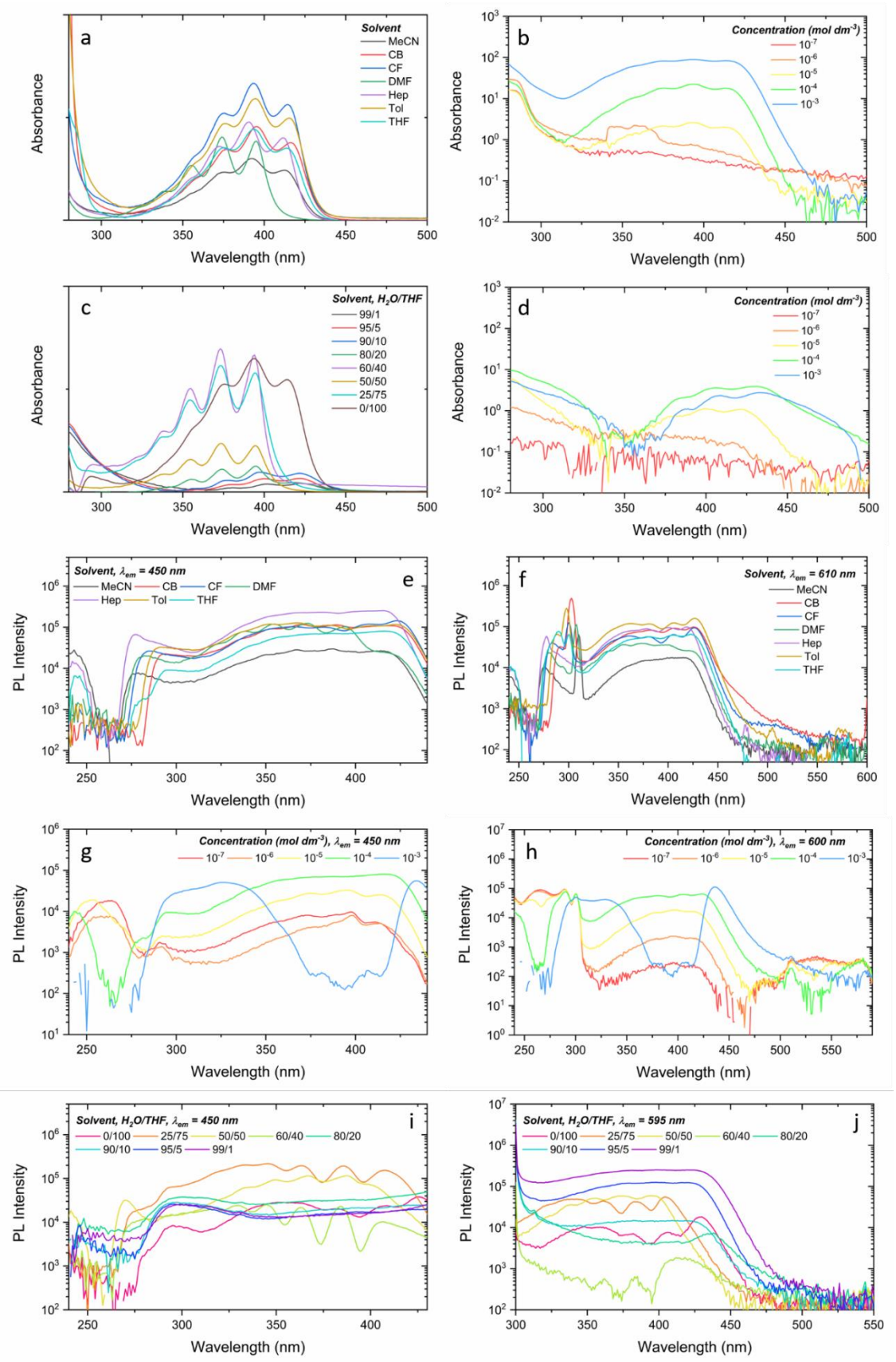


Figure V-2 – Optical studies of ***m*CbAnth**. (a) Solvent-dependent UV-Vis; (b) concentration-dependent UV-Vis; (c) H_2O/THF (v/v) solvent-dependent UV-Vis; (d) solvent-dependent PLE; (e) H_2O/THF (v/v) solvent-dependent PLE; (f) THF, 99/1 H_2O/THF (v/v) and solid-state PLE; (g) solvent-dependent PL (non-norm.); (h) H_2O/THF (v/v) solvent-dependent PL (norm.); (i) temperature-dependent PL (chloroform); (j) time-resolved PL in THF; (k) time-resolved PL in 99/1 H_2O/THF (v/v) solution.


a
Solvent
MeCN
CB
CF
DMF
Hep
Tol
THF
Absorbance
Wavelength (nm)
b
Concentration (mol dm-3)
10-7
10-6
10-5
10-4
10-3
Absorbance
Wavelength (nm)
c
Solvent, H2O/THF
99/1
95/5
90/10
80/20
60/40
50/50
25/75
0/100
Absorbance
Wavelength (nm)
d
Concentration (mol dm-3)
10-7
10-6
10-5
10-4
10-3
Absorbance
Wavelength (nm)
e
Solvent, λem = 450 nm
MeCN
CB
CF
DMF
Hep
Tol
THF
PL Intensity
Wavelength (nm)
f
Solvent, λem = 610 nm
MeCN
CB
CF
DMF
Hep
Tol
THF
PL Intensity
Wavelength (nm)
g
Concentration (mol dm-3), λem = 450 nm
10-7
10-6
10-5
10-4
10-3
PL Intensity
Wavelength (nm)
h
Concentration (mol dm-3), λem = 600 nm
10-7
10-6
10-5
10-4
10-3
PL Intensity
Wavelength (nm)
i
Solvent, H2O/THF, λem = 450 nm
0/100
25/75
50/50
60/40
80/20
90/10
95/5
99/1
PL Intensity
Wavelength (nm)
j
Solvent, H2O/THF, λem = 595 nm
0/100
25/75
50/50
60/40
80/20
90/10
95/5
99/1
PL Intensity
Wavelength (nm)

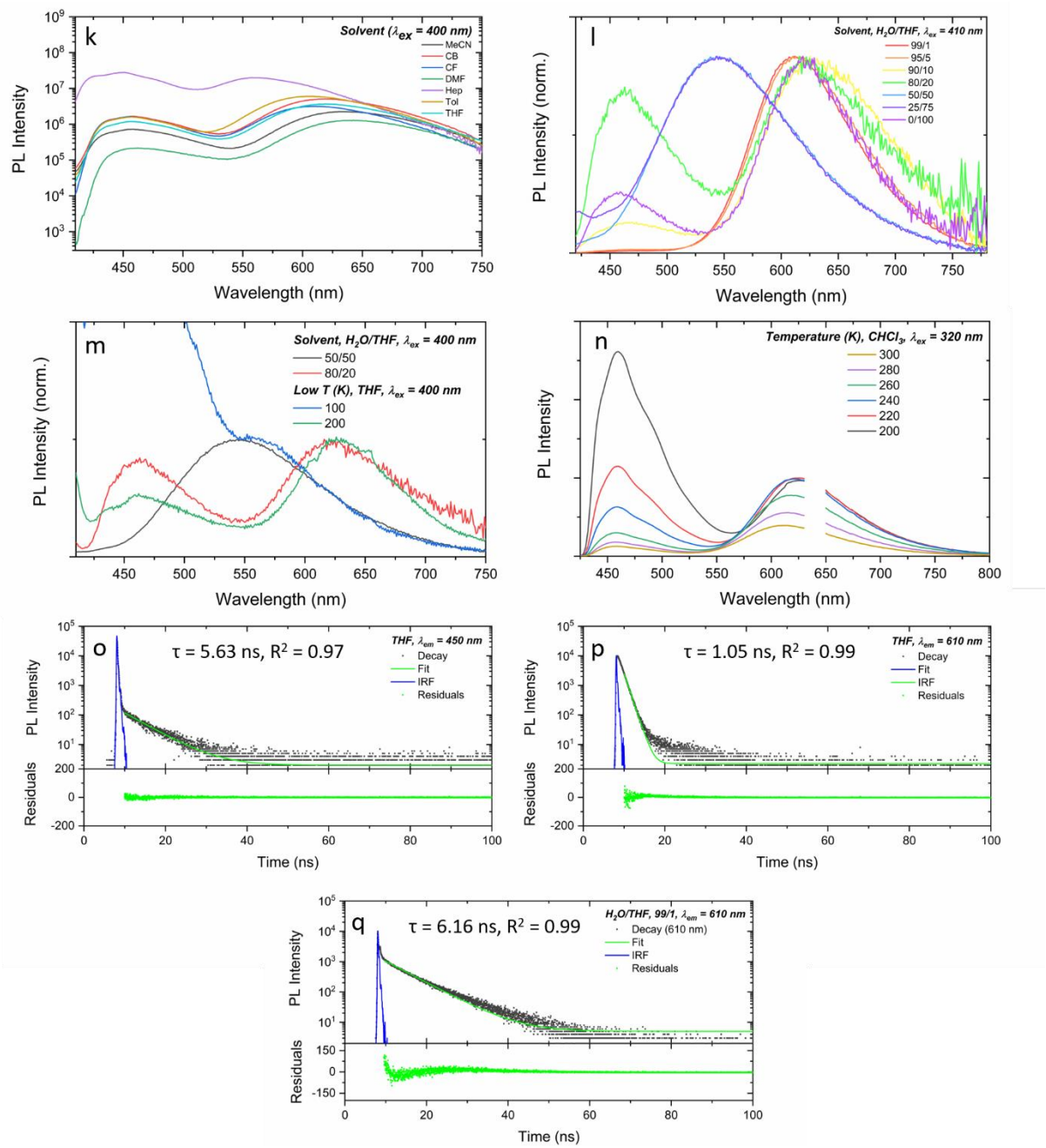


Figure V-3 – Optical studies of ***o*CbAnth**. (a) Solvent-dependent UV-Vis; (b) concentration-dependent UV-Vis; (c) H_2O/THF (v/v) solvent-dependent UV-Vis; (d) concentration-dependent UV-Vis of 99/1 H_2O/THF (v/v) solution; (e) solvent-dependent PLE of LE; (f) solvent-dependent PLE of TICT emission; (g) concentration-dependent PLE of LE; (h) concentration-dependent PLE of TICT emission; (i) H_2O/THF (v/v) solvent-dependent PLE of LE; (j) H_2O/THF (v/v) solvent-dependent PLE of TICT emission; (k) solvent-dependent PL (non-norm.); (l) H_2O/THF (v/v) solvent-dependent PL (norm.); (m) comparison of H_2O/THF (v/v) solvent-dependent and temperature-dependent PL; (n) temperature-dependent PL; (o) time-resolved PL of LE in THF; (p) time-resolved PL of TICT emission in THF; (q) time-resolved PL of TICT in 99/1 H_2O/THF (v/v) solution.

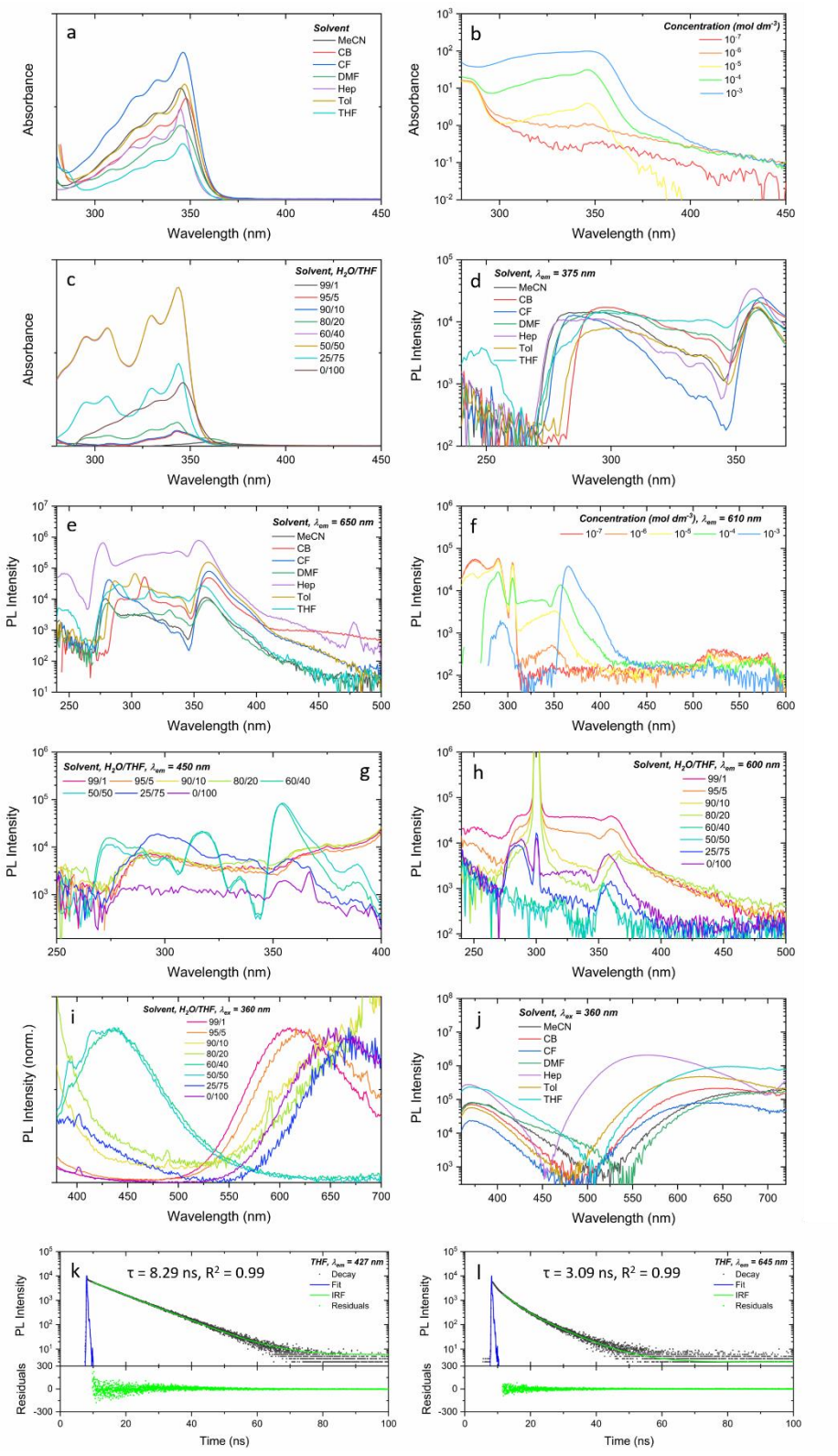


Figure V-4 – Optical studies of ***o*CbBDT**. (a) Solvent-dependent UV-Vis; (b) concentration-dependent UV-Vis; (c) H_2O/THF (v/v) solvent-dependent UV-Vis; (d) solvent-dependent PLE of LE; (e) solvent-dependent PLE of TICT emission; (f) concentration-dependent PLE; (g) H_2O/THF (v/v) solvent-dependent PLE of LE; (h) H_2O/THF (v/v) solvent-dependent PLE of TICT; (i) H_2O/THF (v/v) solvent-dependent PL (norm.); (j) solvent-dependent PL (non-norm.); (k) time-resolved PL of LE in THF; (l) time-resolved PL of TICT in THF.

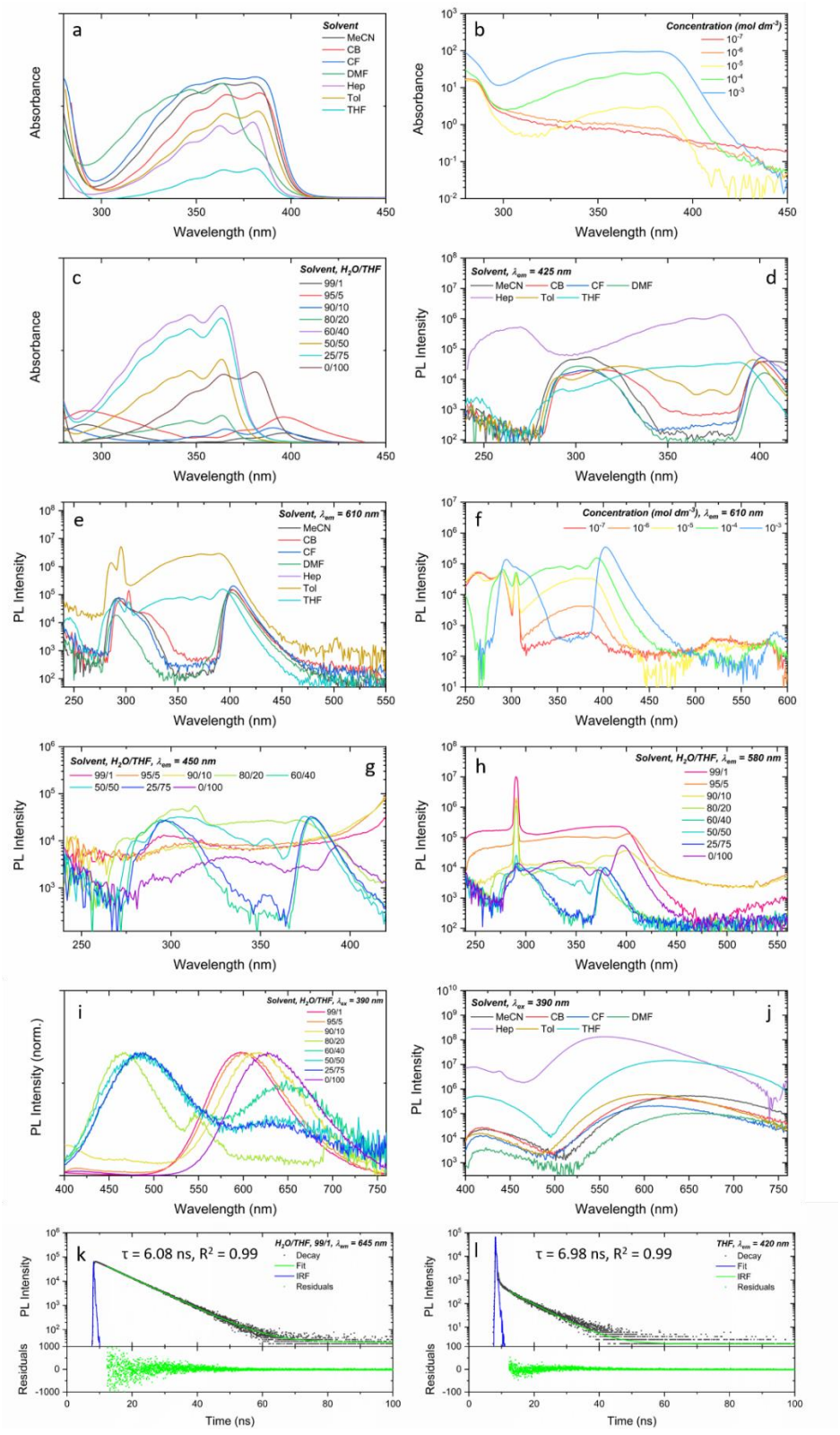


Figure V-5 – Optical studies of ***o*CbNTP**. (a) Solvent-dependent UV-Vis; (b) concentration-dependent UV-Vis; (c) H_2O/THF (v/v) solvent-dependent UV-Vis; (d) solvent-dependent PLE of LE; (e) solvent-dependent PLE of TICT emission; (f) concentration-dependent PLE; (g) H_2O/THF (v/v) solvent-dependent PLE of LE; (h) H_2O/THF (v/v) solvent-dependent PLE of TICT; (i) H_2O/THF (v/v) solvent-dependent PL (norm.); (j) solvent-dependent PL (non-norm.); (k) time-resolved PL of LE in THF; (l) time-resolved PL of TICT in THF.

	Compound	Absorption Maximum (nm)	Extinction Coefficient (M^{-1} cm^{-1})	High Energy Emission Maximum (nm)	Excited State Lifetime (ns); R^2	Stokes Shift (cm^{-1})	Low Energy Emission Maximum (nm)	Excited State Lifetime (ns); R^2	Stokes Shift (cm^{-1})	Φ; λ_{ex} (nm)
THF	*p*CbAnth	411	15400	450	8.62; 0.99	2109	-	-	-	0.70; 412
	*m*CbAnth	411	9630	450	7.21; 0.99	2109	-	-	-	0.85; 412
	*o*CbAnth	415	13900	458	5.63; 0.97	2262	620	1.05; 0.99	8712	0.02; 412
	*o*CbBDT	346	5250	403	8.29; 0.99	4088	660	3.09; 0.99	13750	0.004; 350
	*o*CbNTP	386	9700	439	6.01; 0.99	3128	627	6.98; 0.99	9958	0.09; 390

Table V-1 – Summary of PL data in THF solutions.

	Compound	Absorption Maximum (nm)	Extinction Coefficient (M^{-1} cm^{-1})	Emission Maximum (nm)	Excited State Lifetime (ns); R^2	Stokes Shift (cm^{-1})	Φ; λ_{ex} (nm)	Solid state Φ; λ_{ex} (nm)
99/1 H_2OTHF (v/v)	*p*CbAnth	421	1120	483	1.36; 0.99	3049	0.09; 412	0.31; 412
	*m*CbAnth	421	2160	486	0.98; 0.99	3177	0.11; 412	0.08; 412
	*o*CbAnth	428	4100	609	6.16; 0.99	6944	0.18; 350	0.38; 410
	*o*CbBDT	353	1050	613	-	12015	0.04; 350	0.04; 350
	*o*CbNTP	388	446	598	-	9050	0.21; 390	0.02; 390

Table V-2 – Summary of PL data in 99/1 H_2O/THF (v/v) solutions.

Appendix VI – Lippert-Mataga Equation

The Lippert-Mataga equation relates the orientation polarisability (Δf) to the solvent dielectric constant (ε), and refractive index (n):

$$\Delta f = f(\varepsilon) - f(n^2)$$

where,

$$f(\varepsilon) = \frac{(\varepsilon - 1)}{(2\varepsilon + 1)}, \qquad f(n^2) = \frac{(n^2 - 1)}{(2n^2 + 1)}.$$

The relevent solvent parameters are defined in **Table VI-1**.

Solvent (abbreviation)	Solvent dielectric constant (ε)	Refractive index (n)	Orientation polarisability (Δf)	Hildebrand polar parameter ($MPa^{1/2}$)
Acetonitrile (MeCN)	37.5	1.3441	0.305	18.0
Chlorobenzene (CB)	5.62	1.5248	0.143	4.3
Chloroform (CF)	4.81	1.4459	0.148	3.1
DMF	36.7	1.4305	0.274	13.7
Heptane (Hep)	2.1	1.3855	0.022	0.0
THF	7.6	1.4050	0.211	5.7
Toluene (Tol)	2.38	1.4961	0.013	1.4

Table VI-1 – Selected solvent quality parameters for the solvents used in the solvatochromic PL studies presented in this thesis.

Appendix VII – Optical Data from Chapter 4

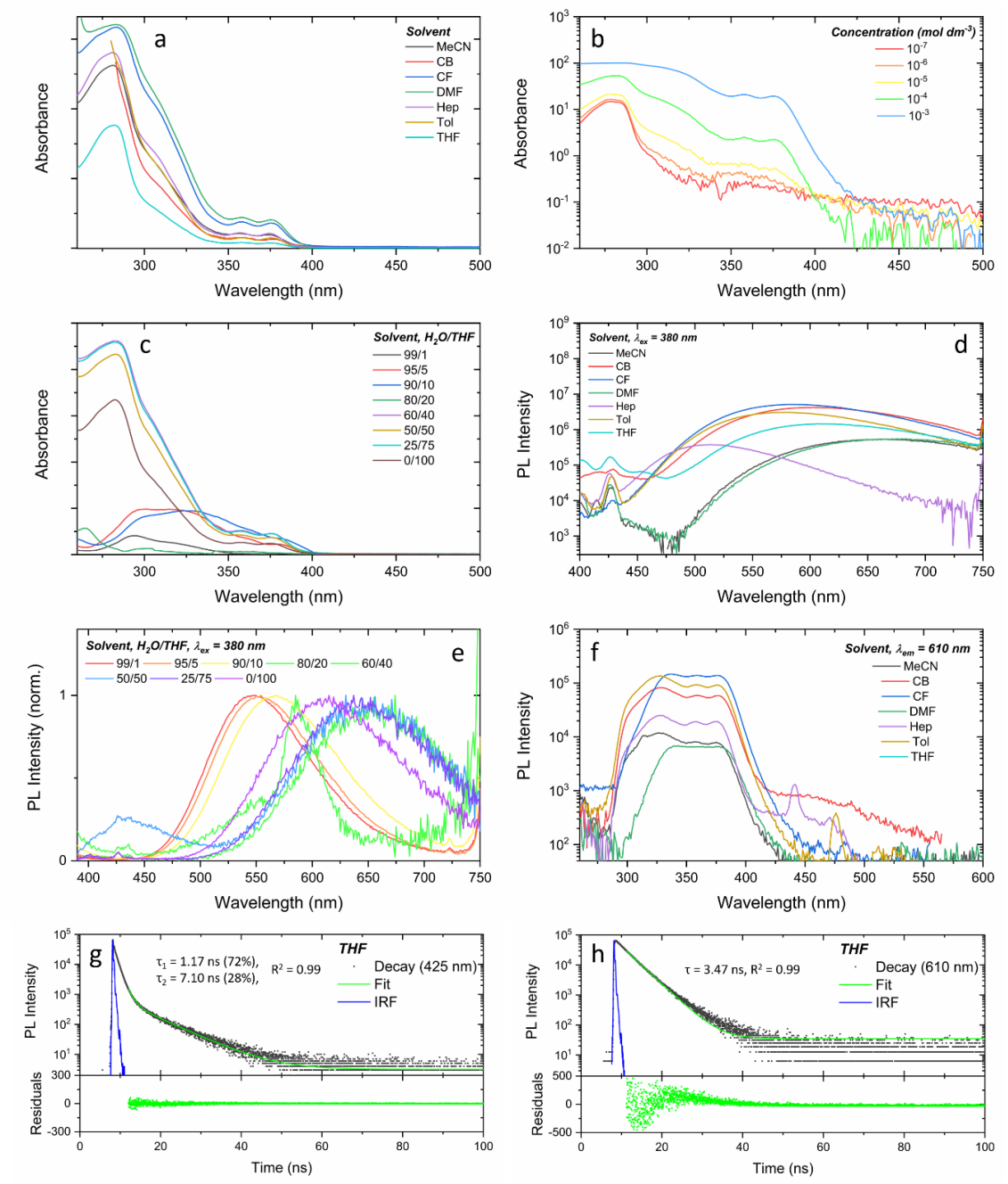


Figure VII-1 – Optical studies of **PhoCbPhen**. (a) Solvent-dependent UV-Vis; (b) concentration-dependent UV-Vis; (c) H_2O/THF (v/v) solvent-dependent UV-Vis; (d) solvent-dependent PL; (e) H_2O/THF (v/v) solvent-dependent PL (norm.); (f) solvent-dependent PLE; (g) time-resolved PL in THF, LE and; (h) time-resolved PL in THF, long-wavelength.

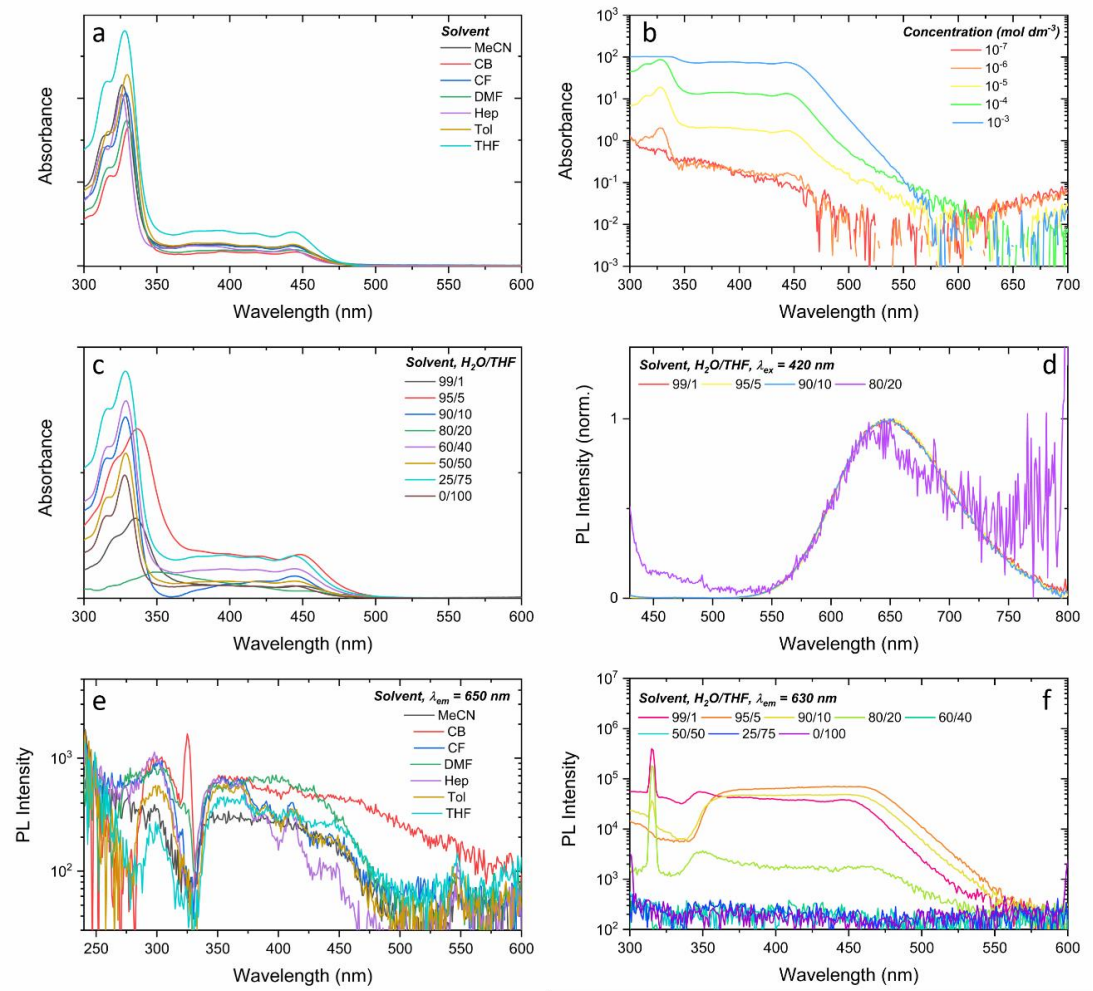


Figure VII-2 – Optical studies of **Pho*C*bBKT**. (a) Solvent-dependent UV-Vis; (b) concentration-dependent UV-Vis; (c) H_2O/THF (v/v) solvent-dependent UV-Vis; (d) H_2O/THF (v/v) solvent-dependent PL (norm.); (e) solvent-dependent PLE; (f) H_2O/THF (v/v) solvent-dependent PLE.

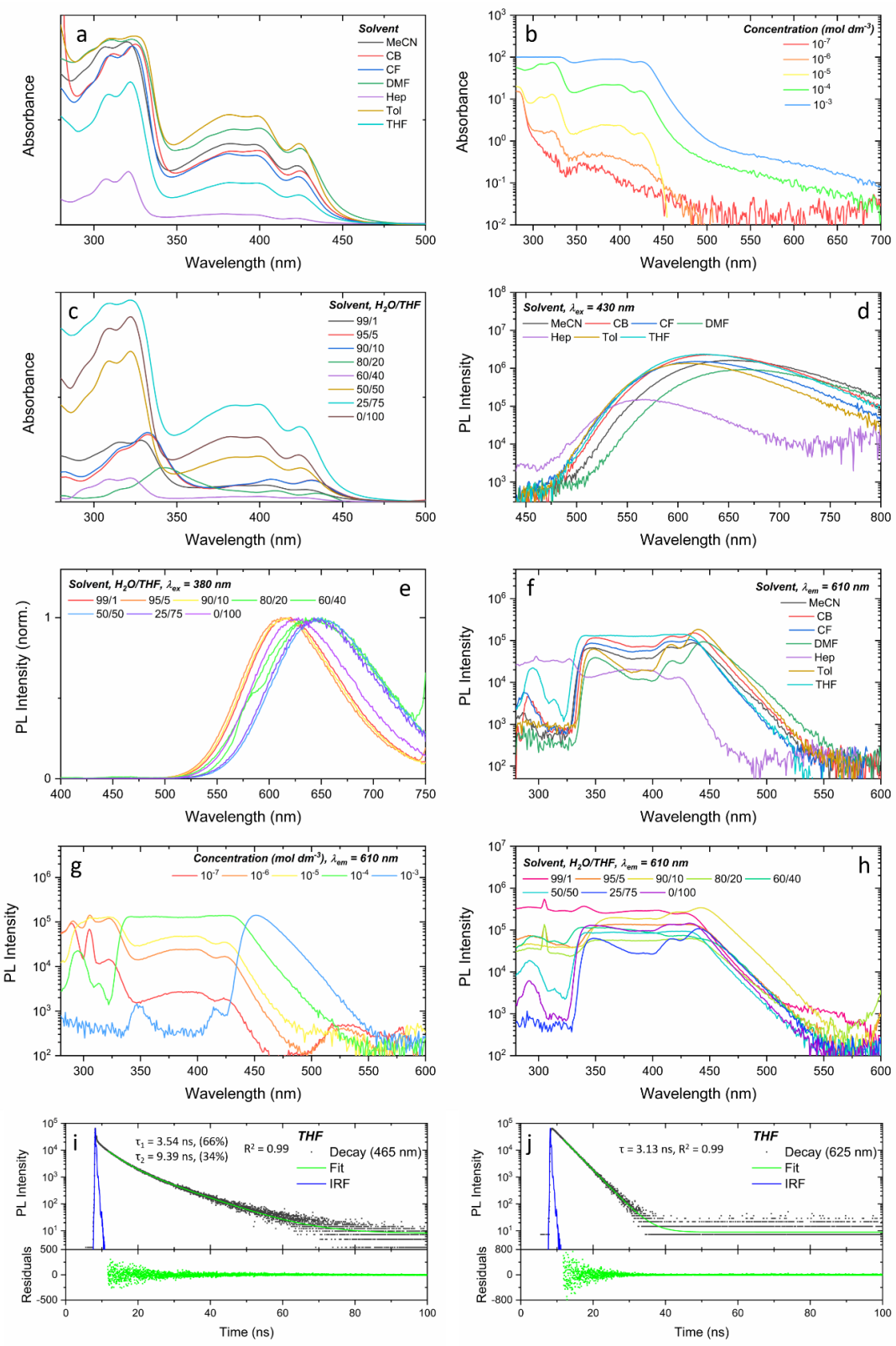


Figure VII-3 – Optical studies of **PhoCbBMT**. (a) Solvent-dependent UV-Vis; (b) concentration-dependent UV-Vis; (c) H_2O/THF (v/v) solvent-dependent UV-Vis; (d) solvent-dependent PL; (e) H_2O/THF (v/v) solvent-dependent PL (norm.); (f) solvent-dependent PLE; (g) concentration-dependent PLE; (h) H_2O/THF (v/v) solvent-dependent PLE; (i) time-resolved PL in THF, LE and; (j) time-resolved PL in THF, long-wavelength.

	Compound	Absorption Maximum (nm)	Extinction Coefficient (M^{-1} cm^{-1})	High Energy Emission Maximum (nm)	Excited State Lifetime (ns); R^2	Stokes Shift (cm^{-1})	Low Energy Emission Maximum (nm)	Excited State Lifetime (ns); R^2	Stokes Shift (cm^{-1})	Φ; λ_{ex} (nm)
THF	Pho*o*CbPhen	376	16500	426	1.17 (72%), 7.10 (28%); 0.99	3122	615	3.47; 0.99	10283	0.003; 380
	Pho*o*CbBKT	443	4900	-	-	-	-	-	-	0.00; 448
	Pho*o*CbBMT	424	4270	465	3.54 (66%), 9.39 (34%); 0.99	2080	628	1.05; 0.99	7600	0.22; 380

Table VII-1 – Summary of PL data in THF solutions.

	Compound	Absorption Maximum (nm)	Extinction Coefficient (M^{-1} cm^{-1})	Emission Maximum (nm)	Stokes Shift (cm^{-1})	Φ; λ_{ex} (nm)	Solid state Φ; λ_{ex} (nm)
99/1 H_2OTHF (v/v)	Pho*o*CbPhen	381	1833	550	8065	0.50; 380	0.50; 350
	Pho*o*CbBKT	447	1424	651	7010	0.11; 448	0.38; 350
	Pho*o*CbBMT	427	1342	618	7234	0.44; 380	0.50; 350

Table VII-2 – Summary of PL data in 99/1 H_2O/THF (v/v) solutions.

Appendix VIII – Optical Data from Chapter 5

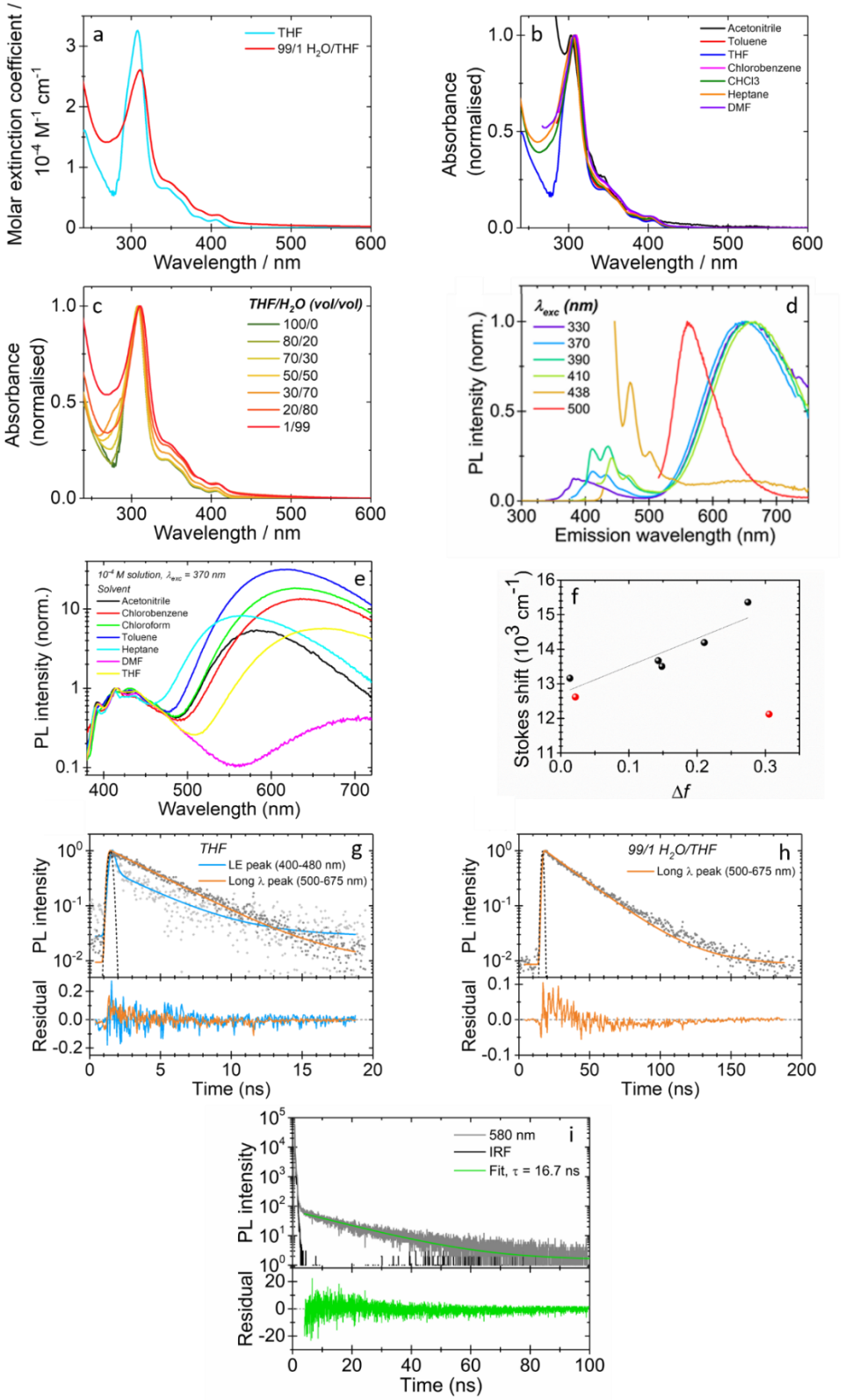


Figure VIII-1 – Optical studies of **PhoCb_2Chry**. (a) UV-Vis in THF and 99/1 H_2O/THF; (b) solvent-dependent UV-Vis; (c) varying H_2O/THF proportion UV-Vis; (d) normalised PL, excitation-dependent; (e) solvent-dependent PL; (f) Lippert-Mataga plot; (g) TRES PL in THF solution; (h) TRES PL in 99/1 H_2O/THF solution; and (i) TRES PL in the solid-state.

Appendix IX – Biodegradable UV Filters

IX.1 – Introduction

Without ultraviolet (UV) light this thesis would have been short; the excitation wavelengths used for the various PL studies presented are almost entirely UV (λ = 10-400 nm). Outside of the laboratory however, UV light is less useful and often dangerous. As a black body, our sun radiates at all UV wavelengths and, whilst most of the higher energy radiation is absorbed by the Earth's atmosphere, the longer wavelengths reach the Earth's surface and the organisms inhabiting it. These wavelengths are subdivided into three, UVC, UVB and UVA, according to their ability to penetrate the ozone layer, **Figure IX-1**.

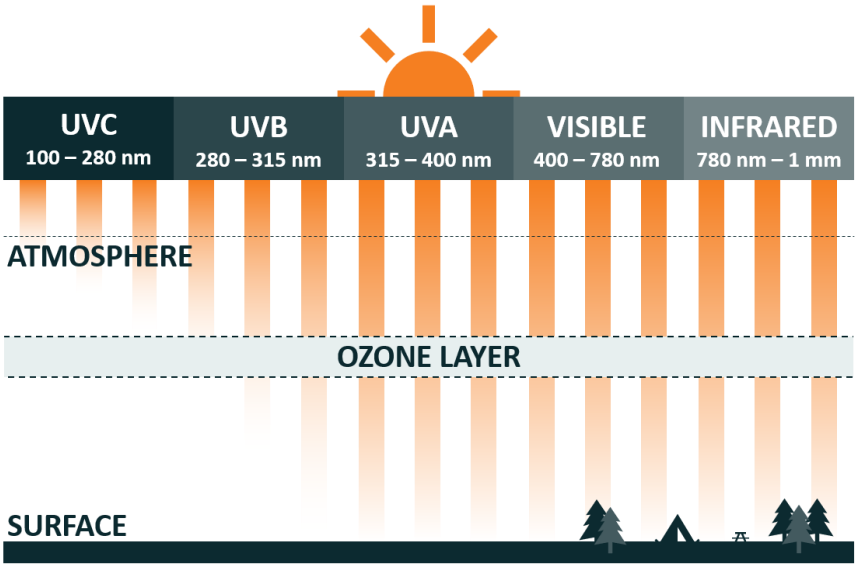
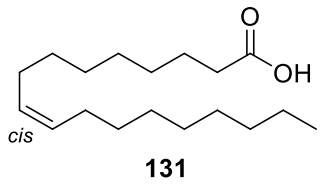


Figure IX-1 – Wavelength-dependent light penetration of the ozone layer. Figure adapted from [1].

Some degree of UV light exposure is beneficial for humans; the synthesis of vitamin D in the skin occurs via a reaction with cholesterol that requires UVB radiation. The optimum time period to achieve this effect is surprisingly short, however. For a person with fair skin in the summer, exposure of the hands, face, and arms for a period of approximately ten minutes is enough to keep vitamin D levels in the normal range.[1] However, extended periods of sun exposure are now well-known to be severely detrimental to health. UVB radiation can cause sunburn, eye damage, and directly damage DNA to form skin cancer;[2] UVA radiation contributes to malignancies through the formation of free radicals and reactive oxygen species in the skin, and all forms of UV damage collagen fibres and destroy vitamin

A, which accelerates skin aging.[2] It is therefore important to physically block UV radiation from entering the body using external UV filters, also known as sunscreens.

Sunscreens are not new; the ancient Greeks used olive oil,[3] and there are many other examples of natural products being used as a primitive form of UV protection. Olive oil is essentially a mixture of various mono and polyunsaturated carboxylic acids, with the key moiety being the *cis* double bond(s), **Figure IX-2**.



131

Figure IX-2 – The structure of oleic acid, a monounsaturated ester that is the primary ingredient in olive oil.

Conjugated systems, even isolated double bonds, are excellent absorbers of UV light, and *cis-trans* isomerism allows for efficient non-radiative relaxation of the excited state. Whilst the ancient Greeks could not have known any of this, they were clearly on to something with oleic acid (**131**) and this type of chemistry.

Modern sunscreens contain ingredients which protect from UV light by two main methods, light scattering inorganics and light absorbing organics. Inorganic compounds found in sunscreens are essentially limited to titanium dioxide and zinc oxide, and these act as physical barriers to UV light. Whilst they offer excellent broad-spectrum protection, they suffer the significant disadvantage of being aesthetically unappealing, due to appearing white on the skin.[4] Australian cricket players famously used such products in the early 2000s. Recently, the use of inorganic nanoparticles have allowed for virtually transparent sunscreens with a much wider market appeal, however, serious questions remain about their long-term toxicity and environmental impact.[5,6]

The organic compounds work fundamentally differently. They absorb the light, acting as UV filters, and release the energy non-radiatively. There are many such compounds on the market, a representative few are presented in **Figure IX-3**.

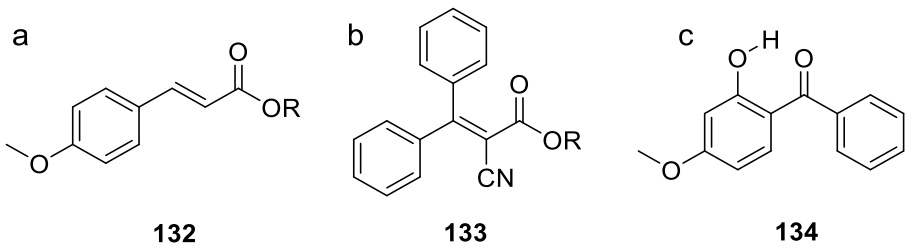


Figure IX-3 – The structures of common organic UV filters (a) octinoxate, (b) octocrylene, and (c) oxybenzone. R = 2-ethylhexyl solubilising group.

All three molecules are strikingly similar, they contain large, delocalised, aromatic systems which are the UV absorbing moieties. The alkene groups in octinoxate (**132**) and octocrylene (**133**) allow for non-radiative relaxation of the excited state through *cis-trans* isomerism, and the six-membered ring made by the alcohol and ketone of oxybenzone (**134**) achieves the same through excited state intramolecular proton transfer (ESIPT). The use of branched alkyl chains aids solubility in hydrophobic emollients which, apart from water, is the main ingredient in sunscreens, **Figure IX-4**.

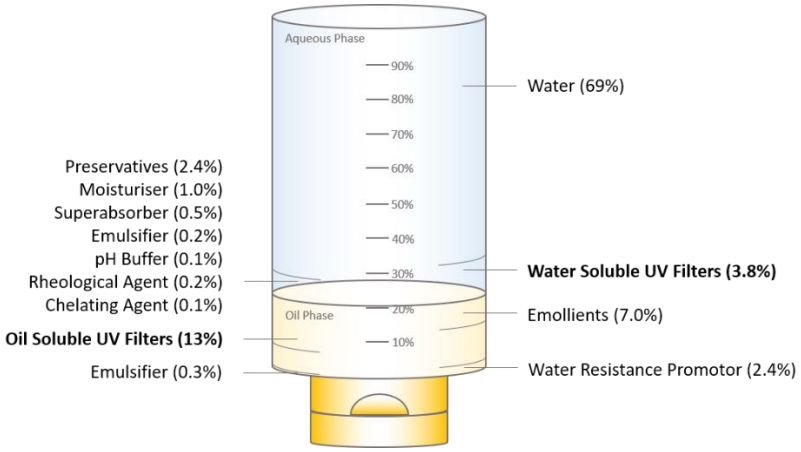


Figure IX-4 – The approximate composition of modern sunscreens.[7]

These compounds are very effective UV filters, but each has considerable known, or suspected, health or environmental issue associated with them. Oxybenzone is a derivative of benzophenone, which is phototoxic compound, forming free radicals in the presence of UV light. Some studies suggest oxybenzone is significantly less phototoxic than benzophenone,[8] but it *is* an endocrine disruptor,[9] as are octinoxate and octocrylene.[10] This is an intense area of study, and there are now reports of UV filters exhibiting estrogenic activity,[11] and have been proved to affect the development of sex glands in rats.[12]

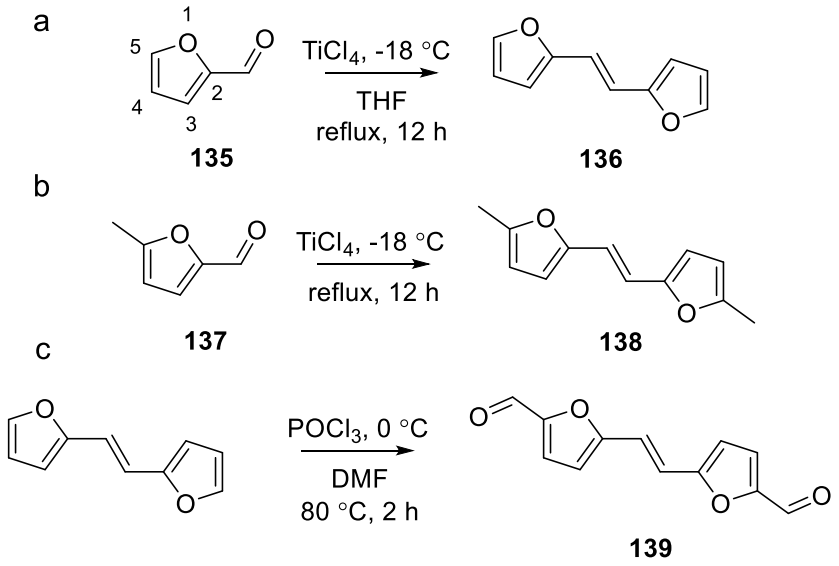
IX.2 – Aims

Recently there has also been significant environmental concern regarding both the organic and inorganic ingredients on sunscreens, and their effects on aquatic systems, especially corals, following bioaccumulation.[13,14] Seemingly without exception, the active UV protecting ingredients in modern sunscreens cause coral bleaching.[15–18] There is now significant push-back from society on this issue, and some countries are even banning the selling of products containing these chemicals.[19] Sunscreen manufacturers are now looking for new UV absorbers which are readily biodegradable, decomposing into CO_2 and biomass, such that they do not bioaccumulate and impact the functioning of fragile aquatic environments.

We began this project by considering which chemical building blocks offer the potential of being simultaneously good UV absorbers, readily biodegradable and cheap to synthesise. Furanic compounds have been demonstrated to be readily metabolised by Gram-negative aerobic bacteria.[20] In addition, both furfural and hydroxymethylfurfural are considered renewable feedstock chemicals, being derived from biomass,[21] and polymers of bifuran diester have been shown to be excellent UV blockers.[22] Inspired by this, we aimed to synthesise a series of simple furan-based compounds with good UV absorption properties, and to assess their photostability and biodegradability, with a view to creating the next generation of environmentally friendly UV filters for sunscreens.

IX.3 – Synthesis

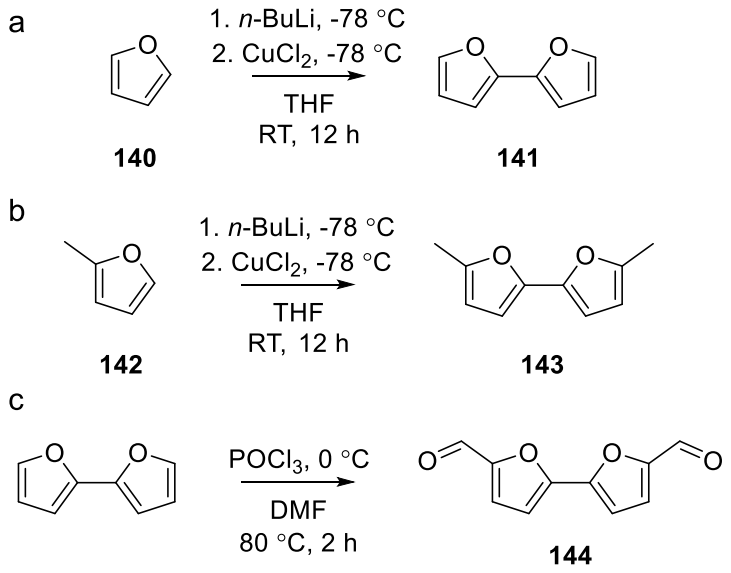
Borrowing from the architecture of optical brighteners, which are excellent UV absorbers (but also fluorescent),[23] a furanyl *trans*-stilbene was envisioned in which the phenyl groups are replaced with furan. A series of similar derivatives were designed, and synthesis was carried out as in **Scheme IX-1**.



Scheme IX-1 – The synthesis of furanyl stilbene derivatives with (a) proton, (b) methyl, and (c) aldehyde groups at the 2 and 5 furanyl positions.

The parent furanyl stilbene (**136**) was synthesised via a classic McMurray reaction according to a literature procedure, using furfural (**135**) starting material. Unfortunately, this compound is unstable, browning over a period of hours in light and air. Furfural is itself unstable but is more stable after the introduction of a methyl group, making 5-methyl-furfural (**137**) which blocks reactions at the 5 position.[24] The resulting stilbene (**138**) is more stable, but also slowly browns over a period of days. Both molecules are highly electron rich systems, and it was therefore theorised that introducing electron-withdrawing groups, such as aldehydes, on the furan rings may help stabilise the molecule. This was achieved using a Vilsmeier-Haak reaction on the parent furanyl stilbene. The product (**139**) is the most stable of furanyl stilbenes studied, however, the UV-Vis absorbance has a tail that extends well into the visible region (UV-Vis of all compounds are presented at the end of this Appendix in **Figure XI-5**). This makes solutions of the compound brown, which is undesirable for cosmetic applications. The $E_{1,1}$ value however, which is the absorbance of a 1 cm cuvette of a solution whose concentration is 1%, is large for these compounds (c.f. $E_{1,1}$ for octocrylene is 850 at λ = 310 nm). This was encouraging, but the instability issues meant it seemed sensible to look at other, less electron-rich, furan systems.

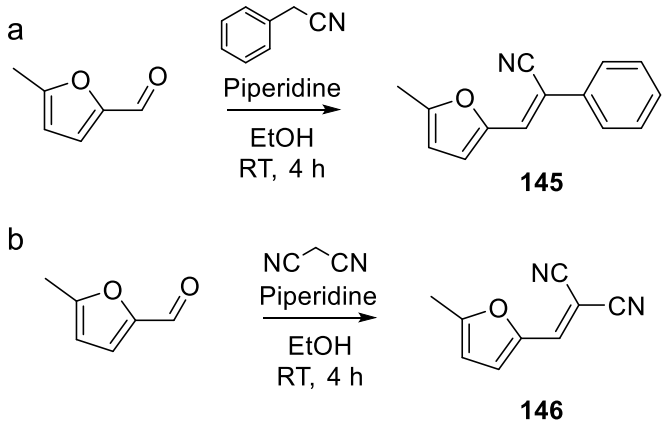
One such system is bifuran. It was theorised that the lack of the electron-rich alkene between the furans should make the system more stable towards oxidation relative to the furanyl stilbenes. Accordingly, three bifuran derivatives were synthesised from furan and 2-methylfuran starting materials (the latter of which is also being a renewable feedstock chemical),[25] **Scheme IX-2**.



Scheme IX-2 – The synthesis of bifuran derivatives with (a) proton, (b) methyl, and (c) aldehyde groups at the 2 and 5 furanyl positions.

The bifuran derivatives were synthesised via copper cross-coupling reactions from the deprotonated furan (**140**). Bifuran (**141**) itself is formed in a reasonable yield (~45%), as a colourless oil, but this slowly discolours over a period of days when exposed to light and air, suggesting once again that protection of the furanyl α-protons is required for stability, and so 2-methyl-furan (**142**) was used. The methyl-protected bifuran (**143**) is reported to be formed in good yield of 72%,[26] but the best yield we achieved is much lower, at 20%. A thorough inspection of the reported synthesis, however, shows a miscalculation with the percentage yield, and in fact the real literature value is 18%. Therefore, whilst still low, our yield matches favourably with that reported. This compound proved to be much more stable than bifuran, likely aided by the fact it crystallises upon standing. However, the absorbance is concentrated at relatively high energies in the UVB range, with much of the energy being absorbed at wavelengths lower than 280 nm. The lack of UVA absorbance is undesirable; therefore, an attempt was made to red-shift the absorbance with electron-withdrawing aldehyde groups. A Vilsmeier-Haak reaction on bifuran yielded the desired compound (**144**) in good yield (68%), but, like in the case of the furanyl stilbene, the compound absorbs into the visible light range and appears brown in solution. All compounds were very soluble (>60%) in emollients; mixtures of decane and similar long chain hydrocarbons which make up the hydrophobic portion of sunscreens. Solubility of 20% is a good benchmark value, and UV filters can be dissolved in either the oil or aqueous phase. Therefore, whilst the methyl protected bifuran absorbs at quite high energy, it was considered a good candidate to take forward for photostability and biodegradability testing, and 20 g were synthesised.

Encouraged by the ability to bathochromically shift the absorbance, albeit too far, for the furanyl stilbene and bifuran compounds, a different architecture was envisaged containing one electron-rich furan, and an electron-poor acceptor group, in a push-pull system. Two compounds were synthesised, as shown in **Scheme IX-3**.



Scheme IX-3 – The Knoevenagel condensation synthesis of 5-methylfurfural and (a) benzyl cyanide, or (b) malononitrile.

Reactions of 5-methylfurfural with both benzyl cyanide and malononitrile in Knoevenagel condensations formed the products (**145** and **146** respectively) in high yield. These compounds both have excellent broad-spectrum and intense absorbance in the UVA range, with the dinitrile compound having a slightly higher $E_{1,1}$ value. This is probably a result of the lower molecular weight of the dinitrile compared to the benzyl nitrile furan. Solubility in emollients was low however; approximately 2% in decane. Whilst this is too low for commercial applications, it is easy to see how one could increase solubility by replacing the methyl group with a longer alkane. Addition of atoms which do not contribute to UV light absorption has the effect of reducing the $E_{1,1}$ value, as it is dependent on molecular weight, but the absorption of these compounds is sufficiently high that such a compromise is acceptable in this case. On this basis, the dinitrile compound was chosen as the second candidate for further testing, and 20 g of this compound was synthesised.

IX.4 – Photostability and Biodegradability*

Photostability testing is in two parts. First, a fast screening test in which compounds are dissolved (2% by weight) in dry and deoxygenated ethanol. They are then subjected to a 10 minimal erythemal dose (MED), which is the minimum exposure to UV light that causes reddening of the skin, occurring within

* Both photostability and biodegradability measurements were carried out externally. Detailed experimental information and results are not available for this thesis.

1-6 hours, but disappearing within 24 hours, of exposure. A photostable compound will have 80% recovery after this test (as measured by UV-Vis). Compounds which pass this test are then dissolved in a model sunscreen formulation, containing water and oxygen, and submitted to the same testing. An 80% recovery after a 20 MED dose is required to pass this second test.

After the first test, the bifuran compound **143** was mostly destroyed, with only 19% recovery after a 10 MED dose in dry and deoxygenated ethanol. For a compound which did not have any obvious photostability problems in the laboratory, it was surprising it performed so poorly. It was additionally surprising given that **146** showed 99.8% recovery following the same procedure. It may be that the highly electron-withdrawing nitrile groups help stabilise the excited states of this compound, such that the molecule does undergo photodissociation.

The dinitrile compound **146** was then taken forward into the formulation test. It was found to be completely unstable; after 10 MED there was 0% recovery of the compound. It is likely that the oxygen and water in the formulation allowed for facile oxidation and decomposition of the energetic excited states. Similar other furan-based compounds synthesised by other researcher suffered precisely the same fate. The furan-based UV filters are very good absorbers of UV light, but the in-built mechanism for efficient non-radiative decay, namely *cis-trans* isomerism, is seemingly not sufficient to stabilise them towards photodecomposition.

Whilst the furan compounds were found to be photounstable, it was hoped that they would at least be eminently biodegradable. This would allow scope for redesigning the structures, to increase photostability whilst maintaining biodegradability. The biodegradability studies were carried out in biochemical oxygen demand test bottles, which measures the amount of oxygen consumed by biological organisms during their aerobic activities. The organisms are extracted from sewage water and placed in the bottle, in aqueous solution, before the sample for biodegradability testing is added. The organisms then consume and break-down the sample, and the extent of this is measured as a function of consumed oxygen. According to OECD Test No. 301, compounds which show 70% degradation after 28 days are considered readily biodegradable.[27]

After 28 days the bifuran compound **143** showed essentially 0% biodegradability, with only a small increase in the oxygen uptake hardly indistinguishable from the baseline. The dinitrile compound **146** is more interesting; a lag time of 6 days preceded accelerated degradation, leading to ca. 40% degradation after 28 days. The lag time is not unusual for these measurements, the organisms sometimes take time to produce the enzymes needed to digest their new food source. Therefore, a period of zero aerobic activity precedes intense metabolism. Whilst interesting, the results for these

compounds are disappointing, and other furan-based UV filters were found to be similarly resistant to biodegradation. This is somewhat surprising based on the literature precedent for biodegradation of furanyl compounds, however, the results demonstrate that biodegradability is highly sensitive to even small changes in molecular structure.

IX.5 – Conclusions

In conclusion, several furan-based UV filters were synthesised, and their absorbance in solution was measured. The $E_{1,1}$ values and spectral coverage in the UV region were generally very good, however many of the compounds suffered from clear instability towards light and air. Two of the most promising candidates were chosen for photostability and biodegradability testing, however there were problems in both regards. Neither compound passed both photostability tests, with the bifuran compound degrading completely in even dry and deoxygenated ethanol upon UV irradiation. The dinitrile furan compound was similarly unstable when irradiated in a model formulation. The compounds showed large differences in biodegradability; the bifuran compound showed no degradation after 28 days, but the dinitrile compound had degraded 40% in the same time. The resistance to degradation of the furanyl compounds was a surprising result based on literature precedence on this subject. This, coupled with the photoinstability issues, makes it unlikely that a furan-based approach will yield any commercially viable, biodegradable, UV filters for sunscreens.

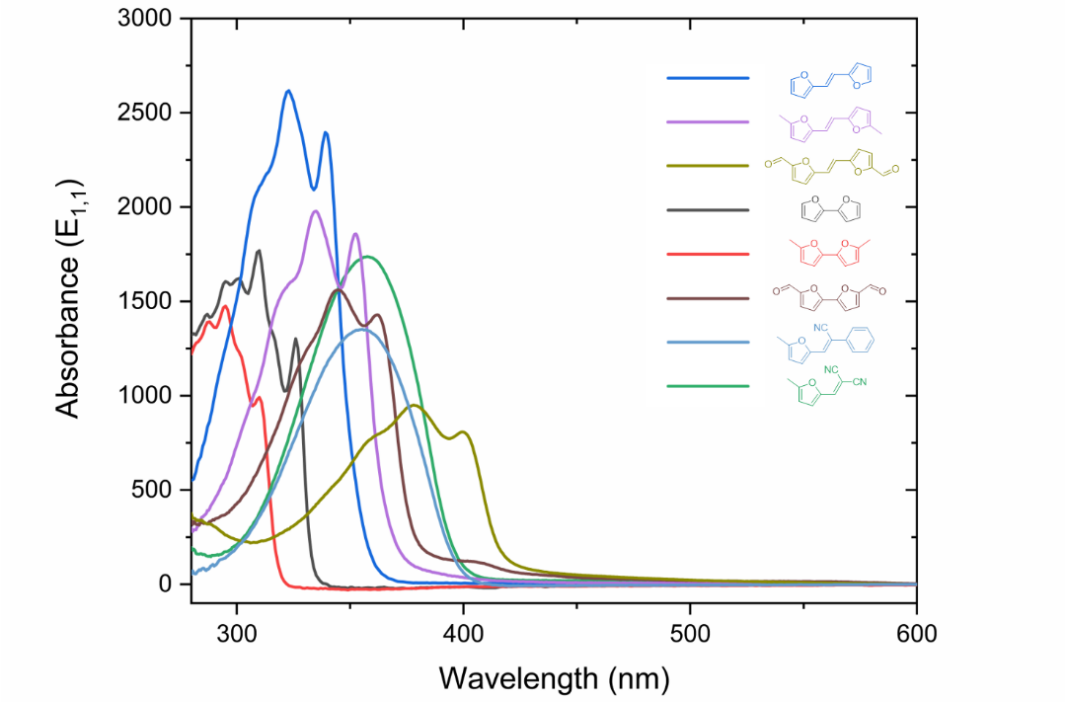
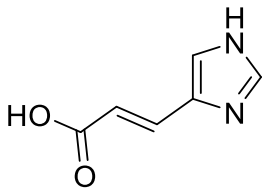


Figure IX-5 – UV-Vis spectra of all the synthesised UV filters in this study; concentrations ~10 µM, in 1,4-dioxane.

IX.6 – Further Work

Due to the photoinstability of the furan-based compounds, it seems rational to find a new chromophore around which to build a photostable UV absorber. Imidazole is promising in this regard; it forms, as part of a fused heterocycle with pyrimidine, the purines which comprise half the base pairs in DNA. The photostability of DNA is highly dependent upon the purines, and specifically the 'pyrrole-like' nitrogen site. Indeed, urocanic acid (**147**) is an imidazole containing biomolecule concerned with UV protection of the skin, **Figure IX-6**.



147

Figure IX-6 – Urocanic acid.

This acid is was once thought to be a 'natural' sunscreen,[28] however it has since been shown that the quantities present in the skin only provide minimal protection against sunburn.[29] It is now thought it acts as a photoreceptor in the skin to regulate the immune system following doses of UV-radiation; the accumulation of the cis-isomer following photoinduced isomerisation acts as the signal to activate regulatory T-cells.[30]

Clearly, the spectral coverage of this molecule is in the energy region of interest for skin protection - being that it is used for that exact purpose in the body - and the *cis*-*trans* isomerisation is one route to relaxation of the excited state. Importantly however, the N-H group in the imidazole is also able to dissipate energy through reversible H-atom elimination.[31] Further, in the case of the purine, this nitrogen site is also thought to help dissipate energy of excited state, even though the proton is substituted for the sugar, ribose. It seems likely that a large proportion of the excited states can relax from the $n\pi^*$ state into the ground state via a conical intersection.[32] The exact processes which concern this photostability are outside the scope of this project, however, this information may provide some guidance for molecular design strategies.

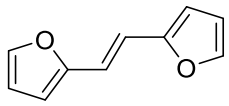
The literature highlights a few points of caution regarding imidazole, however. Imidazoles are used as anti-fungal agents,[33] and some imidazole containing compounds have also shown anti-bacterial properties,[34,35] which may reduce the biodegradability of the compounds, at least in the test procedure.

Some imidazole compounds are also fluorescent, even when the N-H group is present,[36,37] however in these cases the LUMO seems to be localised away from the imidazole subunit. It is not clear that this is the reason why the imidazole chromophore does not quench the fluorescence through the non-radiative decay pathways in these molecules, but this may be a guiding principle for the design of imidazole UV absorbers.

IX.7 – Experimental

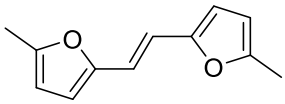
Experimental details for this appendix are identical to those detailed in **Chapter 2**.

(E)-1,2-di(furan-2-yl)ethene (136)



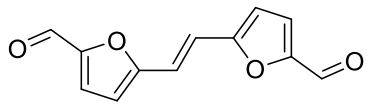
Synthesised according to literature procedure.[38]

(E)-1,2-bis(5-methylfuran-2-yl)ethene



To a solution of 5-methylfuran-2-carbaldehyde (1.54 g, 14.0 mmol) in THF (25 mL) at −18 °C was added $TiCl_4$ (1.84 mL, 16.8 mmol) dropwise over a period of 30 min. The mixture was stirred for 30 min and Zn powder (2.20 g, 33.6 mmol) was added in four portions over the course of 30 min. Stirring was continued for a further 1 h before being the mixture was warmed to room temperature, and then refluxed overnight. The reaction was quenched by adding ice water (200 mL) and extracted with DCM (3 × 100 mL). The organic phases were combined and dried over anhydrous $MgSO_4$. Solvent was removed *in vacuo*, and the residue was subjected to column chromatography, eluting with 1:1 DCM:Pet. ether. Recrystallisation from Pet. ether yielded the *title compound* as a yellow solid (0.83 g, 7.0 mmol, 50% yield). Characterisation matched literature reports.[39]

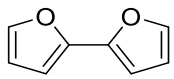
(E)-5,5'-(ethene-1,2-diyl)bis(furan-2-carbaldehyde) (138)



(E)-1,2-di(furan-2-yl)ethene (500 mg, 3.12 mmol) was dissolved in DMF (5 mL) at 0°C, and treated dropwise with $POCl_3$ (0.66 mL, 7.00 mmol) over a period of 10 mins, stirred for 1 h at room temperature and then heated to 80 °C for 2 h. The mixture was cooled back to room temperature and poured over ice water (50 g). Basifying the solution with solid K_2CO_3 precipitated a dark brown solid which was filtered, washed with water (200 mL), -78 °C methanol (100 mL) and recrystallised from hot

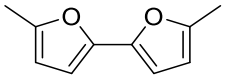
ethanol to yield the *title compound* as brown crystals (506 mg, 2.34 mmol, 75%). Characterisation matched literature reports.[40]

2,2'-Bifuran (141)



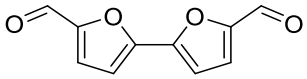
Synthesised according to literature procedure.[41]

5,5'-Dimethyl-2,2'-bifuran (143)



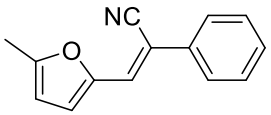
Synthesised according to literature procedure.[26]

[2,2'-Bifuran]-5,5'-dicarbaldehyde (144)



2,2'-Bifuran (1.40 g, 10.4 mmol) was dissolved in DMF (20 mL) at 0°C, and treated dropwise with $POCl_3$ (2.33 mL, 25.0 mmol) over a period of 10 mins, stirred for 1 h at room temperature and then heated to 80 °C for 2 h. The mixture was cooled back to room temperature and poured over ice water (200 g). Basifying the solution with solid K_2CO_3 precipitated a brown solid which was filtered, washed with water (200 mL), -78 °C methanol (100 mL) and recrystalised from ethanol to yield the *title compound* as yellow-brown crystals (1.34 g, 7.07 mmol, 68%). Characterisation matched literature reports.[42]

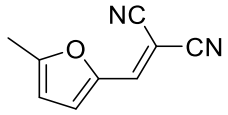
(Z)-3-(5-methylfuran-2-yl)-2-phenylacrylonitrile (145)



To benzyl cyanide (2.34 g, 20 mmol) dissolved in EtOH (40 mL) was added 5-methylfuran-2-carbaldehyde (2.20g, 20 mmol) followed by 2 drops of piperidine. The reaction was stirred at room temperature for 4 hours before being poured in to water, filtered and washed with water (100 mL) and cold methanol (100 mL) to obtain the product as a yellow solid. Recrystallisation from ethanol

afforded the *title compound* as yellow crystals (1.63 g, 7.80 mmol, 39%). Characterisation matched literature reports.[43]

2-((5-Methylfuran-2-yl)methylene)malononitrile (146)



To malononitrile (1.32 g, 20 mmol) dissolved in EtOH (40 mL) was added 5-methylfuran-2-carbaldehyde (2.20g, 20 mmol) followed by 2 drops of piperidine. The reaction was stirred at room temperature for 4 hours before being poured in to water, filtered and washed with water (100 mL) and cold methanol (100 mL) to obtain the product as a yellow solid. Recrystallisation from ethanol afforded the *title compound* as yellow crystals (1.42 g, 9.00 mmol, 45%). Characterisation matched literature reports.[44]

IX.8 – References

1 R. M. Lucas, M. H. Repacholi and A. J. McMichael, *Bull World Health Organ*, 2006, **84**, 485–491.
2 J. D'Orazio, S. Jarrett, A. Amaro-Ortiz and T. Scott, *Int J Mol Sci*, 2013, **14**, 12222–12248.
3 A. S. Aldahan, V. V. Shah, S. Mlacker and K. Nouri, *JAMA Dermatol*, 2015, **151**, 1316–1316.
4 G. P. Dransfield, *Radiat Prot Dosimetry*, 2000, **91**, 271–273.
5 M. Ates, V. Demir, R. Adiguzel and Z. Arslan, Bioaccumulation, Subacute Toxicity, and Tissue Distribution of Engineered Titanium Dioxide Nanoparticles in Goldfish (Carassius auratus), https://www.hindawi.com/journals/jnm/2013/460518/, (accessed 25 January 2019).
6 J. A. Ruszkiewicz, A. Pinkas, B. Ferrer, T. V. Peres, A. Tsatsakis and M. Aschner, *Toxicology Reports*, 2017, **4**, 245–259.
7 World Intellectual Property Organization, WO2008097223A1, 2008.
8 M. Placzek, M. Dendorfer, B. Przybilla, K.-P. Gilbertz and B. Eberlein, *Acta Derm. Venereol.*, 2013, **93**, 30–32.
9 A. Santovito, S. Ruberto, G. Galli, C. Menghi, M. Girotti and P. Cervella, *Drug and Chemical Toxicology*, 2018, **0**, 1–8.
10 J. Wang, L. Pan, S. Wu, L. Lu, Y. Xu, Y. Zhu, M. Guo and S. Zhuang, *Int J Environ Res Public Health*, , DOI:10.3390/ijerph13080782.
11 M. Schlumpf, P. Schmid, S. Durrer, M. Conscience, K. Maerkel, M. Henseler, M. Gruetter, I. Herzog, S. Reolon, R. Ceccatelli, O. Faass, E. Stutz, H. Jarry, W. Wuttke and W. Lichtensteiger, *Toxicology*, 2004, **205**, 113–122.
12 Hofkamp Luke, Bradley Sarahann, Tresguerres Jesus, Lichtensteiger Walter, Schlumpf Margret and Timms Barry, *Environmental Health Perspectives*, 2008, **116**, 867–872.
13 P. Gago-Ferrero, M. S. Díaz-Cruz and D. Barceló, *Science of The Total Environment*, 2015, **518**–**519**, 518–525.
14 L. Vidal-Liñán, E. Villaverde-de-Sáa, R. Rodil, J. B. Quintana and R. Beiras, *Chemosphere*, 2018, **190**, 267–271.
15 R. Danovaro, L. Bongiorni, C. Corinaldesi, D. Giovannelli, E. Damiani, P. Astolfi, L. Greci and A. Pusceddu, *Environmental Health Perspectives*, 2008, **116**, 441–447.
16 C. A. Downs, E. Kramarsky-Winter, J. E. Fauth, R. Segal, O. Bronstein, R. Jeger, Y. Lichtenfeld, C. M. Woodley, P. Pennington, A. Kushmaro and Y. Loya, *Ecotoxicology*, 2014, **23**, 175–191.
17 C. A. Downs, E. Kramarsky-Winter, R. Segal, J. Fauth, S. Knutson, O. Bronstein, F. R. Ciner, R. Jeger, Y. Lichtenfeld, C. M. Woodley, P. Pennington, K. Cadenas, A. Kushmaro and Y. Loya, *Arch Environ Contam Toxicol*, 2016, **70**, 265–288.
18 C. Corinaldesi, F. Marcellini, E. Nepote, E. Damiani and R. Danovaro, *Science of The Total Environment*, 2018, **637**–**638**, 1279–1285.
19 Research leads to first nationwide sunscreen chemicals ban in Palau, https://phys.org/news/2018-11-nationwide-sunscreen-chemicals-palau.html, (accessed 25 January 2019).
20 N. Wierckx, F. Koopman, H. J. Ruijssenaars and J. H. de Winde, *Appl Microbiol Biotechnol*, 2011, **92**, 1095–1105.
21 R. Mariscal, P. Maireles-Torres, M. Ojeda, I. Sádaba and M. L. Granados, *Energy Environ. Sci.*, 2016, **9**, 1144–1189.
22 T. P. Kainulainen, J. A. Sirviö, J. Sethi, T. I. Hukka and J. P. Heiskanen, *Macromolecules*, 2018, **51**, 1822–1829.
23 A. E. Siegrist, C. Eckhardt, J. Kaschig and E. Schmidt, in *Ullmann's Encyclopedia of Industrial Chemistry*, ed. Wiley-VCH Verlag GmbH & Co. KGaA, Wiley-VCH Verlag GmbH & Co. KGaA, Weinheim, Germany, 2003.
24 K. J. Zeitsch, Ed., in *Sugar Series*, Elsevier, 2000, vol. 13, pp. 28–33.

25 W. Wang, N. Li, S. Li, G. Li, F. Chen, X. Sheng, A. Wang, X. Wang, Y. Cong and T. Zhang, *Green Chem.*, 2016, **18**, 1218–1223.

26 S. Gadakh, L. J. W. Shimon and O. Gidron, *Angewandte Chemie International Edition*, 2017, **56**, 13601–13605.

27 OECD, *Test No. 301: Ready Biodegradability, OECD Guidelines for the Testing of Chemicals, Section 3*, OECD Publishing, Paris, 1992.

28 M. Norval, *Progress in Biophysics and Molecular Biology*, 2006, **92**, 108–118.

29 F. de Fine Olivarius, H. C. Wulf, J. Crosby and M. Norval, *Acta Derm. Venereol.*, 1999, **79**, 426–430.

30 T. Schwarz, *Keio J Med*, 2005, **54**, 165–171.

31 G. M. Roberts, C. A. Williams, M. J. Paterson, S. Ullrich and V. G. Stavros, *Chem. Sci.*, 2012, **3**, 1192–1199.

32 H. Satzger, D. Townsend, M. Z. Zgierski, S. Patchkovskii, S. Ullrich and A. Stolow, *PNAS*, 2006, **103**, 10196–10201.

33 D. J. Sheehan, C. A. Hitchcock and C. M. Sibley, *Clin. Microbiol. Rev.*, 1999, **12**, 40–79.

34 H.-S. Kim, J. R. Jadhav, S.-J. Jung and J.-H. Kwak, *Bioorganic & Medicinal Chemistry Letters*, 2013, **23**, 4315–4318.

35 N. Rani, A. Sharma and R. Singh, *Mini Rev Med Chem*, 2013, **13**, 1812–1835.

36 N. Nagarajan, G. Velmurugan, P. Venuvanalingam and R. Renganathan, *Journal of Photochemistry and Photobiology A: Chemistry*, 2014, **284**, 36–48.

37 V. Barone, F. Bellina, M. Biczysko, J. Bloino, T. Fornaro, C. Latouche, M. Lessi, G. Marianetti, P. Minei, A. Panattoni and A. Pucci, *Phys. Chem. Chem. Phys.*, 2015, **17**, 26710–26723.

38 Y. Wang, T. Hasegawa, H. Matsumoto, T. Mori and T. Michinobu, *Advanced Functional Materials*, 2017, **27**, 1604608.

39 Z. A. Krasnaya, S. S. Yufit, T. S. Levchenko and V. F. Kucherov, *Tetrahedron*, 1967, **23**, 3687–3697.

40 E. H. Elandaloussi, P. Frère, A. Benahmed-Gasmi, A. Riou, A. Gorgues and J. Roncali, *J. Mater. Chem.*, 1996, **6**, 1859–1863.

41 Jun Zhang, Peijun Ye, Lu He, Ting Yuan and Qiancai Liu, *Heterocycles*, 2015, **91**, 2190–2196.

42 B. Taljaard and G. J. Burger, *Advanced Synthesis & Catalysis*, 2002, **344**, 1111–1114.

43 I. Esen, C. Yolacan and F. Aydogan, *Bulletin of the Korean Chemical Society*, 2010, **31**, 2289–2292.

44 M. Mantri, O. de Graaf, J. van Veldhoven, A. Göblyös, J. K. von Frijtag Drabbe Künzel, T. Mulder-Krieger, R. Link, H. de Vries, M. W. Beukers, J. Brussee and A. P. IJzerman, *J. Med. Chem.*, 2008, **51**, 4449–4455.